# MODELLING, DESIGN AND STABILITY ANALYSIS OF MULTI-INPUT MULTI-OUTPUT DC-DC CONVERTERS TO INTEGRATE RENEWABLE ENERGY SOURCES

A Thesis Submitted in Partial Fulfillment of the Requirements for the Degree of

### **DOCTOR OF PHILOSOPHY**

in

**Electrical Engineering** 

by

Ashutosh (2k20/Ph.D./EE/504)

**Under the Supervision of** 

Dr. Dheeraj Joshi Professor, Electrical Engineering Delhi Technological University, Delhi



Department of Electrical Engineering

DELHI TECHNOLOGICAL UNIVERSITY

(Formerly Delhi College of Engineering)

Shahbad Daulatpur, Main Bawana Road, Delhi-110042, India

January, 2025



#### **DELHI TECHNOLOGICAL UNIVERSITY**

(Formerly Delhi College of Engineering) Shahbad Daulatpur, Main Bawana Road, Delhi-42

### **CANDIDATE'S DECLARATION**

I, Ashutosh hereby certify that the work which is being presented in the thesis entitled "MODELLING, DESIGN AND STABILITY ANALYSIS OF MULTI-INPUT MULTI-OUTPUT DC-DC CONVERTERS TO INTEGRATE RENEWABLE ENERGY SOURCES" in partial fulfillment of the requirements for the award of the Degree of Doctor of Philosophy, submitted in the Department of Electrical Engineering, Delhi Technological University is an authentic record of my own work carried out during the period from January 2021 to December 2024 under the supervision of Dr. Dheeraj Joshi.

The matter presented in the thesis has not been submitted by me for the award of any other degree of this or any other Institute.

Candidate's Signature

# DELTECH \*

#### **DELHI TECHNOLOGICAL UNIVERSITY**

(Formerly Delhi College of Engineering) Shahbad Daulatpur, Main Bawana Road, Delhi-42

#### **CERTIFICATE BY THE SUPERVISOR**

Certified that <u>Ashutosh</u> (2K20/Ph.D./EE/504) has carried out their search work presented in this thesis entitled "<u>Modelling, Design and Stability Analysis of Multi-Input Multi-Output DC-DC Converters to integrate Renewable Energy Sources</u>" for the award of <u>Doctor of Philosophy</u> from Department of Electrical Engineering, Delhi Technological University, Delhi, under my supervision. The thesis embodies results of original work, and studies are carried out by the student himself and the contents of the thesis do not form the basis for the award of any other degree to the candidate or to anybody else from this or any other University/Institution.

Signature

Dr. Dheeraj Joshi
Professor
Department of Electrical Engineering
Delhi Technological University
Delhi

Date:

#### ACKNOWLEDGEMENTS

I would like to take this opportunity to express my deepest gratitude to my supervisor, Dr. Dheeraj Joshi, Professor, Electrical Engineering Department, Delhi Technological University. His persistent and inspiring guidance, innovative ideas, constant support, and encouragement have been instrumental in helping me achieve my goals. Working under his supervision has been a privilege, and despite his busy schedule, he has always been willing to discuss and resolve my issues, especially during weekends. Conducting research under his direction has provided me with significant opportunities for professional development and lifelong learning.

I extend my sincere thanks to the Head of the Department (EED) and all the faculty members of the Electrical Engineering Department, DTU, for their invaluable advice and engaging manner during coursework and progress presentations. I am deeply grateful to the EED staff, Miss Vandana and Miss Renu for their cooperation and support throughout this process. My heartfelt thanks go to Dr. Simmi Sharma, Dr. Sandeep Banerjee, Mrs. Ritambhara Katoch, Mrs. Manvi Mishra, and Mr. Md Masoom, whose assistance was crucial in resolving numerous complex issues.

I express my profound appreciation to my parents for their love, blessings, and sacrifices. Special thanks are due to my wife, Mrs. Megha, who made significant adjustments to accommodate my hectic schedule and to my lucky charm daughter Aadya. I am also grateful to my friend, Mr. Saurabh Mishra, Faculty, EED, for his timely advice and support. Lastly, I thank my extended family for their unwavering support during challenging times.

Ashutosh 2K20/Ph.D./EE/504

Research Scholar
Department of Electrical Engineering
Delhi Technological University
email: ashutoshgupta.nitm@gmail.com

# MODELLING, DESIGN AND STABILITY ANALYSIS OF MULTI-INPUT MULTI-OUTPUT DC-DC CONVERTERS TO INTEGRATE RENEWABLE ENERGY SOURCES

#### **ABSTRACT**

Multiple-input multiple-output (MIMO) converters are emerging as a cost-effective and efficient solution for energy harvesting and distribution in hybrid power systems, including applications such as smart homes and DC microgrids. Unlike traditional single-input single-output (SISO) converters, which often require complex setups involving multiple units interconnected at a common DC bus, MIMO converters simplify the system architecture by integrating multiple energy sources and loads within a single converter. This results in several advantages, including reduced component count, increased power density, and the ability to implement centralized control, making MIMO converters an attractive choice for modern energy systems.

This thesis explores various aspects of MIMO converter development, addressing both theoretical and practical challenges. It introduces both non-isolated and isolated MIMO converter topologies designed to handle the diverse demands of hybrid power systems. The non-isolated MIMO converters, such as isolated converters, like flyback topologies, multiport boost converter and high gain z-source converter topologies, are thoroughly analyzed. Steady-state performance and dynamic behavior are examined in detail, providing insights into their operational efficiency and reliability. One of the key contributions of this research is the development of innovative switching strategies and control algorithms tailored to MIMO converters. These strategies enable precise power distribution among multiple energy sources and loads while maintaining stable output voltages. The ability to dynamically allocate power based on load requirements and source availability ensures optimal utilization of resources, enhancing system efficiency. A novel method for designing non-isolated MIMO converters featuring Single inductors (SI) is proposed. By applying a simple set of synthesis rules, this method facilitates the systematic derivation of MIMO converter topologies. The design approach leverages the concept of time-sharing, wherein multiple energy sources supply power during one phase of operation, and multiple loads consume power during the subsequent phase. This time-sharing mechanism allows for effective power management while minimizing interference between sources and loads.

The thesis also provides general guidelines for transforming conventional SISO converters into MIMO configurations. This is achieved by replacing specific components in SISO topologies with multiport structures, enabling seamless integration of multiple inputs and outputs. The proposed framework not only extends the functionality of existing converter designs but also opens new avenues for customization and optimization in various applications. This thesis demonstrates the potential of MIMO converters to revolutionize power management in hybrid systems. By addressing critical design, modeling, and control aspects, it lays the foundation for the widespread adoption of MIMO converters in future DC distribution systems. The proposed topologies and methodologies are expected to find applications in emerging technologies such as renewable energy systems, electric vehicles, and smart grids. As the demand for efficient and sustainable energy solutions grows, the integration of MIMO converters into industrial and residential energy systems offers a promising pathway toward achieving energy efficiency and sustainability. This thesis provides valuable contributions to the field, bridging the gap between theoretical advancements and practical implementations of MIMO converters in modern energy systems.

## LIST OF TABLES

Table 3.1	FAMILY OF SIDO AND DISO CONVERTERS DERIVED FROM BOOST CONVERTER
Table 4.1	SPECIFICATION FOR FLYBACK CONVERTER
Table 4.2	TIME DOMAIN SPECIFICATIONS
Table 4.3	SPECIFICATION FOR FLYBACK TRANSFORMER
Table 5.1	COMPARISION ANALYSIS OF DIFFERENT CONVERTER TOPOLOGIES
Table 5.2	HARDWARE COMPONENT AND SIMULATION PARAMETERS OF PROPOSED SYSTEM
Table 5.3	OPERATING MODES WITH SWITCHING PATTERNS OF PROPOSED MULTIPORT CONVERTER
Table 5.4	POLE-ZERO VALUE OF TRANSFER FUNCTION
Table 5.5	STABILITY ANALYSIS OF THE MPBC CONVERTER
Table 5.6	PERFORMANCE INDICES ON LOAD CHANGE FOR FIGURE 5.12
Table 5.7	THE VOLTAGE STRESS ON DIODES AND POWER SWITCHES
Table 5.8	THE CURRENT STRESS ON DIODES AND POWER SWITCHES
Table 5.9	EXPERIMENTAL SETUP SPECIFICATIONS OF MPBC
Table 6.1	VARIOUS TOPOLOGIES FOR HIGH GAIN Z SOURCE NCG/CG DC-DC CONVERTER FOR DUAL OUTPUT CONFIGURATION AS PER FIGURE 6.2
Table 6.2	DIFFERENT CONVERTER CONFIGURATIONS FOR SINGLE INPUT DUAL OUTPUT Z-SOURCE BASED DC-DC CONVERTER
Table 6.3	HARDWARE COMPONENT AND SIMULATION PARAMETERS OF PROPOSED SYSTEM
Table 6.4	COMPARISON OF VARIOUS PERFORMANCE PARAMETERS FOR DIFFERENT FEASIBLE CONFIGURATIONS OF HIGH OUTPUT VOLTAGE SIDO CONVERTERS, $R_1=R_2=450\Omega, D=0.2$
Table 6.5	COMPARISON OF VARIOUS PERFORMANCE PARAMETERS FOR SELECTED CONFIGURATIONS [1,2,7,9,11,22,24] OF HIGH OUTPUT VOLTAGE, HIGH EFFICIENCY SIDO CONVERTERS FOR D=0.2 UNDER VARYING LOAD CONDITION
Table 6.6	COMPARISON OF AVERAGE CURRENT AND CURRENT RIPPLES OF $L_1$ and $L_2$ FOR SELECTED CONFIGURATIONS

	[1,2,22,24] OF Z-SOURCE SIDO CONVERTERS FOR $R_1 = R_2 = 450 \Omega$ UNDER VARYING DUTY CYCLE CONDITION
Table 6.7	COMPARISON OF VOLTAGE STRESSES ON CAPACITORS DIODES AND ACTIVE SWITCH OF Z-SOURCE SIDE CONVERTERS, $R_1=R_2=450~\Omega$ UNDER VARYING DUTY CYCLE CONDITION
Table 6.8	VOLTAGE OF EACH COMPONENT IN DIFFERENT STATES
Table 6.9	CURRENT OF EACH COMPONENT IN DIFFERENT STATES
Table 6.10	COST OF FARRICATED 7 SOURCE-RASED SIDO CONVERTER

# LIST OF FIGURES

Fig 1.1	Rural Power Distribution System
Fig 1.2	Conventional distribution system with multiple SISO converters
Fig 1.3	Proposed distribution system with MIMO converter
Fig 2.1	Source wise Power Installed Capacity in India [Source: Central Electricity Authority, GOI]
Fig 2.2	Renewable Energy Sources in India [Source: Central Electricity Authority, GOI]
Fig 3.1	Conventional dc-dc converter architecture for integrating various input sources and output loads based on dc-dc converters.
Fig 3.2	MIMO converter.
Fig 3.3	MIMO converter with parallel-connected input cells and output cells. All power cells are voltage-source-mode converter cells.
Fig 3.4	MIMO converter with series connected input cells and output cells. Here, all output cells are current-source mode converter cells.
Fig 3.5	Three ports of a basic PWM converter.
Fig 3.6	Topological structures of the six basic PWM converters. (a) Buck converter. (b) Buck-boost converter. (c) Boost converter. (d) ' Cuk converter. (e) SEPIC converter. (f) Zeta converter.
Fig 3.7	Unfeasible SEPIC converter with centre capacitor in the common output stage.
Fig 3.8	Feasible input cell. Connection terminals are marked with the black dots.
Fig 3.9	Current-source conditioning filter for the feasible input cell in Fig. 3.4.
Fig 3.10	Unfeasible cells. Connection terminals are marked with black dots.
Fig 3.11	Additional feasible cells if the assumption of common components maximization is relaxed in the corresponding unfeasible input cells in Fig. 3.6. Connection terminals are marked with black dots.
Fig 3.12	Three MIMO cells with connection to different ports of the inductor: (a) outflow, (b) inflow, and (c) both.
Fig 3.13	Three types of MIMO topologies deriving from the four typical SISO converter. (a) SISO. (b) $MIMO_1$ . (c) $MIMO_2$ . (d) $MIMO_3$ .
Fig 3.14	MIMO topologies with the combination of three MIMO cells. (a) $MIMO_1 + MIMO_2$ . (b) $MIMO_1 + MIMO_3$ . (c) $MIMO_2 + MIMO_3$ . (d) $MIMO_1 + MIMO_2 + MIMO_3$ .
Fig 3.15	Simplification of switches.

of boost converter and  $MIMO_3$  cell with one output branch. DIDO topologies based on boost converter with different MIMO cells. (a)  $MIMO_1 + MIMO_1$ . (b)  $MIMO_2 + MIMO_2$ . (c)  $MIMO_3 +$ Fig 3.17  $MIMO_3$ . (d)  $MIMO_1 + MIMO_2$ . (e)  $MIMO_1 + MIMO_3$ . (f)  $MIMO_2 + MIMO_3$ . Fig 4.1 Multiport Flyback Converter Topology Fig 4.2 Electrical model of Flyback converter with parasitics components Steady-state waveform of Voltage and Current during switching of Fig 4.3 Flyback converter Operation Mode of Flyback Converter with parasitics: (a) State 1 (0 < Fig 4.4  $t \leq DT$ ) and (b) State 2 ( $DT < t \leq T$ ) Open Loop Bode Plot for Flyback Converter (a) Output voltage to Fig 4.5 duty, (b) Inductor Current to duty Proposed Lyapunov-based flyback CCM converter control system Fig 4.6 with parasitics. Fig 4.7 Input and Output profile of PI-controlled Flyback Converter Control schematic for ISMC for nonlinear flyback converter with Fig 4.8 voltage and current loop Performance profile of ISMC-controlled Flyback Converter for (a) 5V Fig 4.9 output voltage (b) 180V output profile. Performance profile of Lyapunov Based-controlled Flyback Converter Fig 4.10 for 5V output voltage Closed Loop Bode Plot for Flyback Converter considering circuit Fig 4.11 parasitics (a) Output voltage to duty, (b) Inductor Current to duty Simulation output voltage waveforms of Lyapunov controlled flyback Fig 4.12 converter under load variations. (a) Simulation graphs demonstrate the behaviour of the non-ideal flyback converter when the proposed controller is applied in response Fig 4.13 to changes in input voltage. (b) Comparative analysis of different controller applied on the converter. Fig 4.14 Multi-output flyback converter circuit with the controller Surface graph of the flyback converter for variations in V(e) with respect to  $e_{i_{Ln}}$  and  $e_{v_T}$  when the proposed controller is applied for (a) Fig 4.15 Line Variation, (b) Load Variation, (c) Both Line and Load Variation

Topology derivation process of the SIDO converter with combination

Fig 3.16

Fig 4.16	Surface graph of the flyback converter for variations in $\dot{V}(e)$ with respect to $e_{i_{Lp}}$ and $e_{v_T}$ when the proposed controller is applied for (a) Line Variation, (b) Load Variation, (c) Both Line and Load Variation
Fig 4.17	PCB layout of Hardware Model for Flyback Converter with two outputs
Fig 4.18	Experimental setup for hardware implementation A. Multiport flyback converter prototype, B. Input Source, C. TMS320F28379D Microcontroller, D. Rheostat, E. Current Sensor, F. Voltage Sensor, G. DSO, H. Voltage and Current Probe and I. Computer
Fig 4.19	Hardware steady-state waveforms of the flyback converter
Fig 4.20	Experimental waveforms of the flyback converter under input voltage variation with the steady-state error of 3%.
Fig 4.21	Experimental waveforms of the flyback converter when utilizing the proposed controller while undergoing variations in the output load
Fig 4.22	Voltage stress on the Switch and Diode of the flyback converter
Fig 4.23	Variation of output voltage with input voltage under no load condition
Fig 4.24	Efficiency for non-ideal flyback converter for load variation
Fig 5.1	Generalized MIMO Converters
Fig 5.2	Topology 1: Non-isolated dc-dc converter with multiple inductor on source with parasitics
Fig 5.3	Topology 2: Non-isolated single inductor dc-dc converter with parasitics
Fig 5.4	Topology 3: Proposed three input two output converter with parasitics in circuit
Fig 5.5	(a) Multiport extension for the proposed converter to interface multiple inputs and outputs, (b) Circuit diagram of proposed MPBC with DC load, integrated single phase inverter with AC load and control unit
Fig 5.6	Equivalent circuit of battery discharging mode considering ESRs, (a) switching state-1, (b) switching state-2, (c) switching state-3, (d) switching state-4, and (e) switching state-5 of proposed MPBC
Fig 5.7	Battery Discharging Mode steady state waveform of proposed converter
Fig 5.8	Equivalent circuit of battery charging mode considering ESRs, (a) switching state-1, (b) switching state-2, (c) switching state-3, (d) switching state-4, and (e) switching state-5 of proposed MPBC
Fig 5.9	Root locus for (a) $q_{11}$ , (b) $q_{22}$ , (c) $q_{33}$ , (d) $q_{44}$ for open and close loop transfer function of proposed MPBC and bode plot for (e) $q_{11}$ , (f) $q_{22}$ ,

- (g)  $q_{33}$ , (g)  $q_{44}$  with and without applying controller of proposed MPBC at.  $R_1 = R_2 = 30\Omega$
- Fig 5.10 Inductor profile and output voltage waveform of MPBC at  $R_1 = R_2 = 30\Omega$
- Fig 5.11 Input current waveform of MPBC at  $R_1 = R_2 = 30\Omega$
- Fig 5.12 Load Variation (a) When DC load is connected at A and AC load at B, (b) when both DC and AC load connected at A
  - Stresses on semiconductor switches of MPBC at  $R_1 = R_2 = 30\Omega$ : (a)
- Fig 5.13 Voltage Stress on each diode and switches, (b)Current Stress on each diode and switches
  - Laboratory setup for converter's prototype: (A) Proposed MIMO converter, (B) Input power supply for sources and ESE, (C) Controller
- and sensor power circuit, (D) DC Resistive Load, (E) Probes for measurements, (F) Digital Storage Oscilloscope and (G) Motor Setup (H) Inverter Configuration (I) Computer setup (J) TMS320F28379D DSP
- Fig 5.15 (a) Topology 2 switching stress on S3 and S4, (b) Proposed Converter switching stress on S3 and S4 at  $R_1 = R_2 = 30\Omega$
- Fig 5.16 Inductor and output voltage waveforms of MPBC at  $R_1 = R_2 = 30\Omega$
- Fig 5.17 Stresses on semiconductor devices of MPBC at  $R_1 = R_2 = 30\Omega$ : (a) Voltage stress on switches. (b) The voltage stress on diodes
- Fig 5.18 Input currents conduction of all sources  $(V_1, V_2 \text{ and } V_3)$  during discharging modes.
- Fig 5.19 Effect of DC load variation on terminal voltage during discharging mode (a) under open loop and (b) under closed loop operation.
- Fig 5.20 (a) Inverter section to the proposed converter loaded with single phase motor, (b) PWM inverter switching and output AC voltage waveform.
- Fig 5.21 (a) Efficiency plot for different duty cycle combination of proposed MPBC at different loading conditions, and (b) efficiency plot for the controlled output of the proposed MPBC showing various loading conditions.
- Fig 6.1 Conventional Z source DC-DC converter.
- Fig 6.2 Family of non-isolated multi-input multi-output Z Source DC-DC converter
- Fig 6.3 Converter configuration for single input dual output Z source DC-DC converter
- Fig 6.4 Different converter configurations for single input dual output Z-source based dc-dc converter

- Comparison of efficiency for selected configurations [1,2,7,
- Fig 6.5 9,11,22,24] of high output voltage, high efficiency SIDO converters for D=0.2 under varying load condition.
- Comparison of various parameters for selected configurations
- Fig 6.6 [1,2,22,24] of high output voltage, high efficiency SIDO converters for  $R_1 = R_2 = 450\Omega$  under varying duty cycle condition. (a) Output voltages  $(V_{o1} = V_{o2})$ , (b) Output power  $(P_o)$ , (c) Efficiency (%)
- Fig 6.7 Proposed Converter (a) Configuration, (b) Operating state DT, (c) Operating state (1-D)T
- Fig 6.8 Waveforms of the Topology 22 SIDO converter
- Fig 6.9 Open Loop simulation results at (a) D = 0.05 and  $R_1 = R_2 = 150\Omega$ , (b) D = 0.2 and  $R_1 = R_2 = 150\Omega$
- Prototypes of the proposed converter and control board where (A)
- Fig 6.10 Proposed SIDO converter (B) Control circuit (C) Sensor board (D) TMS320F28379D control board
- Fig 6.11 Experimental result of proposed converter at (a) D = 0.05 and  $R = 150\Omega$ , (b) D = 0.2 and  $R = 450\Omega$ , (c) D = 0.3 and  $R = 150\Omega$
- Fig 6.12 Experimental waveform of inductor currents and capacitor voltages at (a) D = 0.05, (b) D = 0.2
- Fig 6.13 Experimental waveform of inductor voltages and currents at (a) D = 0.05, (b) D = 0.2
- Fig 6.14 Experimental waveform of switch S and diodes  $D_1$ ,  $D_2$  and  $D_3$  voltage stress at (a) D = 0.05, (b) D = 0.2
  - Experimental comparisons of proposed converter w.r.t. duty ratio at
- Fig 6.15  $R_1 = R_2 = 450\Omega$  of (a) Input Current, (b) Inductor Current, (c) Capacitor Voltage, (d) Output Voltages, (e) Output Power, (f) Efficiency

#### LIST OF ABBREVIATIONS

MIMO Multiple-Input Multiple-Output SISO Single-Input Single-Output

DC Direct Current SI Single Inductor

GDP Gross Domestic Product RES Renewable Energy Sources

kW Kilowatts
MW Megawatts
GW Gigawatts
TW Terawatt
PV Photovoltaics
WT Wind Turbines
FC Fuel Cell

ESS Energy Storage Systems
MICs Multi-Input Converters
MOCs Multiple Output Converters

EVs Electric Vehicles

PWM Pulse Width Modulation

CCM Continuous Conduction Mode
DCM Discontinuous Conduction Mode

PIV Peak Inverse Voltage

FCHEVs Fuel Cell-Based Hybrid Electric Vehicles

MO Multiple Outputs

DAHB Dual Active Half-Bridge

HGMPC High-Gain Multiple Ports DC-DC Converters

BSS Battery Storage System
TPC Three Port Converter
DIC Dual-Input Converters
DOC Dual-Output Converters

MPPT Maximum Power Point Tracking

MOB Multi-Output Boost

IGBT Insulated-Gate Bipolar Transistor

SVM Space Vector Modulation NPC Neutral Point Clamped MLI Multilevel Inverters

MMC Modular Multilevel Converter
ISSDC-DC Isolated Single-Switch DC-DC
PID Proportional—Integral—Derivative
ESR Equivalent Series Resistance
SMC Sliding Mode Controller
MFC Multiport Flyback Converter
EMI Electromagnetic Interference

MOSFET Metal-Oxide-Semiconductor Field-Effect Transistor

ISMC Integral Sliding Mode Controller

MPBC Multiport Boost Converter

ESE

Energy Storage Elements Dual-Output High-Gain Z-Source Converters Common Ground DOHGZSC

CG Non-Common Ground NCG Isolated Microgrid **IMG** 

## TABLE OF CONTENTS

Undertaking Certificate i Acknowledgements i Abstract List of Tables v List of Figures i List of Symbols and Abbreviations	
	PTER 1 RODUCTION1
1.1.	OVERVIEW1
1.2.	INTRODUCTION: Transforming Agriculture Practices
1.3.	RENEWABLE ENERGY INTEGRATION AND MANAGEMENT4
1.4.	POWER DISTRIBUTION AND LOAD MANAGEMENT6
1.5.	MIMO CONVERTERS IN AGRICULTURAL APPLICATIONS6
	1.5.1. Enhanced Renewable Energy Integration:6
	1.5.2. Electrification of Agricultural Machinery and Tools:
	1.5.3. Optimized Energy Distribution and Load Management:
	1.5.4. Support for Automation and Smart Agriculture:
	1.5.5. Flexibility and Scalability:7
	1.5.6. Energy Storage Integration:7
1.6.	CONCLUSIONS
	PTER 2 CRATURE REVIEW9
2.1.	OVERVIEW9
2.2.	LITERATURE SURVEY9
	2.2.1. Topology and Modelling Studies:
	2.2.2. Analysis and Control Algorithms for DC-DC converter:16
	2.2.3. Topologies, Analysis and Control Algorithms for Inverter:18

	2.2.4. Modelling, Stability and Performance Studies:	19
2.3.	MAJOR FINDINGS AFTER LITERATURE REVIEW	20
2.4.	AUTHOR'S CONTRIBUTION	21
	2.4.1. Modeling and Analysis of DC/DC Converters for Renewable Energy Systems (RES) Integration:	
	2.4.2. Development of Robust Control Algorithms:	22
	2.4.3. Stability Study for Simulation and Hardware Prototyping:	22
	2.4.4. Performance Tracking with Different RES Inputs and Variable Loc Conditions:	
OVE	PTER 3 RVIEW OF CONVERTERS AND IDEOLOGY TO MULTIPOR FIGURATION	
3.1.	OVERVIEW	24
3.2.	INTRODUCTION	24
3.3.	BRIEF REVIEW OF BASIC PWM CONVERTER TOPOLOGIES	28
3.4.	FEASIBLE TOPOLOGIES FOR MULTIPORT DC-DC CONVERTERS	31
	3.4.1. Basic Input Cells for Multiport Configurations	34
	3.4.2. Ideology for Multiport Configurations	37
3.5.	MIMO TOPOLOGY DERIVATION FOR BOOST CONVERTER	41
3.6.	CONCLUSIONS	44
LYAP	PTER 4 PUNOV FUNCTION APPROACH TO STABILIZE MULTIPOR BACK CONVERTER TO INTEGRATE RESs	
4.1.	INTRODUCTION	46
	DYNAMIC MODELLING OF FLYBACK CONVERTER WIT	
4.3.	CONTROL METHODOLOGY AND STABILITY INVESTIGATION .:	55
4.4.	DUTY RATIO FEEDFORWARD CONTROLLER	56

4.5.	FEEDBACK CONTROL SYSTEM UTILIZING LYAPUNOV FUNC	
4.6.	CONTROLLER IMPLEMENTATION ON CONVERTER	61
	4.6.1. Linear PI controller	62
	4.6.2. Sliding mode controller	63
	4.6.3. Lyapunov function-based controller	64
4.7.	VERIFICATION AND RESULTS	69
4.8.	CONCLUSIONS	76
DYN	APTER 5  IAMIC MODELING AND EFFICIENCY ANALYSIS OF MIMO F  IVERTERS WITH RENEWABLE SOURCES FOR AGRICUL  IDS	LTURE
5.1.	OVERVIEW	78
5.2.	INTRODUCTION	78
5.3.	TOPOLOGY DERIVATION AND COMPARISON STUDY	81
5.4.	CONVERTER STRUCTURE AND OPERATION MODES	84
	5.4.1. First Operation Mode (Discharging Mode)	88
	5.4.2. Second Operation Mode (Battery Charging)	93
5.5. CON	AVERAGED AND DYNAMIC ANALYSIS OF MPBC TROLLER DESIGN	
5.6.	VERIFICATION AND RESULTS	102
	5.6.1. Profile Analysis of Prototype Converter	103
	5.6.2. Voltage and Current Stress on Switching Devices	106
	5.6.3. Experimental Results	108
5.7.	CONCLUSIONS	117

CHAPTER 6 COMPARATIVE ANALYSIS AND SELECTION OF MULTIPORT Z-SOURCE CONVERTER TOPOLOGIES FOR RESs	
6.1.	OVERVIEW118
6.2.	INTRODUCTION
6.3.	PRINCIPLE AND TOPOLOGY
	6.3.1. Topology Derivation of SIDO Z-source DC–DC Converters based on the Voltage-Type Ports
	6.3.2. Topology Optimization and Performance Analysis
6.4.	ANALYSIS OF SELECTED SIDO TOPOLOGIES134
6.5.	ANALYSIS OF TOPOLOGY 22 Z-SOURCE SIDO CONVERTER
	6.5.1. Dynamic Operation and Analysis
	6.5.2. Steady State Analysis
	6.5.3. Cost Analysis of proposed SIDO converter143
6.6.	VERIFICATION AND RESULTS
6.7.	CONCLUSIONS 152
_	TER 7 CLUSION AND FUTURE SCOPE154
	CONTRIBUTIONS OF THE THESIS
7.2.	FUTURE WORK
REFE	RENCES156
LIST	OF PUBLICATION167

# CHAPTER 1 INTRODUCTION

#### 1.1. OVERVIEW

Agriculture is fundamental to human survival and economic stability, providing essential resources such as food, fiber, and raw materials. It sustains livelihoods for millions, especially in rural areas, and is critical to national economies, contributing significantly to GDP and employment. Beyond its economic impact, agriculture shapes cultural practices and social structures, influencing community dynamics and traditional lifestyles. As the global population grows and urbanization accelerates, the demand for agricultural produce increases, necessitating innovations that boost productivity, enhance efficiency, and ensure sustainability. Modern challenges, including climate change, resource scarcity, and environmental degradation, compel the agricultural sector to adopt advanced technologies and sustainable practices. Integrating renewable energy sources and innovative power management systems into agriculture is essential for meeting these challenges and advancing towards a resilient and sustainable agricultural future.



Figure 1.1. Rural Power Distribution System

#### 1.2. INTRODUCTION: Transforming Agricultural Practices

Agriculture is a vital sector that feeds billions, and it has evolved significantly over the centuries. Yet, modern challenges such as climate change, energy sustainability, and increasing demand for food have necessitated the integration of advanced technologies into agricultural practices. One such transformative technology is power electronics, with power electronics converters at the forefront. Power electronics converters are integral to modernizing agricultural energy systems, offering unprecedented efficiency and sustainability through their ability to manage and optimize power flows from diverse energy sources. Traditionally, agriculture has relied heavily on fossil fuels for machinery operation, irrigation, and other critical processes. This dependence not only increases operational costs but also contributes to environmental degradation. Power electronics converters, particularly Multi-Input Multi-Output (MIMO) converters, address these challenges by facilitating the integration of renewable energy sources (RES) such as solar panels, wind turbines, and energy storage systems. Unlike conventional Single-Input Single-Output (SISO) converters that handle only one source and one load, MIMO converters can simultaneously manage multiple energy inputs and distribute power to various outputs, thereby enhancing the flexibility and reliability of agricultural energy systems.

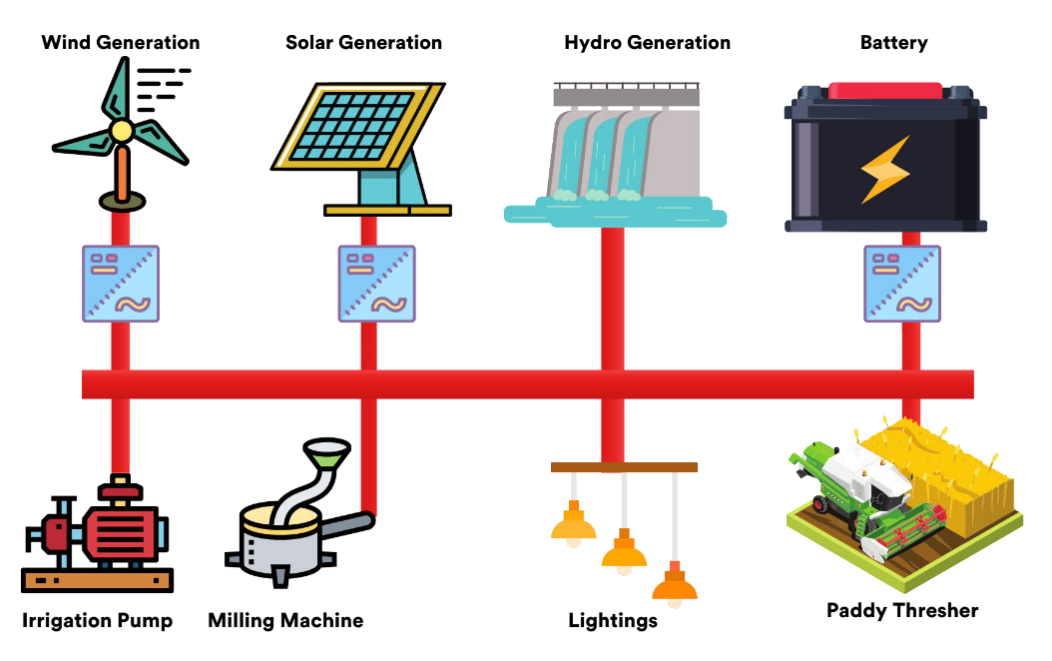


Figure 1.2. Conventional distribution system with multiple SISO converters

The fundamental components of MIMO converters include:

- 1. **Multiple Inputs:** Capable of receiving power from diverse sources, improving energy flexibility and reliability.
- **2. Multiple Outputs:** Providing different voltage levels to cater to various agricultural applications.
- **3. Integrated Control:** Advanced control algorithms to manage power flow, optimize energy use, and maintain system stability.

This multi-port functionality enables seamless integration and management of renewable energy sources, enhancing the sustainability and efficiency of agricultural practices. In agricultural applications, MIMO converters enable the seamless integration of RES, thereby reducing reliance on non-renewable energy sources and lowering greenhouse gas emissions. These converters can dynamically balance the power contributions from solar, wind, and battery systems, ensuring a stable energy supply even when individual sources are intermittent. For instance, during cloudy or calm days when solar or wind energy production is low, MIMO converters can switch to stored energy, maintaining continuous operation of essential agricultural equipment. This capability is crucial for irrigation systems, grain dryers, and climate control systems in greenhouses, where a consistent power supply is necessary to maintain optimal conditions and productivity.

Moreover, MIMO converters are pivotal in powering electric agricultural machinery, which is increasingly replacing traditional diesel-powered equipment. Electric tractors, harvesters, and irrigation motors powered through MIMO converters benefit from reduced operational costs, lower emissions, and decreased maintenance requirements. The converters provide the precise voltage levels needed for different equipment, adapting to varying power demands and operational modes. This transition not only supports more sustainable farming practices but also aligns with global efforts to reduce carbon footprints in agriculture.



Figure 1.3. Proposed distribution system with MIMO converter

In addition to managing energy sources, MIMO converters enhance energy distribution and load management. They can provide multiple output voltages, catering to a wide range of agricultural loads, from high-power equipment to low-power sensors. This capability allows for efficient energy allocation, minimizing waste and optimizing the use of available resources. For example, in a microgrid setting, MIMO converters can prioritize power distribution to critical loads during peak demand periods, ensuring essential operations are not disrupted.

Furthermore, MIMO converters support the integration of smart agriculture technologies and automation. They enable the connection of various IoT devices and sensors that monitor soil moisture, weather conditions, and crop health, providing real-time data for automated decision-making processes. This integration facilitates precision agriculture, where resources are used more efficiently, and farming practices are optimized based on accurate data. The converters' ability to handle diverse power requirements and provide stable voltage levels is essential for the reliable operation of these advanced systems. Power electronics converters modify electrical energy from one form to another, facilitating efficient energy conversion, control, and distribution from various sources to agricultural loads.

#### 1.3. RENEWABLE ENERGY INTEGRATION AND MANAGEMENT

Agriculture increasingly relies on renewable energy sources to reduce dependence on fossil fuels and mitigate environmental impacts. MIMO converters play a crucial role in integrating and managing these diverse energy inputs.

- 1. Solar and Wind Energy Integration: MIMO converters can simultaneously manage power from solar panels and wind turbines, adjusting the energy mix based on availability and demand. This capability ensures a consistent energy supply for agricultural operations, even when individual sources are intermittent.
- 2. Hybrid Energy Systems: In agricultural settings, hybrid systems combining solar, wind, and possibly hydro or biomass energy can provide a reliable and diversified energy supply. MIMO converters effectively integrate these sources, optimizing their combined output to match agricultural energy needs.
- 3. Energy Storage and Dispatch: MIMO converters facilitate the integration of energy storage systems, such as batteries, to store excess energy generated during peak production periods. This stored energy can be dispatched during low-generation periods or high-demand scenarios, ensuring a steady power supply for critical agricultural processes.

The electrification of agricultural machinery and tools is transforming modern farming practices. MIMO converters support this transition by providing versatile and efficient power solutions for various applications.

- 1. Irrigation Systems: Advanced irrigation systems require precise control over water pumps to optimize water usage and energy consumption. MIMO converters can manage power delivery to these loads, ensuring they operate efficiently and adapt to changing water demands and energy availability.
- 2. Electric Tractors and Harvesters: MIMO converters can power electric motors in tractors and harvesters, providing the necessary voltage levels for different operational modes. This flexibility enhances the performance of electric agricultural machinery, reducing emissions and fuel costs.

3. Portable Agricultural Tools: Handheld and portable tools, such as electric pruners and chainsaws, benefit from the power management capabilities of MIMO converters. They ensure reliable and efficient power delivery, improving the tools' functionality and reducing the need for frequent recharging.

#### 1.4. POWER DISTRIBUTION AND LOAD MANAGEMENT

Efficient energy distribution and load management are critical for optimizing agricultural operations and reducing energy waste. MIMO converters excel in this domain by providing multiple output voltages tailored to specific loads.

- Load Matching and Prioritization: MIMO converters can match power delivery to the specific requirements of various agricultural loads, such as lighting systems, ventilation fans, and processing equipment. They can prioritize critical loads and ensure optimal energy distribution based on realtime demand.
- 2. Microgrid Integration: In remote agricultural areas, microgrids provide a reliable and self-sufficient energy supply. MIMO converters play a key role in integrating various energy sources into the microgrid, managing power flow, and ensuring stable operation.
- **3. Dynamic Load Control:** MIMO converters enable dynamic control of loads, allowing for adjustments based on energy availability, demand fluctuations, and operational priorities. This capability enhances overall system efficiency and responsiveness.

#### 1.5. MIMO CONVERTERS IN AGRICULTURAL APPLICATIONS

#### 1.5.1. Enhanced Renewable Energy Integration:

MIMO converters facilitate the seamless incorporation of various RES into agricultural systems. By managing multiple energy inputs, they ensure a reliable power supply for farm operations, even as individual renewable sources vary in output. This capability reduces reliance on fossil fuels and mitigates environmental impact.

#### 1.5.2. Electrification of Agricultural Machinery and Tools:

Traditional agricultural machinery, often powered by diesel engines, is being replaced by electric alternatives. MIMO converters power electric tractors, harvesters, and irrigation systems by providing precise voltage levels required for different equipment. This shift reduces greenhouse gas emissions, operational costs, and noise pollution.

#### 1.5.3. Optimized Energy Distribution and Load Management:

MIMO converters dynamically distribute energy to various agricultural loads to processing machinery. Their ability to deliver multiple output voltages allows for efficient energy use tailored to specific needs, enhancing productivity, and reducing energy waste.

#### 1.5.4. Support for Automation and Smart Agriculture:

As agriculture embraces automation and smart farming technologies, MIMO converters provide the necessary power management to support these advancements. They enable real-time control and monitoring, integrating with IoT devices to optimize operations, from soil moisture monitoring to automated feeding systems.

#### 1.5.5. Flexibility and Scalability:

MIMO converters offer flexibility in handling diverse energy inputs and outputs, adapting to the varying energy requirements of modern farms. This scalability supports both small-scale operations and large agricultural enterprises, making them suitable for a wide range of applications.

#### 1.5.6. Energy Storage Integration:

Effective integration of energy storage systems with MIMO converters allows for efficient management of energy generated by RES. This stored energy can be used during periods of low renewable output or peak demand, ensuring continuous operation of critical agricultural processes.

#### 1.6. CONCLUSIONS

Multi-Input Multi-Output (MIMO) power electronics converters hold transformative potential for modernizing agriculture, offering a path towards greater

efficiency, sustainability, and productivity. By seamlessly integrating diverse renewable energy sources such as solar, wind, and battery storage, MIMO converters provide a reliable and stable power supply essential for continuous agricultural operations. Their ability to dynamically manage and distribute power across various agricultural loads ensures optimized energy use, reducing dependence on fossil fuels and minimizing environmental impact.

The electrification of agricultural machinery through MIMO converters brings significant benefits, including lower operational costs, reduced emissions, and decreased maintenance needs. This shift supports global sustainability goals and promotes more eco-friendly farming practices. Additionally, MIMO converters enable the effective implementation of smart agriculture technologies, facilitating precision farming through real-time data monitoring and automated decision-making.

While challenges such as initial costs and technical complexity exist, the long-term advantages of MIMO converters in agriculture far outweigh these barriers. Financial incentives, technological advancements, and increased awareness will drive their wider adoption, ensure the agricultural sector benefits from the latest innovations in power electronics.

In summary, MIMO power electronics converters are pivotal in the evolution of sustainable and efficient agricultural systems. Their integration into farming practices will not only enhance productivity and energy efficiency but also contribute to a more resilient and environmentally responsible agricultural sector. By embracing these advanced technologies, agriculture can meet the demands of a growing population while safeguarding natural resources for future generations.

#### **CHAPTER 2**

#### LITERATURE REVIEW

#### 2.1. OVERVIEW

A literature review forms the cornerstone of any research study. It should aim to achieve the following objectives:

- Conduct a comprehensive examination of literature pertinent to the study topic
- Summarize the insights derived from the existing research
- Analyze the identified research gaps
- Organize and reshape the gathered data to inform future research

By reviewing prior research, this chapter establishes the authenticity of the Ph.D. work. It highlights what has been learned from previous studies and demonstrates how the current research serves as a foundation for new ideas. Additionally, it offers a systematic analysis of research publications, providing clarity on the objectives to be pursued.

#### 2.2. LITERATURE SURVEY

As the global population continues to grow, the need for clean and sustainable energy solutions is becoming increasingly urgent. Societies can no longer rely on fossil fuels due to rising oil and natural gas prices, environmental damage, and the depletion of these resources. In response, distributed renewable energy sources such as photovoltaics (PV) and fuel cells are gaining significant traction. Wind energy is also playing a crucial role in the transition to renewable energy. The capacity of installed PV systems has expanded dramatically, from kilowatts (kW) to megawatts (MW), and now to gigawatts (GW), with projections indicating that global PV capacity will soon reach 1 terawatt (TW). Transitioning to clean and green energy is essential for ensuring a sustainable future [1]-[5]. Exhausting conventional resources and their adverse environmental impact creates the need for energy systems to utilize Renewable Energy Sources (RESs) to fulfil the present energy demand. The renewable energy sector in India has emerged as a significant player in the grid connected power generation

system. Solar Photovoltaic has turned up as an integral part of the solutions to meet the country energy needs and become an essential requirement for energy access.

Renewable energy has a great potential to usher in universal energy access. In a decentralized or standalone mode, renewable energy is an appropriate, scalable and viable solution for providing power to un-electrified or power deficient villages and hamlets. Figure 2.1 shows the source wise power installed capacity in India as of 11-2-2022 and estimated renewable energy potential from commercially exploitable sources, viz. Solar power 50.30 GW, Wind – 40.1 GW; Hydro – 46.51 GW; bioenergy–8.3 GW [1].

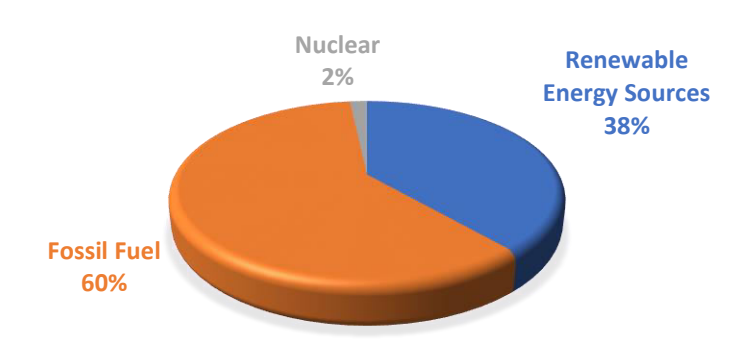


Figure 2.1. Source wise Power Installed Capacity in India [Source: Central Electricity Authority, GOI]

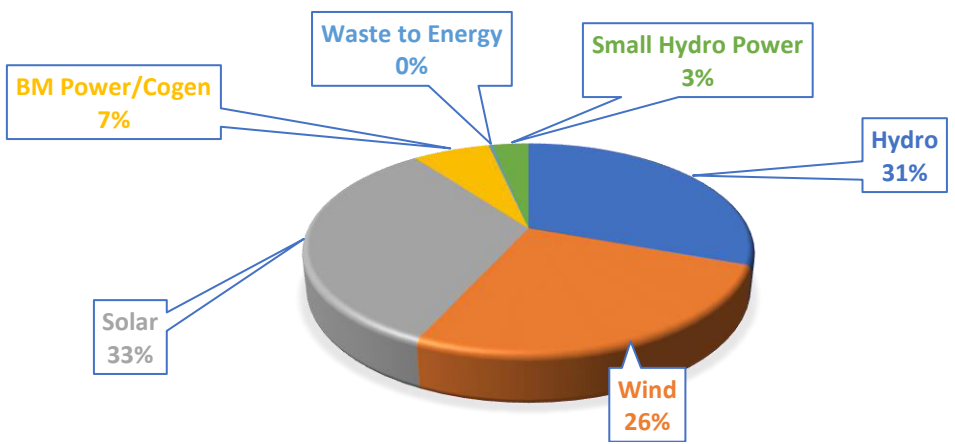


Figure 2.2. Renewable Energy Sources in India [Source: Central Electricity Authority, GOI]

RESs can be implemented in many locations, including remotely located communities and farms. Wind and solar energy make it possible for going off-grid, especially for farms, as they have adequate terrain for installation of solar PV and wind turbines

(WT) [2]. RESs can provide significant reduction in monthly electricity bill. Due to various advantages, research for hybrid wind and solar energy systems for numerous applications is growing day to day. WT's are considered as energy source in RESs. WTs can generate large amounts of power so they are promising sources to meet the load demand in remote areas [3]. Due to this number of systems with the use of solar energy, are coming up. Furthermore, new design of previously existing system is also imperative. Therefore, integration of solar energy to an existing system is studied and a new design is proposed.

Certain gaps are identified in research area of RESs.

- 1. Little attention has been paid to investigate off-grid renewable systems for farming. Recent literature study shows that developed RESs for farms still relies on utility grid while wind turbine and solar Photovoltaic system are used as supplementary sources [4].
- 2. Even this hybrid model of solar and wind has no greenhouse gas Emission [5].
- 3. The reduced maintenance and cost declination of solar panels over past few years, have made such systems inexpensive against the diesel and other energy sources. It is inexpensive, trustworthy and eco-friendly [5].

These factors motivate this study to develop an off-grid RESs for supplying power to farms often located in remote areas where access to utility grid may not be available. However, because these renewable energy sources are unpredictable and intermittent, they are not reliable when used on their own. To address this challenge, renewable resources are often combined with other energy sources, such as fuel cells, supercapacitors, and energy storage systems (ESS). Recently, multi-input converters (MICs) have emerged as a solution for connecting multiple renewable energy sources. These converters offer simplified circuit designs, lower manufacturing costs, centralized control, and compact size [2]-[7]. The increasing adoption of renewable energy, electric vehicles (EVs), consumer electronics, and other sustainable technologies has driven the development of new power electronic converter topologies. There is a growing need for converters with multiple ports and various voltage levels to meet the diverse demands of these applications [1]-[2]. While multiple independent single-input single-output (SISO) converters can be used to

regulate voltage and control power across different ports, this approach leads to an excessive number of components, which increases overall cost and system size [3]-[4]. To overcome this issue, a family of multi-input multi-output (MIMO) DC-DC converters has been developed.

These converters offer significant advantages, including fewer conversion stages, improved system efficiency, higher power density, reduced size and cost, and centralized power management across multiple ports. This makes them more efficient than using multiple single-input DC-DC converters in renewable energy systems. Various multiport DC-DC converters have been designed, encompassing both isolated and non-isolated topologies.

In [8], a novel isolated multi-input dc-dc converter based on the concept of flux additivity, uses phase-shifted pulse width modulation (PWM) control on two input current-fed full-bridge dc-dc converters. This approach offers several advantages, including the ability to deliver power separately and simultaneously from multiple dc sources, soft switching technology, and electric isolation via a transformer. In [9], a modular non-isolated multi-input step-up high gain converter topology with continuous current conduction provides high gain using the same number of devices and has the least number of device counts. The switches and diodes' peak inverse voltage (PIV) are controlled within acceptable limits to maintain high voltage gain.

In [10], a new bidirectional dc-dc converter is presented for grid-connected renewable energy systems and hybrid electric vehicles. It eliminates the need for an additional transformer, combining two parallel buck converters with series switches for input sources to avoid short circuits, reducing the need for inductors and capacitors, enhancing cost-efficiency. However, it faces power flow control challenges. In many applications, integrating power electronics into multiple output converters (MOCs) is crucial for reducing size, weight, maintenance needs, and costs, as explained in references [14]-[15]. A comprehensive classification of fuel cell-based hybrid electric vehicles (FCHEVs). A key component in these FCHEVs is the DC-DC power converter. A multi-input DC-DC power converter is employed to connect multiple energy sources, simplifying the system and enhancing its overall efficiency [16].

Voltage regulation for each dc output in converters is crucial. Post-regulation is used to ensure robustness against line or load variations. Multiple loads require different low voltages, so efficiently supplying multiple-and-low output voltages is essential [17]. It [18] presents an accurately regulated multiple outputs (MO) ZVS dc-dc converter with operation and control analysis. Isolated multiport DC-DC converters are heavy and expensive and utilize transformers for electrical isolation. Non-isolated multi-input DC-DC converters provide a practical and cost-effective solution without the need for transformers or high-frequency components, resulting in improved efficiency [19].

Multi-Input Multi-Output (MIMO) converters provide a medium of interaction between different renewable resources, energy-storing elements, and advanced electric loads with a centralized control system. A generalised form of MIMO converter is shown in Fig 1. Integrating MIMO systems with sources and loads provides compact packaging, relatively easier control, simultaneous power management, and voltage regulation. In [20] and [21], presented a topology that can interface between diversified renewable energy sources and diode-clamped multilevel inverters for ac loads. As the sources are intermittent, ESE is a must, and the impossibility of energy transfer between sources is a drawback of this converter. In [22]-[29] discusses a non-isolated MIMO converter with individual inductors for each source but lacks power transfer between inputs. The individual inductors make the converter larger, and a cascading approach increases device count and complexity.

A novel MIMO converter is introduced in [30], capable of distributing power among sources and the load. Dynamic analysis is conducted on a 2-in-2-out system with two inputs (35V and 48V), two outputs (40V and 80V), and 236W output power using ideal parameters. The chapter explores n-input and m-output configurations, but increasing the number of sources leads to switching stress and duty cycle issues with the in-line switches. The study proposes a lead-lag compensator to regulate the system by adjusting poles and zeros, but this approach may be unreliable when faced with uncertainties in load power variations. In [31], discusses the design, implementation, and control of a scalable DC microgrid that uses a hybrid of renewable energy sources. It employs a multi-input, multi-output dual active half-bridge (DAHB) converter.

The primary advantages of such converters include the fewer conversion stages, increased system efficiency, higher power density, size, cost, and centralized power management across multiple ports compared to using multiple single-input DC-DC converters in renewable energy systems. Various multiport DC-DC converters have been developed encompassing both isolated and non-isolated topologies. Isolated topologies [5]-[8] and non-isolated topologies [9]-[12] represent two main subdivisions within these multiport converter designs. A single inductor MIMO boost converter is proposed for electric vehicle (EV) application [13]. Despite having multiple outputs with varying voltage levels, the converter's gain is low. In [14], a new multiport DC-DC converter is introduced for DC Microgrid applications. While the proposed configuration offers numerous advantages such as minimizing multiple power conversions, decreasing the number of components, and providing voltage boosting capability, it also presents drawbacks including high switch count and controller complexity, coupled with low voltage gain.

To achieve a high voltage conversion ratio, traditional DC-DC converters operate with duty cycles below 0.1 for step-down and above 0.9 for step-up modes. However, such extreme duty cycle operation can compromise converter efficiency and transient performance [15][16]. To tackle this issue, a family of high-gain integrated multiport DC-DC converters has been introduced. High-gain multiple ports DC-DC converters (HGMPC) have gained significant attention for scenarios demanding multiple independent supply voltage levels. In a recent study, a novel collection of five nonisolated multiport DC-DC converter designs characterized by bipolar symmetric outputs with high gain. The feasibility of integrating these converters with a multilevel inverter to generate high-quality AC voltages is demonstrated [17]. A new non-isolated high step-up multiport DC-DC converter, integrated with PV modules and a Battery Storage System (BSS), is proposed for high-voltage DC bus-based hybrid renewable energy systems. It offers high voltage gain, low semiconductor stress, ZCS diodes, MPPT for PV inputs, and flexible port extension [18]. A double input high gain DC-DC boost topology with six switching states is introduced and subsequently expanded to an n-input version [19]. A high step-up DC-DC boost converter [20] with a single input and three outputs was introduced, featuring an expandable structure achieved by

increasing the voltage multiplier modules, and capable of delivering high voltage gains at its output terminals without the need for higher duty cycles or the inclusion of transformers or coupled inductors in its design. A newly developed multiport DC-DC converter with high gain [21], designed to incorporate low-voltage energy storage devices into a DC microgrid, presents a three-port interface employing just a single two-winding transformer, thereby substantially simplifying control complexities. Studies [17]-[21] highlight the importance of high-gain converters in multiport configurations, emphasizing their benefits in terms of efficiency, size, cost, and control complexities.

#### 2.2.1. Topology and Modelling Studies:

Hongfei Wu, Kai Sun, et. al., [6] presented a non-isolated three port converter (TPC) topologies based on dual-input converters (DIC) and dual-output converters (DOC), which serves as an interface for a renewable source, a storage battery, and a load simultaneously. The power flow in a TPC is analysed and compared with that in a DIC or a DOC, respectively. The power flow in a TPC is analysed and compared with that in a DIC or a DOC, respectively. Beginning with building the power flow paths of a TPC from a DIC or a DOC, the general principles and detailed procedures for the generation and optimization of TPC topologies are presented. Based on these works, a family of non-isolated TPC topologies is developed. The derived TPCs feature single-stage power conversion between any two of the three ports, and result in high integration and high efficiency.

Jianwu Zeng, Wei Qiao, et. al., [7] presented a new isolated multiport dc-dc converter for simultaneous power management of multiple renewable energy sources, which can be of different types and capacities. The proposed dc-dc converter only uses one controllable switch in each port to which a source is connected. It has the advantages of simple topology and minimum number of power switches. The proposed converter is applied for simultaneous maximum power point tracking (MPPT) control of a wind/solar hybrid generation system consisting of one wind turbine generator (WTG) and two different photovoltaic (PV) panels.

- H. Behjati and A. Davoudi, [8] presented topology that can interface between diversified energy sources and diode-clamped multilevel inverter. Regulating series output voltages for the dc-link of the diode-clamped multilevel inverter, diversifying energy sources, improving availability of the energy source, employing a single inductor, and cost effectiveness are the advantages of the proposed MIMO converter.
- B. G. Dobbs and P. L. Chapman, [9] presents a topology for multiple energy source conversion. The topology is capable of interfacing sources of different voltage-current characteristics to a common load, while achieving a low part count. A fixed frequency switching strategy is investigated and the resulting operating modes are analysed.

A. Nami, F. Zare, A. Ghosh, et. al., [10] presents a new DC–DC multi-output boost (MOB) converter which can share its total output between different series of output voltages for low- and high-power applications. This configuration can be utilised instead of several single output power supplies. This is a compatible topology for a diode-clamed inverter in the grid connection systems, where boosting low rectified output-voltage and series DC link capacitors is required.

#### 2.2.2. Analysis and Control Algorithms for DC-DC converter:

P. Thounthong, S. Pierfederici, et. al., [16] presents an innovative control law for distributed dc generation supplied by a fuel cell (FC) (main source) and supercapacitor (auxiliary source). This kind of system is a multi-converter structure and exhibits nonlinear behaviour. The operation of a multi-converter structure can lead to interactions between the controls of the converters if they are designed separately. Interactions between converters are studied using impedance criteria to investigate the stability of cascaded systems. In this paper, a nonlinear control algorithm based on the flatness properties of the system is proposed. Flatness provides a convenient framework for meeting a number of performance specifications for the hybrid power source. Using the flatness property, we propose simple solutions to hybrid energy management and stabilization problems. The design controller parameters are autonomous of the operating point; moreover, interactions between converters are taken into account by the controllers, and high dynamics in disturbance rejection is achieved.

L. Wang, E. G. Collins, et. al., [17] presented an optimization problem to minimize power consumption. To implement this optimized power sharing in real time, a novel energy management strategy is proposed, which includes battery power reference generation, UC state-of-charge regulation, and forecast control based on the driver commands. Finally, simulations and experiments in which the flywheel + generator + controlled load is used to emulate the vehicle drivetrain are provided to verify the reduced stress on the battery current and the improved fuel economy achieved by the proposed method.

A. Payman, S. Pierfederici, et. al., [18] presents a flatness-based control method that is used to control the dc/dc converters of an electrical hybrid system. This system is composed of an ultracapacitor, which is connected in parallel to a fuel cell through a bidirectional converter. This association supplies a load through another dc/dc converter. To control these converters, the mathematical model of the studied system is first presented, and then, it is proven that the system is flat. Considering the electrostatic energy stored in the dc-bus capacitors as the system output, the state variables and control variables are extracted as functions of the system output and its derivative. The system is controlled by planning the desired reference trajectories on the flat output components, and forcing them to follow their own references. The fuel-cell-dynamics control is also studied to observe the criterion of (di/dt) max.

J. D. Dasika, B. Bahrani, et. al., [20] presents a multivariable digital controller to suppress the cross regulation of a single-inductor dual-output (SIDO) buck converter in continuous conduction mode (CCM) operation. The controller design methodology originates from the open-loop shaping of the multi-input multi-output (MIMO) systems. The control design procedure includes: 1) determination of a family of nonparametric models of the SIDO converter at operating points of interest, 2) determination of the class of the controller, and 3) system open-loop shaping by the convex minimization of the summation of the square second norm of the errors between the system open-loop transfer function matrices and a desired open-loop transfer function matrix.

#### 2.2.3. Topologies, Analysis and Control Algorithms for Inverter:

G. A. Covic, G. L. Peters, et.al., [24] presented a low cost four quadrant single phase to three phase converter for AC drives. The technique uses a single-phase reversible rectifier operating at unity power factor to produce a balanced DC supply at a controlled high voltage using two IGBT power transistors. Four additional IGBT power switches operate on this high voltage to produce two pulse width modulated (PWM) waveforms using a novel space vector modulation (SVM) strategy. A three-phase motor load is then connected to the centre of the DC supply, and the two PWM voltages, to give a four-quadrant reversing AC drive. The unique feature of this system is the modulation strategy, which achieves higher motor voltages than any previous published method while achieving excellent harmonic suppression at high efficiency in motor sizes restricted to the rating of the single-phase supply (typically 2 kW).

Albert Alexander S, et. al., [25] designed and developed a solar Photovoltaic inverter suitable for the Indian sub-continent is proposed and reviewed in terms of survey, simulation and experimental results. The proposed multi-stage inverter provides the advantage of reduced harmonic distortions and suitable for standalone and grid connected systems. The reduction of harmonics is governed by proper switching sequences required for the inverter switches.

I. Abdalla, J. Corda, et. al., [26] presented the "PV permutation algorithm," as a new method, for the control of the inverter so as to extract the maximum power form each PV source under partial shading and to deliver all that power to the load. The algorithm is based on combination of the direct pulse width modulation, the sequential permutation PV sources, and the output generation to control the multilevel dc-link inverter. The algorithm is applied successfully to a seven-level inverter with separate maximum power point tracking algorithm for each PV source and under non-uniform irradiance.

Jibanesh Roy, Phanikumar Chamarthi, et. al., [27] proposed a new hybrid 9-level inverter topology for single phase grid connected PV systems. Inverter has combined the features of neutral point clamped (NPC), flying capacitor (FC) multilevel inverters (MLI) and coupled inductor phenomenon. It produces 9-level output voltage with

minimum number of power components, which improves the efficiency of the system and reduces the cost as well. Another advantage of this topology is that there is no need of additional balancing circuit to regulate the input DC capacitors and auxiliary capacitor.

Asha Gaikwad, et. al., [28] presented cascaded H-Bridge multilevel inverter with SPWM technique is presented. Multilevel inverter has high power application & low harmonics due to these applications it is used widely in the area of control and energy distribution. It includes performance of 3-Level,5-Level & 7-Level cascaded H-Bridge multilevel inverter with respect to number of switches, total harmonic distortion, waveform pattern, harmonic spectrum, output voltage, voltage stress across the switch & input DC voltage with the help of simulation by using MATLAB/SIMULINK and implementation of Five level cascaded H-bridge multilevel inverter.

Ebrahim Babaei, Concettina Buccella, et. al., [29] presented most recent advances in inverter control with topics such as the following: 1) new multilevel inverter topologies; 2) new modulation and control strategies for multilevel inverters; 3) industrial applications of multilevel inverters; 4) multilevel inverters for renewable energy applications; 5) common-mode voltage reduction methods in multilevel inverters; 6) fault-tolerant design of multilevel inverters.

#### 2.2.4. Modelling, Stability and Performance Studies:

F. H. Aghdam and M. Abapour, [34] intends to the determine the number of the stages in an interleaved boost converter interfacing PV panels for achieving a reliable and costly optimized structure. A comparative study has been done on different modes of operation. including redundant operation or parallel operation in a two-stage interleaved converter. The comparison indicates that working in simultaneous mode would be more reliable. Contemplating this fact, reliability equation of a three-stage interleaved converter is calculated for simultaneous mode of operation.

A. Khosroshahi, M. Abapour et. al., [35] presents interleaved boost converters having several stages, which can be used to increase the reliability. A reliability comparison is done between the conventional boost converter and the interleaved structure. Two different operation modes are defined for the interleaved boost converter: half-power

and full-power operation modes. The reliability calculation is based on the Markov model of the converters. The power loss effect of converter components on their failure rates, and therefore, on the reliability of converter has been assessed.

M. J. Sathik, J. D. Navamani, et. al., [36] presents a generalized restructured topology for boost, buck-boost and its derived dc/dc converters with rearranging branches to enhance the reliability of the converter. This paper instigates the derivation of state-of-the-art topologies with reduced capacitor voltage stress. Mainly in the restructured topology, the capacitor branch is rearranged in the converter and this redesign venture results in profuse advantages like a better choice of the capacitor with low voltage rating, low equivalent series resistance and reduced voltage stress of the converter. The investigation of the capacitor voltage stress and reliability test is carried out. No extra components are required in this method, the same component count as the conventional converter is maintained.

H. Tarzamni et. al., [37] presents the reliability analysis of conventional isolated pulse width modulation DC-DC (IDC-DC) converters. The IDC-DC converters are categorized into isolated single-switch DC-DC (ISSDC-DC) or multiple-switch DC-DC (IMSDC-DC) converters [38]-[41]. The proposed framework encompasses analysing the impacts of duty cycle, input voltage, output power, transformer turns ratio, components characteristics and time duration on the overall reliability performance of the IDC-DC converters. The suggested reliability assessment is centred on Markov models characterized by taking into consideration all open and short circuit faults on the components in both continuous and discontinuous conduction modes.

#### 2.3. MAJOR FINDINGS AFTER LITERATURE REVIEW

Based on the literature review, several critical research gaps have been identified that highlight the need for focused exploration and innovation in the field of power electronics, particularly in agricultural applications. Despite agriculture being a cornerstone of livelihoods globally, much of the recent advancement in power electronics has been concentrated on electric vehicles (EVs). However, the application of these advancements in rural areas, specifically through the development of multiport

converters, has the potential to significantly enhance the quality of life and productivity in agriculture. The current research on DC-DC converters is still emerging, particularly in the context of multiport converters, which are underexplored and lack comprehensive design and analysis.

Moreover, control algorithms for converters predominantly rely on PI controllers, which face challenges related to convergence speed, complexity, and performance under varying conditions. Given the nonlinear nature of converters, linear controllers often fall short under uncertain parameters. Therefore, the development of robust nonlinear controllers is crucial for improving system reliability and performance.

Additionally, transient stability, particularly in relation to energy storage elements like capacitors and inductors, has not received adequate attention. The design and study of these components are essential for efficient energy flow and stability in power conversion systems. Furthermore, the integration of Renewable Energy Sources (RES) with energy storage systems in multiport converters offers a promising area for research, especially in designing multilevel inverters for driving AC machines in agriculture.

Finally, while multilevel inverters are commonly used in AC applications, they introduce more switches, leading to increased switching losses that impact performance. Research into improved modulation techniques to mitigate these losses is necessary. Addressing these gaps through targeted research will not only advance the field of power electronics but also provide significant benefits to agricultural productivity and sustainability.

#### 2.4. AUTHOR'S CONTRIBUTION

In this thesis, the author has made several significant contributions to the field of power electronics converters, particularly in the context of agricultural applications. These contributions are detailed below:

## 2.4.1. Modeling and Analysis of DC/DC Converters for Renewable Energy Systems (RES) Integration:

- The author has developed comprehensive models for DC/DC converters designed to integrate various renewable energy sources (RES), such as solar, wind, and fuel cells, with energy storage systems (ESS).
- The work involved selecting appropriate topologies that optimize the efficiency and performance of these converters in agricultural settings.
- Additionally, the author has focused on inverter integration, ensuring that the converted power is suitable for driving AC machines commonly used in agriculture, thereby enhancing overall system performance.

#### 2.4.2. Development of Robust Control Algorithms:

- Recognizing the limitations of existing control strategies, the author has developed advanced control algorithms tailored for the proposed DC/DC converters.
- These algorithms are designed to optimize the performance of the converters under varying conditions, including changes in input from different RESs and fluctuating load demands.
- The algorithms also address issues related to speed of convergence, static error, and response during steady-state and dynamic conditions, which are critical for the reliability and efficiency of agricultural power systems.

#### 2.4.3. Stability Study for Simulation and Hardware Prototyping:

- The author has conducted an in-depth stability analysis of the proposed converter system, both in simulation and through the development of a hardware prototype.
- This study is crucial for ensuring that the system remains stable under different operating conditions, particularly in isolated agricultural applications where reliability is paramount.
- The stability analysis also includes examining the impact of energy storage components such as capacitors and inductors, which are integral to the overall system performance.

## 2.4.4. Performance Tracking with Different RES Inputs and Variable Load Conditions:

- The author has implemented a detailed tracking mechanism to monitor the
  performance of the converter when subjected to various RES inputs and load
  variations, such as those seen in induction motors and other agricultural
  utilities.
- This contribution is essential for understanding how the system performs in real-world scenarios, where input and load conditions can be highly variable.
- The insights gained from this tracking have been used to further refine the design and control algorithms, ensuring that the converter system is both efficient and adaptable to the dynamic needs of agricultural applications.

Through these contributions, the author has addressed key research gaps identified in the literature and advanced the field of power electronics converters with a specific focus on enhancing agricultural productivity and sustainability.

#### **CHAPTER 3**

### OVERVIEW OF CONVERTERS AND IDEOLOGY TO MULTIPORT CONFIGURATION

#### 3.1. OVERVIEW

This chapter presents a systematic and straightforward approach to deriving multiple-input multiple-output (MIMO) converter topologies, aiming to explore a wide range of possibilities. The proposed topology derivation method involves three simple yet effective steps. First, three fundamental cells are introduced, each consisting of a single inductor paired with multiple sets of unidirectional switches and input/output ports. These cells serve as the foundational building blocks for developing MIMO topologies.

Next, the fundamental cells are integrated with the inductor branch of conventional single-input single-output (SISO) converters. This integration bridges the gap between existing SISO designs and their MIMO counterparts, providing a versatile framework for generating various configurations. Finally, unnecessary components, such as redundant switches and diodes, are removed to simplify the topology while maintaining functionality and efficiency.

Using this principle, a significant number of single-inductor MIMO (SI-MIMO) topologies are derived, spanning second-order, third-order, and fourth-order converters. These designs offer enhanced performance characteristics, making them suitable for a wide range of engineering applications. The proposed method demonstrates a scalable and efficient approach to developing advanced MIMO converters tailored to modern power management needs.

#### 3.2. INTRODUCTION

Conventionally, multiple power sources are connected to a shared DC voltage bus through independent DC–DC converters, while various loads are supplied via separate converters, as illustrated in Fig. 3.1. These standalone converters manage the input sources and regulate the output power for different loads. To improve the efficiency and performance of such multisource, multiload systems, multi-input multi-output (MIMO) converters have been introduced as an alternative solution, as shown

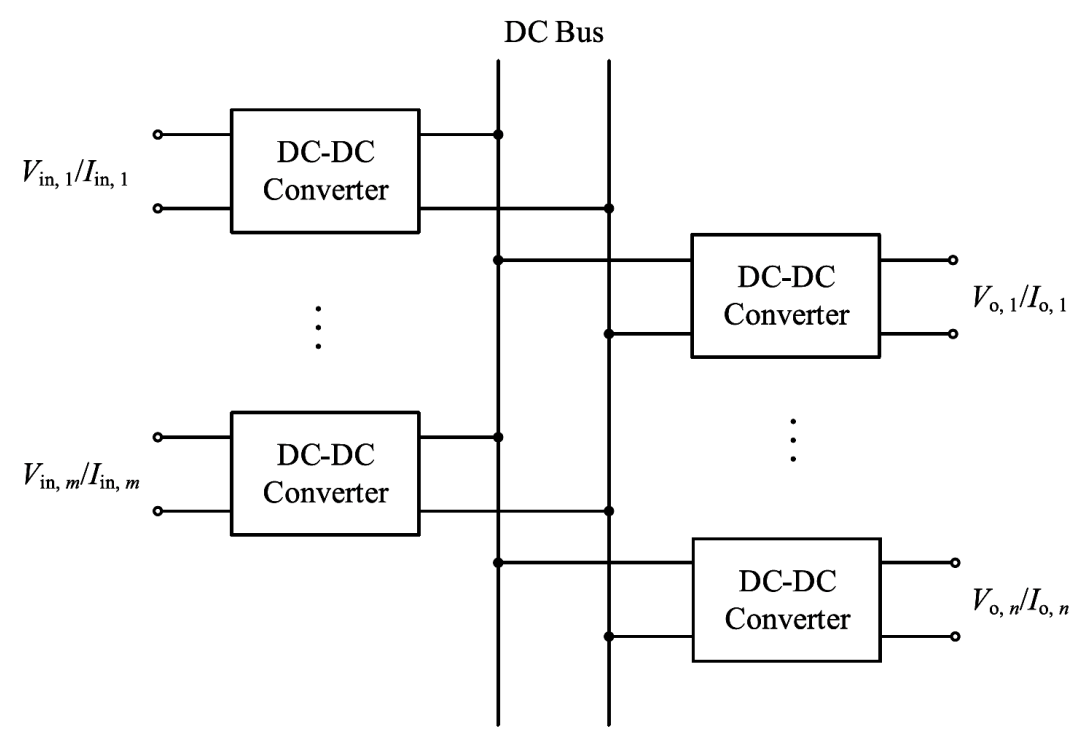


Figure 3.1. Conventional dc–dc converter architecture for integrating various input sources and output loads based on dc–dc converters.

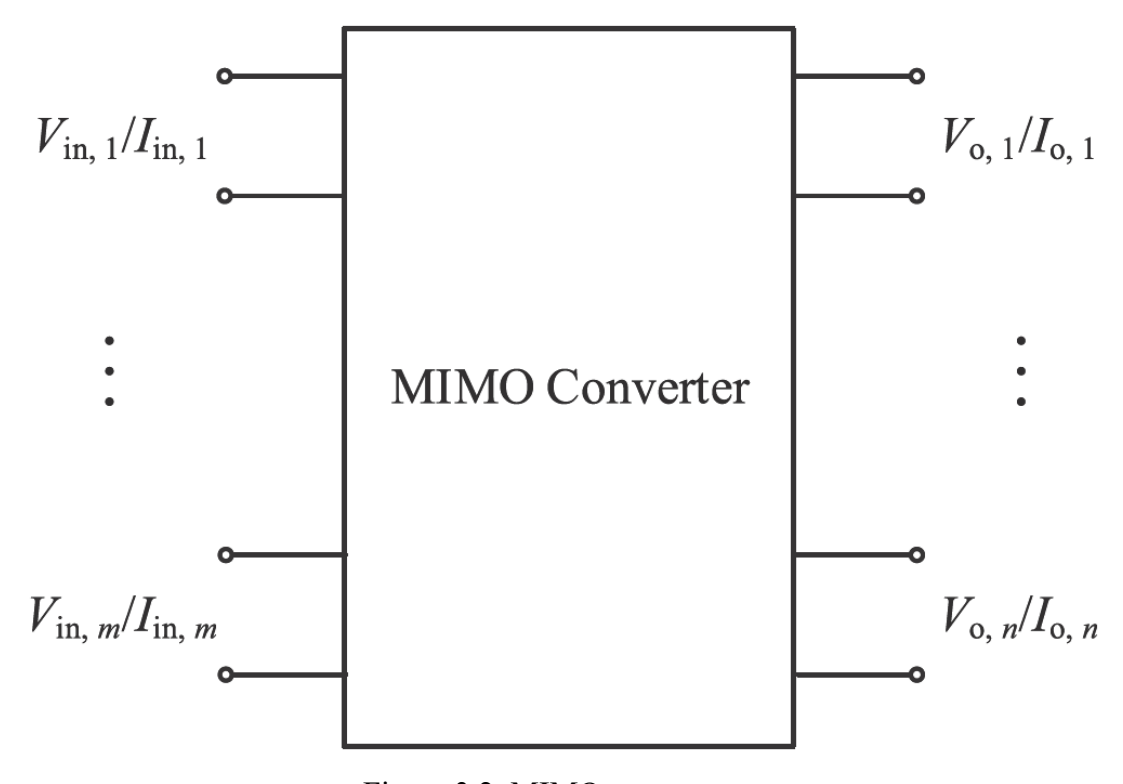


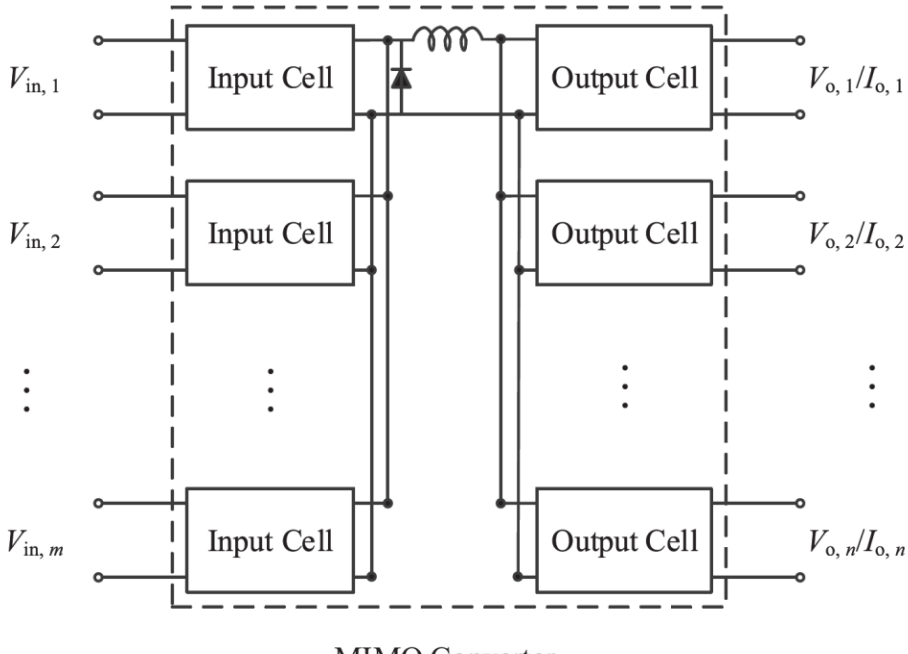
Figure 3.2. MIMO converter.

in Fig. 3.2 [42]— [47]. Compared to traditional architectures with independent converters, MIMO DC–DC converters provide significant advantages, including a

reduction in the number of components, increased power density, and fewer power conversion stages [47]. Among these, single-inductor MIMO converters are particularly attractive due to their compact size, reduced electromagnetic interference, and cost-effectiveness. These advantages become even more pronounced in systems involving a large number of sources and loads.

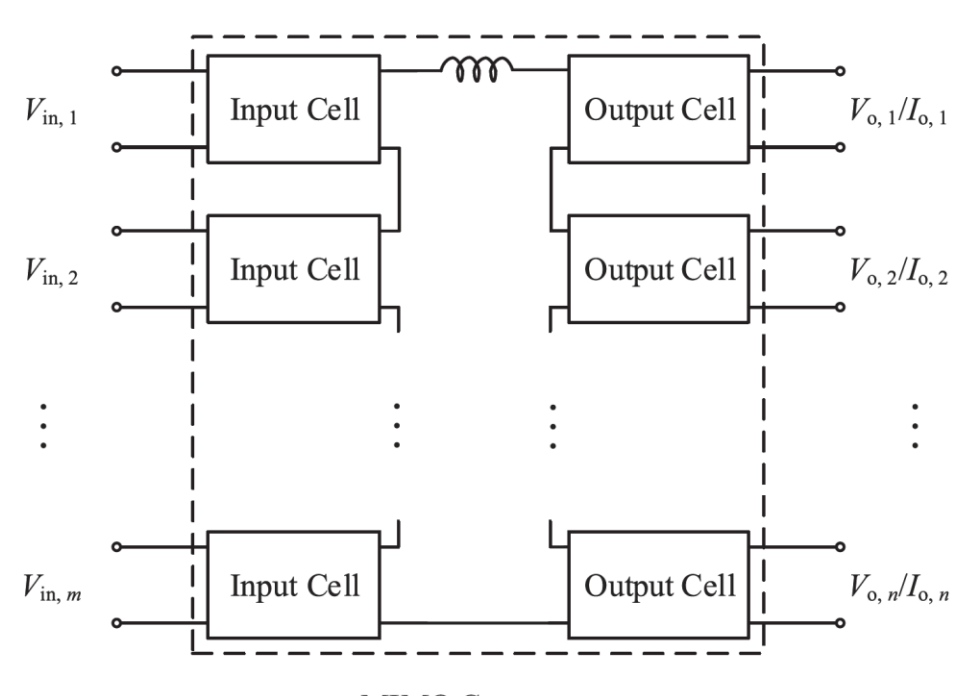
In many single-inductor MIMO converters, input cells are often connected in parallel on the input side, while output cells are arranged either in parallel or in series [48]–[63]. However, parallel-connected input cells face a significant limitation: due to voltage-programmed control, input sources cannot operate simultaneously without violating Kirchhoff's laws. To address this issue, time-multiplexing control is typically employed, which ensures that only one source delivers power to the loads at any given moment. This method, however, restricts the practical number of input sources. Similarly, parallel-connected output cells suffer from cross-regulation issues caused by the shared inductor. Managing the coupling effect between parallel-connected output cells requires complex control mechanisms, increasing system design complexity.

Various control strategies have been proposed to address these challenges, particularly in energy harvesting systems [52]–[56]. For example, a single-inductor two-input-two-output converter for solar energy harvesting [56] employs a specific control scheme to manage fluctuating PV cell voltages and battery charging. However, such configurations are highly specialized and lack the flexibility to accommodate an arbitrary number of input sources or loads. Resonant MIMO DC–DC converters [57] have also been introduced, achieving zero-voltage switching during turn-on and turn-off operations. However, these systems rely on specific switching patterns and are not easily adaptable to general configurations. A more versatile configuration, as shown in Fig. 3.3, has been explored in previous studies [58], [59]. Control approaches, such as model predictive control [62] and deadbeat-based regulation [63], have been proposed to improve performance by addressing cross-regulation issues and ensuring precise control of input currents and output voltages.



MIMO Converter

Figure 3.3. MIMO converter with parallel-connected input cells and output cells. All power cells are voltage-source-mode converter cells.



MIMO Converter

Figure 3.4. MIMO converter with series connected input cells and output cells. Here, all output cells are current-source mode converter cells.

Another MIMO converter with series-connected input cells and series-connected output cells are depicted in Fig. 3.4. In this configuration, input sources are connected

in series through series-connected input cells, enabling simultaneous power delivery to the loads. The output cells are also connected in series but are electrically independent, eliminating cross-regulation problems. This design significantly simplifies the control scheme, as it does not rely on time-multiplexing, and allows for flexible addition or removal of inputs and outputs without requiring modifications to the control structure. The configuration thus offers high generality for extension, simple control, and enhanced flexibility while avoiding cross-regulation issues.

#### 3.3. BRIEF REVIEW OF BASIC PWM CONVERTER TOPOLOGIES

To combine more than one energy source, such as the solar array, wind turbine, fuel cell, and commercial ac line, to get the regulated output voltage, different circuit topologies of multi-port converters (MPCs) have been proposed in recent years. The six fundamental PWM converters—buck, boost, buck-boost, Cúk, zeta, and single-ended primary inductance converter (SEPIC)—are widely employed in various power electronics applications [64]-[66]. Structurally, these converters can be categorized into two or three key portions: the input port (IP), the energy buffer port (EBP), and the output port (OP) as shown in Fig. 3.5. Among these, the buck and boost converters lack an energy buffer port. The topological structures of these six converters are defined with distinct identification of the input, energy buffer, and output portions.

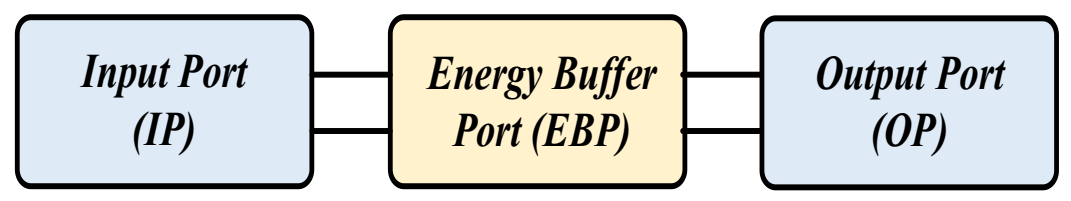


Figure 3.5. Three ports of a basic PWM converter.

In the energy buffer portion, inductors, and capacitors function as energy storage elements. Within each switching cycle, the inductor or capacitor alternately stores energy from the input portion and releases it to the output portion without any energy loss. Inductors operate as current buffers by maintaining a non-zero DC current, while capacitors act as voltage buffers by sustaining a nonzero DC voltage. For simplified representation of PWM converter topologies, the rectangular components are used to denote either current or voltage buffers.

In the input portion, a voltage or current source is chopped into a high-frequency pulse-train waveform using a switching device. This pulse-train voltage or current is then transferred to the output portion, where it is filtered to produce a stable DC voltage or current. When the pulse-train voltage waveform interacts with a current buffer, it passes through the buffer. Similarly, the pulse-train current waveform is transformed into a pulse-train voltage waveform via the voltage buffer. The high-frequency waveform—whether voltage or current—is eventually filtered by the output portion to achieve a DC output, ensuring efficient energy conversion and delivery. Topological structures of the six basic PWM converters are shown in Fig. 3.6 with input portions, energy buffer portions, and output portions marked.

The content of this chapter builds upon the foundational work presented in [67], which introduced a comprehensive set of DC–DC converter topologies without intermediate AC transformations. The discussion begins by outlining the assumptions, restrictions, and conditions underpinning the analysis. These parameters serve as the basis for deriving feasible input and output cells that enable the realization of multiple-input converters (MICs) and multiple-output converters (MOCs) from their single-input and single-output counterparts. Four basic rules guide the identification of these cells, while unfeasible cells are also analyzed, highlighting configurations that fail to meet essential multiport topology requirements, such as independent power flow control in each leg.

The rules for identifying feasible input and output cells not only support manual derivation but also provide a framework for developing computational methods to automatically detect valid configurations. However, given the analysis shows that feasible topologies represent a small subset of all possible configurations, the computational approach is deemed unnecessary for achieving the objectives of this chapter. Instead, the rules are applied systematically to explore potential MICs and MOCs.

The chapter further identifies specific single-input topologies from [67] that are suitable for expansion into MICs. These findings present an alternative to the multiple-input configurations suggested in [68], as the topologies derived from [69] are more diverse and do not require simultaneous power delivery from all sources. Additionally,

the approach presented here simplifies and enhances the work in [67], making it more flexible and practical for a wider range of applications [70].

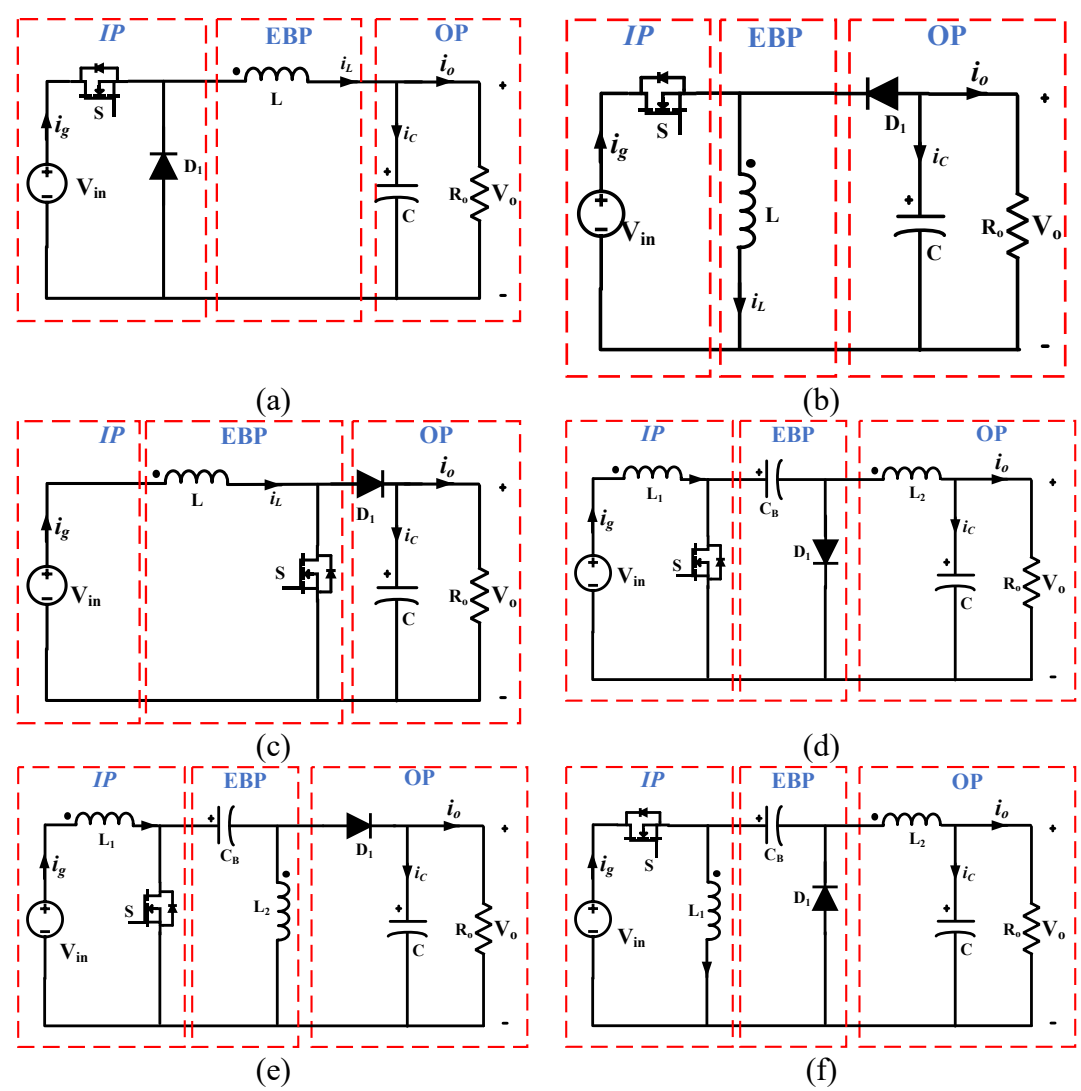


Figure 3.6. Topological structures of the six basic PWM converters. (a) Buck converter. (b) Buck-boost converter. (c) Boost converter. (d) 'Cuk converter. (e) SEPIC converter. (f) Zeta converter.

Finally, this chapter introduces novel MIC and MOC topologies derived from the study. These new configurations expand the design possibilities for multiport DC–DC converters, offering practical solutions with improved adaptability for applications requiring independent power flow control and flexible integration of multiple sources or loads. The findings contribute to advancing the development of innovative, efficient, and versatile converter systems.

## 3.4. FEASIBLE TOPOLOGIES FOR MULTIPORT DC-DC CONVERTERS

The analysis of MIC topologies is based on several key assumptions and restrictions aimed at simplifying the design and operation of the converters. First, power flow is assumed to be unidirectional, from source to load, in all converter inputs. This eliminates reverse power flow scenarios for simplification. Second, configurations with trivial connections between input legs, such as directly paralleling inputs at the output capacitor or using an alternating flux in a transformer core, are excluded.

The study prioritizes minimizing the total number of components by maximizing the use of shared components across inputs, thereby reducing the number of elements in individual input cells. As a result, only the simplest topologies within a family of similar converters are analyzed. For example, flyback converters are excluded since they are considered derivatives of buck-boost converters. While this approach can lower costs in standard designs, it may reduce reliability, as shared components can act as single points of failure. Nonetheless, MIC systems with modular designs and diverse input sources can enhance overall system availability compared to traditional architectures.

The analysis assumes continuous conduction mode operation using ideal components, with the goal of regulating a specified output voltage. Another important assumption is that all input cell switches are forward-conducting and bidirectional-blocking (FCBB). This assumption differentiates the study from prior works, such as [67], and allows for maximizing shared components. However, FCBB switches introduce a restriction on simultaneous power transfer from all sources to the load, as required in [67]. Additionally, implementing FCBB functionality with certain devices, like MOSFETs, may require adding components such as diodes, which seems to contradict the goal of component minimization. Furthermore, the reverse-blocking diode added with certain switches is often a built-in feature when bidirectional power flow capability is required—a common aspect of MIC designs.

These assumptions and restrictions lead to several operational conditions. The study focuses solely on direct DC-DC conversion topologies, excluding converters like forward converters. MICs are expected to handle inputs with varying nominal voltages while maintaining the ability to control power flow in each input leg independently. Even if some inputs are limited in the power they can draw from their respective sources, it must still be possible to independently control power flow within a certain range in each leg. The inclusion of FCBB switches imposes additional constraints, as the total input power must equal the output power, and sources may not always be able to deliver power simultaneously. These considerations ensure that the proposed MIC designs meet operational requirements while balancing simplicity, cost, and performance.

All multiple-input converter (MIC) topologies are derived from their single-input counterparts by multiplying the number of input stages (input cells) and connecting them to a shared output stage. The process of creating an MIC from a single-input version must adhere to several fundamental rules to satisfy the assumptions, restrictions, and conditions discussed earlier. These rules ensure the practical and functional realization of MICs.

#### **Rule 1:Required Input Cell Components:**

Each input cell must include at least one independently controlled forward-conducting bidirectional-blocking (FCBB) switch. This ensures a degree of control over the power delivered by each source, meeting the condition of independent input control. Additionally, since every input cell incorporates at least one FCBB switch, the common stage must include at least one dependent switch, such as a shared diode. While this rule does not limit the number of passive components in the MIC, the goal of minimizing the total number of components necessitates reducing passive components in each input cell. Passive elements should only be added to input cells if they cannot be incorporated into the common stage, as is the case with the input inductor in current-source converters.

#### **Rule 2: Independent Switch Redundancy:**

To maintain independent control of each input, the connection between input cells and the common stage must avoid redundancy in switches, specifically parallel independent switches. This rule requires that both terminals of an independent switch should not serve as connection points for the input cell. Ensuring non-redundant configurations allows for efficient and reliable power control in each input.

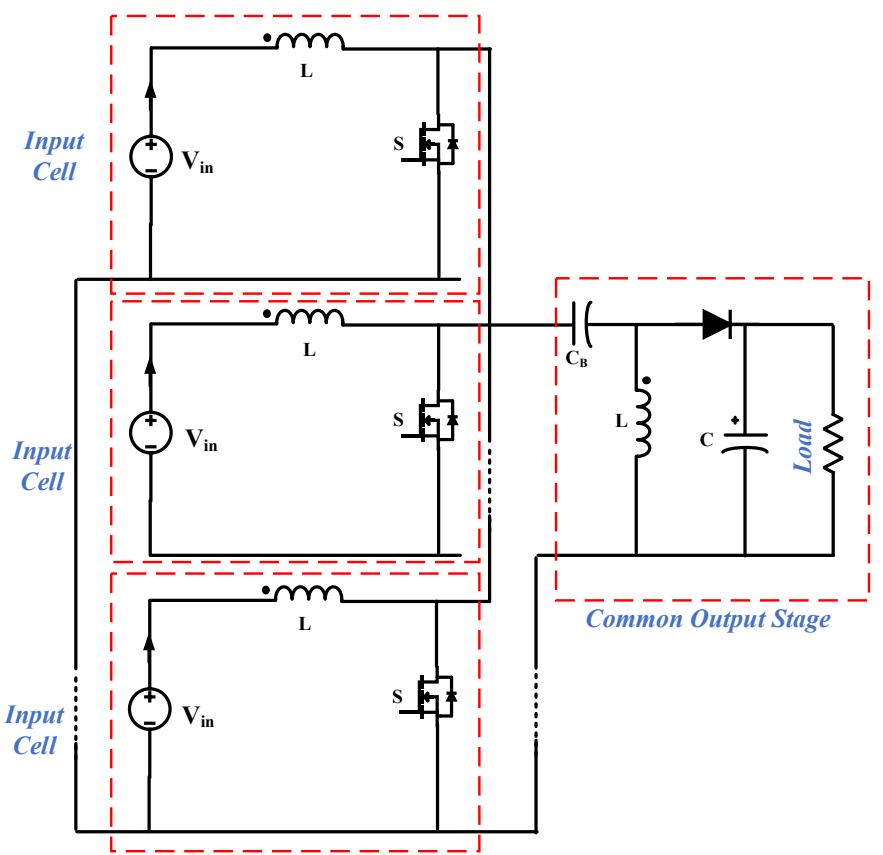


Figure 3.7 Unfeasible SEPIC converter with centre capacitor in the common output stage.

#### **Rule 3: Common-Stage Capacitor Voltage:**

In MICs derived from single-input topologies with center capacitors—such as the single-ended primary inductance converter (SEPIC) and the Ćuk converter—the average voltage of the common-stage center capacitor must not depend on the input voltage. For instance, in a multiple-input SEPIC topology, the center capacitor's average voltage would simultaneously equal all input voltages (as shown in Fig 3.7), making such a configuration unfeasible unless the assumption of minimizing components is relaxed. If the assumption is relaxed, the center capacitor can be divided

among the input cells. However, certain topologies may still be unfeasible if the capacitor's terminals are shared with the common stage, and their average voltage depends on their respective source voltages.

#### **Rule 4: Source Terminals:**

Both terminals of the input source must not serve as connection points for the input cell. Otherwise, when input cells are connected to sources with different voltages, a short circuit could occur. This rule ensures the safe and stable operation of MICs under varying input conditions.

By adhering to these rules, MIC topologies can be systematically developed while balancing the trade-offs between component minimization, functionality, and operational reliability. These guidelines form the foundation for the design and realization of MICs that meet the desired performance and efficiency criteria.

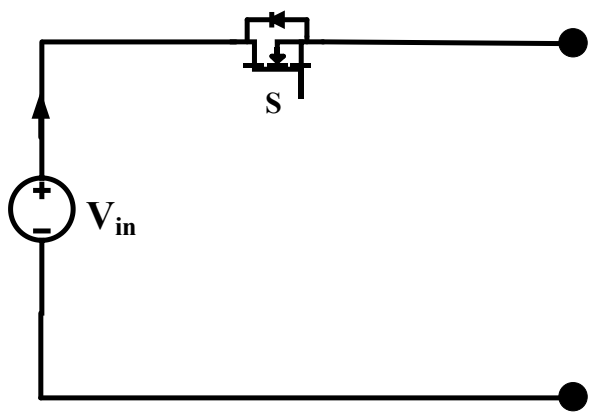


Figure 3.8. Feasible input cell. Connection terminals are marked with the black

#### 3.4.1. Basic Input Cells for Multiport Configurations

The application of the four rules outlined in Section 3.4 results in three categories of input cells: always feasible input cells, always unfeasible input cells, and alternative input cells. The latter category can lead to feasible MIC topologies if the assumption of minimizing the total number of components is relaxed, and the center capacitor in the common stage is distributed across the individual input cells.

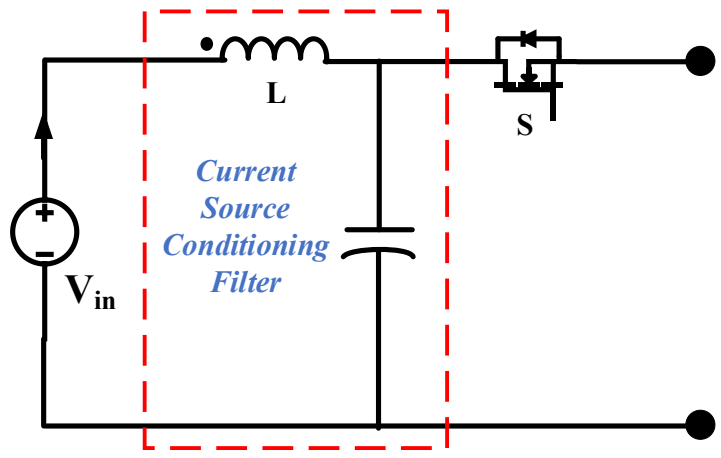
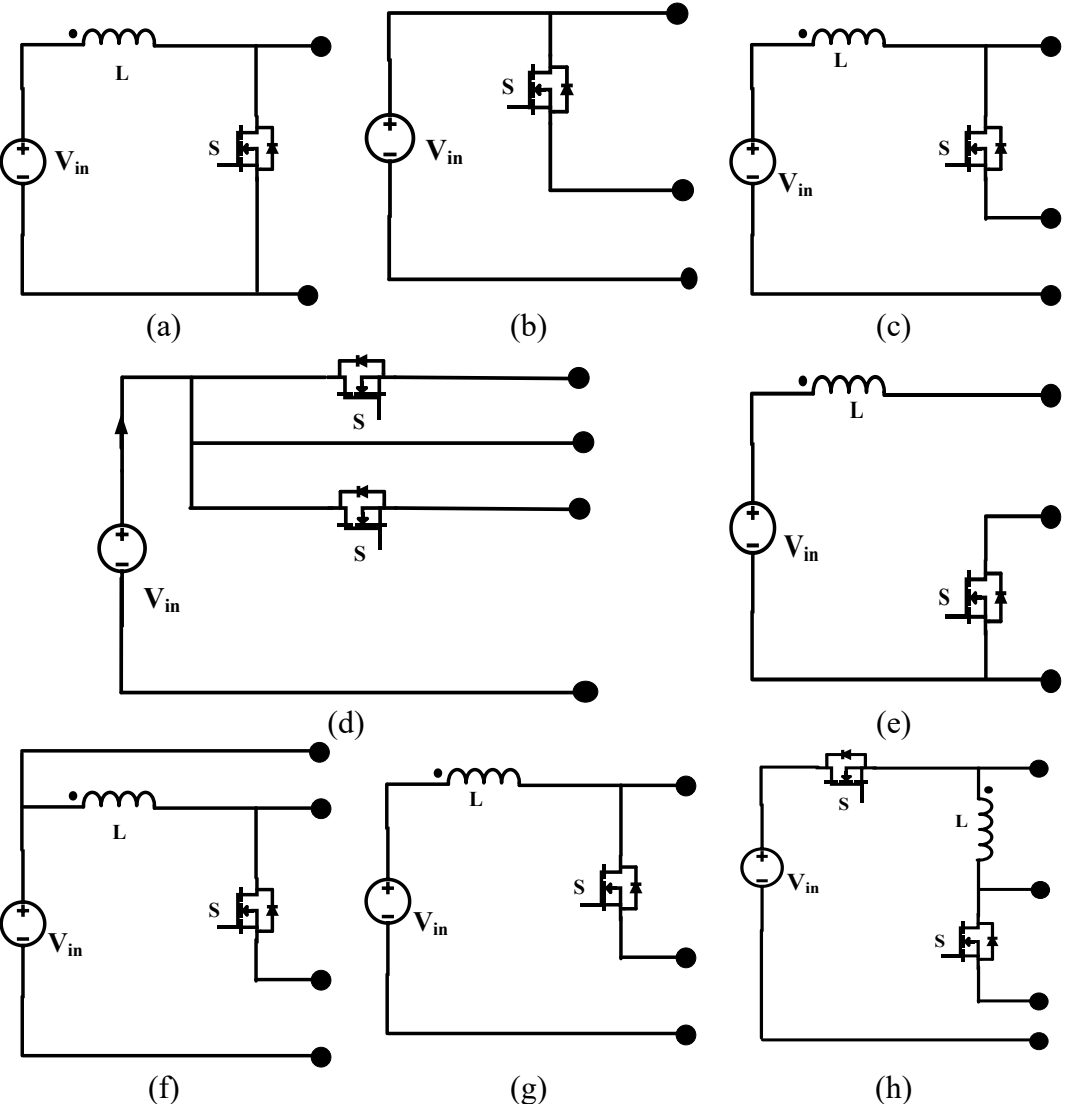


Figure 3.9. Current-source conditioning filter for the feasible input cell in Fig. 3.4. The input cell that consistently produces feasible MIC topologies is depicted in Fig. 3.8. This input cell is commonly associated with voltage source converters, such as the buck converter. However, its primary limitation is that it generates a switched input current, which is unsuitable for certain sources, such as fuel cells. This drawback can be mitigated by incorporating an input current-source conditioning filter, as illustrated in Fig. 3.9.

On the other hand, unfeasible input cells are more prevalent, as shown in Fig. 3.10. These cells fail to comply with at least Rule 2, which prohibits configurations where the terminals of an input cell overlap with both terminals of the same switch. Additionally, most unfeasible cells for converters featuring four switches, as referenced in [46], are excluded from Fig. 3.10. This is primarily because these cells involve an independently controlled switch separated from the other components of the input cell, with both terminals of the switch acting as connection points to the common stage.

In practice, many of the unfeasible input cells depicted in Fig. 3.6. also violate Rule 3. This is because the average voltage of any common-stage center capacitor connected to the input-source terminal—either directly or via an inductor—depends on the input voltage. This issue highlights a potential solution: to make unfeasible input cells feasible, the center capacitor in the common stage can be distributed across each input cell. The resulting modified input cells are illustrated in Fig 3.11., corresponding to the input cells with the same names in Fig 3.10. When diverse input sources are used, redistributing the center capacitor to each input cell also provides an additional benefit.



(f) (g) (h) Figure 3.10. Unfeasible cells. Connection terminals are marked with black dots. It enhances the converter's availability by eliminating the center capacitor as a single point of failure, especially since capacitors are often considered one of the less reliable components in the system.

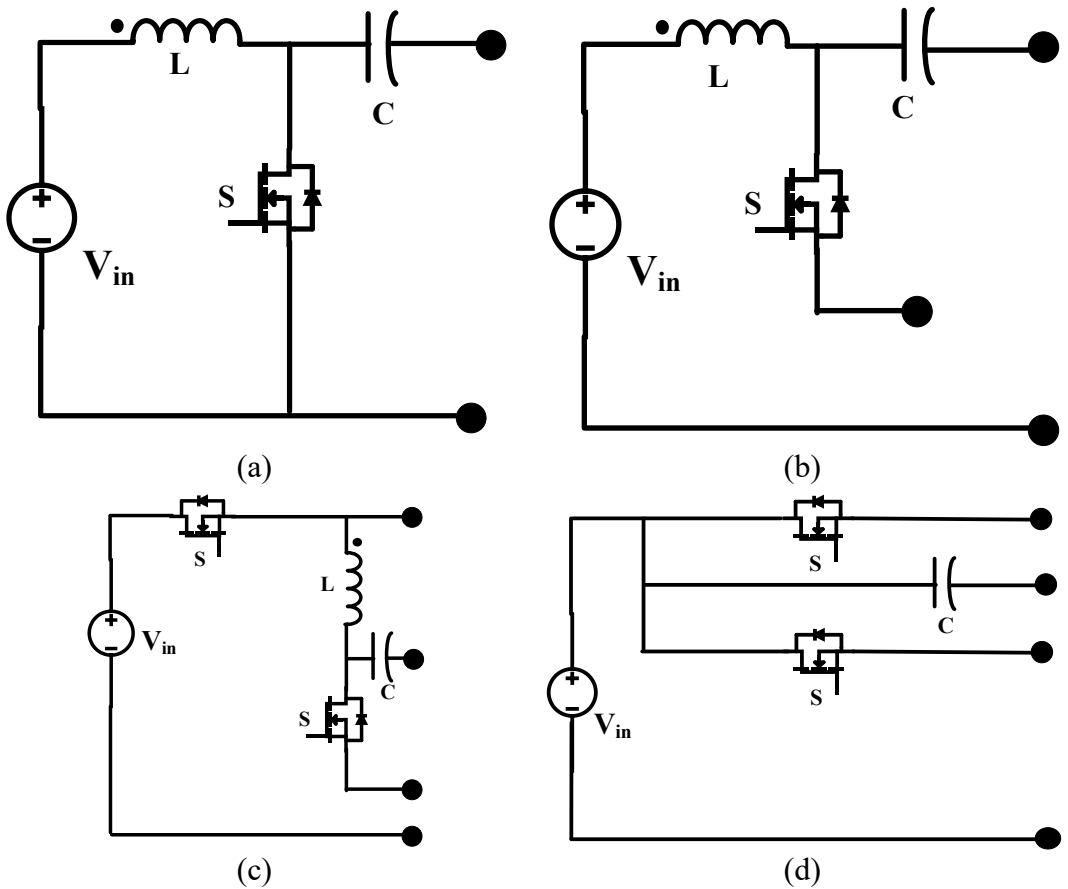


Figure 3.11. Additional feasible cells if the assumption of common components maximization is relaxed in the corresponding unfeasible input cells in Fig. 3.6.

Connection terminals are marked with black dots.

#### 3.4.2. Ideology for Multiport Configurations

This section outlines the principle and process for deriving MIMO converter topologies from the standard boost SISO converters shown in Fig. 3.6(c). The method involves just three straightforward steps, making it simple to implement. Additionally, under certain operating conditions, some of the derived topologies can be further optimized to reduce the number of semiconductor components.

This chapter presents the principle and methodology for deriving MIMO converter topologies from typical SISO converters, as shown in Fig. 3.6. The process involves three primary steps, ensuring simplicity and ease of implementation. Additionally, under suitable conditions, the resulting topologies can be optimized by reducing unnecessary semiconductor components.

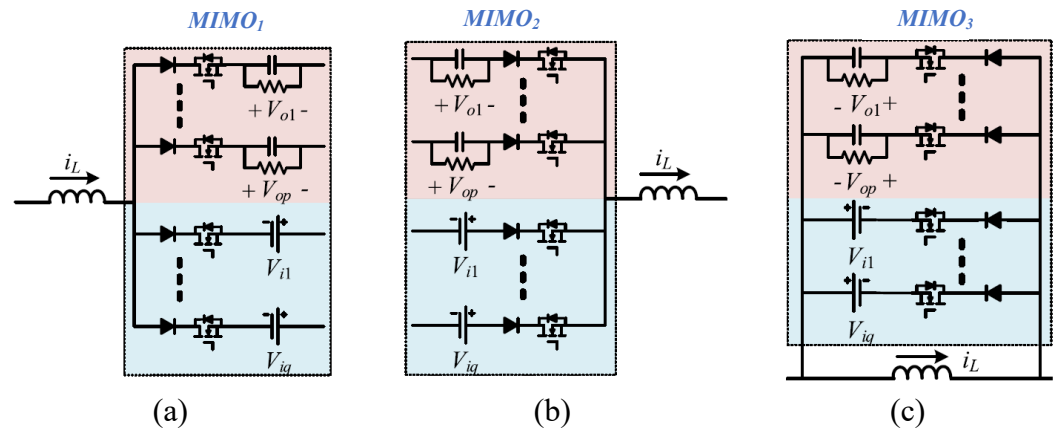


Figure 3.12. Three MIMO cells with connection to different ports of the inductor: (a) outflow, (b) inflow, and (c) both.

#### **Step 1: Proposal of Basic MIMO Cells**

Three fundamental MIMO cells, referred to as  $MIMO_1$ ,  $MIMO_2$ , and  $MIMO_3$ , each with p outputs and q inputs, are proposed in Fig. 3.12. These cells are developed based on the operational principles and structural features of existing MIMO converters. The cells multiplex the inductor current  $i_L$  by connecting multiple inputs/outputs and unidirectional switches to the outflow, inflow, or both ports of the inductor, as illustrated in Fig. 3.12(a)–(c).

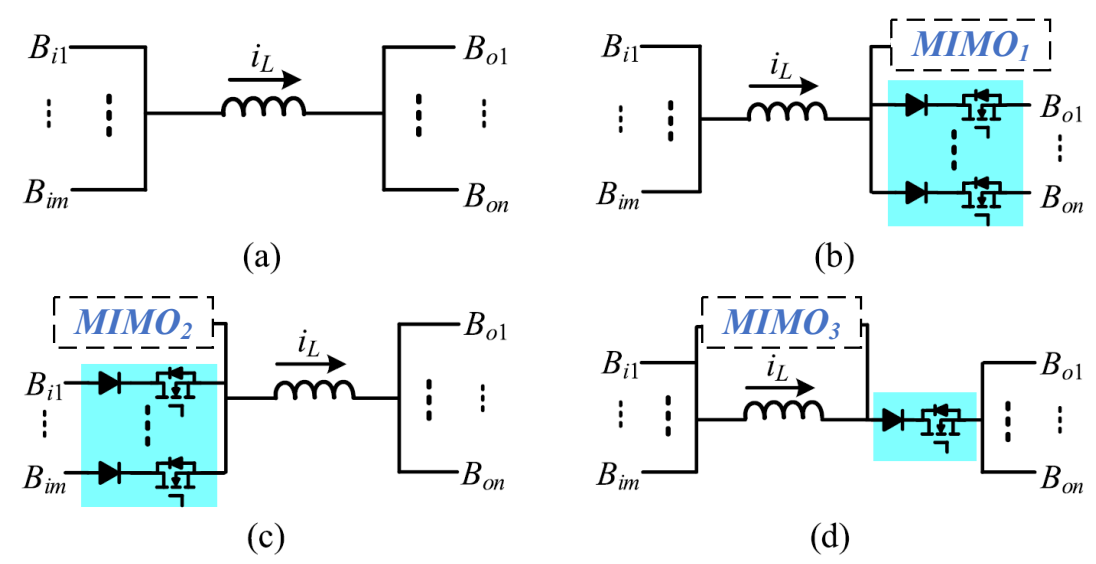


Figure 3.13 Three types of MIMO topologies deriving from the four typical SISO converter. (a) SISO. (b)  $MIMO_1$ . (c)  $MIMO_2$ . (d)  $MIMO_3$ .

- $MIMO_1$  Cell: Integrated at the inductor's outflow port, with additional unidirectional switches included in each original branch  $B_{o1} B_{on}$ , ensuring that  $i_L$  flows through only one path at a time.
- $MIMO_2$  Cell: Integrated in a similar manner to  $MIMO_1$ , as shown in Fig. 3.13(c).
- *MIMO*<sub>3</sub> *Cell*: Requires only a single additional unidirectional switch since it is connected in parallel with the inductor, as shown in Fig. 3.13(d).

Multiple MIMO cells can also be combined and integrated into SISO converters, as demonstrated in Fig. 3.14. The extra unidirectional switch in  $MIMO_3$ , shown in Fig. 3.14(d), can be removed when combined with  $MIMO_1$ ,  $MIMO_2$ , or both, as depicted in Figs. 3.14(b)–(d), due to the presence of unidirectional switches in branches  $B_{i1} - B_{im}$  or  $B_{o1} - B_{on}$ .

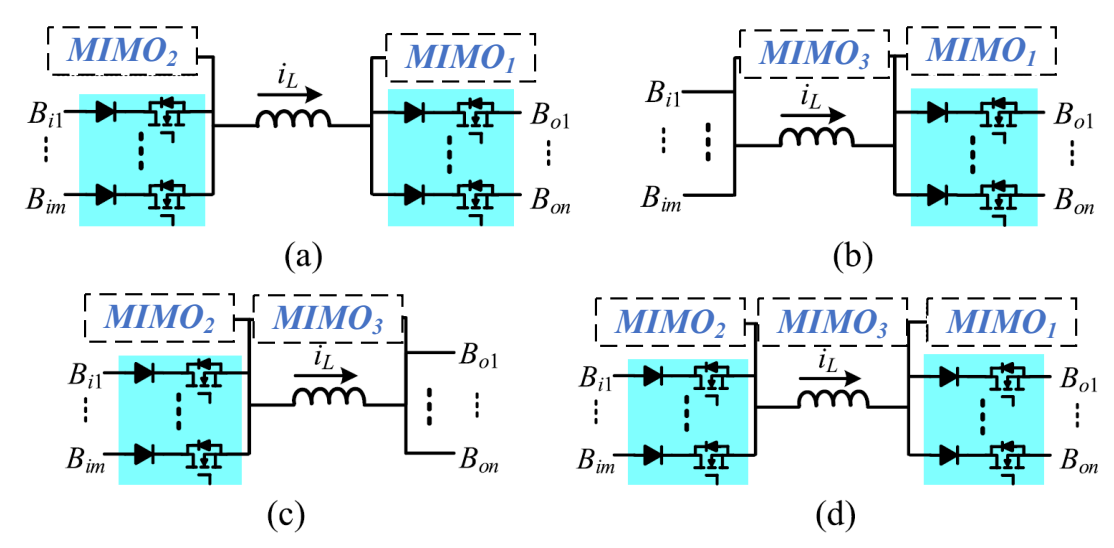


Figure 3.14. MIMO topologies with the combination of three MIMO cells. (a)  $MIMO_1 + MIMO_2$ . (b)  $MIMO_1 + MIMO_3$ . (c)  $MIMO_2 + MIMO_3$ . (d)  $MIMO_1 + MIMO_2 + MIMO_3$ .

#### **Step 2: Integration with SISO Converters**

The MIMO cells are then integrated with the inductor branches of typical SISO converters, including buck, boost, buck-boost, and non-inverting buck-boost converters. The inductor branches of these converters are generalized, as shown in Fig. 3.13(a), with the parameters m and n set to 1 or 2, depending on the converter type.

**Integration Example:** The process of integrating a single MIMO cell with the inductor branch is detailed in Figs. 3.13(b)–(d) for  $MIMO_1$ ,  $MIMO_2$ , and  $MIMO_3$ , respectively.

For MIMO topologies shown in Figs. 3.13(b), 3.13(c), and 3.14(a)–(d), employing  $MIMO_1$  or  $MIMO_2$  cells results in one port of each output  $V_{o1} - V_{op}$  or input  $V_{i1} - V_{iq}$  being left unconnected. These suspended ports can theoretically be connected to any node in the SISO converters, other than the inductor's nodes, leading to the development of multiple MIMO topologies. For example, integrating  $MIMO_1$  or  $MIMO_2$  cells with a boost converter can yield two SIDO/DISO topologies.

#### **Step 3: Simplification of Derived Topologies**

The final step involves simplifying the derived MIMO topologies by removing redundant or unnecessary switches. Many added unidirectional switches are either duplicated or serve no purpose.

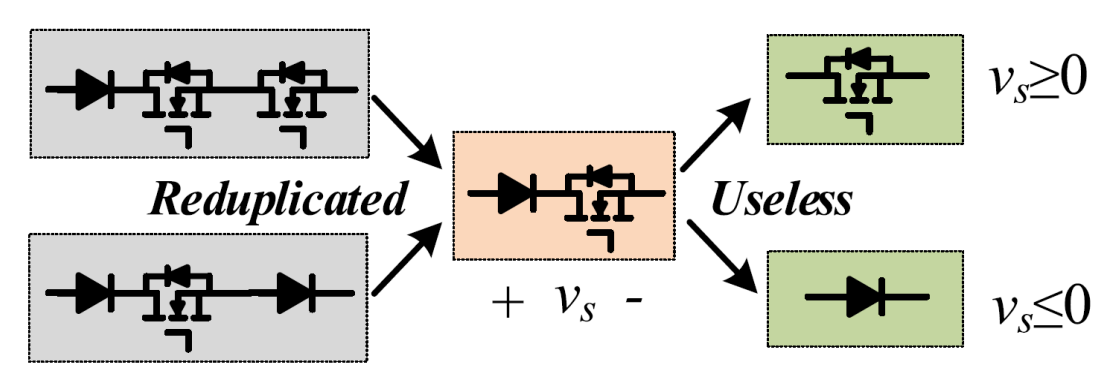


Figure 3.15. Simplification of switches.

- **Redundant Switches:** As shown in Fig. 3.15, redundant MOSFETs/diodes in series can be removed by deleting one of the duplicates.
- Voltage Analysis: If the voltage  $v_s$  across a unidirectional switch is always greater than or equal to zero, the diode remains forward-biased and can be removed. Conversely, if  $v_s$  is always less than or equal to zero, the parallel diode of the MOSFET conducts continuously, allowing for its removal as well.

By following these steps, the methodology provides a structured approach to derive efficient and optimized MIMO converter topologies from their SISO counterparts.

#### 3.5. MIMO TOPOLOGY DERIVATION FOR BOOST CONVERTER

By applying the previously discussed principles, various multi-input multi-output converters can be derived with relative ease. To illustrate this process, the combination of a boost converter and the  $MIMO_3$  cell with one output branch (p = 1, q = 0) is taken as an example, with its topology derivation detailed in Fig. 6. Initially, the  $MIMO_3$  cell is integrated with the boost converter, as depicted in Fig. 3.16(a). The extra unidirectional switches are then repositioned to connect in series with switch  $S_1$  and diode  $D_{S2}$ , resulting in the configuration shown in Fig. 3.16(b). Simplification, as explained in Fig. 3.15, is applied next, where redundant MOSFETs and diodes are eliminated, as shown in Fig. 3.16(c).

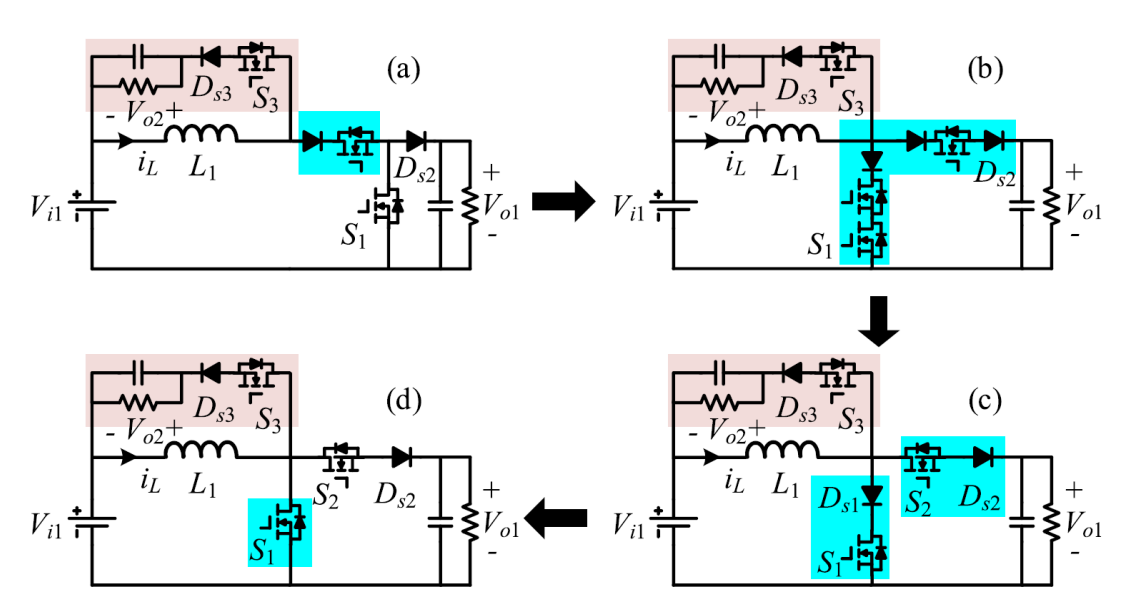
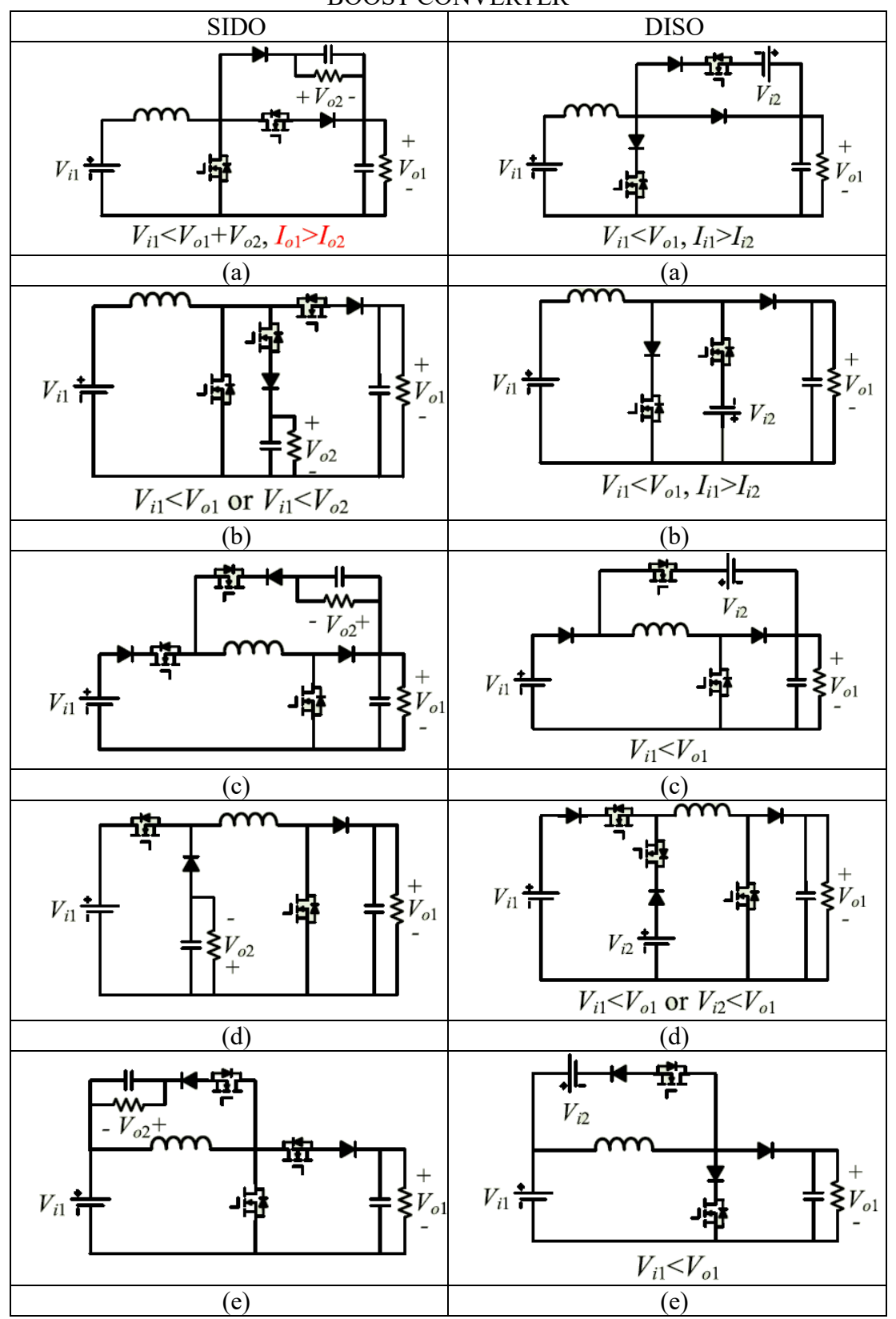


Fig. 3.16. Topology derivation process of the SIDO converter with combination of boost converter and  $MIMO_3$  cell with one output branch.

Subsequently, during a switching period, the inductor current  $i_L$  is directed through different paths by sequentially turning  $S_1$ ,  $S_2$ , and  $S_3$  ON. When  $S_1$  is OFF, the voltage across  $D_{s1}$  and  $S_1$  equals  $V_{o1}$  or  $V_{i1} + V_{o2}$  during the intervals in which  $S_2$  and  $S_3$  are ON, respectively. As this voltage is consistently greater than zero, diode  $D_{s1}$  can be removed. The final topology, shown in Fig. 3.16(d), represents a viable single-input dual-output converter.

TABLE 3.1. FAMILY OF SIDO AND DISO CONVERTERS DERIVED FROM BOOST CONVERTER



Additionally, Tables 3.1 present a family of SIDO and DISO converters derived from standard boost converters using the proposed topology derivation method. Each topology exhibits unique performance characteristics, allowing researchers to select the most appropriate configuration for specific applications. For instance, in the topology shown in Table 3.1(i)-(a), the inductor voltage alternates between  $V_{i1}$ ,  $V_{i1}$  –  $V_{o1}$ , and  $V_{i1} - V_{o1} - V_{o2}$  during different switching intervals. This behavior requires  $V_{i1}$  to remain smaller than  $V_{o1} + V_{o2}$ ; otherwise, the inductor's average voltage over a switching period would not be zero. Furthermore, based on the ampere-second balance for capacitors, the average output current  $I_{o1}$  must equal the sum of the second output current  $I_{o2}$  and the current through the unidirectional switch, resulting in  $I_{o1} > I_{o2}$ . Consequently,  $V_{o1}$  must be prioritized to ensure the proper operation of  $V_{o2}$ . These requirements can be further refined with more detailed parameter specifications. As the number of input and output ports increases, more viable MIMO topologies can be developed. For example, a boost converter-based DIDO topology has 25 viable configurations, which can be grouped into six categories based on the different MIMO cells used. Representative topologies from each category are illustrated in Fig. 3.17. In Figs. 3.17(a)–(c), two identical MIMO cells are simultaneously integrated into the boost converter, while in Figs. 3.17(d)–(f), two of the three cells are combined. Compared to conventional MIMO converters with additional parallel-connected inputs/outputs [26]–[31], the new topologies feature diverse additional port characteristics, making them more suitable for applications requiring varying inputs and outputs.

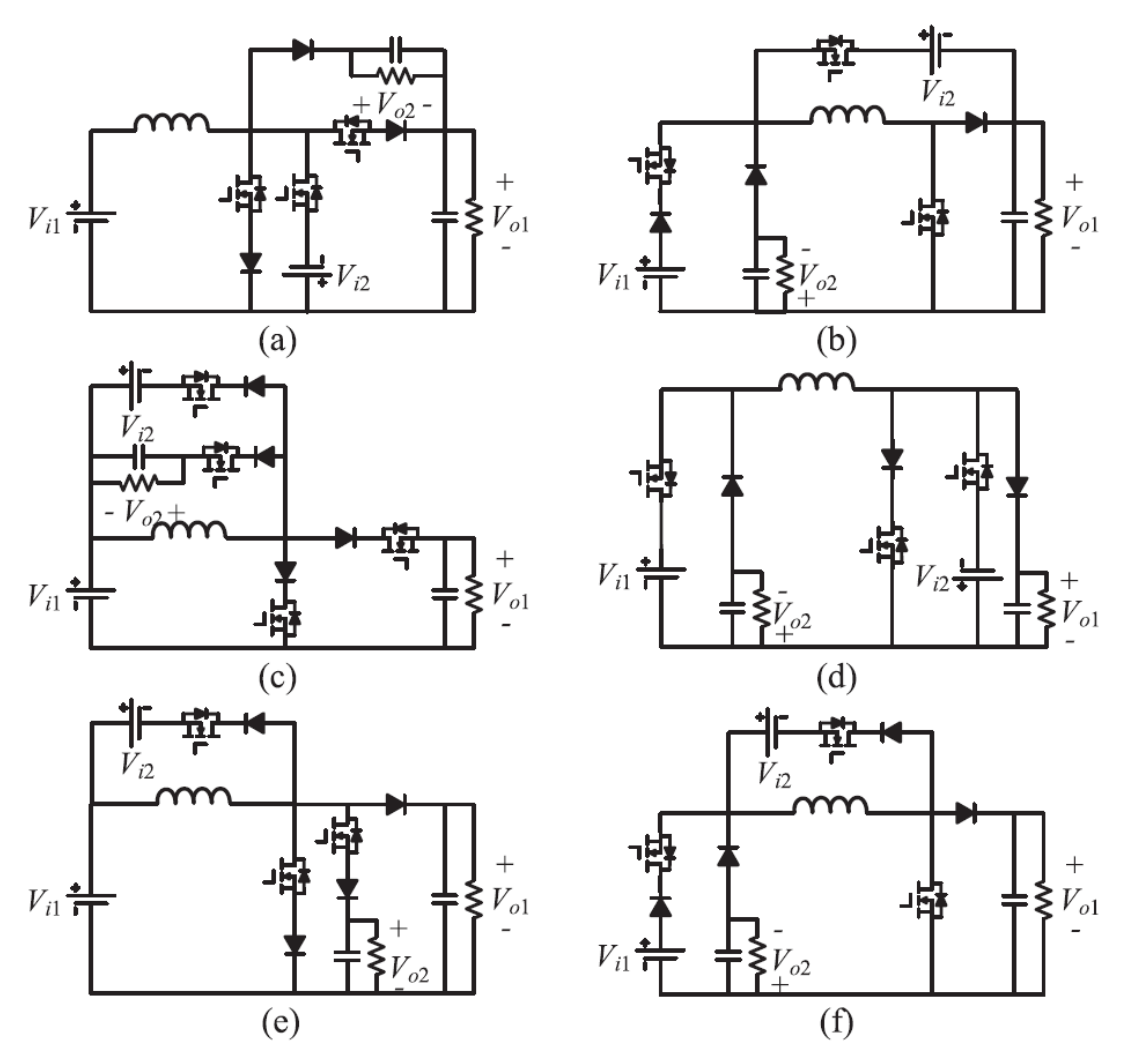


Figure 3.17. DIDO topologies based on boost converter with different MIMO cells. (a)  $MIMO_1 + MIMO_1$ . (b)  $MIMO_2 + MIMO_2$ . (c)  $MIMO_3 + MIMO_3$ . (d)  $MIMO_1 + MIMO_2$ . (e)  $MIMO_1 + MIMO_3$ . (f)  $MIMO_2 + MIMO_3$ .

To facilitate this selection, Tables 3.1 summarize the basic voltage and current requirements for these topologies based on the principles of voltage-second balance and ampere-second balance, respectively.

#### 3.6. CONCLUSIONS

In this chapter, a systematic approach for deriving multi-input multi-output (MIMO) converter topologies from typical boost converters was presented. The proposed method, requiring only three straightforward steps, was demonstrated in detail using a range of derived single-input dual-output (SIDO), dual-input single-output (DISO), and dual-input dual-output (DIDO) topologies. By applying this methodology, engineers gain access to a broader spectrum of MIMO configurations,

enabling the selection of an optimal topology tailored to specific engineering applications.

Furthermore, the development of multiple-input converters (MICs) from their corresponding single-input counterparts was explored. Through the application of defined assumptions, constraints, and conditions, the analysis identified both feasible and unfeasible input cells for MIC design. Four fundamental rules were used to determine which single-input topologies could be extended into multiple-input circuits. These contributions provide a practical framework for the design and implementation of advanced MIC systems in diverse engineering contexts.

#### **CHAPTER 4**

# LYAPUNOV FUNCTION APPROACH TO STABILIZE MULTIPORT FLYBACK CONVERTER TO INTEGRATE RESs

#### 4.1. INTRODUCTION

Over the past two decades, renewable energy sources such as photovoltaic (PV) and wind energy have become increasingly important due to their clean, pollution-free nature and abundance. Researchers and scientists are actively investigating PV energy generation systems, focusing on improving inverter designs and control strategies to boost efficiency [71][72]. However, despite these technological advancements, the high costs have limited their widespread use, mainly residential applications. Flyback topology-based DC/DC converters, known for their simplicity, low cost, ease of isolation, and ability to provide multiple outputs, have found broad acceptance in automotive systems, telecommunications equipment, and electronic devices. These converters can function in both continuous conduction mode (CCM) and discontinuous conduction mode (DCM). In [73], a grid-connected system for renewable energy source (RES) applications, comprising a modified switched-

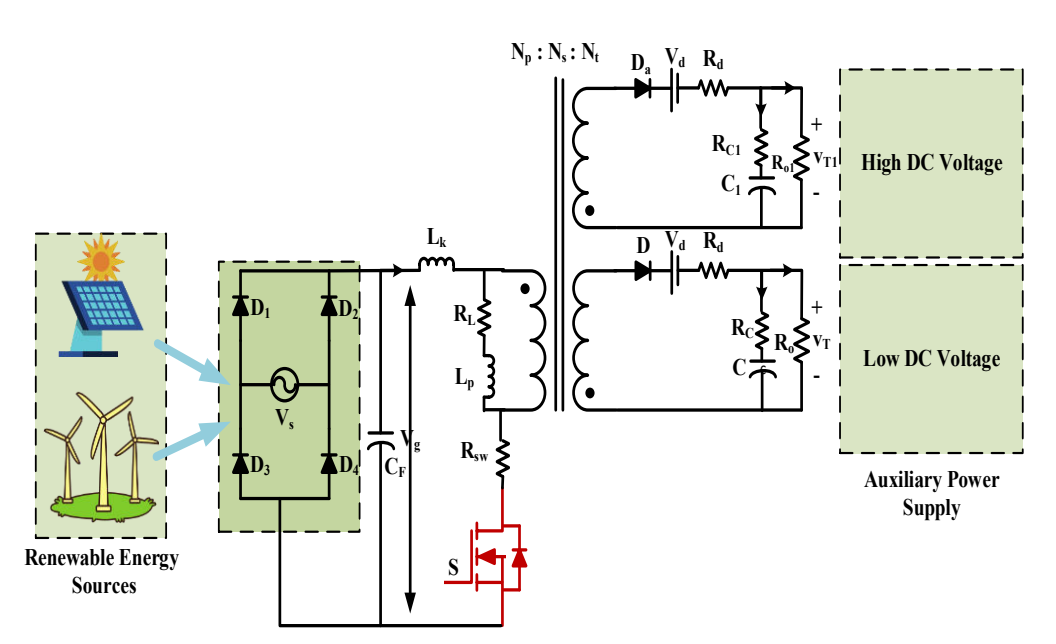


Figure 4.1. Multiport Flyback Converter Topology

capacitor (SC) based multilevel inverter paired with a DC-DC flyback converter, is presented.

When operating in the continuous conduction mode (CCM), the non-ideal flyback DC/DC converter exhibits higher efficiency, lower voltage and current stress, and a more straightforward filter design than the DCM mode. As a result, there is considerable interest in utilizing the flyback CCM converter for industrial applications [74]-[77].

However, the flyback CCM converter faces a challenge due to its nonminimum phase behaviour, which is attributed to its transfer function from the control duty to the output voltage having a right-half-plane zero [78]. Consequently, achieving precise output voltage control for the flyback converter with equivalent series resistances poses a challenging issue. The MFC architecture of the Renewable Energy based system is shown in Fig. 4.1, having an isolated flyback converter.

Control designs for these converters are usually implemented using small signal analysis around the operating point to enable the application of linear control strategies [79]-[80]. Linear control design techniques are popular for the flyback CCM converter around a fixed operating point, but their use requires a linearized model that does not capture the entire dynamic behaviour, making it difficult to ensure stability under large perturbations. Researchers have proposed nonlinear control strategies derived directly from the converter's model, avoiding the need for linearization. Based on Lyapunov functions, backstepping control stabilizes the inductor current and output voltage, but it is sensitive to parameter variations and exhibits slow transient responses due to inherent singularities [81]-[83]. On the other hand, sliding-mode control (SMC) ensures robustness against variations and disturbances with faster transient performance. However, SMC generates a bang-bang-type control input, leading to chattering and significant switching frequency variation with varying input voltage and output load [84]. In [85], it employs a control strategy grounded in Lyapunov functions to ensure the stability of a cascaded DC-DC converter.

Meanwhile, [86] introduced a technique for calculating the switching control signals for the Cuk DC-DC converter utilizing the Lyapunov theory. It is important to note

that the concepts outlined in [87] have not yet been implemented in a practical experimental setup. A notable challenge with the Lyapunov controller is achieving fast convergence of the Lyapunov function while maintaining robustness against variations in the controller coefficients, as mentioned in [88]. Therefore, developing a practical approach for selecting these coefficients is essential to ensure rapid response and stability across a wide range of operating conditions.

In [89], a SISO flyback converter employing Lyapunov function control is introduced. The study accounts for parasitic elements in the diode, inductor, and switch but overlooks the inclusion of capacitor equivalent series resistances ESR. The chapter digs into the design of the converter's controller but does not discuss the aspects of converter stability and the stress placed on the switches. In [89], the authors introduce a new seven-level inverter based on switched capacitors that operates with a single DC power supply. The design can produce a seven-level output voltage waveform while also boosting the voltage. Remarkably, the inverter achieves a voltage gain factor of 3 without the need for an additional DC-DC boost converter.

This chapter proposes a CCM flyback converter considering ESR of all components, including the capacitor, having two outputs. This converter's nonminimum phase behaviour, caused by a right-half-plane zero in its transfer function, leads to poor transient response under large signal perturbations [90]-[92]. The converter stability is analyzed by deriving the transfer function for one of the outputs. However, the Lyapunov-function-based feedback controller makes the system's response globally exponentially stable during the transient response compared to the linear PID controller and the integral mode sliding mode controller. We strengthen it by adding a duty-ratio feedforward controller to lessen its load. By considering parasitic elements, we create a dynamic model for the flyback CCM converter, allowing precise control of the desired output voltage. Numerical simulations demonstrate better performance and stability, while practical tests confirm the effectiveness of our proposed control method in different applications. In [93], the authors propose a five-level boost inverter with a single DC source, featuring a DC-DC boost converter for voltage transfer, PCC method for switching pattern, component design, power loss analysis, performance

comparison, and a laboratory prototype tested with the local grid for active and reactive power control.

# 4.2. DYNAMIC MODELLING OF FLYBACK CONVERTER WITH PARASITIC COMPONENTS

The flyback CCM converter's modelling and controller design process can be challenging and complex, leading to the omission of parasitic components. This results in an ideal/lossless model that simplifies the development and aids in understanding the converter's main features. However, accounting for parasitic elements becomes crucial for enhancing model accuracy and studying dynamic performance. Including these components can lead to improved steady-state and transient performance. Therefore, we consider the parasitic components in our approach to construct a more comprehensive dynamic model of the flyback CCM converter.

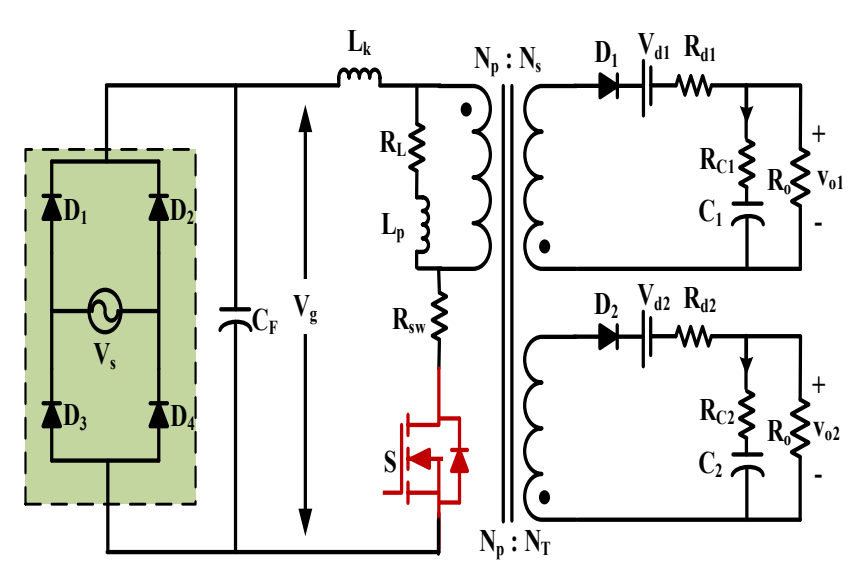


Figure 4.2. Electrical model of Flyback converter with parasitics components.

Figure 4.2 describes the circuit diagram of the non-ideal flyback converter with ESRs. This electrical model presents the transformer as an equivalent inductor Lp. Within this model, the parameters  $V_g$ , S,  $R_{sw}$ ,  $L_p$ ,  $L_k$ , D, C,  $R_o$ ,  $n = \frac{N_p}{N_s}$ ,  $i_{Lp}$ ,  $V_d$ ,  $R_L$ ,  $R_d$ ,  $R_c$ ,  $v_c$ , and  $v_T$  symbolize the input voltage, MOSFET switch, switch resistance, transformer inductance, leakage inductance, diode, output filter capacitor, load resistor, transformer turns ratio, inductor current, diode forward drop, inductor

resistance, parasitic diode resistance, ESR of the capacitor, output capacitor voltage and output voltage of the non-ideal Flyback converter, respectively.

In any converter, two primary states of a switch are employed to formulate the voltage gain equation. The voltage and current waveforms for PWM switching of the Flyback converter are illustrated in Fig. 4.3 to depict this relationship. The working of the flyback converter is expressed as:

Switch S (0 < t < DT) is turned ON, as shown in Fig. 4.4(a), the primary side of transformer T experiences an increasing current flow as the input DC voltage supplies power to it. Consequently, energy is stored in the transformer's magnetizing inductance  $L_p$ . Due to the polarity of the transformer's dot, diode D becomes reverse-biased, causing the secondary side to be disconnected and not conduct electricity. In this state, the load is powered by the current supplied from the output capacitor C.

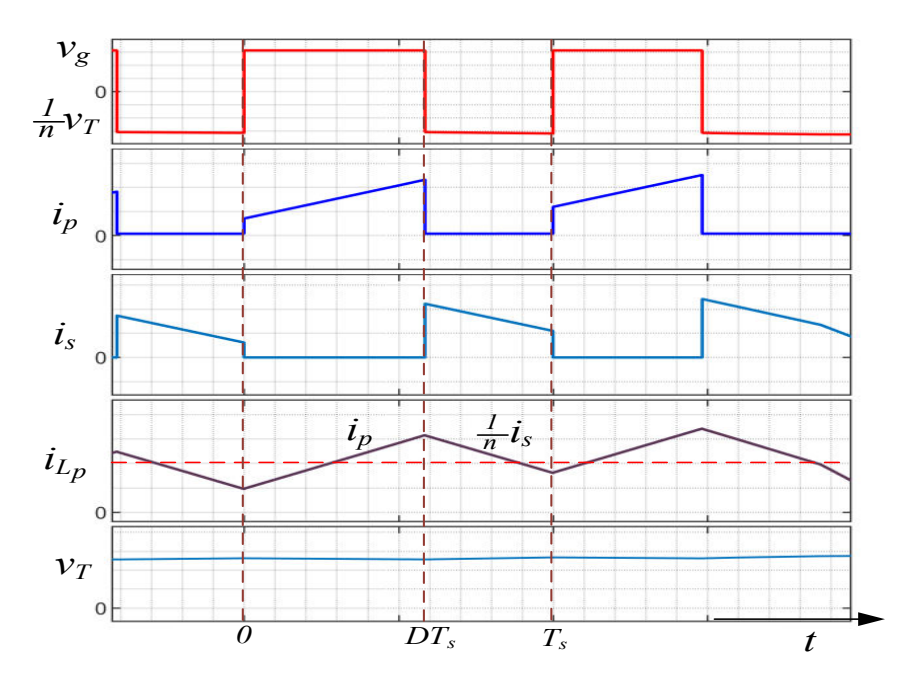


Figure. 4.3. Steady-state waveform of Voltage and Current during switching of Flyback converter.

When switch S(DT < t < T) is toggled OFF, as shown in Fig. 4.4(b), by the transformer's dot polarity, the inductor  $L_p$  Undergoes a transfer of energy to capacitor C in a unidirectional manner. This causes diode D on the secondary side to become forward-biased and initiate conduction based on Faraday's Law of Electromagnetic

Induction. This cyclic process concludes, resulting in the load resistance receiving a direct current (DC) voltage.

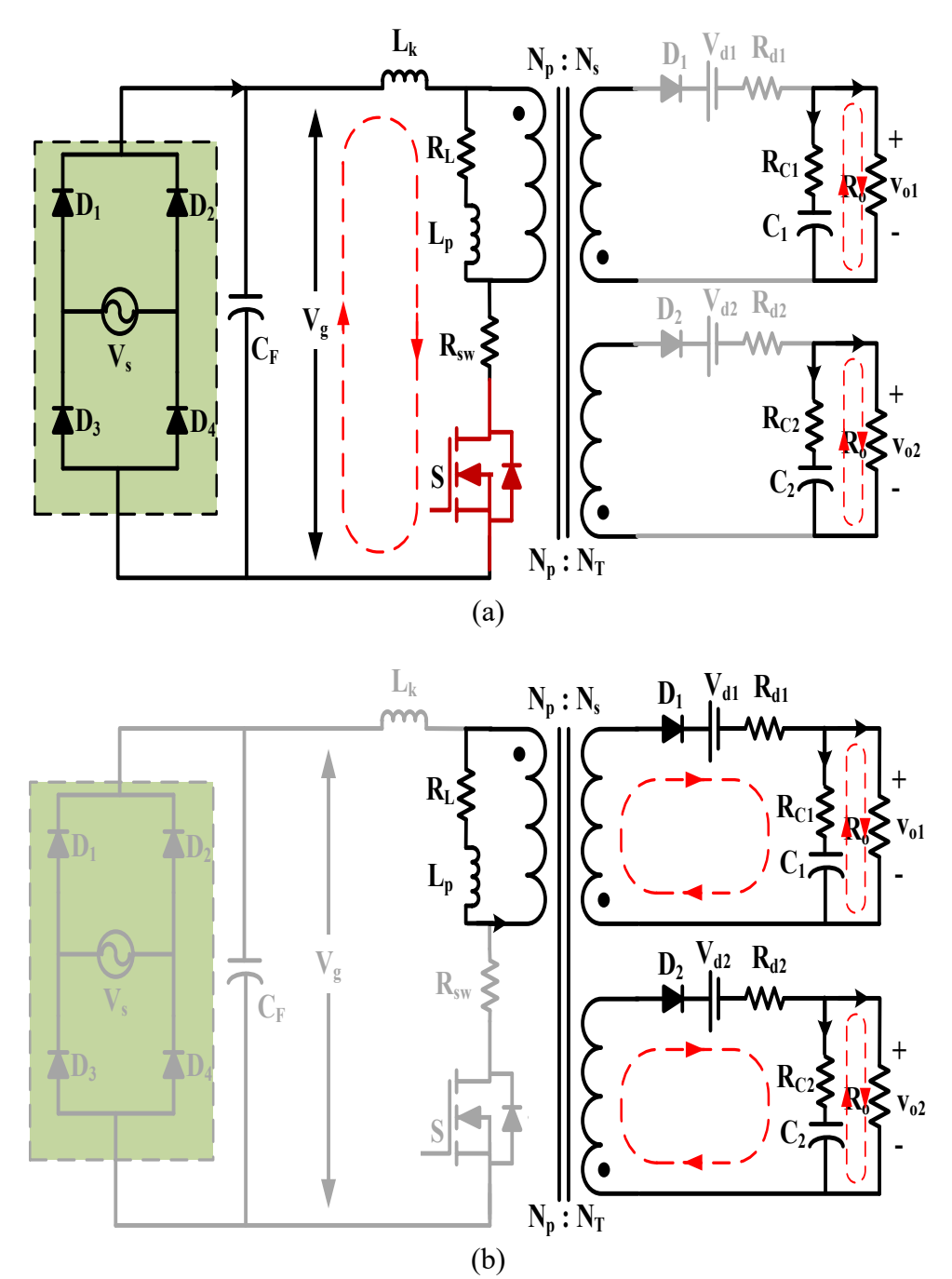


Figure. 4.4. Operation Mode of Flyback Converter with parasitics: (a) State 1 ( $0 < t \le DT$ ) and (b) State 2 ( $DT < t \le T$ ).

Assuming minimal resistance in the windings and leakage inductance and acknowledging the presence of a nonzero core reluctance, the transformer can be

simplified as two inductors with the magnetizing inductance  $L_p$  along with inductor resistor  $R_L$  and leakage inductance  $L_k$  on the primary side of an ideal transformer. This system involves two crucial variables: the current  $i_{Lp}$  and the voltage  $v_T$ .

By utilizing Kirchhoff's voltage and current principles, we can deduce the state-space equations for both the cases when the switch is in the on and off positions, expressed as follows, respectively.

Switch turned-ON (1 < t < DT):

$$\begin{bmatrix} \frac{di_{L_p}}{dt} \\ \frac{dv_c}{dt} \end{bmatrix} = \begin{bmatrix} -\frac{(R_L + R_{SW})}{(L_p + L_k)} & 0 \\ 0 & -\frac{1}{C(R_0 + R_c)} \end{bmatrix} \begin{bmatrix} i_{L_p} \\ v_c \end{bmatrix} + \begin{bmatrix} \frac{1}{(L_p + L_k)} & 0 \\ 0 & 0 \end{bmatrix} \begin{bmatrix} V_g \\ V_d \end{bmatrix} \tag{4.1}$$

$$\begin{bmatrix} V_{o1} \\ V_{o2} \end{bmatrix} = \begin{bmatrix} \frac{R_{o1}}{(R_{o1} + R_{c1})} & 0 \\ \frac{R_{o2}}{(R_{o2} + R_{c2})} & 0 \end{bmatrix} \begin{bmatrix} i_{Lp} \\ v_c \end{bmatrix} + \begin{bmatrix} 0 & 0 \\ 0 & 0 \end{bmatrix} \begin{bmatrix} V_g \\ V_d \end{bmatrix}$$
(4.2)

Switch turned-OFF (DT < t < T):

$$\begin{bmatrix} \frac{di_{L_{p}}}{dt} \\ \frac{dv_{c}}{dt} \end{bmatrix} = \begin{bmatrix} -\frac{\left(R_{L} + n^{2}R_{d} + \frac{n^{2}R_{c}R_{o}}{R_{o} + R_{c}}\right)}{L_{p}} & -\frac{nR_{o}}{L_{p}(R_{o} + R_{c})} \\ \frac{nR_{o}}{C(R_{o} + R_{c})} & -\frac{1}{C(R_{o} + R_{c})} \end{bmatrix} \begin{bmatrix} i_{L_{p}} \\ v_{c} \end{bmatrix} \\ + \begin{bmatrix} 0 & \frac{n}{L_{p}} \\ 0 & 0 \end{bmatrix} \begin{bmatrix} V_{g} \\ V_{d} \end{bmatrix}$$

$$(4.3)$$

$$\begin{bmatrix} V_{o1} \\ V_{o2} \end{bmatrix} = \begin{bmatrix} \frac{nR_{o1}R_{c1}}{(R_{o2} + R_{c2})} & \frac{R_{o1}}{(R_{o1} + R_{c1})} \\ \frac{nR_{o2}R_{c2}}{(R_{o2} + R_{c2})} & \frac{R_{o2}}{(R_{o2} + R_{c2})} \end{bmatrix} \begin{bmatrix} i_{Lp} \\ v_c \end{bmatrix} + \begin{bmatrix} 0 & 0 \\ 0 & 0 \end{bmatrix} \begin{bmatrix} V_g \\ V_d \end{bmatrix}$$
(4.4)

In these equations  $i_{L_k}$  represents the current flowing through the leakage inductor,  $i_{L_P}$  is the current flowing through the magnetizing inductor,  $V_S$  stands for the input AC voltage,  $V_g$  represents the DC voltage after passing through the filter  $C_F$ , and  $v_T$  is the output voltage.

The basis of an optimized controller design lies in the small-signal model. Particularly in a flyback converter, a well-constructed model proves precious for achieving closed-loop control, fine-tuning, and optimizing the converter's dynamics. Equations (4.1) - (4.4) can be represented in the single switched model of the Flyback converter considering both averaged and small signal disturbances as

$$\frac{d\bar{\iota}_{L_p}}{dt} = (d - 1) \left\{ \frac{nV_d}{L_p} + \frac{nR_o\bar{v}_c}{L_p(R_o + R_c)} + \bar{\iota}_{L_p} \frac{(n^2R_d + R_L + \frac{n^2R_oR_c}{R_o + R_c})}{L_p} \right\} + d \left\{ \frac{V_g}{(L_k + L_p)} - \bar{\iota}_{L_p} \frac{(R_L + R_{sw})}{(L_k + L_p)} \right\}$$
(4.5)

$$\frac{d\bar{\iota}_{L_k}}{dt} = d\left(\frac{V_g}{(L_p + L_k)} - \bar{\iota}_{L_p} \frac{(R_L + R_{sw})}{(L_p + L_k)}\right) \tag{4.6}$$

$$\frac{d\bar{v}_c}{dt} = -\left(\frac{\bar{v}_c}{(R_o + R_c)C} - \frac{nR_o\bar{\iota}_{Lp}}{(R_o + R_c)C} + \frac{dR_on\bar{\iota}_{Lp}}{(R_o + R_c)C}\right) \tag{4.7}$$

where d is the duty  $(0 \le d \le 1)$  and  $\bar{\iota}_{L_p}$ ,  $\bar{\iota}_{L_k}$  and  $\bar{v}_T$  represent the average values of  $i_{L_p}$ ,  $i_{L_k}$  and  $v_T$  over each switching cycle, respectively. The dynamic model will be subjected to averaging, followed by circuit averaging, during which small perturbations in variables will be introduced, finally resulting in the linearization of the model.

$$s\hat{x}(s) = A\hat{x}(s) + B\hat{u}(s) + ((A_1 - A_2)X(s) + (B_1 - B_2)U(s))\hat{d}(s)$$

$$\hat{y}(s) = C\hat{x}(s) + D\hat{u}(s) + ((C_1 - C_2)X(s) + (D_1 - D_2)U(s))\hat{d}(s)$$
(4.8)

where,

$$A = A_1 d + A_2 (1 - d) = (A_1 - A_2) d + A_2$$
  

$$B = B_1 d + B_2 (1 - d) = (B_1 - B_2) d + B_2$$
(4.9)

From equation (4.8), the transfer function corresponding outputs to the duty cycle can be expressed as

$$\frac{\hat{V}_{o1}(s)}{\hat{d}(s)} = \frac{-4.9448(s + 7.779e04)(s - 2.848e04)}{(s + 7.692e04)(s + 2.963e04)} \tag{4.10}$$

$$\frac{\hat{\iota}_{L_p}}{\hat{d}} = \frac{3.8112e05(s + 2653)}{(s + 7.692e04)(s + 2.963e04)} \tag{4.11}$$

Utilizing MATLAB software, we constructed open-loop Bode diagrams to illustrate the relationship between the system's output and control input, employing the simulation parameters drawn in Table 4.1. Upon analysis of these Bode plots, the inductor current to duty shown in Fig. 4.5(a) is comparably stable, while output voltage to duty as shown in Fig. 4.5(b), has become evident that the system exhibits an inadequate gain margin of -13.9 dB and instability in the open-loop configuration. Consequently, to improve the gain margin and enhance system stability, developing a dedicated controller is considered necessary. A closed-loop controller is designed with different linear and nonlinear controllers for stability and performance analysis of the converter. PID controller is applied on the linearized and perturbated transfer function (4.10), whereas SMC and Lyapunov stability function is directly implemented on the differential equation as obtained in (4.1)-(4.4).

Table 4.1. SPECIFICATION FOR FLYBACK CONVERTER

Description	Parameter	Value				
Power	$P_o$	140 W				
Input Voltage	$V_s$	220V (R.M.S.)				
Output Voltages	$V_{o1}/V_T$	180V / 5V (DC.)				
Frequency	$f_s$	100 kHz				
Inductance	$L_p$	1.5 mH				
Leakage Inductance	$L_k$	1.3 μΗ				
Capacitance	C	220 μF				
Parasitic Capacitor Resistance	Rc	$0.01~\Omega$				
Parasitic Inductor Resistance	$R_L$	$2.1 \Omega$				
Parasitic Diode Resistance	$R_d$	$0.1~\Omega$				
Forward Voltage Drop	$V_d$	0.7 V				
Switch Resistance	$R_{sw}$	$0.8\Omega$				
Load Resistance	$R_o$	$2.5\Omega$				
Turn Ratio	n	320/6				

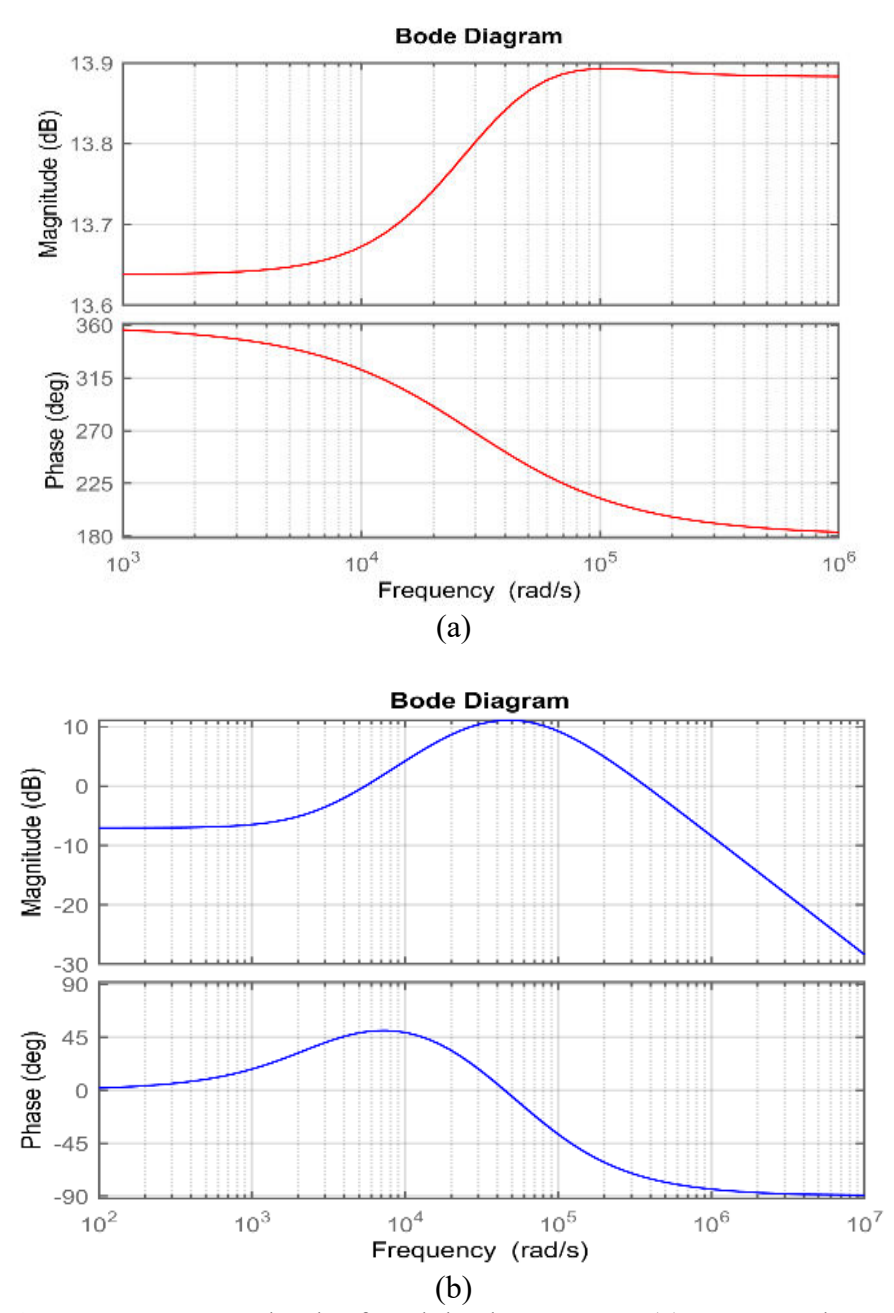


Figure 4.5. Open Loop Bode Plot for Flyback Converter (a) Output voltage to duty, (b) Inductor Current to duty

# 4.3. CONTROL METHODOLOGY AND STABILITY INVESTIGATION

Controller designing is a critical aspect of system control, aimed at developing control strategies that ensure desired system behaviour and performance [85]. The main objective of the non-ideal flyback converter controller is to keep the DC link

voltage as close as possible to the reference value. This voltage regulation is necessary for both operating modes, resulting in the same steady-state duty cycle for both modes. Traditionally, a proportional-integral control scheme based on a linearized model has been commonly employed to stabilize the converter. However, when subjected to significant disturbances, this technique produces a poor transient response because the accuracy of the small-signal model at each operational point is limited. To address these limitations, we propose a Lyapunov-function-based controller that achieves quick dynamic response and global exponential stability even in the presence of notable disturbances. This controller consists of two units. The proposed control unit, the first, enables fast dynamic responses for the flyback converter and assures global exponential stability despite significant disturbances. The second component, referred to as the duty-ratio feedforward controller, reduces the burden for the feedback controller.

#### 4.4. DUTY RATIO FEEDFORWARD CONTROLLER

The duty-ratio feedforward control element, which is essential for analyzing the error dynamics, is introduced in this section. The suggested feedback controller is designed using the findings from the dynamic error model. For further progress, we will establish the reference magnetizing inductor current as  $I_{Lp}$  and the reference output voltage as  $V_T$ . The flyback converter is assumed to function under stable, steady-state conditions. By substituting  $I_{Lp}$  and  $V_T$  into the expressions for  $\bar{\iota}_{Lp}$  and  $\bar{\nu}_T$  We proceed with the analysis, equating (3) to (5) with zero.

$$I_{L_p} = -\frac{\frac{d_{ff} * V_g}{L_k + L_p} + \frac{(d_{ff} - 1)}{L_p} \left\{ nV_d + \frac{nV_c R_o}{R + R_c} \right\}}{\frac{\left(R_d n^2 + R_L + \frac{n^2 R_o R_c}{R_o + R_c}\right) * \left(d_{ff} - 1\right)}{L_p} - \frac{d_{ff} (R_L + R_{sw})}{L_k + L_p}}$$
(4.12)

$$V_c = n(1 - d_{ff})I_{L_p}R_o (4.13)$$

Substituting (4.12) in (4.13), we then obtain the following expression, which can be arranged as

$$\alpha_1 d_{ff}^2 + \alpha_2 d_{ff} + \alpha_3 = 0$$
 (4.14)

where,

$$\begin{aligned} & \propto_2 = \ L_p R_o^2 V_g n \ + \ 2 L_k R_o^2 V_c n^2 \ + \ 2 L_p R_o^2 V_c n^2 \ + \ 2 L_k R_o^2 V_d n^2 \\ & + \ 2 L_p R_o^2 V_d n^2 \ + \ L_k R_o R_L V_c \ - \ L_p R_o R_s w V_c \ + \ L_p R_o R_c V_g n \ + \ L_k R_o R_c V_c n^2 \\ & + \ L_p R_o R_c V_c n^2 \ + \ 2 L_k R_o R_c V_d n^2 \\ & + \ L_k R_o R_d V_c n^2 \ 2 L_p R_o R_c V_d n^2 \ + \ L_p R_o R_d V_c n^2 \\ & + \ L_k R_c R_d V_c n^2 \ + \ L_p R_o R_d V_c n^2 \end{aligned}$$

$$(4.16)$$

$$\begin{aligned} & \propto_{3} = -L_{k}R_{o}^{2}V_{c}n^{2} - L_{p}R_{o}^{2}V_{c}n^{2} - L_{k}R_{o}^{2}V_{d}n^{2} - L_{p}R_{o}^{2}V_{d}n^{2} - L_{k}R_{o}R_{L}V_{c} \\ & -L_{p}R_{o}R_{L}V_{c} - L_{k}R_{c}R_{L}V_{c} - L_{p}R_{c}R_{L}V_{c} - L_{k}R_{o}R_{c}V_{c}n^{2} \\ & -L_{p}R_{o}R_{c}V_{c}n^{2} - L_{k}R_{o}R_{c}V_{d}n^{2} - L_{k}R_{o}R_{d}V_{c}n^{2} \\ & -L_{p}R_{o}R_{c}V_{d}n^{2} - L_{p}R_{o}R_{d}V_{c}n^{2} - L_{k}R_{c}R_{d}V_{c}n^{2} \\ & -L_{p}R_{c}R_{d}V_{c}n^{2} \end{aligned}$$

$$(4.17)$$

 $d_{ff}$  can be calculated from equation (4.14) as

$$d_{ff} = \frac{A_1 \pm \sqrt{A_2}}{A_3} \tag{4.18}$$

where,  $d_{ff} = \frac{A_1 - \sqrt{A_2}}{A_3}$  is considered since its value is less than one. The output voltage of the flyback CCM converter is not directly influenced by  $d_{ff}$  itself. Instead,  $d_{ff}$  serves as a feedforward input to closely track the reference output voltage. This approach improves the feedback controller's workload, allowing it to operate with lower gain since it no longer needs to regulate the output voltage precisely.

# 4.5. FEEDBACK CONTROL SYSTEM UTILIZING LYAPUNOV FUNCTIONS

Apply the feedforward duty  $d_{ff}$  to extract the error dynamics to generate the proposed feedback controller for the converter. The error dynamics  $ei_{Lp} = \bar{\iota}_{Lp} - I_{Lp}$ ,  $ev_c = \bar{v}_c - V_c$ , and feedback control input as  $d_{fb} = d - d_{ff}$ . Substituting  $ei_{Lp}$ ,  $ev_c$  and  $d_{fb}$  into Equations (4.3) to (4.5) results to

$$\frac{dei_{L_p}}{dt} = \left(\frac{V_g - (R_L + R_{sw})(I_{L_p} + ei_{L_p})}{L_k + L_p} + \frac{(I_{L_p} + ei_{L_p})(R_L + R_d n^2 + \frac{R_o R_c n^2}{R_o + R_c})}{L_p} + \frac{nV_d}{L_p} + \frac{nR_o(V_c + ev_c)}{L_p(R_o + R_c)}\right) d_{fb} + (d_{ff} - 1) \left(\frac{(I_{L_p} + ei_{L_p})(R_L + R_d n^2 + \frac{R_o R_c n^2}{R_o + R_c})}{L_p} + \frac{V_d n}{L_p} + \frac{R_o n(V_c + ev_c)}{L_p(R_o + R_c)}\right) + \frac{d_{ff}(V_g - (R_L + R_{sw})(I_{L_p} + ei_{L_p}))}{L_k + L_p}$$
(4.19)

$$\frac{dev_c}{dt} = \left(-\frac{R_o n \left(I_{L_p} + ei_{L_p}\right)}{C(R_o + R_c)}\right) d_{fb}$$

$$-\frac{V_c + ev_c - R_o n \left(I_{L_p} + ei_{L_p}\right) + R_o d_{ff} n \left(I_{L_p} + ei_{L_p}\right)}{C(R_o + R_c)} \tag{4.20}$$

The error dynamics (4.19) and (4.20) can be summarized as

$$\dot{e} = Ge + (He + h)d_{fb} \tag{4.21}$$

where,

$$e = \left[ ei_{L_p} \ ev_c \right]^T \tag{4.22}$$

$$\frac{G}{E} = \begin{bmatrix}
-\frac{(R_L + R_{sw})}{L_k + L_p} d_{ff} - \frac{(R_d n^2 + R_L + \frac{R_o R_c n^2}{R_o + R_c})(1 - d_{ff})}{L_p} & -\frac{nR_o (1 - d_{ff})}{L_p (R_o + R_c)} \\
\frac{nR_o (1 - d_{ff})}{C(R_o + R_c)} & -\frac{1}{C(R_o + R_c)}
\end{bmatrix} (4.23)$$

$$H = \begin{bmatrix} -\frac{R_L + R_{sw}}{L_k + L_p} + \frac{(R_d n^2 + R_L + \frac{R_o R_c n^2}{R_o + R_c})}{L_p} & \frac{nR_o}{L_p (R_o + R_c)} \\ -\frac{nR_o}{C(R_o + R_c)} & 0 \end{bmatrix}$$
(4.24)

$$h = \begin{bmatrix} \left( -\frac{R_L + R_{sw}}{L_k + L_p} + \frac{\left( R_d n^2 + R_L + \frac{R_O R_C n^2}{R_O + R_C} \right)}{L_p} \right) I_{L_p} + \frac{V_g}{L_k + L_p} + \frac{nR_o}{L_p (R_o + R_c)} V_c + \frac{n}{L_p} V_d \\ -\frac{nR_o}{C (R_o + R_c)} I_{L_p} \end{bmatrix}$$
(4.25)

The Lyapunov stability theorem states that a system attains exponential stability when the specified condition is satisfied: The function V(x) satisfies  $c_1 ||x||^{\alpha} \le V(x) \le$ 

 $c_2 \|x\|^{\alpha}$  and  $\dot{V}(x) \le -c_3 \|x\|^{\alpha}$  criteria, where  $0 < c_1 < c_2 < c_3$ , and  $\alpha$  is a positive constant. The potential Lyapunov function represents the energy held in inductors and capacitors.

Using the Lyapunov function, we can depict the energy stored in the inductor and output capacitor:

$$V(e) = \frac{1}{2}L_p e i_{L_p}^2 + \frac{1}{2}Cev_c^2 = \frac{1}{2}e^T Pe$$
 (4.26)

where  $P = diag[L_p \ C]$ , then it holds that

$$\frac{1}{2}min(L_p, C) \|e\|_2^2 = \frac{1}{2}\lambda_{min}(P) \|e\|_2^2 \le V(e)$$

$$\le \frac{1}{2}\lambda_{max}(P) \|e\|_2^2 = \frac{1}{2}max(L_p, C) \|e\|_2^2$$
(4.27)

Taking the derivative of equation (4.27) with respect to time, we obtain the following result:

$$\dot{V}(e) = \frac{1}{2}\dot{e}^{T}Pe + \frac{1}{2}e^{T}P\dot{e}$$

$$= -e^{T}Qe + d_{fb}e^{T}Ke + d_{fb}h^{T}Pe$$
(4.28)

where,

$$Q = -\frac{1}{2}(G^{T}P + PG) =$$

$$\begin{bmatrix} L_{p} \left( \frac{d_{ff}(R_{L} + R_{sw})}{L_{k} + L_{p}} - \frac{(d_{ff} - 1)(R_{L} + R_{d}n^{2} + \frac{R_{o}R_{c}n^{2}}{R_{o} + R_{c}})}{L_{p}} \right) & 0 \\ 0 & \frac{1}{R_{o} + R_{c}} \end{bmatrix}$$

$$> 0$$

$$K = \frac{1}{2}(H^{T}P + PH)$$

$$= \begin{bmatrix} L_{p} \left( \frac{R_{L} + R_{d}n^{2} + \frac{R_{o}R_{c}n^{2}}{R_{o} + R_{c}}}{L_{p}} - \frac{R_{L} + R_{sw}}{L_{k} + L_{p}} \right) & 0 \\ 0 & 0 \end{bmatrix}$$
(4.30)

By choosing feedback controller as

$$d_{fb} = -\alpha(e^T K e + h^T P e) \tag{4.31}$$

where  $\alpha > 0$ , substituting (4.31) in (4.28)

$$\dot{V}(e) = -e^{T}Qe - \alpha(e^{T}Ke + h^{T}Pe)^{2}$$

$$\leq \frac{1}{2}\lambda_{min}(P)\|e\|_{2}^{2}$$

$$= -min \left( L_{p} \left( \frac{d_{ff}(R_{L} + R_{sw})}{L_{k} + L_{p}} - \frac{(d_{ff} - 1)\left(R_{L} + R_{d}n^{2} + \frac{R_{o}R_{c}n^{2}}{R_{o} + R_{c}}\right)}{L_{p}} \right) \quad 0$$

$$= 0$$

$$= 0$$

$$(4.32)$$

$$\leq 0$$

From (4.27) and (4.32), the stability theorem  $eiL_p \rightarrow 0 \& ev_T \rightarrow 0$ 

Exponentially fast as  $t \to 0$ . Relating (4.27) and (4.32), we obtain

$$\dot{V}(e) \le -\frac{2\lambda_{min}(Q)}{\lambda_{max}(P)}V(e) \tag{4.33}$$

and solving (4.33) gives

$$V(e(t)) \le V(e(t_o)) exp \left\{ -\frac{2\lambda_{min}(Q)}{\lambda_{max}(P)} (t - t_o) \right\}$$
(4.34)

For all  $t \ge t_o$ , then the error trajectory[24] is bounded as

$$||e||_{2} \leq \sqrt{\frac{2V(e(t))}{\lambda_{min}(P)}} \leq \left[\frac{\lambda_{max}(P)||e||_{2}^{2}exp\left\{-\frac{2\lambda_{min}(Q)}{\lambda_{max}(P)}(t-t_{o})\right\}}{\lambda_{min}(P)}\right]^{\frac{1}{2}}$$

$$= \left\{\frac{\lambda_{max}(P)}{\lambda_{min}(P)}\right\}^{\frac{1}{2}}||e(t_{o})||_{2}exp\left\{-\frac{\lambda_{min}(Q)}{\lambda_{max}(P)}(t-t_{o})\right\}$$
(4.35)

As a result, the error trajectories converge rapidly to zero with an exponential rate of  $-\frac{\lambda_{\min}(Q)}{\lambda_{\max}(P)}.$ 

The complete control input is subsequently determined using equations (4.18) and (4.31) as follows:

$$d = d_{ff} + d_{fb} = \frac{A_1 - \sqrt{A_2}}{A_3} - \alpha (e^T K e + h^T P e)$$
 (4.36)

Following equation (4.36), the complete control strategy for the flyback converter considering ESRs is shown in Fig. 4.6. This average value of inductor current  $I_{Lp}$  and capacitor voltage  $V_c$  is sensed and compared with their references, thereby generating errors. These errors are minimized using the proposed controller, whose derivation is discussed earlier, and a control law (4.36) is developed.

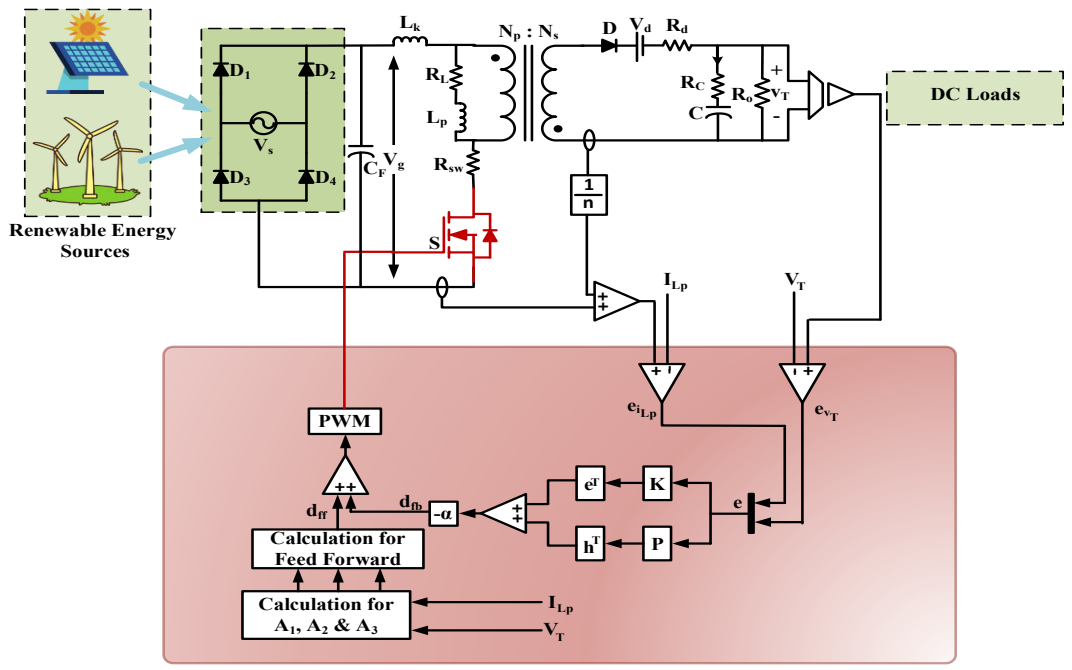


Figure 4.6. Proposed Lyapunov-based flyback CCM converter control system with parasitics.

#### 4.6. CONTROLLER IMPLEMENTATION ON CONVERTER

To confirm the validity of the theoretical analysis, we establish the following design specifications.  $V_{in} = 220 \, VAC$ ,  $V_{o1} = 180 \, V$ ,  $V_{T} = 5 \, V$ ,  $P_{o} = 10 \, W$ , and switching frequency  $f_{S} = 100 \, kHz$  and the remaining parameters are shown in Table 4.1. The closed-loop system was simulated to evaluate how it reacts to changes in the reference output voltage, input voltage, and output load. These tests help us understand the system's transient behavior under various conditions.

## 4.6.1. Linear PI controller

The chapter presents the development of a simulation model for a Flyback Converter using PI control, where essential parameters are considered, and the calculated values of  $K_p$  and  $K_i$  are implemented.

$$u(t) = K_P e(t) + K_I \int e(t)dt \qquad (4.37)$$

where

$$e(t) = v_{ref} - v_c \tag{4.38}$$

Through successive trial and error, the values of  $K_p$  and  $K_i$  are determined as 10 and 3.2, respectively. Fig. 4.7 illustrates the flyback Converter's output performance under PI control for its voltage and current control loops, respectively. The Flyback Converter, operating with the PI controller, achieves a peak output voltage of 5.042V, with a rise time of 49.438  $\mu$ s to reach the desired output voltage of 5V. However, when subjected to PI control, the voltage and current output exhibit some ripple. Furthermore, the Flyback Converter demonstrates a steady-state error of 5.16%.

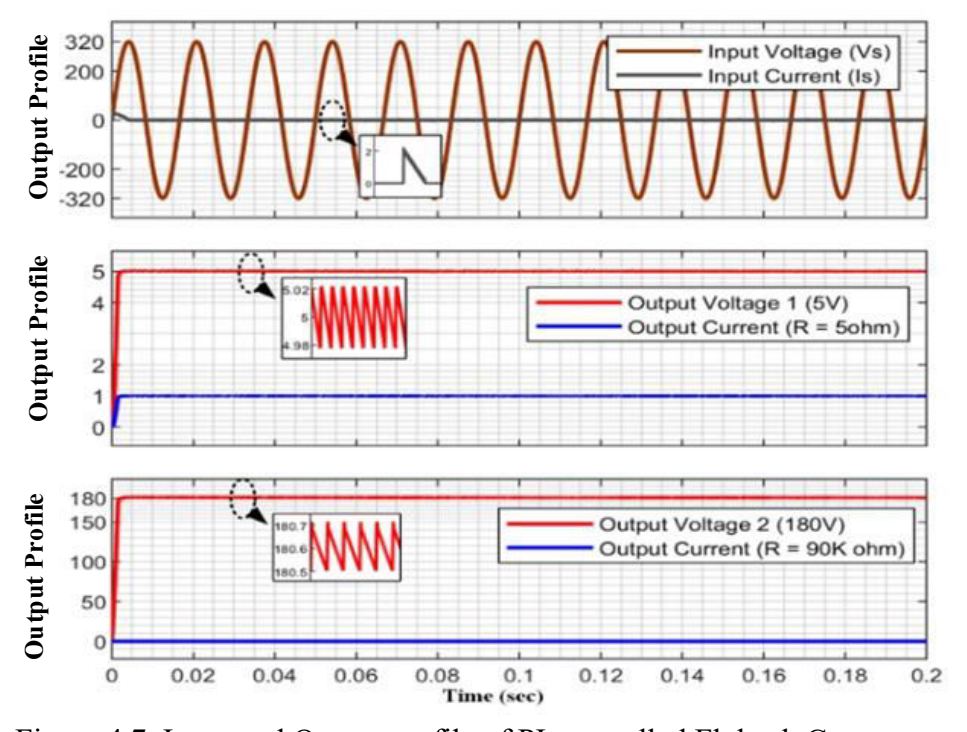


Figure 4.7. Input and Output profile of PI-controlled Flyback Converter.

#### 4.6.2. Sliding mode controller

The flyback converter undergoes simulation using a developed model based on the proposed design. The results of this simulation model are precisely analyzed. To ensure a regulated 5V output voltage, a Simulink model for the flyback converter is established, including a Sliding Mode Controller (SMC) for closed-loop control. Initially, a sliding surface is formulated to minimize voltage and current errors, adhering to the principles of sliding mode control, where the sliding surface s(x) is set to 0. These are the SMC state variables:

$$x_1 = i_{ref} - i_{Lp}$$
 $x_2 = v_{ref} - v_c$ 
 $x_3 = \int (x_1 + x_2)dt$ 
(4.39)

The suggested controller sliding surface S is specified as follows:

$$S = \alpha_1 x_1 + \alpha_2 x_2 + \alpha_3 x_3 \tag{4.40}$$

Fig. 4.9 shows the output voltage waveforms observed while utilizing the sliding-mode controller, the schematic diagram of which is depicted in Fig. 4.8.

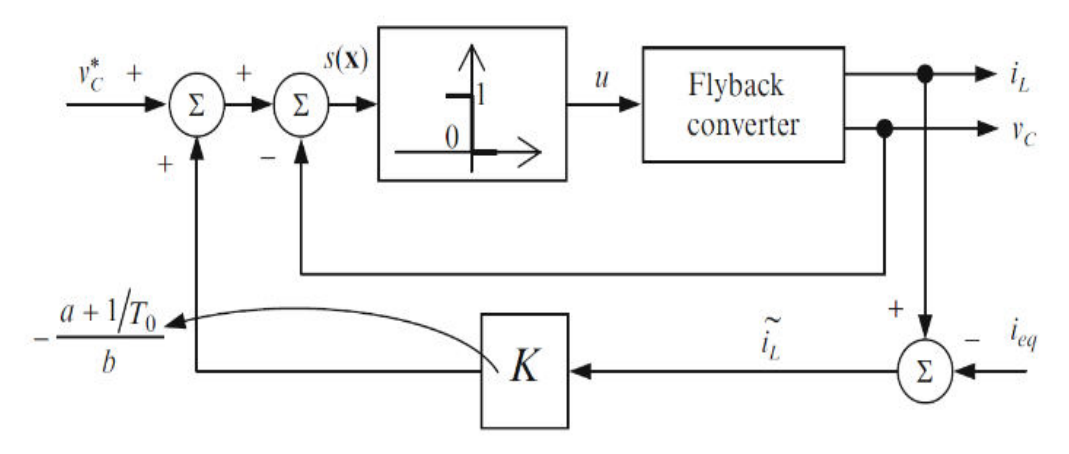


Figure 4.8. Control schematic for ISMC for nonlinear flyback converter with voltage and current loop.

Before obtaining stability at the desired reference output voltage, the actual output voltage exhibits significant overshooting and minor oscillations. However, the settling time for this waveform is smaller than that depicted in Fig. 4.7.

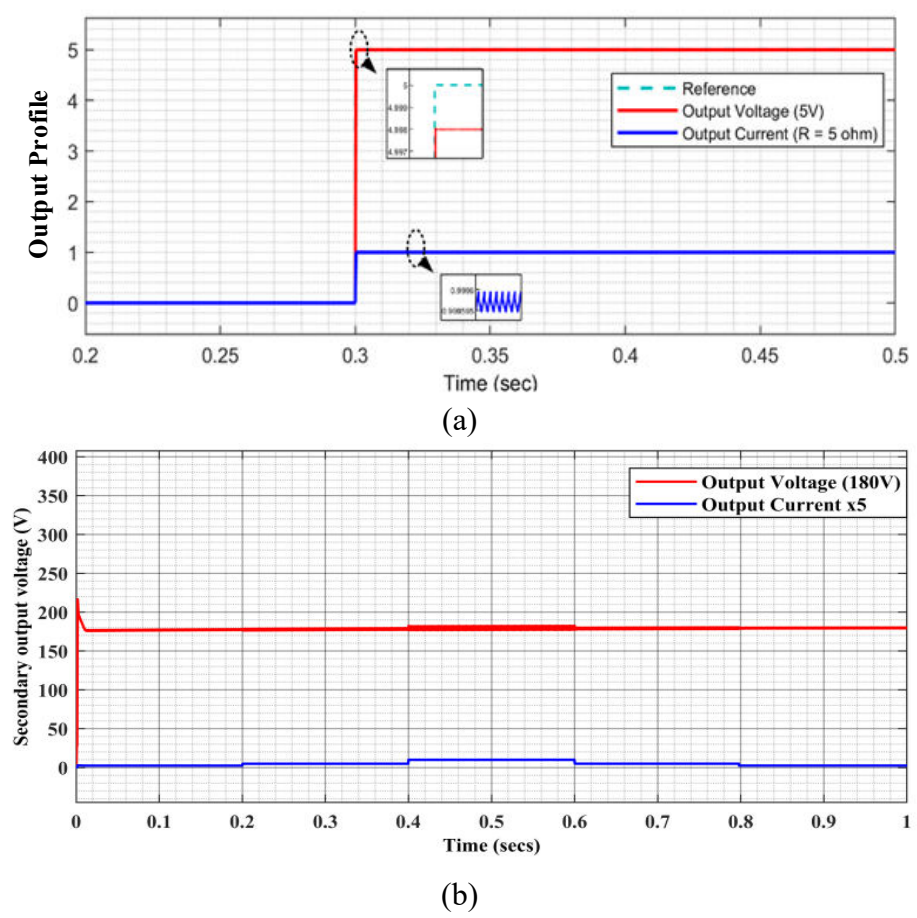


Figure 4.9. Performance profile of ISMC-controlled Flyback Converter for (a) 5V output voltage (b) 180V output profile.

The peak output voltage achieved by the flyback converter with the SMC controller is measured at 4.997V. The rise time required to attain the desired state for the 5V output voltage is determined to be 470.15 ns. Additionally, the steady-state error for the flyback converter under closed-loop control using sliding mode is calculated to be 0.4%.

### 4.6.3. Lyapunov function-based controller

Fig. 4.6 illustrates the control scheme employed for the multiport flyback Converter (MFC) system. Lyapunov function-based controllers use mathematical functions to analyze and ensure the stability of dynamic systems. Simulation results are used to calculate the controller's efficiency and the converter's performance. The converter's responses are examined when both the input voltage and the load change. The parameter  $\alpha$  within the designated controller is increased to evaluate the

controller's response. Employing a parameter tuning approach, a gain of 0.0004 is achieved in the simulation.

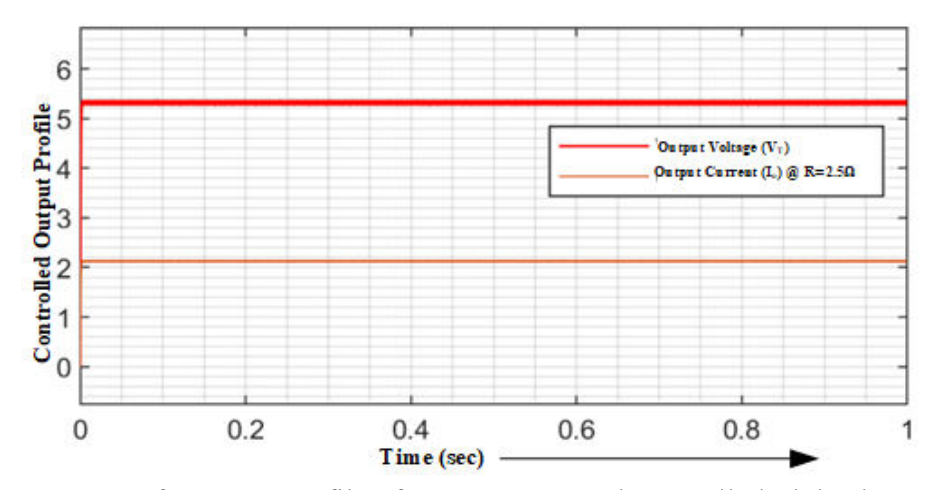


Figure 4.10. Performance profile of Lyapunov Based-controlled Flyback Converter for 5V output voltage.

Fig. 4.10 shows the waveforms of both the actual and reference output voltages, considering variations in the output load. Lyapunov controller offers a rise time of 517.4 ns and a settling time of 0.4 ms. Notably, the Lyapunov controller outperforms the SMC in this scenario. This superiority can be attributed to the closed-loop system's output impedance, which is smaller under SMC than under PI control. The output voltage demonstrates reduced peak behavior when the sliding-mode controller is used (Fig. 4.9). However, the proposed controller performs even better, maintains its output voltage under load variations (as shown in Fig. 4.10)

The proposed converter stability analysis is performed for a closed loop for output voltage and inductor current to duty. The parasitic resistances of the inductors and the capacitors are included while predicting the magnitude and phase margin. The gain margin is improved to 89 dB for output voltage when the controller is applied, which can be observed from the bode plot, as shown in Fig. 4.11. The gain margin is positive, and the phase margin is sufficiently large, suggesting that the converter is stable under the specified operating conditions. The load is adjusted between 0.25A and 4A within a duration of 1 second, while the output voltage remains constant at 5V when the controller is implemented as shown in Fig. 4.12. In Fig. 4.13, the input voltage is depicted varying between 290V to 350V, while the output voltage remains fixed at 5V due to the Lyapunov controller. The graph demonstrates the controller's effective

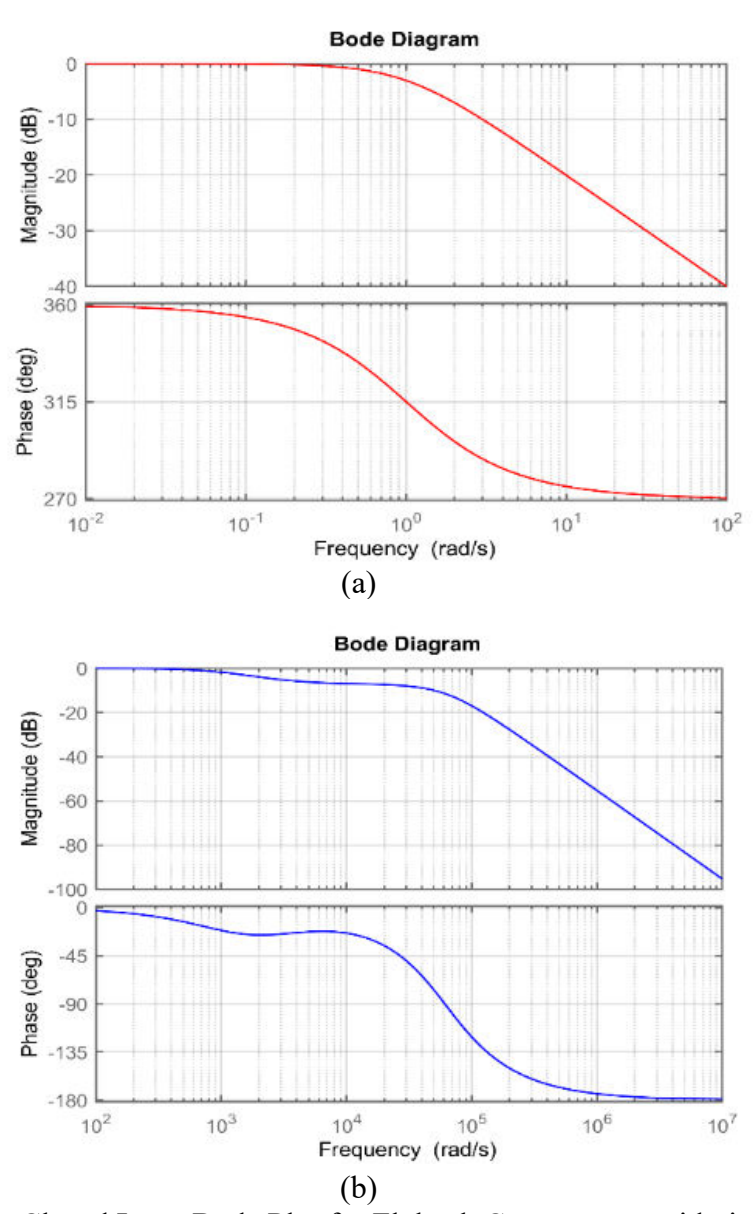


Figure 4.11. Closed Loop Bode Plot for Flyback Converter considering circuit parasitics (a) Output voltage to duty, (b) Inductor Current to duty.

regulation, ensuring a constant output voltage despite changes in the input voltage range, highlighting its reliability and stability. The load is adjusted between 0.25A and 4A within a duration of 1 second, while the output voltage remains constant at 5V when the controller is implemented. The graph demonstrates the controller's effective regulation, ensuring a constant output voltage despite changes in the input voltage range, highlighting its reliability and stability.

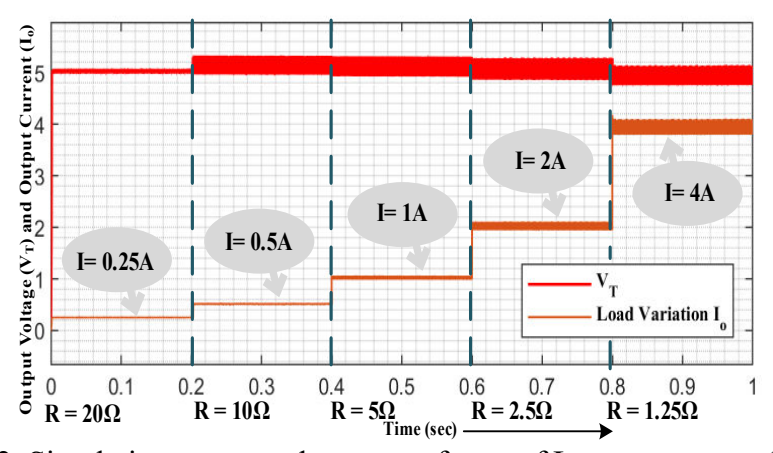


Figure 4.12. Simulation output voltage waveforms of Lyapunov controlled flyback converter under load variations.

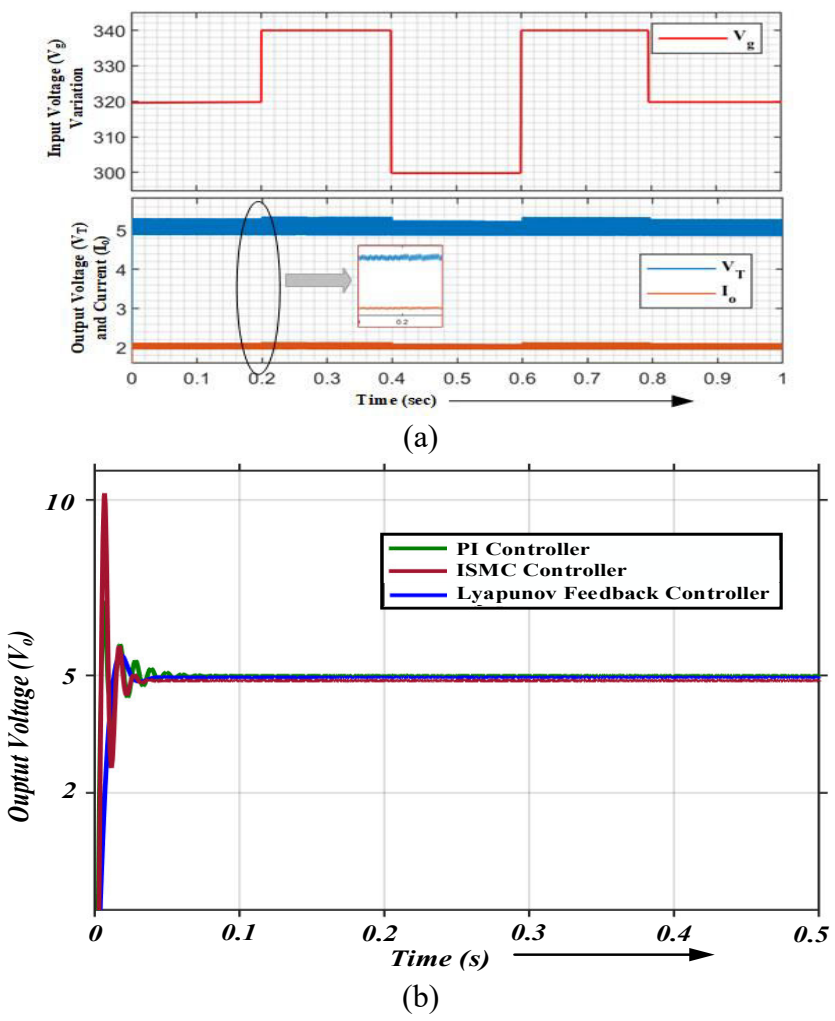


Figure 4.13. (a) Simulation graphs demonstrate the behaviour of the non-ideal flyback converter when the proposed controller is applied in response to changes in input voltage. (b) Comparative analysis of different controller applied on the converter.

Figure 4.12 showcases the simulation output voltage waveforms of the Lyapunov-controlled flyback converter when subjected to load variations. This provides a visual representation of how the converter responds to changes in the load. In Fig 4.13(a), simulation graphs demonstrate the behavior of the non-ideal flyback converter when the proposed controller is applied in response to fluctuations in input voltage. This allows for an examination of how the converter behaves under varying input conditions with the proposed control strategy. Additionally, Figure 4.13(b) presents a comparative analysis of the converter's performance with different controllers applied. This comparison offers insights into the effectiveness of the proposed controller in comparison to other control strategies in regulating the flyback converter.

In assessing the effectiveness of the proposed controller, we examined various parameters. These parameters included the rise time and settling time of transient responses when subjected to changes in the reference output voltage and the percentage of overshoot and settling time in response to variations in the input voltage and output load (refer to Tables 4.2). Notably, when compared to other controllers, the proposed controller has the fastest and most reliable step response.

TABLE 4.2. TIME DOMAIN SPECIFICATIONS

Controller	Rise time	%Peak undershoot	Settling time
PI	49.43 μs	5%	32 ms
SMC	0.47 μs	2.6%	20 ms
Lyapunov Controller	517.4 ns	1.3%	0.4 ms

The comparison reveals that the proposed controller exhibits a significant reduction in settling time and oscillations compared to both PI and SMC controllers. Although there is a slight increase in undershooting, the substantial improvement in settling time outweighs this drawback. Consequently, the overall performance of the proposed controller surpasses that of the PI and SMC controllers. Fig. 4.15 and 4.16 shows the variation of V(e) and  $\dot{V}(e)$  respectively with respect to  $e_{iL_p}$  and  $e(v_T)$  when the proposed controller is applied for various disturbances, the surface shows the convergence of error to zero as the system reaches the steady state at fixed loading conditions without affecting the system stability, even with circuit parasitics.

#### 4.7. VERIFICATION AND RESULTS

The converter was designed with four subsections, namely the rectifier circuit, snubber circuit, feedback circuit, and switch controller circuit. A full bridge rectifier, comprised of four diodes, was used to generate an unregulated DC supply, followed by a pi filter consisting of two capacitors and an inductor. The snubber circuit was designed to prevent voltage surges on the primary side of the transformer during transient conditions, thereby protecting the transformer from spikes. An auxiliary bias winding on the high-frequency Flyback transformer also provided overvoltage protection in case of open feedback loop faults in the circuit. An LED indicates the output state. The subsequent section will delve further into the design and implementation of the Flyback converter using a customized flyback transformer. Parameters for the flyback converter are calculated in steps and initially analyzed on the Simulink model before designing. A flyback transformer is designed using the parameter given in Table 4.3.

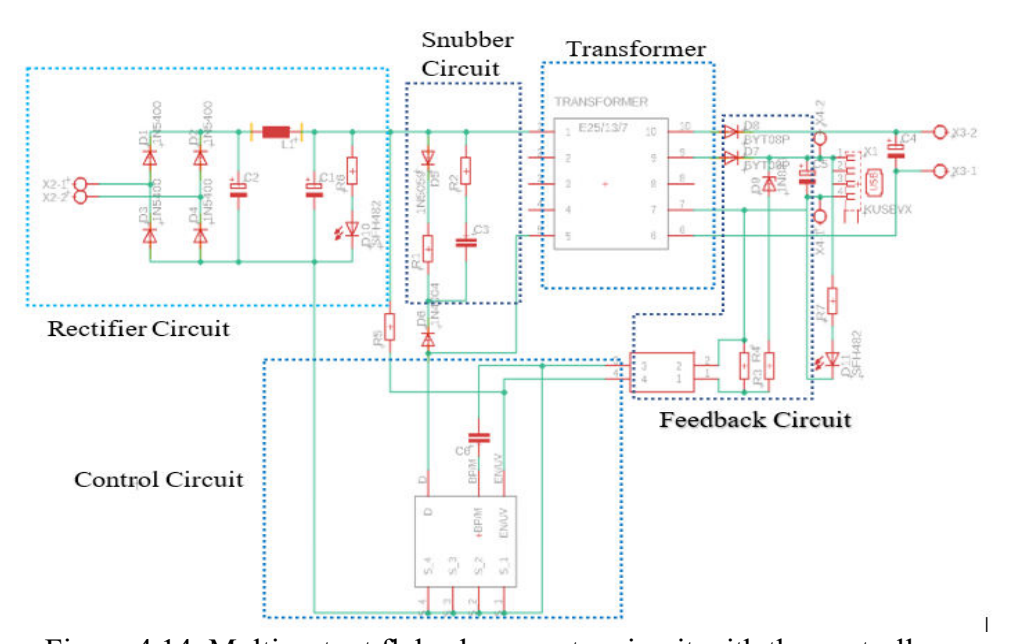


Figure 4.14. Multi-output flyback converter circuit with the controller.

The crucial part was designing the air gap inductance for which an air gap of 0.12 mm was provided using chapter. The complete representation of the converter design can be explained by considering the converter's subparts, as shown in Fig. 4.14. The IN4007 diode was selected for bridge rectification of AC input, ensuring that the maximum voltage across diodes must not exceed 700V. The snubber circuit prevents

voltage surge represented on the transformer's primary side throughout transient conditions, thus protecting the transformer from spikes. The use of parallel RC optimizes both energy efficiency and EMI. Further, additional bias winding on the flyback transformer offers overvoltage protection in the event of open feedback loop faults in the circuit; LED, which is used as an indicator, specifies the output state. A Flyback converter is a coupled inductor with a gapped core. During each cycle, energy is stored in the core's gap when primary winding is induced with input voltage. It is then transferred to the secondary winding to provide power to the load. Now, we can emphasize the transformer design as the necessary constraints for the converter design have been calculated. One of the prevalent methods in the design of high-frequency Is circuit isolation and voltage transformation in a flyback converter. The Flyback Transformer parameter is shown in Table 4.3.

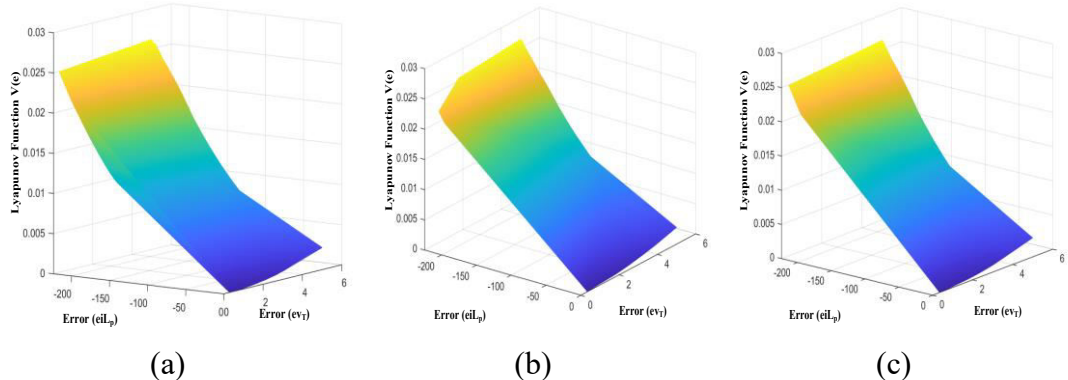


Figure 4.15. Surface graph of the flyback converter for variations in V(e) with respect to  $e_{i_{Lp}}$  and  $e_{v_T}$  when the proposed controller is applied for (a) Line Variation, (b) Load Variation, (c) Both Line and Load Variation

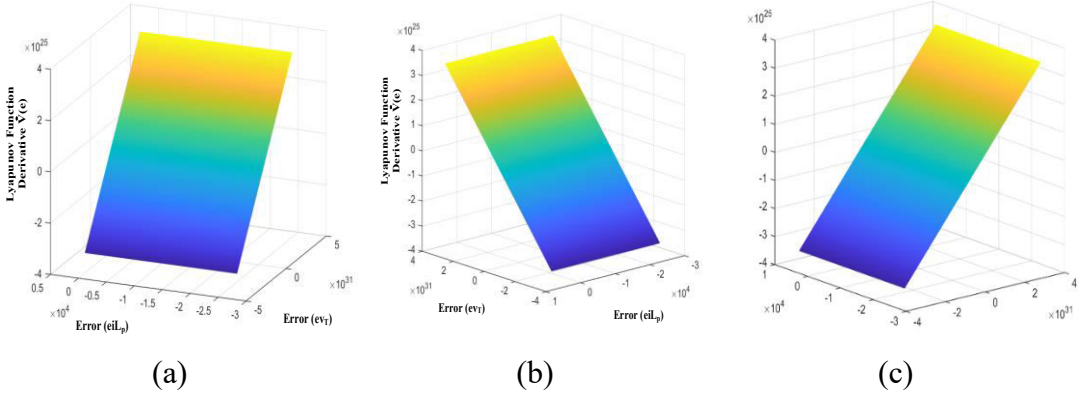


Figure 4.16. Surface graph of the flyback converter for variations in  $\dot{V}(e)$  with respect to  $e_{i_{Lp}}$  and  $e_{v_T}$  when the proposed controller is applied for (a) Line Variation, (b) Load Variation, (c) Both Line and Load Variation

TABLE 4.3. SPECIFICATION FOR FLYBACK TRANSFORMER

Description	Parameter	Value
Value of primary current	$I_1$	0.777 A (R.M.S.)
Value of secondary current	$I_2$	6.24A (R.M.S.)
Value of tertiary current	$I_3$	1 A (R.M.S.)
Packing factor	$K_{w}$	0.5
Frequency	$f_s$	100 kHz
Inductance	$L_p$	1.5 mH
Leakage inductance	$L_k$	1.3 μΗ
Current density	J	$3 A/mm^2$
Core window area	$A_w$	$10.937mm^{2}$
Parasitic inductor resistance	$R_L$	$2.1 \Omega$
Length of Air gap	$l_g$	0.12~mm
Gauge of $a_1$ Winding	$a_1$	SWG = 34
Gauge of $a_2$ Winding	$a_2$	SWG = 15
Gauge of $a_3$ Winding	$a_3$	SWG = 31

By finding all the parameters for the Flyback transformer, the next step is to design converter schematics. The core used here was a high-frequency ferrite EE core. Fig. 4.17 shows the PCB layout of hardware model of a multi-output flyback converter with an output of 5V and 180V DC with 2A and 0.002A current, respectively. The hardware is designed to provide power to charge batteries and power the microcontroller.

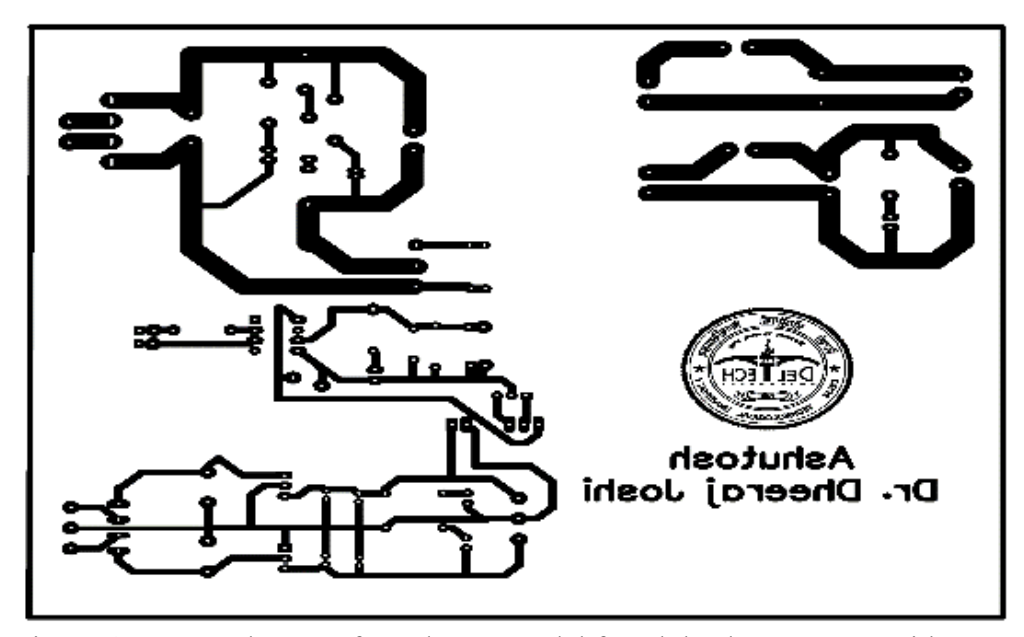


Figure 4.17. PCB layout of Hardware Model for Flyback Converter with two outputs.

The size of the developed prototype is 2.5"x4"x1.5". Its power density is  $0.67 \text{ W/inch}^3$ . This flyback converter module can be incorporated into (Modular Multilevel Converter) MMC to supply three-phase supplies. This design features a snubber circuit to prevent transient spikes. The transformer is designed to provide features such as protection against overvoltage and Undervoltage. It can provide power to instruments with high sensitivity to spikes and transients. The PCB layout is designed using Fusion 360 software. The calculation for the design has been explained in an earlier section.

Fig. 4.18 shows the experimental configuration to employ flyback converter hardware with a standalone PV-connected system. The ac power supply through an autotransformer, a LV25-P voltage sensor and an ACS712 current sensor are used to detect voltage and current, respectively. A TMS320F28379D microcontroller is used for PWM pulse generation. A DSO of type KEYSIGHT DSO-X2024A is used to record the obtained results.

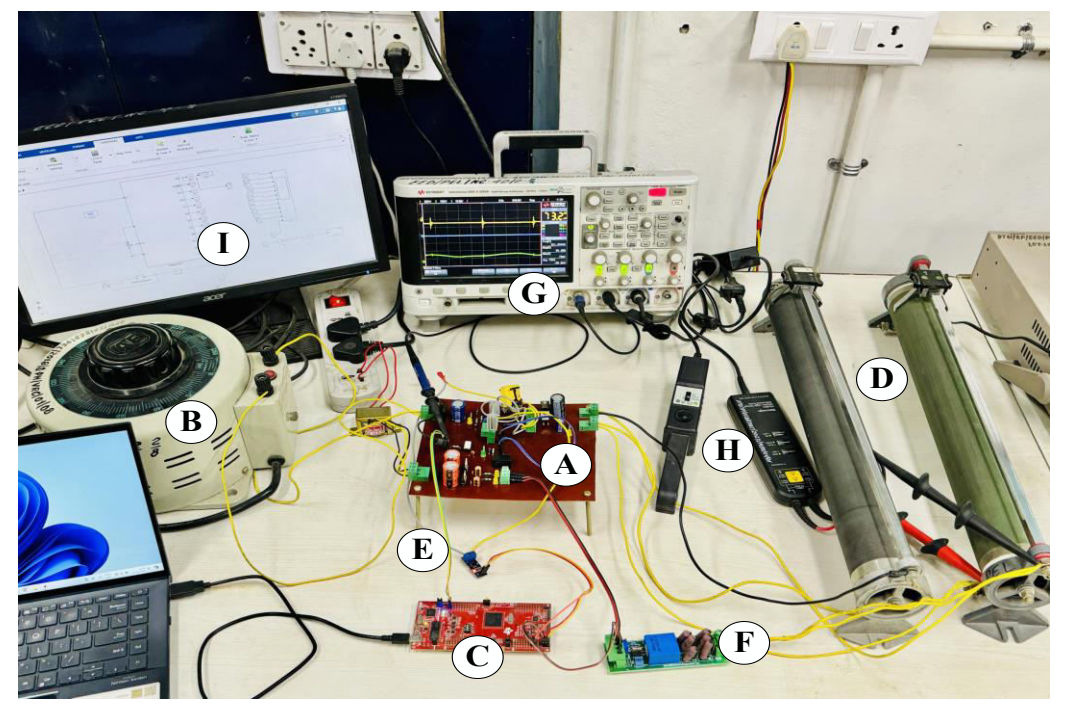


Figure 4.18. Experimental setup for hardware implementation A. Multiport flyback converter prototype, B. Input Source, C. TMS320F28379D Microcontroller, D. Rheostat, E. Current Sensor, F. Voltage Sensor, G. DSO, H. Voltage and Current Probe and I. Computer.

The control algorithm, which generates an adjustable duty cycle gate pulse through a controller, is presented and implemented. Throughout the period when power MOSFET is turned on, drain current keeps rising in the IC and MOSFET is switched

off shortly as the drain-source current limit is reached by the current. Furthermore, a second switch attached to the load helps to highlight load variations and is controlled by its own gate pulse. The complete flyback converter model and all necessary calculations and circuitry are integrated onto a PCB and thoroughly tested in the laboratory. The hardware is subjected to various resistive loads to analyze its regulation characteristics throughout the testing process. A usability test is conducted to improve the hardware design. Furthermore, critical component tests are performed to evaluate their performance before finalizing the prototype. Each section of the setup is labelled with its respective name to facilitate clear identification and comprehension.

Fig. 4.19 to 4.22 show the Flyback converter's DSO output. An input supply is taken from a regular 230V single-phase supply to power the flyback converter to test its performance. This section examines how the proposed control strategy performs on the MFC when there are changes in the reference values of input and output voltages. Before that, it provides the steady-state response with a resistive load of  $R = 10\Omega$ , as illustrated in Fig. 4.19.

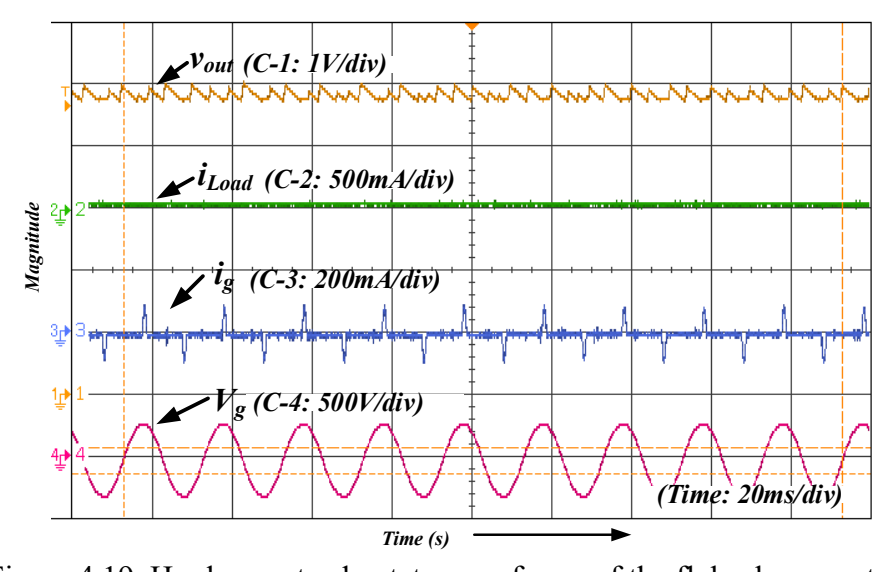


Figure 4.19. Hardware steady-state waveforms of the flyback converter.

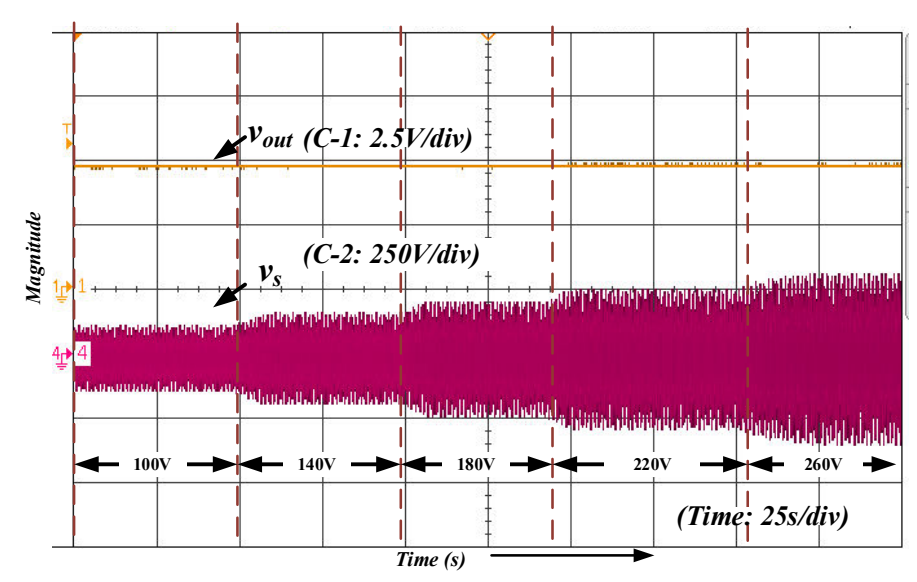


Figure 4.20. Experimental waveforms of the flyback converter under input voltage variation with the steady-state error of 3%.

Similarly, AC input varies from 100V to 260V using a variable in Fig. 4.20 on a close loop-controlled flyback converter, which shows strong reluctance in output voltage to input variation. An error of less than 3% is observed while varying the source. The non-ideal flyback converter has a practical efficiency of 86.4% when it is loaded on rated conditions. The variation in efficiency can be seen in Fig. 4.24. The drop in efficiency is observed due to the ESRs of the components.

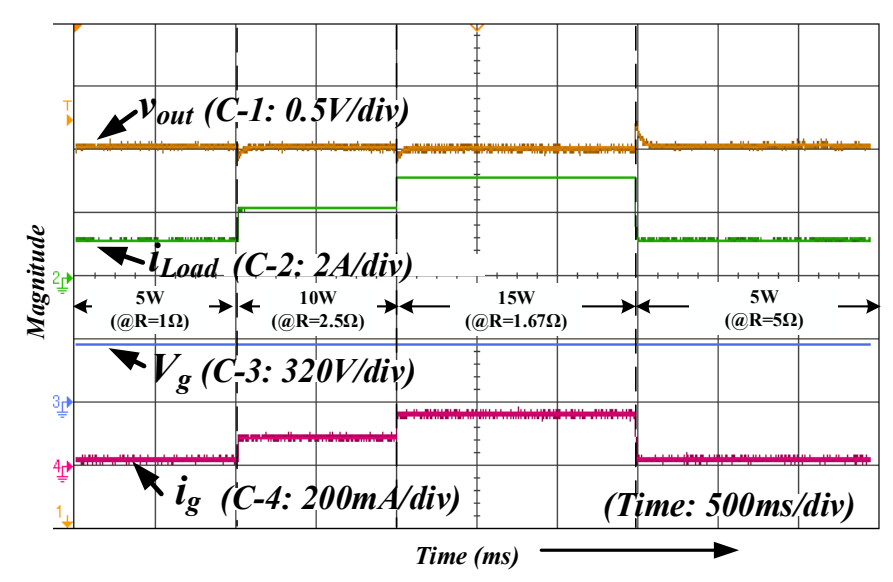


Figure 4.21. Experimental waveforms of the flyback converter when utilizing the proposed controller while undergoing variations in the output load.

Fig. 4.21 also shows the MFC's transient responses when subjected to load fluctuations. As shown in this Fig. 4.21, the output voltage maintains stability with an excellent transient response time, allowing for a proportionate reduction in a portion of the output voltage as needed. A less than 2% percentage error is observed within acceptable limits for resistive load variation from  $1\Omega$  to  $10\Omega$ .

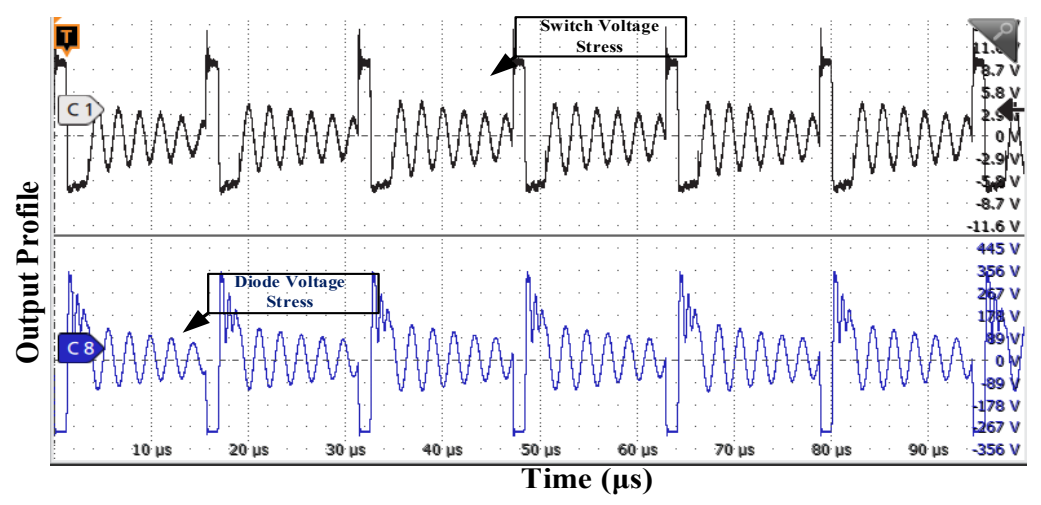


Figure 4.22. Voltage stress on the Switch and Diode of the flyback converter.

Fig. 4.22 typically shows two separate curves representing the stress on the MOSFET and diode, respectively. The x-axis represents time, while the y-axis will show the magnitude of the stress.

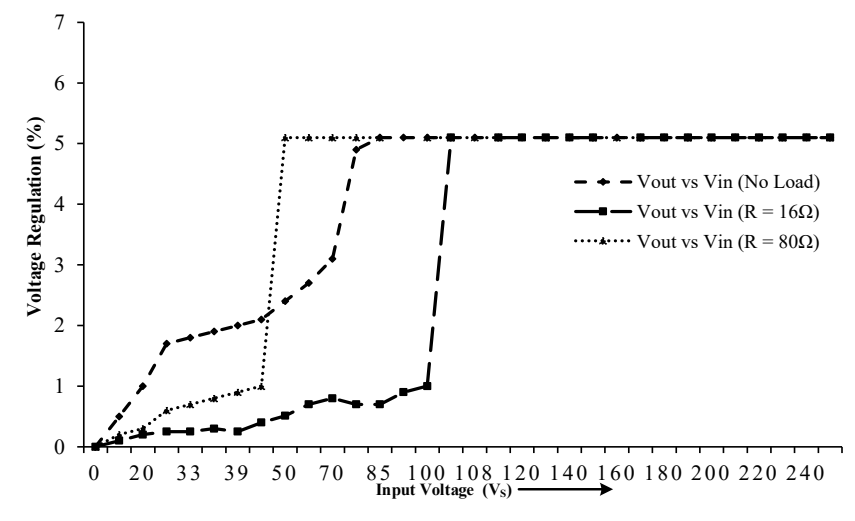


Figure 4.23. Variation of output voltage with input voltage under no load condition.

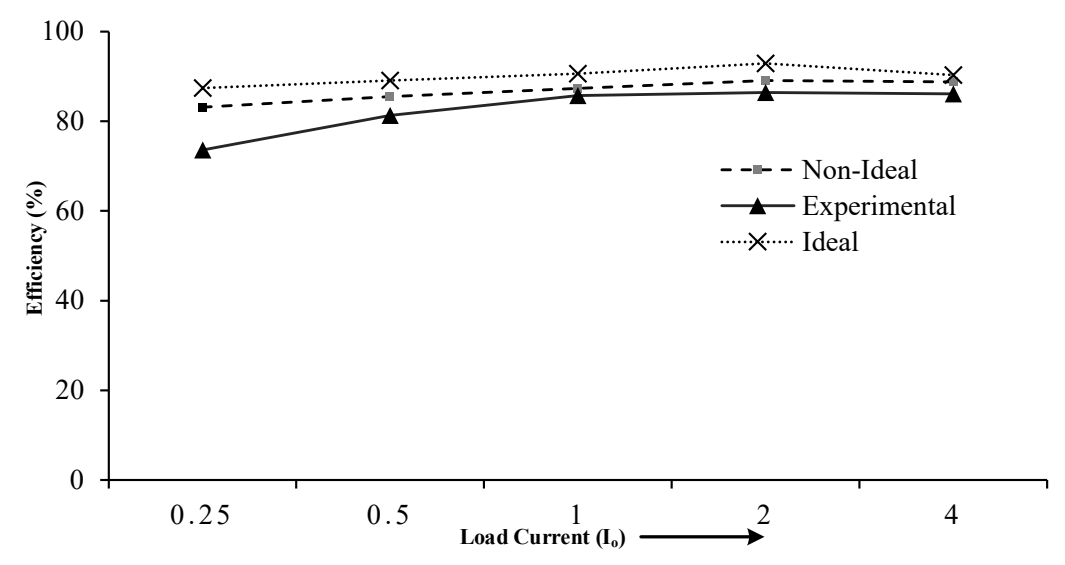


Figure 4.24. Efficiency for non-ideal flyback converter for load variation.

The different plot for input voltage sweeps over output voltage for changed load is shown in Fig. 4.23. The plot shows output voltage regulation concerning the input voltage. The input voltage is varied from 0-230V using a variac, and the load is changed from 2A to very low values, showing no load condition. A percentage error of less than 2% is observed within acceptable limits for the application in gate drivers such as IGBT, MOSFET, etc. Figure 4.24 depicts the efficiency of the non-ideal flyback converter under load variation from below rated condition to above rated condition.

#### 4.8. CONCLUSIONS

This chapter presents a non-ideal flyback converter with dual outputs, controlled by a Lyapunov-function-based approach, highlighting its simplicity, cost-effectiveness, and isolation. Extensive investigations were conducted to enhance the robustness and precision of the control method against load and voltage reference variations. The proposed system ensures global exponential stability, rapid transient response, and good gain and phase margins, even considering the effects of equivalent series resistances (ESRs). The inclusion of the duty ratio in the feedforward loop helps alleviates its burden. The average model, which accounts for parasitic components, improves control accuracy. Both numerical simulations and experimental tests confirm the superior performance of the converter in precisely regulating the reference output voltage. Additionally, this chapter compares the effectiveness of the Lyapunov-based

controller with that of a linear PI controller and a nonlinear Integral Sliding Mode Controller (ISMC) in managing an MFC for DC/DC conversion. Experimental results for closed-loop controlled flyback converters demonstrate the Lyapunov-based controller's advantages in handling various perturbations, reducing steady-state error to under 1%, and achieving quicker settling times. Notable stress on the switch and diode, within an acceptable range, will be addressed in future research.

#### **CHAPTER 5**

# DYNAMIC MODELING AND EFFICIENCY ANALYSIS OF MIMO BOOST CONVERTERS WITH RENEWABLE SOURCES FOR AGRICULTURE LOADS

#### 5.1. OVERVIEW

This chapter introduces a modified Multiport Boost Converter (MPBC) that forms the backbone in hybrid renewable energy systems. The novelty of this chapter is as follows:

- 1. The proposed non-isolated converter utilizes a single inductor (SI) to reduce electromagnetic interference, size, and cost.
- 2. ESRs are considered which are neglected in previous MIMO papers. Rigorous analysis has been implemented as it may affect the stability of the proposed converter.
- 3. Improved switching strategies using TMS320F28379D DSP with faster response.
- 4. It enables seamless addition or removal of input sources with least switching stress. The MPBC configuration includes two input sources, an Energy Storage Elements (ESE) and two DC outputs—one integrated with an inverter for AC loads and the other for auxiliary DC loads.
- 5. The input powers delivered by different dc sources can be individually regulated; thus, power budgeting between input energy sources can be accommodated.
- 6. The output voltages can be individually higher than the maximum input voltage or lower than the minimum input voltage.

#### 5.2. INTRODUCTION

Distributed renewable energy sources such as photovoltaics (PV) and fuel cells are rapidly gaining momentum as a solution to these issues. Wind energy is also making significant contributions to the energy transition. The installation of PV capacity has risen from kW to MW to GW in less than two decades, and it is expected to reach 1 TW of installed global capacity soon. A shift towards clean and green energy

is essential to ensure a sustainable future [96]-[100]. Because these energy sources are uncertain and intermittent, pose reliability challenges in standalone use. To address this, renewable resources are often combined with each other or with fuel cells, supercapacitors, and energy storage elements (ESEs). Recently, multi-input converters (MICs) have been used to connect multiple renewable energy sources. These converters offer simple circuit designs, low manufacturing costs, centralized control, and compact size [97]-[102].

In [103], a novel isolated multi-input dc-dc converter based on the concept of flux additivity, uses phase-shifted pulse width modulation (PWM) control on two input current-fed full-bridge dc-dc converters. This approach offers several advantages, including the ability to deliver power separately and simultaneously from multiple dc sources, soft switching technology, and electric isolation via a transformer. In [104], a modular non-isolated multi-input step-up high gain converter topology with continuous current conduction is explored (or proposed) that provides high gain using the same number of devices and has the least number of device counts. The switches and diodes' peak inverse voltage (PIV) are controlled within acceptable limits to maintain high voltage gain.

In [105], a new bidirectional dc-dc converter is presented for grid-connected renewable energy systems and hybrid electric vehicles. It eliminates the need for an additional transformer, combining two parallel buck converters with series switches for input sources to avoid short circuits, reducing the need for inductors and capacitors, enhancing cost-efficiency. However, it faces power flow control challenges. In many applications, integrating power electronics into multiple output converters (MOCs) is crucial for reducing size, weight, maintenance needs, and costs, as explained in references [109]-[110]. A comprehensive classification of fuel cell-based hybrid electric vehicles (FCHEVs). A key component in these FCHEVs is the DC-DC power converter. A multi-input DC-DC power converter is employed to connect multiple energy sources, simplifying the system and enhancing its overall efficiency [111].

Voltage regulation for each dc output in converters is crucial. Post-regulation is used to ensure robustness against line or load variations. Multiple loads require different low voltages, so efficiently supplying multiple-and-low output voltages is essential [112]. It [113] presents an accurately regulated multiple outputs (MO) ZVS dc-dc converter with operation and control analysis. Isolated multiport DC-DC converters are heavy and expensive and utilize transformers for electrical isolation. Non-isolated multi-input DC-DC converters provide a practical and cost-effective solution without the need for transformers or high-frequency components, resulting in improved efficiency [114].

Multi-Input Multi-Output (MIMO) converters provide a medium of interaction between different renewable resources, energy-storing elements, and advanced electric loads with a centralized control system. A generalised form of MIMO converter is shown in Fig 1. Integrating MIMO systems with sources and loads provides compact packaging, relatively easier control, simultaneous power management, and voltage regulation. In [115] and [116], presented a topology that can interface between diversified renewable energy sources and diode-clamped multilevel inverters for ac loads. As the sources are intermittent, ESE is a must, and the impossibility of energy transfer between sources is a drawback of this converter. [117]-[124] discusses a non-isolated MIMO converter with individual inductors for each source but lacks power transfer between inputs. The individual inductors make the converter larger, and a cascading approach increases device count and complexity.

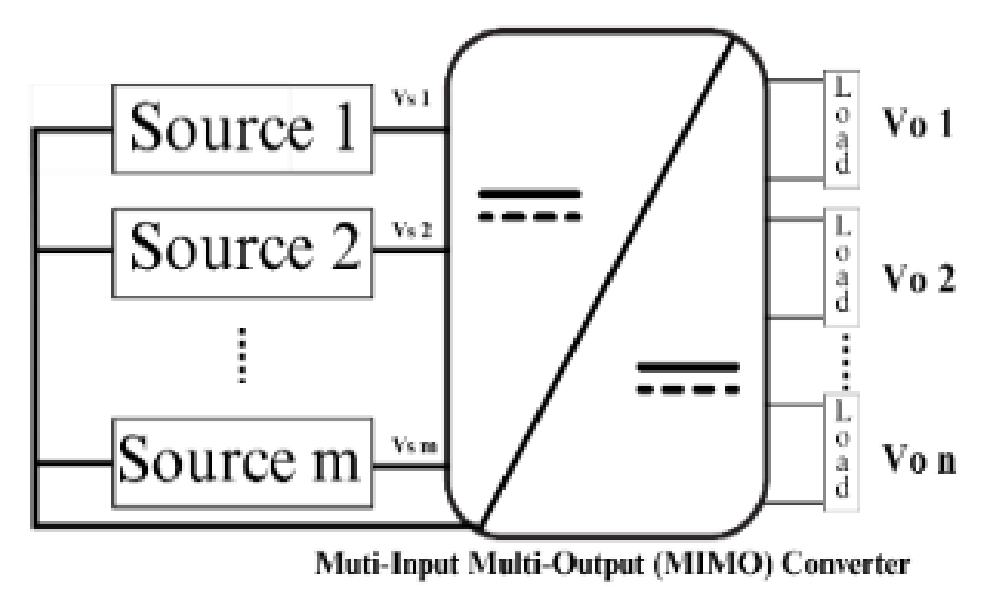


Figure 5.1. Generalized MIMO Converters

A novel MIMO converter is introduced in [125], capable of distributing power among sources and the load. Dynamic analysis is conducted on a 2-in-2-out system with two inputs (35V and 48V), two outputs (40V and 80V), and 236W output power using ideal parameters. The paper explores n-input and m-output configurations, but increasing the number of sources leads to switching stress and duty cycle issues with the in-line switches. The study proposes a lead-lag compensator to regulate the system by adjusting poles and zeros, but this approach may be unreliable when faced with uncertainties in load power variations. In [126], discusses the design, implementation, and control of a scalable DC microgrid that uses a hybrid of renewable energy sources. It employs a multi-input, multi-output dual active half-bridge (DAHB) converter.

#### 5.3. TOPOLOGY DERIVATION AND COMPARISON STUDY

The researchers [100], [114], [116], [117], [122], [124], and [125] have proposed numerous non-isolated multiport converters, emphasizing the need for more efficient and cost-effective solutions for hybrid renewable energy systems as shown in Table I. Specific parasitic effects can influence the converter's characteristics, including its components' equivalent series resistances (ESRs). The crucial question to address is whether and how these ESRs impact the converter's input resistance. Some of these converters have redundant switching components, and most of the converters are shown ideally without parasitic effects, so the topology should be optimized by analyzing the voltages across the switch components, including practical behaviour with parasitics. Two topologies from the family of non-isolated multiple-port converters in Section 5.4 have been selected to create the proposed converter having three inputs including ESEs, which can store energy in the event of low power demand at the load side, and two outputs with their parasities. Fig 5.2 to Fig 5.4, shows the three topologies selected from Table 5.1 of non-isolated dc-dc converters for three input and two output non-isolated dc-dc converters with their parasitic elements. These three topologies use 5 MOSFETs  $S_1$ ,  $S_2$ ,  $S_3$ ,  $S_4$ , and  $S_5$  to perform the circuit operation and their parasities are  $r_{ds1}$ ,  $r_{ds2}$ ,  $r_{ds3}$ ,  $r_{ds4}$  and  $r_{ds5}$  respectively. ESR of switches, inductors and capacitors are included in all the topologies showing the practical behaviour of the circuit. The averaged and dynamic mathematical derived symbols along with specifications are listed in Table 5.4.

Table 5.1. COMPARISION ANALYSIS OF DIFFERENT CONVERTER TOPOLOGIES

-	Converter	[100]	[114]	[116]	[117]	[122]	[124]	[125]	MPBC Converter
•	LInputs M M M		M	M	M	M	M	M	
5	Output	N	N	N	N	N	N	N	N
er	Switch	M+N	M+N	M+N	M	M+N	M+N	M+N	M+N
Number of	Diodes	M+N	M+N	M+N	N	M+N+1	M+N+1	M+N	M+N
<u> </u>	Inductor	1	1	1	M	1	1	1	1
	Capacitor	1	1	1	N	1	1	N	N
Inp	out Current	Disconti nuous	Discontinu ous	Discontinu ous	Continuo us	Discontinu ous	Discontinu ous	Discontin uous	Discontinuous
F	requency	40kHz	100kHz	40kHz	20kHz	20~100kHz	100kHz	10kHz	40kHz
Inj	out Voltage	25V,20V	20V, 9V~40V, 20V	30V,20V	159.3V, 150V	24V, 20V	18V, 22V	35V, 48V	12V, 24V, 60V
	Output Voltage	22V,11V	5.25V, 3V~15V, 32V	21V,8V	155V	12V, 8~10V	12V, 8V	80V, 40V	60V, 60V
Output Power		29.5W	30.4W	35.4W	-	35W	33W	236W	240W
Vo	Output Itage Level	Low	Low	Low	High	Low	Low	Medium	Medium
M	ax. Voltage oss Switch	Medium	Medium	Medium	Low	Medium	Medium	High	Low
F	Efficiency	-	88%	90%	-	92.1%	-	80%	91.6%
	Extension Sapability	Medium	High	Medium	Medium	Medium	Medium	Medium	High
	Cost	Medium	Low	Medium	High	Medium	Medium	Medium	Low

To evaluate the advantages of the proposed converter, a comparison was conducted between the proposed converter and various MIMO converters from previous studies, as outlined in Table 5.1. The comparison primarily focused on factors such as the number of switches, capacitors, inductors, voltage stress, control complexity and expandability.

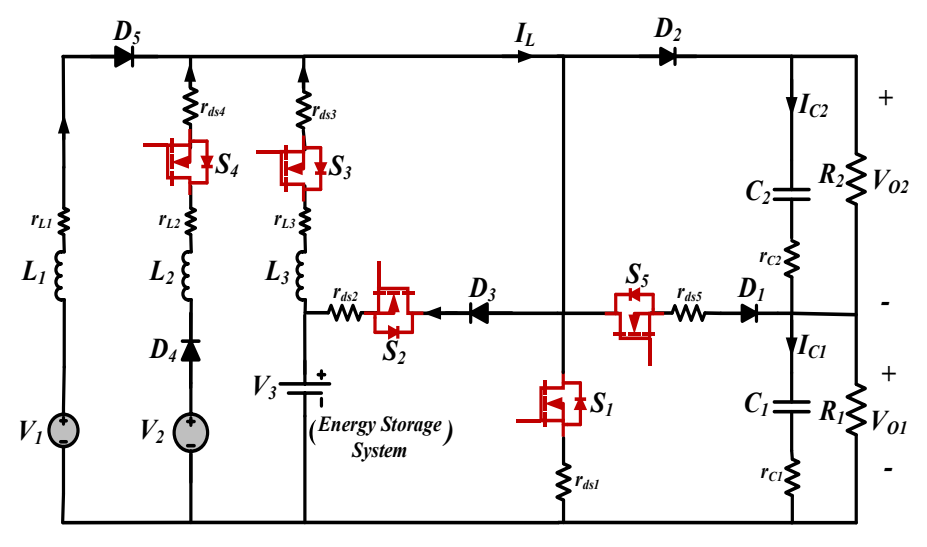


Figure 5.2. Topology 1: Non-isolated dc-dc converter with multiple inductor on source with parasitics[117]

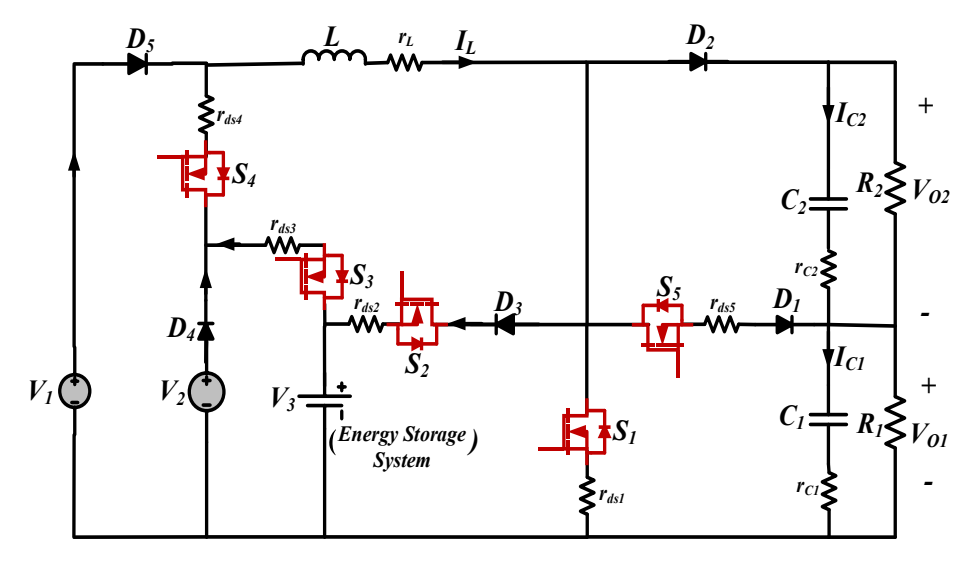


Figure 5.3. Topology 2: Non-isolated single inductor dc-dc converter with parasitics [125].

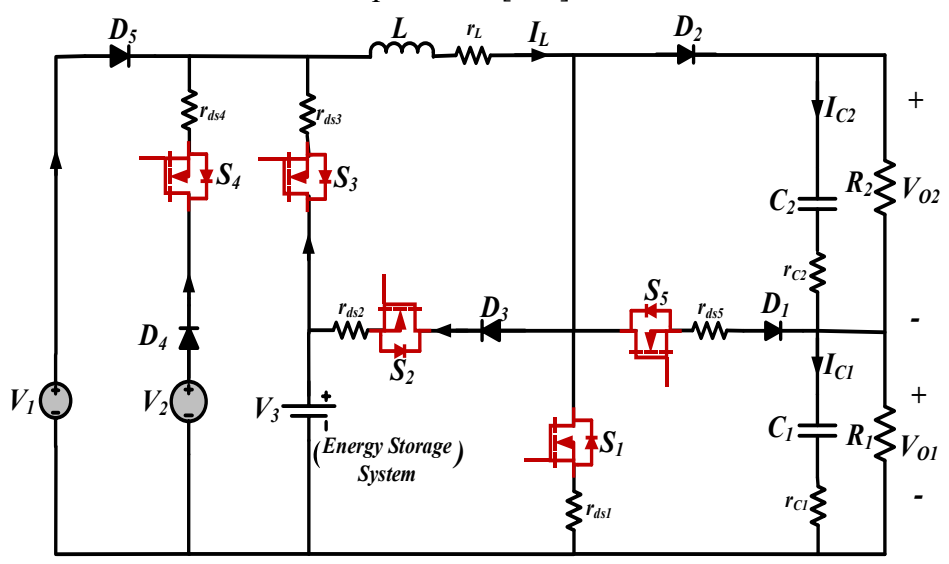


Figure 5.4. Topology 3: Proposed three input two output converter with parasitics in circuit.

The Converters found in references [100],[114],[116],[122],[124] were deemed unsuitable for connecting renewable energy sources to the power grid due to their low voltage outputs except [125]. On the other hand, the proposed converter offers several advantages. Its control system is straightforward, and its design is cost-effective. Additionally, it allows for seamless addition or removal of input sources, and its output terminals function independently. Notably, the converter operates without the need to worry about switch transition times, which enhances its expandability and reduces design complexity. A comparative analysis between the proposed converter and

existing single- inductor MIMO converters as shown in Table 5.1 and in Fig 2-4 clearly highlights the benefits of the proposed design.

#### 5.4. CONVERTER STRUCTURE AND OPERATION MODES

This chapter introduces a highly efficient non-isolated single inductor multiport dc-dc converter that combines state-of-the-art research from [102], [114], and [125]. Fig. 5.5.(a) illustrates the multiport extension of the proposed converter for interfacing multiple inputs and outputs. As shown in Fig. 5.5(b), the proposed MPBC structure facilitates the seamless integration of three input power sources  $V_1, V_2, and V_3$ , where  $V_1 < V_2 < V_3$ . The converter achieves superior performance with just one inductor, two output capacitors, and five switches. The load resistances  $R_1$  and  $R_2$  represent the power feeding to a DC load or single-phase motor as AC loads. Proper switching of the MOSFETs enables precise control of power flow between input sources and voltage boosting. The converter can produce output voltages suitable for connection to a single-phase inverter, with each output having varying or equal voltage levels. The five controllable switches  $S_1, S_2, S_3, S_4$  and  $S_5$  are the primary elements that regulate the converter's power flow and output voltages. ESRs are added for MOSFETs, inductors, and capacitors to understand the circuit practically.

This enhancement significantly improves the system's practical applicability. Notably, the converter's unique design allows  $V_1$  and  $V_2$  to supply power to  $V_3$ , creating a perfect fit for electric vehicle (EV) applications. The configuration optimizes the layout, placing Solar PV in the  $V_1$  position, fuel cell (FC) at  $V_2$ , and energy storage elements (ESEs) like batteries or supercapacitors (SC), which can be recharged, in the  $V_3$  slot.

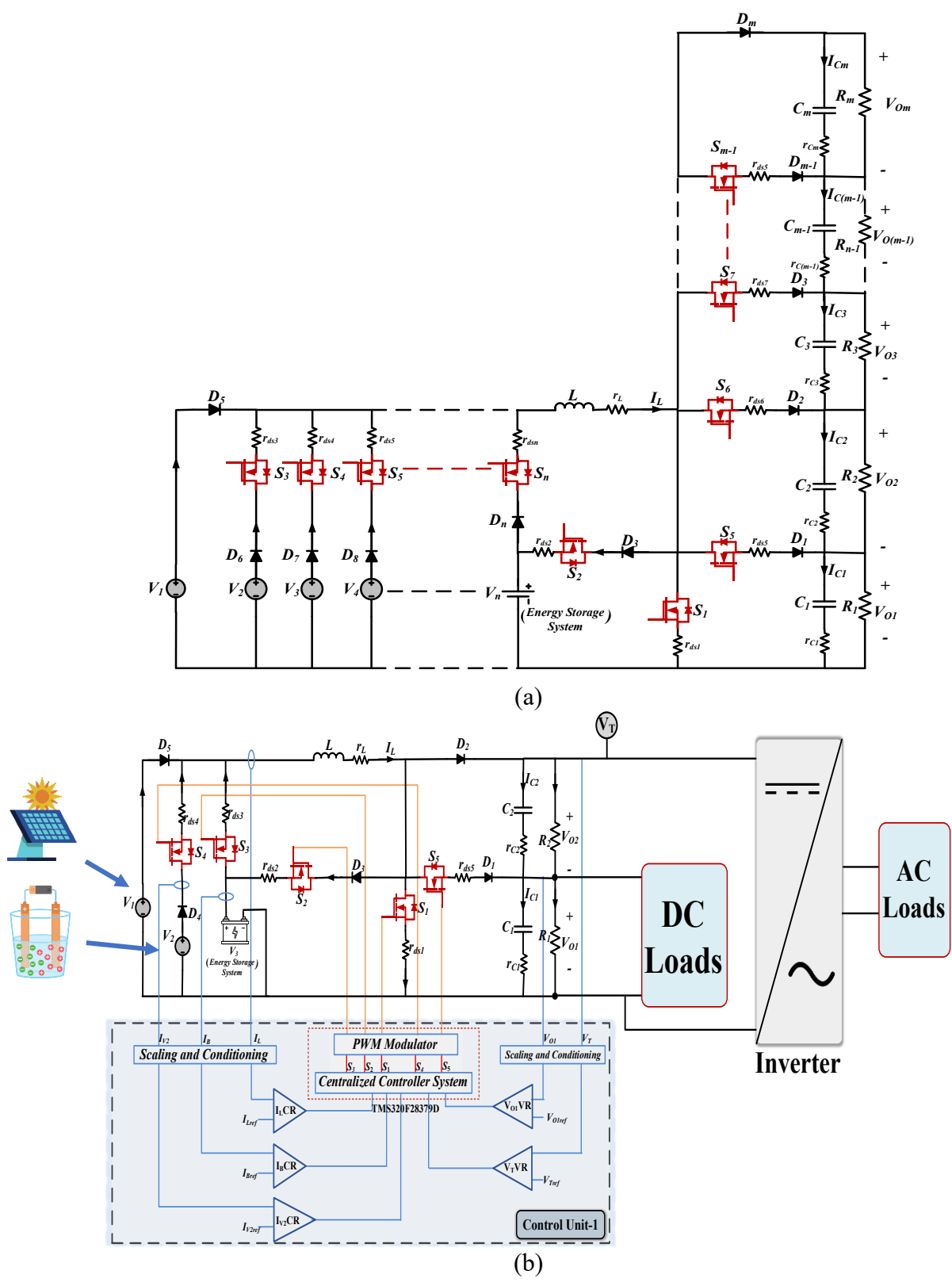


Figure 5.5. (a) Multiport extension for the proposed converter to interface multiple inputs and outputs, (b) Circuit diagram of proposed MPBC with DC load, integrated single phase inverter with AC load and control unit.

In this chapter, Solar PV and FCs serve as robust power sources, while the battery operates as an efficient energy storage system (ESS). The proposed converter introduces two distinct power operation modes based on the battery's usage status, ensuring optimal system performance. During periods of high load demand, all input sources contribute to the load power, with  $S_2$  remaining inactive while  $S_1$ ,  $S_3$ ,  $S_4$ , and  $S_5$  are engaged. In scenarios of low load power and a need to charge  $V_3$ ,  $V_1$  and  $V_2$  provide power for both the loads and  $V_3$ , with  $S_1$ ,  $S_2$ ,  $S_4$ , and  $S_5$  active, and  $S_3$  in a standby state.

To maintain system stability, it is essential to minimize the input current fluctuations in both PV and FCs. The output voltage's dependency on input current necessitates precise power balance between input sources and the load. Due to which, this study thoroughly investigates the converter's steady state and dynamic behavior in Continuous Conduction Mode (CCM). It is important to note that each input source can function independently, allowing the converter to operate as a single-input dc-dc converter, including a standalone mode.

Fig 5.2 and 5.3 provide a comprehensive overview of the topologies for each converter, including their inherent parasitic elements which is neglected in [120] and [125]. It will give better insight for the performance comparison. It is evident that Topology 1, with inductors in each source for energy accumulation, results in a bulky and lossy converter. This setup introduces significant two outputs to hybridize power sources. During the discharging mode, switching state 1 of this converter reveals that three switches are ON at a time, which can increase up to n switches with the addition of n sources. As a result, ON time of inner source will be very limited and the duty cycle range for higher-order sources is limited. This will also create stresses on higher order source switches which is also verified experimentally as shown in section 5. Cascading of switches will increase losses due to the internal resistance of switches, as can be observed from the inductor differential equation in switching state 1 of topology 2 during the discharging mode.

$$L\frac{d_{i_L}}{dt} = v_3 - i_L(r_{ds3} + r_{ds4} + r_{ds1} + r_L)$$
 (5.1)

Controlling of these switches will affect the output response as the recovery rate of each switch in switching state 1 of discharging mode is dependent on each other. Cascading of switches will also delay the applied control technique. From (1), it can be concluded that for n number of sources, differential equation will have (n-1) ESR of switches.

To address the drawbacks of these converters, the proposed solution connects sources in parallel with their switches, eliminating the possibility of multiple switches being activated simultaneously. The proposed MPBC is shown in Fig 5.4, whose parameters are depicted in Table 5.2. Further its switching states for discharging and charging are listed under topology 3 of Fig 5.6 and Fig 5.8, respectively. The proposed MPBC includes two renewable sources integrated with ESEs as a third source and two outputs, where a higher voltage output that is connected to a single-phase inverter for AC loads and a lower DC voltage output that can be used for DC loads or vice versa depending upon the practical requirements as shown in Fig 5.5. The switch for source  $V_3$ , which corresponds to the ESEs, is isolated and connected in parallel with sources  $V_1$  and  $V_2$  in the circuit.

Table 5.2. HARDWARE COMPONENT AND SIMULATION PARAMETERS OF PROPOSED SYSTEM

Simulation & Prototype Parameters	Symbols	Specification(s)
Output Power	$P_{o1}$ , $P_{o2}$	120W, 120W
Switching Frequency	fs	40kHz
Output Voltage	$V_T$ , $V_{O1}$ , $V_{O2}$	120V, 60V, 60V
DC Source 1 and 2	$V_1, V_2$	12V, 24V
DC Source 3 (Battery)	$V_3$	60V of 12V,7Ah (5)
Inductor	L	2mH
Inductor ESR	$r_{\!\scriptscriptstyle L}$	$0.33~\Omega$
Capacitors	$egin{array}{c} C_1 \ C_2 \end{array}$	$1000\mu F~(150V), \ 1000\mu F~(150V)$
Capacitor ESR	$r_{C1}$ , $r_{C2}$	$100m~\Omega~each$
Load Resistances	$egin{array}{c} R_1 \ R_2 \end{array}$	$0-500  \Omega$ , $0-500  \Omega$
MOSFET	SPW20N60C3	650V, 20.7A
On-State Resistance	$r_{ds1}, r_{ds2}, r_{ds3}, r_{ds4}, r_{ds5}$	0.19arOmega
Diode	STTH3012	1200 V, 30 A

Instead of considering ideal switches and elements, switching states are analyzed considering the effect of the parasitics. This design not only offers improved performance and reliability but also enhances the overall safety of the system.

The proposed converter is expected to significantly impact the development of future renewable energy systems by addressing some of the significant challenges associated with existing converter designs. Converter structure, averaged and small signal modelling, voltage and current stress analysis, stability and control structure are explained in detail in the subsequent section. Table 5.3 shows the three operating modes: standalone, discharging and charging mode respectively. Here, the converter has been studied in two primary operational modes, battery discharging and charging mode.

## 5.4.1. First Operation Mode (Discharging Mode)

In this configuration, source  $V_3$ , the battery, is along with two input sources,  $V_1$  and  $V_2$ , is solely responsible for delivering power to the loads. The switches  $S_2$  is completely OFF, while  $S_1$ ,  $S_3$ ,  $S_4$ , and  $S_5$  are actively engaged. Switches  $S_3$  and  $S_4$  are responsible for actively regulating the source currents to a desired value. Ensuring the total output voltage  $V_T$ , the sum of  $V_{O1}$  and  $V_{O2}$ , attains the selected value is controlled by switch  $S_1$ . Switch  $S_5$  regulates the output voltage  $V_{O1}$ . By effectively regulating  $V_T$  and  $V_{O1}$ , the output voltage  $V_{O2}$  is also controlled to the desired value.

Table 5.3. OPERATING MODES WITH SWITCHING PATTERNS OF PROPOSED MULTIPORT CONVERTER.

OPERATION MODES	$V_1$	$V_2$	V <sub>3</sub> (Battery)	$V_{01}$	$V_{02}$	$S_1$	$S_2$	$S_3$	$S_4$	$S_5$	SS
STANDALONE MODE (MODE-1)	Active	Active		Active Active	Active Active	$(1-D_1)T$ $(1-D_1)T$	X X	X X	$(1-D_4)T$ $(1-D_4)T$	X X	2 3
	Active			Active	Active	X	X	X	X	$(1-D_5)T$	4
	Active			Active	Active	X	X	X	X	X	5
BATTERY DISCHARGING MODE (MODE-2)	Active Active Active	Active	Active	Active Active Active Active	Active Active Active Active	$(1-D_1)T$ $(1-D_1)T$ $(1-D_1)T$ X X	X X X X	(1-D <sub>3</sub> )T X X X X	X (1-D <sub>4</sub> )T (1-D <sub>4</sub> )T X	X X X (1-D <sub>5</sub> )T X	1 2 3 4 5
BATTERY CHARGING MODE (MODE-3)	Active Active	Active	Active	Active Active Active Active	Active Active Active Active	$(1-D_1)T$ $(1-D_1)T$ $X$ $X$ $X$	X X (1-D <sub>2</sub> )T X X	X X X X	(1-D <sub>4</sub> )T X X X X	X X X (1-D <sub>5</sub> )T X	1 2 3 4 5

WHERE X= INACTIVE, T= TIME PERIOD AND SS= SWITCHING STATE

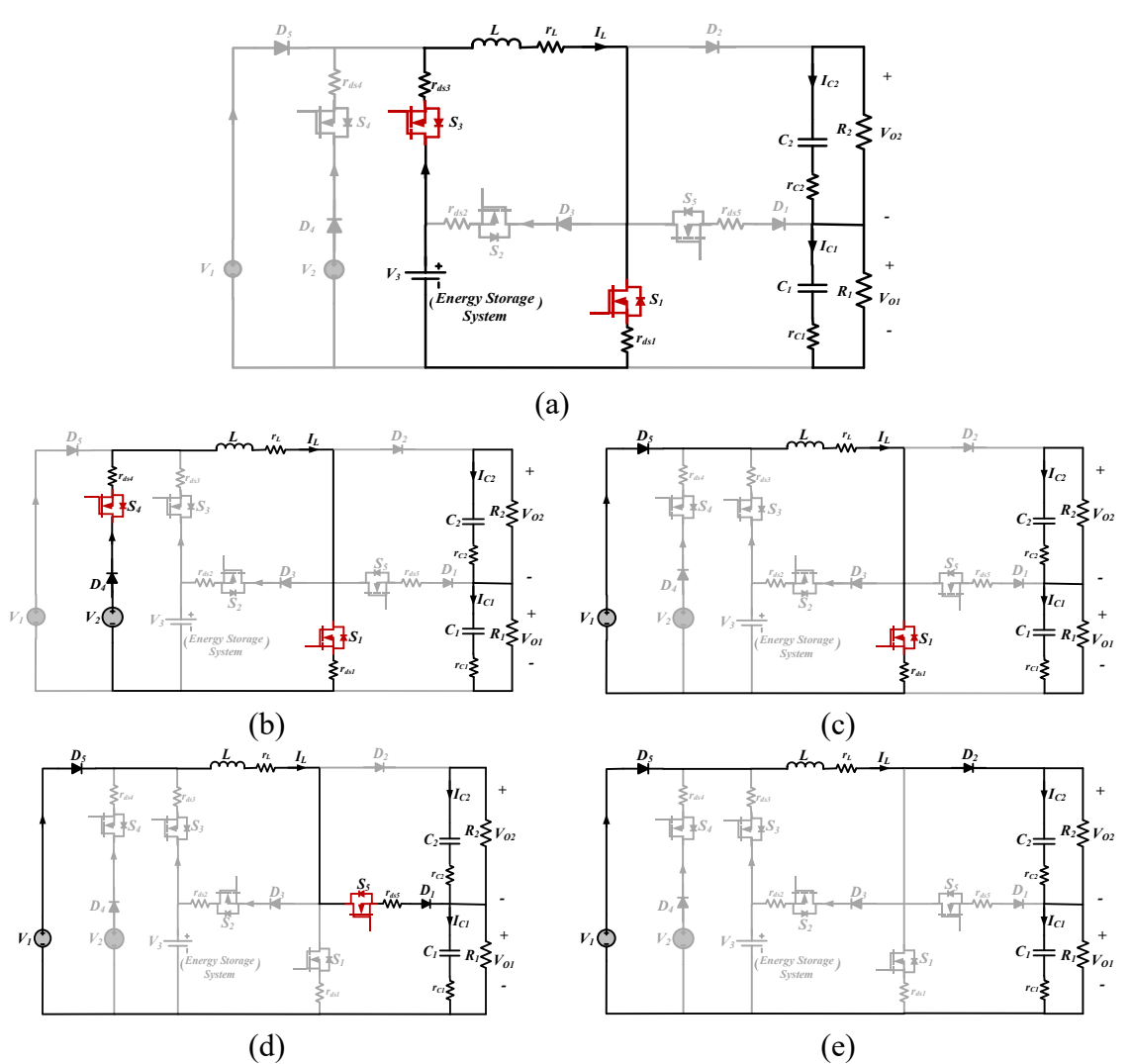


Figure 5.6. Equivalent circuit of battery discharging mode considering ESRs, (a) switching state-1, (b) switching state-2, (c) switching state-3, (d) switching state-4, and (e) switching state-5 of proposed MPBC.

During State 1 (0 < t <  $D_3T$ ), switches  $S_1$  and  $S_3$  are turned ON. Because  $S_1$  is ON, diodes  $D_1$  and  $D_2$  are reversely biased, so switch  $S_5$  is turned OFF. Furthermore, since  $V_1$  <  $V_2$  <  $V_3$  and  $S_3$  is ON and  $S_4$  is OFF, diode  $D_5$  becomes reversely biased. The equivalent circuit of the proposed converter in this state is shown in Fig 5.6(a) where, source  $V_3$  charges inductor L, increasing inductor current  $I_L$ . Additionally, capacitors  $C_1$  and  $C_2$  discharge their stored energy to the load resistances  $R_1$  and  $R_2$ , respectively. In this mode, the inductor current and capacitor voltages considering ESRs are expressed as follows:

$$L\frac{d_{i_L}}{dt} = v_3 - i_L(r_{ds3} + r_{ds1} + r_L)$$
 (5.2)

$$C_1 \frac{dv_{o1}}{dt} = -\frac{v_{o1}}{(R_1 + r_{c1})} \tag{5.3}$$

$$C_2 \frac{dv_{o2}}{dt} = -\frac{v_{o2}}{(R_2 + r_{c2})} \tag{5.4}$$

Steady states waveform are shown in Fig 5.8.

During State 2 ( $D_3T < t < D_4T$ ), switch  $S_4$  is turned ON,  $S_1$  remains ON, and  $S_3$  is turned OFF. Since  $S_1$  is ON, diodes  $D_1$  and  $D_2$  are reverse-biased, so switch  $S_4$  remains OFF. The equivalent circuit of the proposed converter during this state is illustrated in Fig 5.6(b). During this state, source  $V_2$  charges inductor L, leading to an increase in inductor current. Additionally, capacitors  $C_1$  and  $C_2$  are discharged, releasing their stored energy to load resistances  $R_1$  and  $R_2$ , respectively. The equations governing the inductor's and capacitors' behaviour considering ESRs during this state are provided below.

$$L\frac{d_{i_L}}{dt} = v_2 - i_L(r_{ds4} + r_{ds1} + r_L)$$
 (5.5)

$$C_1 \frac{dv_{o1}}{dt} = -\frac{v_{o1}}{(R_1 + r_{c1})} \tag{5.6}$$

$$C_2 \frac{dv_{o2}}{dt} = -\frac{v_{o2}}{(R_2 + r_{c2})} \tag{5.7}$$

During State 3 ( $D_4T < t < D_1T$ ), switch  $S_1$  is still ON,  $S_4$  and  $S_3$  are turned OFF. Because  $S_1$  is ON, diodes  $D_1$  and  $D_2$  are reversely biased, so switch  $S_5$  is still OFF. The equivalent circuit of the proposed converter in this state is shown in Fig 5.6(c).  $V_1$  charges inductor L, so the inductor current increases. In addition, capacitors  $C_1$  and  $C_2$  are discharged and deliver their stored energy to load resistances  $R_1$  and  $R_2$ , respectively. The inductor current and capacitor voltages considering ESRs in this mode are as follows:

$$L\frac{d_{i_L}}{dt} = v_1 - i_L(r_{ds1} + r_L) (5.8)$$

$$C_1 \frac{dv_{o1}}{dt} = -\frac{v_{o1}}{(R_1 + r_{c1})} \tag{5.9}$$

$$C_2 \frac{dv_{o2}}{dt} = -\frac{v_{o2}}{(R_2 + r_{c2})} \tag{5.10}$$

During State 4 ( $D_1T < t < D_5T$ ), the proposed converter operates as follows: switch  $S_1$  is turned OFF, while switches  $S_3$  and  $S_4$  remain OFF. Additionally, switch  $S_5$  is turned ON, causing diode  $D_2$  to be reversely biased. The equivalent circuit of the converter during this state is depicted in Fig 5.6(d). In this mode, inductor L discharges and transfers its stored energy to  $C_1$  and  $R_1$ , decreasing the inductor current. Meanwhile, capacitor  $C_1$  is charged, and capacitor  $C_2$  is discharged, delivering its stored energy to the load resistance  $R_2$ . The expression governing the energy storage elements L,  $C_1$ , and  $C_2$  considering ESRs in this mode are as follows:

$$L\frac{d_{i_L}}{dt} = v_1 - i_L(r_{ds5} + r_L) - v_{o1}$$
 (5.11)

$$C_1 \frac{dv_{o1}}{dt} = i_L - \frac{v_{o1}}{(R_1 + r_{c1})}$$
 (5.12)

$$C_2 \frac{dv_{o2}}{dt} = -\frac{v_{o2}}{(R_2 + r_{C2})} \tag{5.13}$$

None of the switches is active during state 5 ( $D_5T < t < T$ ), causing diode  $D_2$  to be forward-biased. During this phase, inductor L is discharged, transferring its stored energy to capacitors  $C_1$ ,  $C_2$ , and load resistances  $R_1$  and  $R_2$ . Additionally, capacitors  $C_1$  and  $C_2$  are charged. Fig 5.6(e) shows the equivalent circuit of the proposed converter in this state. Expressions governing the inductor current and capacitor voltages considering parasitics during this mode are as follows:

$$L\frac{d_{i_L}}{dt} = v_1 - i_L r_L - (v_{o1} + v_{o2})$$
 (5.14)

$$C_1 \frac{dv_{o1}}{dt} = i_L - \frac{v_{o1}}{(R_1 + r_{C1})}$$
 (5.15)

$$C_2 \frac{dv_{o2}}{dt} = i_L - \frac{v_{o2}}{(R_2 + r_{c2})}$$
 (5.16)

Fig 5.7 shows the steady state voltage and current waveforms of the inductor as well as different output voltages obtained during battery discharging modes. It also shows the switching strategies of the proposed MPBC.

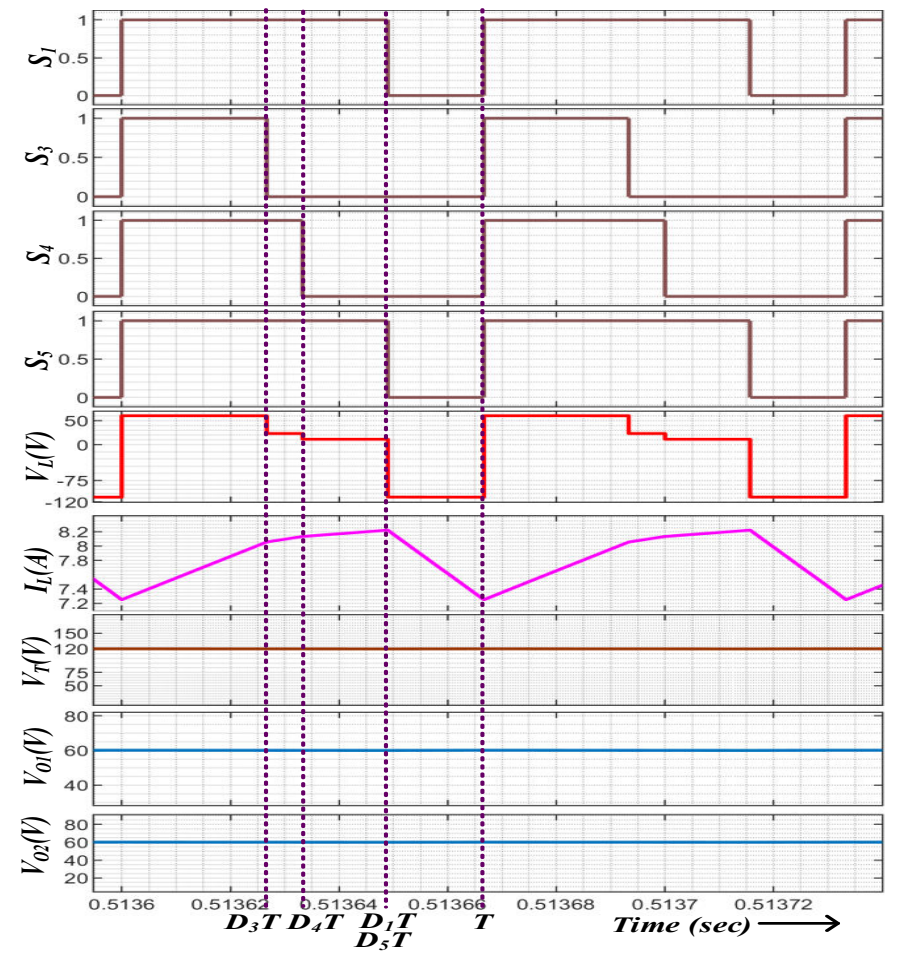


Figure 5.7. Battery Discharging Mode steady state waveform of proposed converter

These five states will combine to form the average model and will be further analyzed for stability and stress determination of proposed MPBC. Slope of the inductor current in equations (5.2), (5.5), (5.8), (5.11) and (5.14) shows that parasitics plays major role causing transfer of energy in the circuit components.

#### 5.4.2. Second Operation Mode (Battery Charging)

In this operational mode, sources  $V_1$  and  $V_2$  supply loads and provide power to  $V_3$  (battery). This occurs when the load power is low, and the battery requires immediate charging. To accomplish this, switches  $S_1$ ,  $S_2$ ,  $S_4$ , and  $S_5$  are activated, while switch  $S_3$  is deactivated. Like the previous operational mode of the converter, each

switch also has a specific duty to perform in this mode. Switch  $S_1$  regulates the overall output voltage  $V_T = V_{O1} + V_{O2}$  to the desired level, while switch  $S_2$  regulates the charging current  $I_b$ .

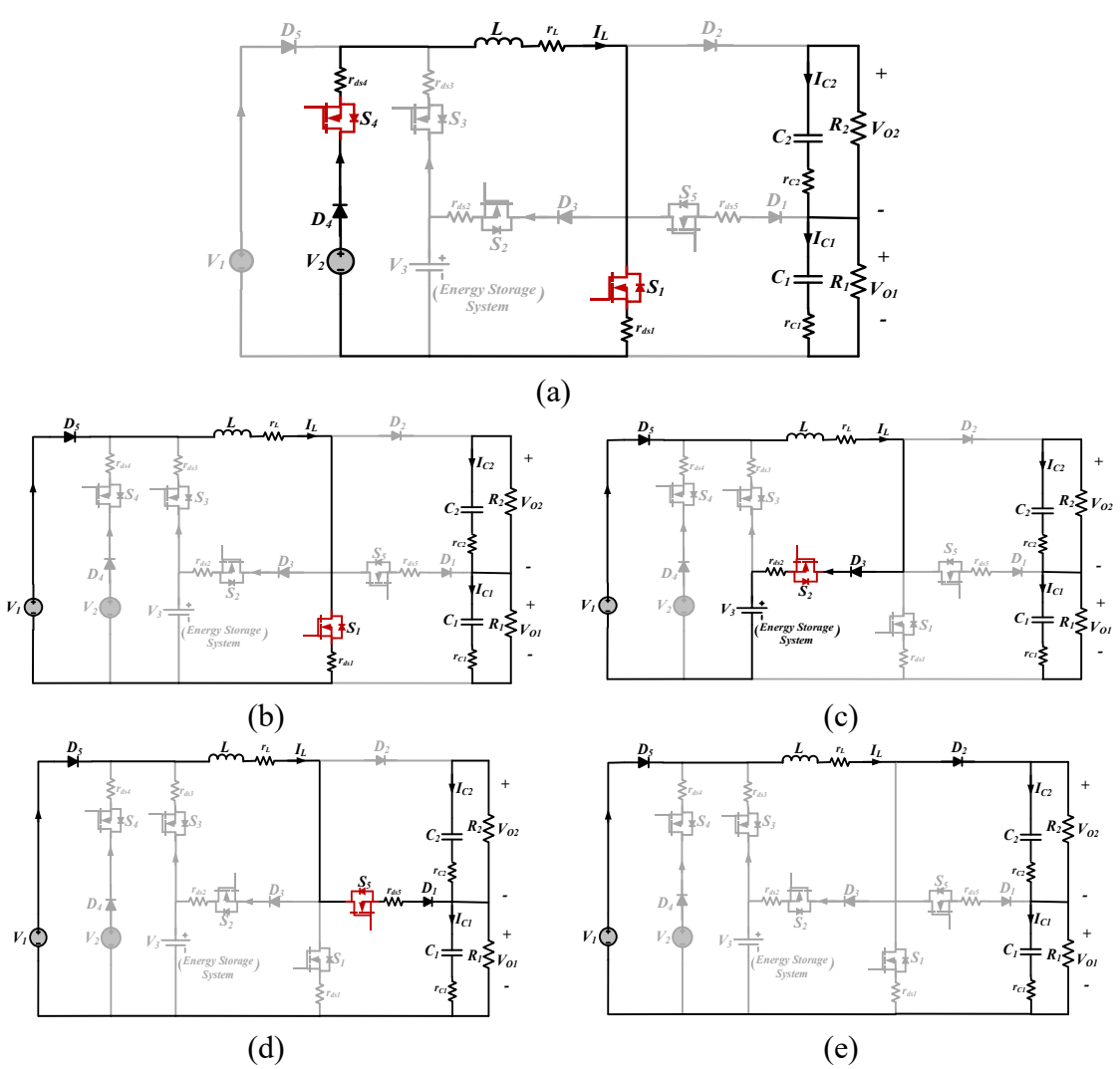


Figure 5.8. Equivalent circuit of battery charging mode considering ESRs, (a) switching state-1, (b) switching state-2, (c) switching state-3, (d) switching state-4, and (e) switching state-5 of proposed MPBC.

Additionally, switch  $S_5$  controls the output voltage  $V_{O1}$ . It is evident that the output voltage  $V_{O2}$  is also controlled while regulating  $V_T$  and  $V_{O1}$ . Depending on the various switch states, five different operational modes are discussed throughout one switching period considering the parasitics.

During State 1 (0 < t <  $D_4T$ ), switch  $S_1$  is turned ON, while  $S_2$  and  $S_5$  are reverse-biased and cannot be activated. Diode  $D_2$  is also reversely biased and does not conduct.

The equivalent circuit of the proposed converter in this state is shown in Fig 5.8(a). In this mode,  $V_2$  charges inductor L, causing an increase in inductor current. Capacitors  $C_1$  and  $C_2$  are discharged, delivering their stored energy to load resistances  $R_1$  and  $R_2$ , respectively. Inductor current and capacitor voltages during this mode are as follows:

$$L\frac{d_{i_L}}{dt} = v_2 - i_L(r_{ds4} + r_{ds1} + r_L)$$
 (5.17)

$$C_1 \frac{dv_{o1}}{dt} = -\frac{v_{o1}}{(R_1 + r_{c1})} \tag{5.18}$$

$$C_2 \frac{dv_{o2}}{dt} = -\frac{v_{o2}}{(R_2 + r_{c2})} \tag{5.19}$$

During State 2 (D<sub>4</sub>T< t < D<sub>1</sub>T), again switch  $S_1$  is turned ON, while  $S_2$  and  $S_5$  are reverse-biased and cannot be turned ON. Diode  $D_2$  is also reversely biased and does not conduct. The equivalent circuit of the proposed converter in this state is shown in Fig 5.8(b). In this mode,  $V_1$  charges inductor L, increasing inductor current. Capacitors  $C_1$  and  $C_2$  are discharged, delivering their stored energy to load resistances  $R_1$  and  $R_2$ , respectively. Expressions governing the inductor current and capacitor voltages during this mode are as follows:

$$L\frac{d_{i_L}}{dt} = v_1 - i_L(r_{ds1} + r_L) (5.20)$$

$$C_1 \frac{dv_{o1}}{dt} = -\frac{v_{o1}}{(R_1 + r_{C1})} \tag{5.21}$$

$$C_2 \frac{dv_{o2}}{dt} = -\frac{v_{o2}}{(R_2 + r_{c2})} \tag{5.22}$$

During State 3 ( $D_1T < t < D_2T$ ), switch  $S_1$  is turned OFF while switch  $S_2$  is turned ON. Diodes  $D_1$  and  $D_2$  are reversely biased, and as a result,  $S_5$  remains OFF. The equivalent circuit of the proposed converter in this state is shown in Fig 5.8(c). Since  $V_1 < V_2 < V_3$ , the inductor current decreases during this period, and the inductor delivers its stored energy to the battery  $V_3$ . Capacitors  $C_1$  and  $C_2$  are discharged, delivering their stored energy to load resistances  $R_1$  and  $R_2$ , respectively. Expressions governing the inductor current and capacitor voltages during this mode are as follows:

$$L\frac{d_{i_L}}{dt} = v_1 - v_3 - i_L(r_{ds2} + r_L)$$
 (5.23)

$$C_1 \frac{dv_{o1}}{dt} = -\frac{v_{o1}}{(R_1 + r_{c1})} \tag{5.24}$$

$$C_2 \frac{dv_{o2}}{dt} = -\frac{v_{o2}}{(R_2 + r_{C2})} \tag{5.25}$$

During State 4 ( $D_2T < t < D_5T$ ), switch  $S_1$  is still OFF, while switch  $S_2$  is turned OFF and switch  $S_5$  is turned ON. Diode  $D_2$  is reversely biased. The equivalent circuit of the proposed converter in this state is shown in Fig 5.8(d). In this mode, inductor L is discharged, and its stored energy is delivered to  $C_1$  and  $R_1$ , resulting in a decrease in inductor current.

Capacitor  $C_1$  is charged, while capacitor  $C_2$  is discharged, delivering stored energy to load resistance  $R_2$ . Expressions governing the energy storage elements  $(L, C_1 \ and \ C_2)$  during this mode are shown as follows:

$$L\frac{d_{i_L}}{dt} = v_1 - i_L(r_{ds5} + r_L) - v_{o1}$$
 (5.26)

$$C_1 \frac{dv_{o1}}{dt} = i_L - \frac{v_{o1}}{(R_1 + r_{c1})}$$
 (5.27)

$$C_2 \frac{dv_{o2}}{dt} = -\frac{v_{o2}}{(R_2 + r_{c2})} \tag{5.28}$$

During State 5 ( $D_5T < t < T$ ), all switches are OFF, causing diode  $D_2$  to be forward biased. The equivalent circuit of the proposed converter in this state is shown in Fig 5.8(e). In this mode, inductor L is discharged, and its stored energy is delivered to capacitors  $C_1$ ,  $C_2$ , and load resistances  $R_1$  and  $R_2$ . Capacitors  $C_1$  and  $C_2$  are charged during this mode. Inductor current and capacitor voltages during this mode are as follows:

$$L\frac{d_{i_L}}{dt} = v_1 - i_L r_L - (v_{o1} + v_{o2})$$
 (5.29)

$$C_1 \frac{dv_{o1}}{dt} = i_L - \frac{v_{o1}}{(R_1 + r_{c1})} \tag{5.30}$$

$$C_2 \frac{dv_{o2}}{dt} = i_L - \frac{v_{o2}}{(R_2 + r_{C2})}$$
 (5.31)

# 5.5. AVERAGED AND DYNAMIC ANALYSIS OF MPBC WITH CONTROLLER DESIGN

Switches  $S_1$ ,  $S_2$ ,  $S_3$ ,  $S_4$ , and  $S_5$  are used to operate the proposed MPBC, as mentioned in the previous section. Each switch performs a specific function. By carefully controlling the switches' duty cycle, the output voltages; charging and discharging current of batteries can be adjusted. Dynamic model needs to be obtained to construct the converter's closed-loop controller while steady-state performance may be analyzed for stress and performance parameter computation.

Present chapter focuses on discharging mode of operation, and thus small signal model is developed. Averaging of the state matrices of proposed MPBC having five switching configuration is shown in Fig. 5.6 and can be represented as:

$$L\frac{di_L}{dt} = (v_3 - i_L(r_{ds3} + r_{ds1} + r_L))d_3 + (v_2 - i_L(r_{ds4} + r_{ds1} + r_L))(d_4 - d_3) + (v_1 - i_L(r_{ds1} + r_L))(d_1 - d_4) + (v_1 - i_L(r_{ds5} + r_L) - v_{o1})(d_5 - d_1) + v_{o2}d_5 + (v_1 - i_Lr_L - (v_{o1} + v_{o2}))(1 - d_5)$$
(5.32)

$$C_{1} \frac{dv_{o1}}{dt} = -\frac{v_{o1}}{(R_{1}+r_{C1})} \cdot d_{3} - \frac{v_{o1}}{(R_{1}+r_{C1})} \cdot (d_{4}-d_{3}) - \frac{v_{o1}}{(R_{1}+r_{C1})} \cdot (d_{1}-d_{4}) + \left(i_{L} - \frac{v_{o1}}{(R_{1}+r_{C1})}\right) (d_{5}-d_{1}) + \left(i_{L} - \frac{v_{o1}}{(R_{1}+r_{C1})}\right) (1-d_{5})$$
(5.33)

$$C_{2} \frac{dv_{o2}}{dt} = -\frac{v_{o2}}{(R_{2}+r_{c2})} \cdot d_{3} - \frac{v_{o2}}{(R_{2}+r_{c2})} \cdot (d_{4}-d_{3}) - \frac{v_{o2}}{(R_{2}+r_{c2})} \cdot (d_{1}-d_{4}) - \frac{v_{o2}}{(R_{2}+r_{c2})} (d_{5}-d_{1}) + \left(i_{L} - \frac{v_{o2}}{(R_{2}+r_{c2})}\right) (1-d_{5})$$

$$(5.34)$$

Small perturbation around the equilibrium point is considered and represented as follows:

$$i_{L} = I_{L} + \hat{\imath}_{L}, v_{1} = V_{1} + \hat{\nu}_{1}, v_{2} = V_{2} + \hat{\nu}_{2}$$

$$v_{3} = V_{3} + \hat{\nu}_{3}, v_{o1} = V_{o1} + \hat{\nu}_{o1}, v_{o2} = V_{o2} + \hat{\nu}_{o2}$$

$$d_{1} = D_{1} + \hat{d}_{1}, d_{2} = D_{2} + \hat{d}_{2}, d_{3} = D_{3} + \hat{d}_{3}$$

$$d_{4} = D_{4} + \hat{d}_{4}, d_{5} = D_{5} + \hat{d}_{5}, d_{5} = D_{5} + \hat{d}_{5}$$

$$(5.35)$$

where  $I_L$ ,  $V_1$ ,  $V_2$ ,  $V_3$ ,  $V_{o1}$ ,  $V_{o2}$ ,  $D_1$ ,  $D_3$ ,  $D_4$  and  $D_5$  are the steady states variables;  $\hat{\iota}_L$ ,  $\hat{v}_1$ ,  $\hat{v}_2$ ,  $\hat{v}_3$ ,  $\hat{v}_{o1}$ ,  $\hat{v}_{o2}$ ,  $\hat{d}_1$ ,  $\hat{d}_3$ ,  $\hat{d}_4$  and  $\hat{d}_5$  are the perturbation in respective steady state variables. After substituting equation (5.35) into (5.32)-(5.34) and neglecting second order terms, the small signal model is written as follows:

$$L\frac{d\hat{\imath}_{L}}{dt} = (V_{o1} - I_{L}(r_{ds1} + r_{L}) + I_{L}(r_{ds5} + r_{L}))\hat{d}_{1} + (V_{3} - V_{2} - I_{L}(r_{ds3} + r_{ds1} + r_{L}) + I_{L}(r_{ds4} + r_{ds1} + r_{L}))\hat{d}_{3} + (V_{2} - V_{1} - I_{L}(r_{ds4} + r_{ds1} + r_{L}) + I_{L}(r_{ds1} + r_{L}))\hat{d}_{4} + (V_{o2} - I_{L}(r_{ds5} + r_{L}) + I_{L}r_{L})\hat{d}_{5} + D_{3}\hat{v}_{3} + (D_{4} - D_{3})\hat{v}_{2} + (1 - D_{4})\hat{v}_{1} + (D_{1} - 1)\hat{v}_{01} + (D_{5} - 1)\hat{v}_{02} + (D_{1}(r_{ds5} - r_{ds1}) + D_{3}(r_{ds4} - r_{ds3}) - D_{4}r_{ds4} - D_{5}r_{ds5} - r_{L})\hat{\imath}_{L}$$

$$(5.36)$$

$$C_1 \frac{d\hat{v}_{o1}}{dt} = (1 - D_1)\hat{i}_L - I_L \hat{d}_1 - \frac{\hat{v}_{o1}}{(R_1 + r_{c1})}$$
 (5.37)

$$C_2 \frac{d\hat{v}_{o2}}{dt} = (1 - D_5)\hat{i}_L - I_L \hat{d}_5 - \frac{\hat{v}_{o2}}{(R_2 + r_{C2})}$$
 (5.38)

State space model represented as:

$$\dot{X} = AX + BU 
Y = CX + DU$$
(5.39)

where matrix X contains state variables, U contains control variables and Y contains system outputs.

$$X = \begin{bmatrix} \hat{\imath}_{L} \\ \hat{v}_{o1} \\ \hat{v}_{o2} \end{bmatrix} Y = \begin{bmatrix} \hat{v}_{o1} \\ \hat{v}_{T} \\ \hat{\imath}_{b} \\ \hat{\imath}_{v2} \end{bmatrix} U = \begin{bmatrix} \hat{d}_{1} \\ \hat{d}_{3} \\ \hat{d}_{4} \\ \hat{d}_{5} \\ \hat{v}_{1} \\ \hat{v}_{2} \\ \hat{v}_{3} \end{bmatrix}$$
(4.40)

The A, B, C and D matrices using (5.36) -(5.38) and (5.40) are represented in (5.41), where  $V_1, V_2$  and  $V_3$  are input voltages and  $V_{o1}$  and  $V_{o2}$  are output voltages. All the parameter except duty cycle of switches  $D_1, D_3, D_4, D_5$  and steady state value of inductor current  $I_L$  are known and can be calculated from steady state values.

The transfer function matrix Q of the converter is obtained from small signal modelling as follows:

$$y = Qu$$
where  $Q = C(sI - A)^{-1}B + D$  (5.42)

Q is a  $4 \times 4$  matrix

$$\begin{bmatrix} q_{11} & q_{12} & q_{13} \\ q_{21} & q_{22} & q_{23} \\ q_{31} & q_{32} & q_{33} \\ q_{41} & q_{42} & q_{43} \end{bmatrix}$$
(5.43)

where y and u are system outputs and inputs vectors,

$$\frac{\hat{v}_{o1}(s)}{\hat{d}_{5}(s)} = q_{11}$$

$$\frac{\hat{v}_{T}(s)}{\hat{d}_{1}(s)} = q_{22}$$

$$\frac{\hat{v}_{b}(s)}{\hat{d}_{3}(s)} = q_{33}$$

$$\frac{\hat{v}_{v2}(s)}{\hat{d}_{4}(s)} = q_{44}$$
(5.44)

Where the corresponding open loop transfer function's pole zero values are descripted in Table 5.4. The four open loop transfer functions for equation (5.44) correspond to an output variable concerning their duty cycle. To assess their stability and formulate a controller design, performing frequency domain root locus and bode plot analysis using MATLAB is essential. The root locus plot of the proposed converter for  $q_{11}$ ,  $q_{22}$ ,  $q_{33}$ , and  $q_{44}$  with and without controller is shown in Fig 5.9(a)-(d) for  $R_1 = R_2 = 30\Omega$ . Denominator of the transfer functions  $q_{22}$  show that the imaginary poles of forward path transfer function of MPBC lies in left half of s-plane and it is shifted away from the imaginary axis with application of controller thus the stability of the system improves whereas as seen from numerator of the transfer function  $q_{11}$ , an extra zero appears in the left half of s-plane because of controller hence the stability of the system improves with respect to open loop transfer function as shown in Fig. 5.9(a).

Table 5.4. POLE-ZERO VALUE OF TRANSFER FUNCTION

T/F	Ope	n Loop	Close Loop			
	Zero	Pole	Zero	Pole		
$q_{11} = \frac{\widehat{v}_{o1}(s)}{\widehat{d}_5(s)}$	-66.67	$-33.33,$ $-16.665$ $\pm 156.020i$	-94.29, -66.67	$-48.9$ $\pm 21.1374i$ , $-236.7$ $\pm 222.200i$		
$q_{22} = \frac{\widehat{v}_T(s)}{\widehat{d}_1(s)}$	738.7, -33.33	$-33.33,$ $-16.665$ $\pm 156.020i$	-748.7	$-11.56$ , $-10 \pm 154.536i$		
$q_{33} = \frac{\hat{\iota}_b(s)}{\hat{d}_3(s)}$	−33.33, −121.95 ± 129.492 <i>i</i>	$-33.33,$ $-16.665$ $\pm 156.020i$	−294.7, −121.95 ± 129.49 <i>i</i>	−36.66, −30.56 ± 177.52 <i>i</i>		
$q_{44} = \frac{\hat{\iota}_{v2}(s)}{\hat{d}_4(s)}$	-33.33, -35.135 ± 156.8933 <i>i</i>	$-33.33,$ $-16.665$ $\pm 156.020i$	$-35.135 \pm 156.8933i$	−208, −28.98 ± 167.54 <i>i</i>		

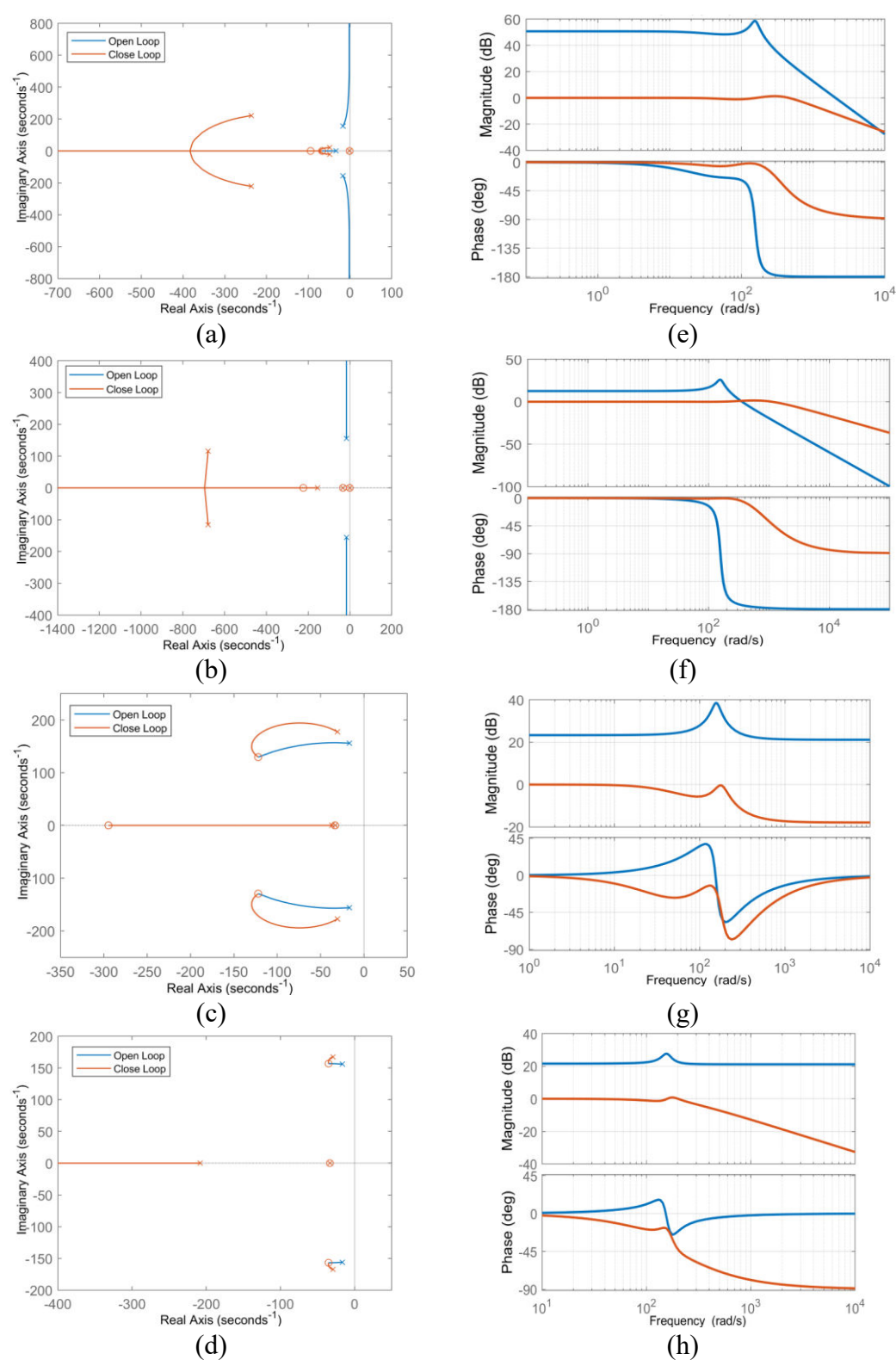


Figure 5.9. Root locus for (a)  $q_{11}$ , (b)  $q_{22}$ , (c)  $q_{33}$ , (d)  $q_{44}$  for open and close loop transfer function of proposed MPBC and bode plot for (e)  $q_{11}$ , (f)  $q_{22}$ , (g)  $q_{33}$ , (g)  $q_{44}$  with and without applying controller of proposed MPBC at.  $R_1 = R_2 = 30\Omega$ 

The objective is to achieve a controller that minimizes steady-state error, ensures an adequate phase margin, promotes high stability, and facilitates a broad bandwidth. Employing MATLAB, we have successfully obtained open-loop Bode diagrams for  $q_{11}$ ,  $q_{22}$ ,  $q_{33}$ , and  $q_{44}$ , considering the simulation parameters outlined in Table 5.2 and the resulting Bode diagrams are presented in Fig 5.9(e)-(h).

TABLE 5.5. STABILITY ANALYSIS OF THE MPBC CONVERTER

	OPEN	LOOP	CLOSE LOOP		
T/F	Gain Margin (dB)	Phase Margin (degree)	Gain Margin (dB)	Phase Margin (degree)	
$q_{11} = \frac{\widehat{v}_{o1}(s)}{\widehat{d}_5(s)}$	Inf	0.00591	Inf	135	
$q_{22} = \frac{\widehat{v}_T(s)}{\widehat{d}_1(s)}$	-50.7	-86.1	5.25	136	
$q_{33} = \frac{\hat{\iota}_b(s)}{\hat{d}_3(s)}$	Inf	Inf	Inf	Inf	
$q_{44} = \frac{\hat{\iota}_{v2}(s)}{\hat{d}_4(s)}$	Inf	Inf	Inf	137	

Upon examining the Bode plots, it is apparent that both phase margin in  $q_{11}$  and both gain and phase margin in  $q_{22}$  fall short, which can be seen from Table 5.5, indicating system instability. To rectify this, an improved PID controller needs to be devised to enhance system stability based on (5.45).

$$K(s) = K_p + K_i \left(\frac{1}{s}\right) + K_d s \tag{5.45}$$

Controlled closed loop transfer function for (5.44) using (5.45) is represented in Table 5.4. Considering the closed loop response, bode diagrams are shown in Fig 5.9. Upon analyzing the controller stability on the proposed converter system, it is found that for  $q_{22}$  closed loop gains margin is 5.25 dB, and the phase margin is  $136^{\circ}$ , which is under the stable region for  $K_P = 0.0128$ ,  $K_I = 3.78$  and  $K_D = 0$  which are determined using Modified Genetic Algorithm (MGA) [32]-[34].

#### 5.6. VERIFICATION AND RESULTS

The proposed MPBC's reliability is analyzed by implementing simulation in MATLAB/Simulink and then verified using experimental findings. Table IV explains all the parameters associated with the proposed MPBC. As previously discussed, switches  $S_1$ ,  $S_3$ ,  $S_4$ , and  $S_5$  actively participate in the discharging operation of the

converter. The converter is integrated with the inverter for powering single-phase ac loads which is an addition achievement, and it also has charging capability when load demand is less. This chapter focuses on the stress analysis and performance of the MPBC considering the parasitics whose simulation results are explained in the subsequent subsections, and verified with the experimental work. Following the stability analysis conducted in section 5.5, the simulation and experimental results are assessed, considering a 30% ripple current and a 2-3% ripple voltage.

#### 5.6.1. Profile Analysis of Prototype Converter

The analysis of a prototype converter encompasses assessing and scrutinizing its characteristics, performance, and behavior, including input voltage and current from sources, inductor behavior, and the profile of output voltage. Fig 5.10 shows the proposed converter's inductor current, voltage, and output voltages. The step behaviour of inductor voltage on the positive side shows the switching of different sources. As the input sources change, the inductor current rate also changes as mention in equations (5.2), (5.5), (5.8), (5.11) and (5.14) respectively while output voltages  $V_T$  and  $V_{O1}$  are stiff to 120V and 60V, respectively. Switching operation results in the discontinuity of source currents, as depicted in Fig 5.11. The switches are controlled based on the power demands of the loads. Specifically, switches  $S_3$  and  $S_4$  facilitate power flow among the three sources.

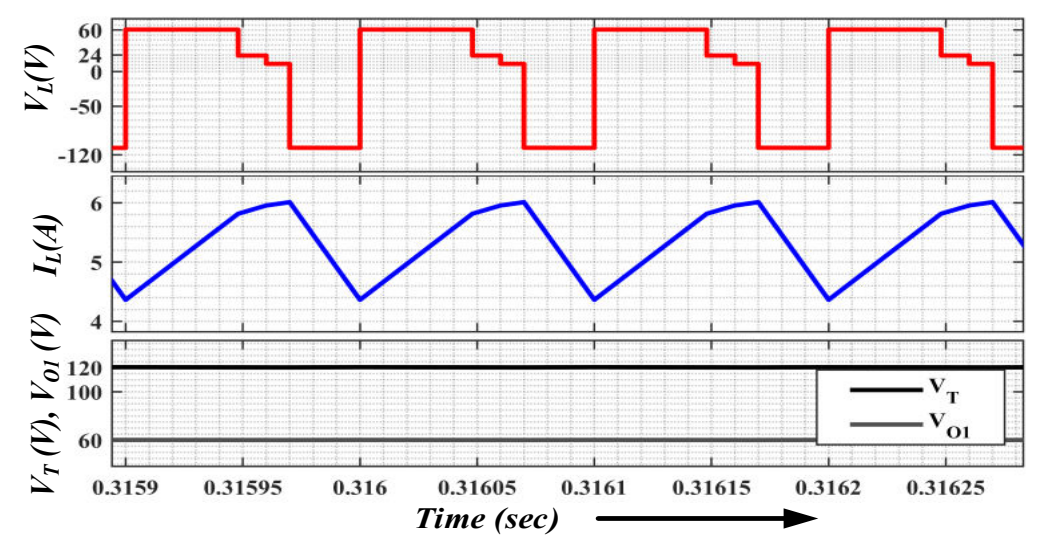


Figure 5.10. Inductor profile and output voltage waveform of MPBC at  $R_1 = R_2 = 30\Omega$ 

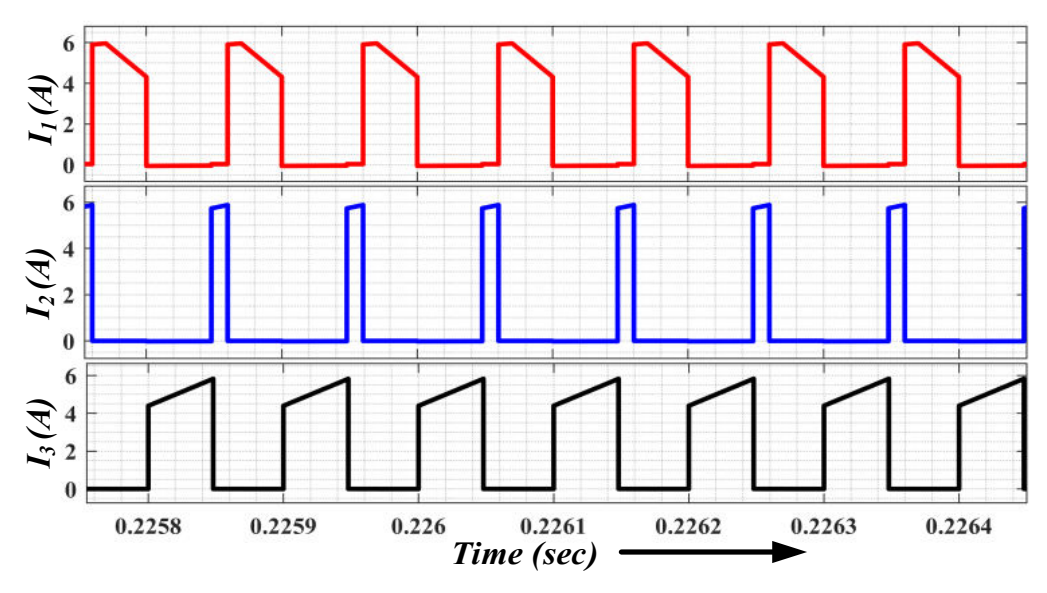


Figure 5.11: Input current waveform of MPBC at  $R_1 = R_2 = 30\Omega$ 

The converter is tested to check its stability and voltage regulation under various load conditions. These tests aim to see how well the converter handles changing AC and DC loads in Fig. 5.12, which is important for its reliable performance in real-world applications where loads can vary unpredictably.

To simulate real scenarios, both AC and DC loads are applied in different ways in Fig 5.12(a). At 0.3 seconds (point A), a DC load is added, testing how the converter deals with sudden load changes. The system quickly stabilizes within 0.003 seconds with a 0.8 V steady-state error, showing that the converter's controls effectively manage the sudden load without major fluctuations. This fast response is crucial for applications needing a constant power supply to avoid performance issues. At 0.7 seconds (point B), a single-phase AC motor is added. This tests the converter's ability to handle AC loads, which can be more challenging due to varying current and potential harmonics. The system stabilizes in 0.002 seconds with a 1.2V steady-state error. This small error indicates that while there's a slight deviation from the ideal output, the converter adjusts well to the AC load, maintaining performance effectively.

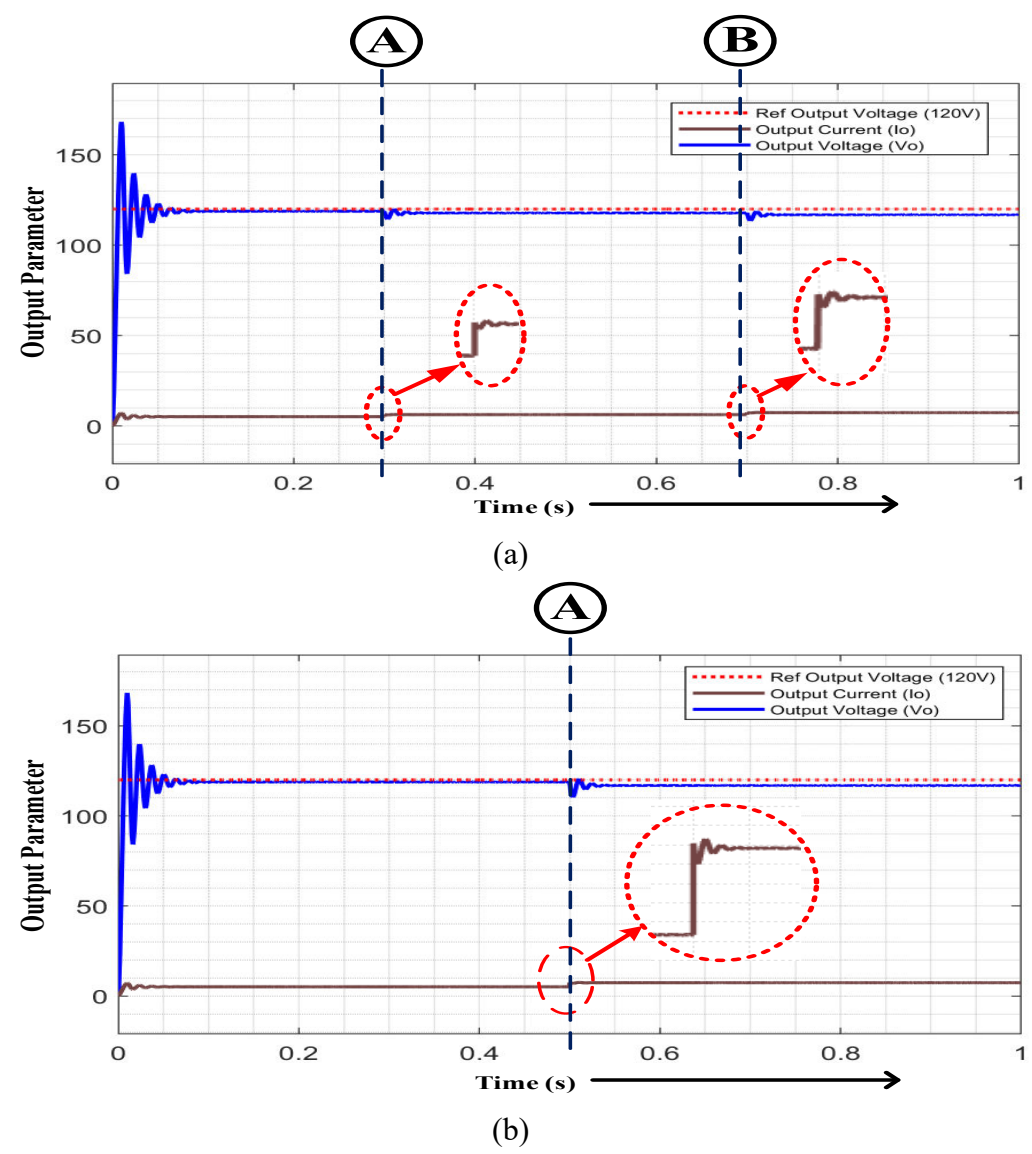


Figure 5.12. Load Variation (a) When DC load is connected at A and AC load at B, (b) when both DC and AC load connected at A.

In a more complex test at 0.5 seconds Fig 5.12(b), both AC and DC loads switch simultaneously. This tests the converter's ability to handle multiple load changes at once. The system stabilizes within 0.006 seconds and keeps a 1.3V steady-state error. This fast response and consistent error rate show the converter's robustness and flexibility, indicating it can handle environments with unpredictable load changes.

Overall, the converter's ability to quickly stabilize with minimal error after both individual and simultaneous load changes highlights its efficiency and reliability for delivering steady power in varying load conditions. Performance indices on load change for Fig 5.12 is tabulated in Table 5.6.

Table 5.6. PERFORMANCE INDICES ON LOAD CHANGE FOR FIGURE 5.12

		RISE TIME	PEAK OVERSHOOT	SETTLING TIME	STEADY STATE ERROR	
Fig	Point A	2ms	0.7%	3ms	0.8 V wrt 120V (ref)	
5.12(a)	Point B	1.5ms	0.9%	2ms	1.2 V wrt 120V (ref)	
Fig 5.12(b)	Point A	4.3 <i>ms</i>	1.2%	6ms	1.3 V wrt 120V (ref)	

#### 5.6.2. Voltage and Current Stress on Switching Devices

Switching devices play a crucial role in controlling the flow of electrical energy. However, their operation involves significant changes in voltage and current characteristics, leading to stresses that can affect device performance and reliability. To find the proper rating of semiconductor's safe operation and improve the system's reliability determination of voltage and current stress is very helpful.

TABLE 5.7. THE VOLTAGE STRESS ON DIODES AND POWER SWITCHES.

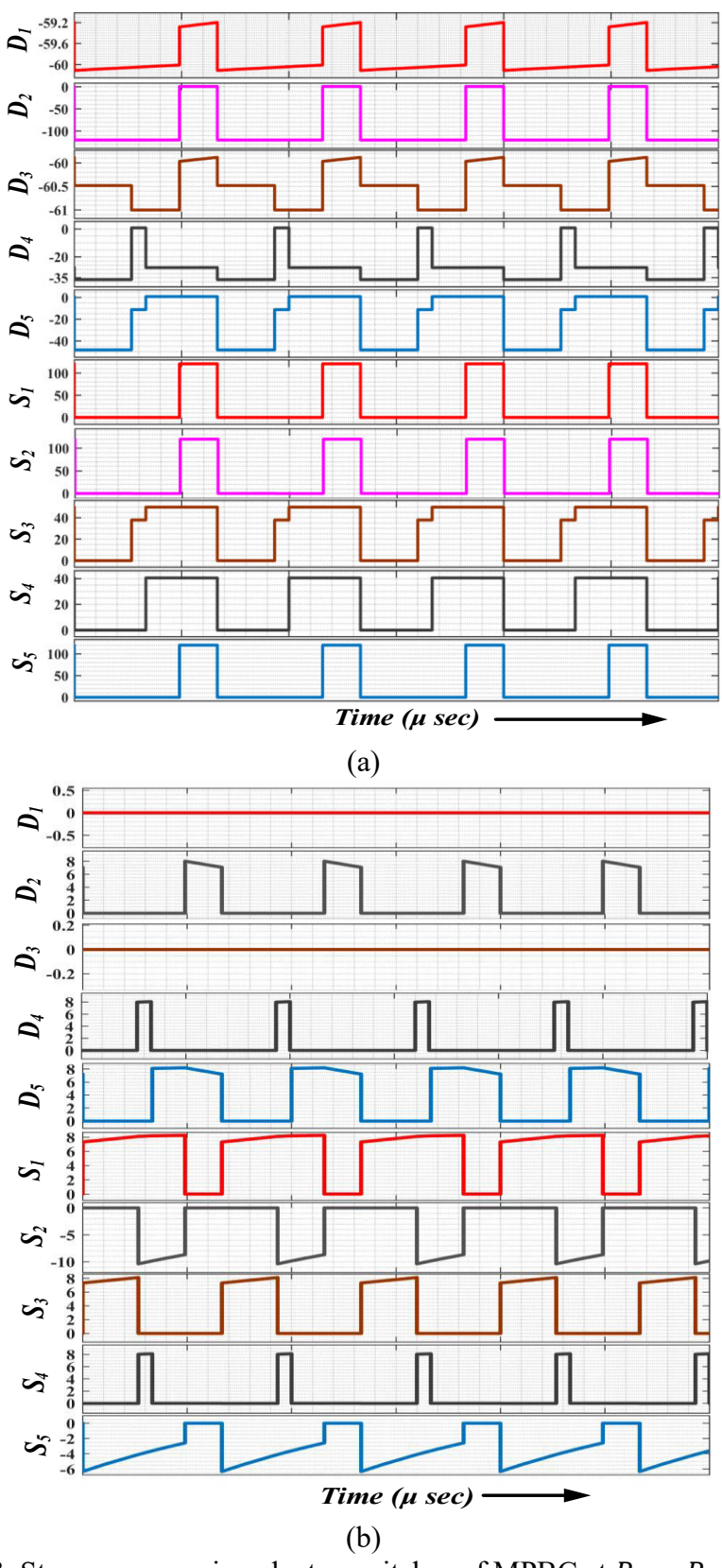
States	SS-1	SS-2	SS-3	SS-4	SS-5
$V_{D1}$	$-V_{O1}$	$-V_{O1}$	$-V_{O1}$	$-V_{O1} + V_d$	$-V_{O1}$
$V_{D2}$	$-V_T$	$-V_T$	$-V_T$	$-V_T$	$-V_T$
$V_{D3}$	$-V_3$	$-V_3$	$-V_3$	$-V_3$	$-V_3$
$V_{D4}$	$-V_3 + V_2$	$V_d$	$-V_2$	$-V_2$	$-V_2$
$V_{D5}$	$-V_3 + V_1$	$-V_2 + V_1$	$V_d$	$V_d$	$V_d$
$V_{S1}$	0	0	0	$V_T$	$V_T$
$V_{S2}$	0	0	0	$V_T$	$V_T$
$V_{S3}$	0	$V_3 - V_2$	$V_3 - V_1$	$V_3 - V_1$	$V_3 - V_1$
$V_{S4}$	0	0	$V_3 - V_1$	$V_T - V_3$	$V_T - V_3$
$V_{S5}$	0	0	0	$V_T$	$V_T$

Where SS-Switching States

TABLE 5.8. THE CURRENT STRESS ON DIODES AND POWER SWITCHES.							
States	SS-1	SS-2	SS-3	SS-4	SS-5		
$I_{D1}$	0	0	0	0	0		
$I_{D2}$	0	0	0	0	$I_L - (I_{C2} + I_O)$		
$I_{D3}$	0	0	0	0	0		
$I_{D4}$	0	$I_L$	0	0	0		
$I_{D5}$	0	0	$I_L$	$I_L$	$I_L$		
$I_{S1}$	$I_L$	$I_L$	$I_L$	0	0		
$I_{S2}$	0	0	0	0	0		
$I_{S3}$	$I_L$	0	0	0	0		
$I_{S4}$	0	$I_L$	0	0	0		
$I_{S5}$	0	0	0	0	0		
Whom SS Switching States							

Where SS-Switching States

Voltage across the switches in each switching state in discharging mode of operation is shown in Table 5.7 and average current through them is shown in Table 5.8.



(b) Figure 5.13. Stresses on semiconductor switches of MPBC at  $R_1 = R_2 = 30\Omega$ : (a) Voltage Stress on each diode and switches, (b)Current Stress on each diode and switches.

Voltage stress on all the diodes  $D_1$ ,  $D_2$ ,  $D_3$ ,  $D_4$ , and  $D_5$  and switches  $S_1$ ,  $S_2$ ,  $S_3$ ,  $S_4$ , and  $S_5$  are shown in Fig 5.13(a). It has lower stress considering the topology 2 [125] as sources are connected directly to inductor via switches. So, the proposed converter is better as compared to topology 2 in terms of switch stresses. Current stresses on each individual switches is shown in Fig 5.13(b). The impact on  $S_3$  is notably diminished in the proposed MPBC, a validation confirmed in the following section through experiments. Reduced voltage stress on switches leads to minimized switching losses.

#### 5.6.3. Experimental Results

A 240W converter is designed in the laboratory to analyze the prototype's effectiveness. Different profiles of the converter are experimented for developed prototype and shown in Fig 5.14. The improved switching strategies are implemented using the TMS320F28379D DSP. Table 5.9 presents the hardware specification of the developed prototype.

Table 5.9. EXPERIMENTAL SETUP SPECIFICATIONS OF MPBC

Components	Part Number	Specification(s)		
MOSFET	SPW20N60C3	650V, 20.7A		
Diode	STTH3012	1200 V, 30 A		
Voltage Sensor	LV - 25P	500 V		
Current Sensor	LA - 55P	50 A		
DSP	TMS320F28379D	200 MHz, Dual Core, 32 bit		
Optocoupler	TLP350	For isolation		
Voltage Regulator	IC7815 and IC7915	15 V and − 15 V		
Rheostat	$R_1$	$0-500\Omega$ ,		
Kneostat	$R_2$	0-500arOmega		
Inductor	EE65/32/27 Ferrite Core	2mH		
Consoitors	$C_1$	$1000\mu F~(150V)$ ,		
Capacitors	$C_2$	$1000\mu F (150V)$		

In the experimental setup, the DC power supply is configured to maintain constant voltage levels of 12V and 24V, representing fuel cell (FC) and photovoltaic sources, respectively. Experimental setup is evaluated under two distinct operation modes of the converter. Detailed descriptions of the experimental results for battery discharging are provided in this section. The prototype system integrates several input sources: a dual-channel DC power supply delivering 12V and 24V, and a 60-volt battery composed of five series-connected 12-volt, 7 Ah lead-acid batteries.



Figure 5.14. Laboratory setup for converter's prototype: (A) Proposed MIMO converter, (B) Input power supply for sources and ESE, (C) Controller and sensor power circuit, (D) DC Resistive Load, (E) Probes for measurements, (F) Digital Storage Oscilloscope and (G) Motor Setup (H) Inverter Configuration (I) Computer setup (J) TMS320F28379D DSP.

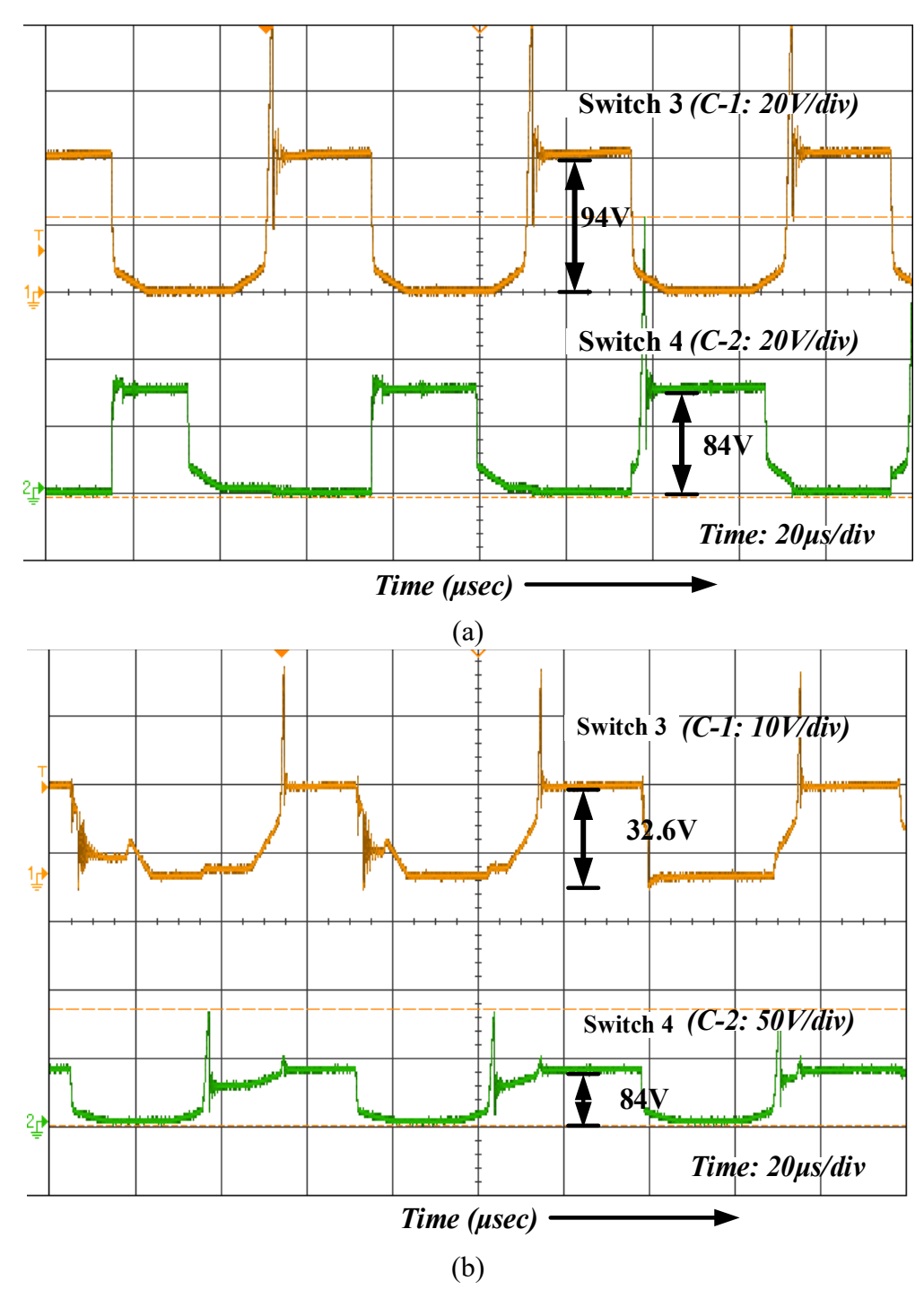


Figure 5.15. (a) Topology 2 switching stress on S3 and S4, (b) Proposed Converter switching stress on S3 and S4 at  $R_1 = R_2 = 30\Omega$ 

The single inductor L is connected such that it stores energies of all the sources within their time interval in the proposed converter. During the experiments, specific values are defined for the battery current and output voltages. Battery current is denoted as  $I_b = 1.9A$ , while the output voltages are specified as  $V_{O1} = 60V$  and  $V_{O2} = 60V$ 

respectively. The resistances  $R_1$  and  $R_2$  are approximately equal to 30  $\Omega$ . Stress Comparison for topology 2 and proposed converter which is discussed in section 5.4 is verified from experimental waveform in Fig. 5.15 where voltage stress on Switch  $S_3$  is higher in topology 2 (94V) due to cascading of switches. The peak-to-peak stress on switch  $S_3$  of proposed converter is 32.6V which is 65.31% less than earlier topology.

Experimental results of discharging mode are shown in Fig 5.16 to Fig 5.20. The  $V_T = 120V$  is achieved with the duty ratio of switch 1 (S<sub>1</sub>), which is approximately the same as that of the results obtained in the simulation. In battery discharging mode,  $P_{in1} \cong 22W$ ,  $P_{in2} \cong 60W$ ,  $P_b \cong 180W$ ,  $P_{O1} \cong 130W$  and  $P_{O2} \cong 110W$  with an efficiency of  $\eta = 91.6\%$ .

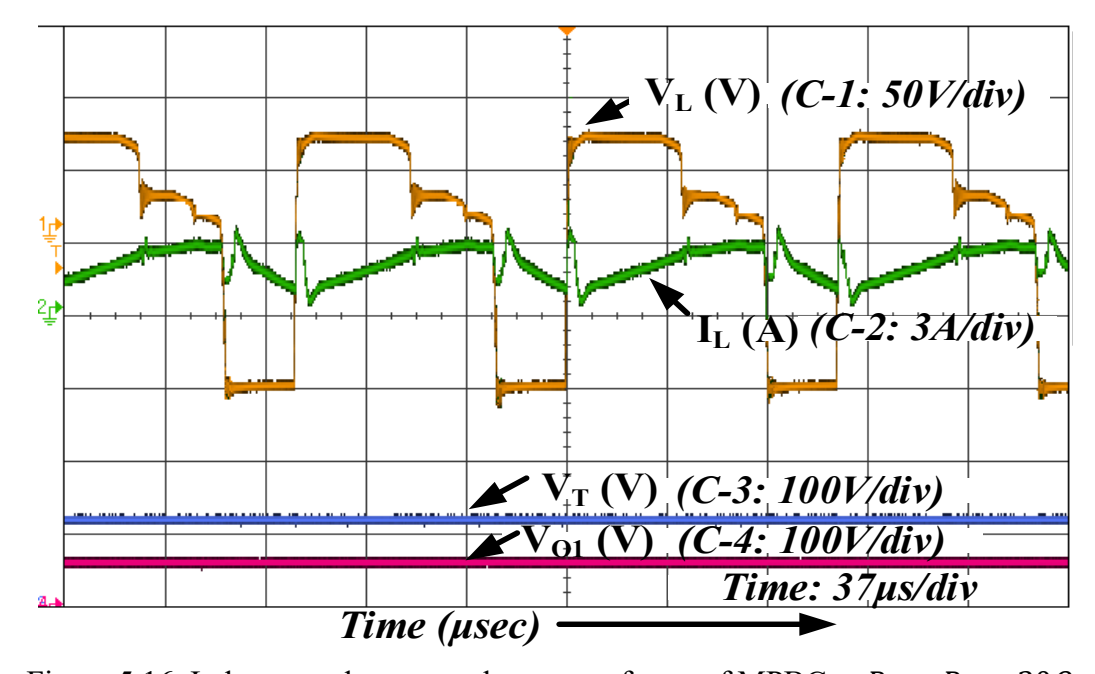


Figure 5.16. Inductor and output voltage waveforms of MPBC at  $R_1 = R_2 = 30\Omega$ . Fig 5.16 depicts the converter's output waveforms during steady-state conditions, showcasing the inductor voltage, inductor current, the combined output voltage  $V_T = V_{O1} + V_{O2}$ , and output voltage  $V_{O1}$ . The stepped behaviour of inductor voltage on the positive side is due to the interaction of different sources and ESE to the inductor while switching. Inductor voltage peaks at 62 V due to discharging behaviour of ESE. In Fig 5.17, different stresses on semiconductors are illustrated to assess the switch's reliability which is within a significant range.  $S_1$  and  $D_2$  are subjected to a maximum

voltage stress of -120V each. Fig 5.18 displays current sharing among different sources, including ESE, revealing that the load power is distributed based on their duty ratio. Additionally, the waveforms allow observation of the impact of parasitics. Fig 5.18 also shows the drawn current from input sources  $V_1$ ,  $V_2$ , and ESE,  $V_3$ .

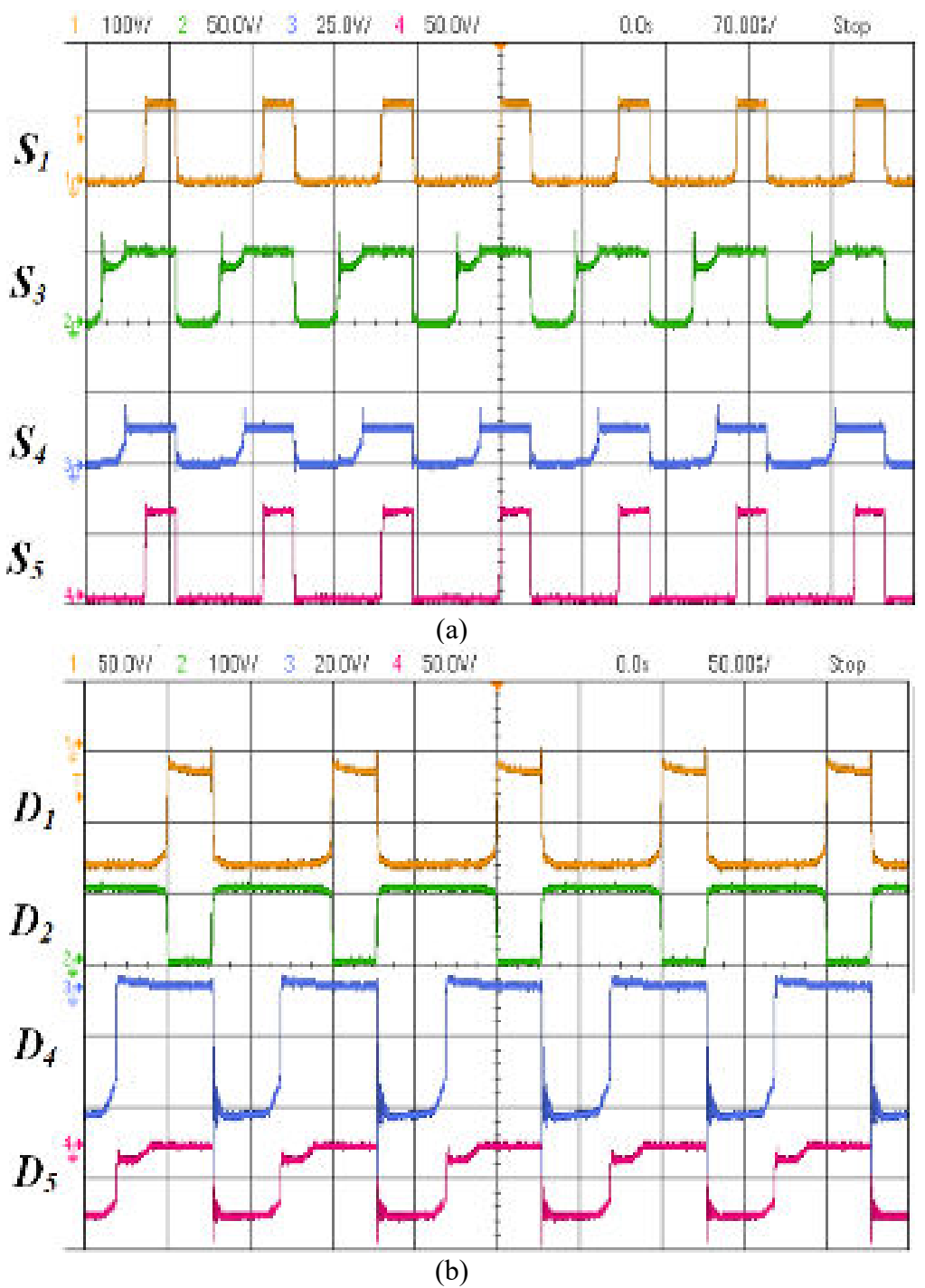


Figure 5.17. Stresses on semiconductor devices of MPBC at  $R_1 = R_2 = 30\Omega$ : (a) Voltage stress on switches. (b) The voltage stress on diodes.

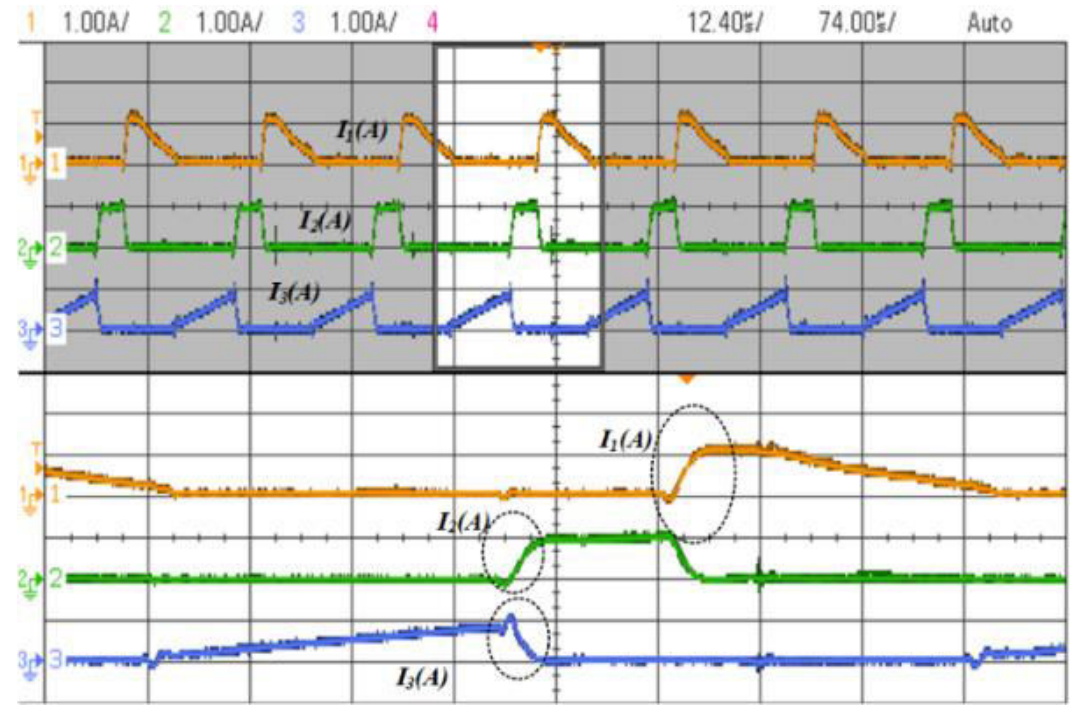


Figure 5.18. Input currents conduction of all sources  $(V_1, V_2 and V_3)$  during discharging modes.

Unidirectional port and ESE source currents achieve maximum values of 1.5A, 1.3A and 1.9A, respectively, with an average output current of approximately 1.8 A. Regulation of battery current allows proper distribution of loads power between input sources. The three sources combine to charge the inductor for energy storage. The behaviour of terminal voltage  $V_T$  is observed on varying load to twice the rated condition using a  $500\Omega$  rheostat which is illustrated in Fig 5.19(a). A slight dip is observed at twice the rated condition, but the converter is still stable under open loop condition. After the controller is applied to the converter, the output terminal voltage remains stable and fixed at 120V on load variation which can be seen from Fig. 5.19(b) with a steady state error of less than 5%.

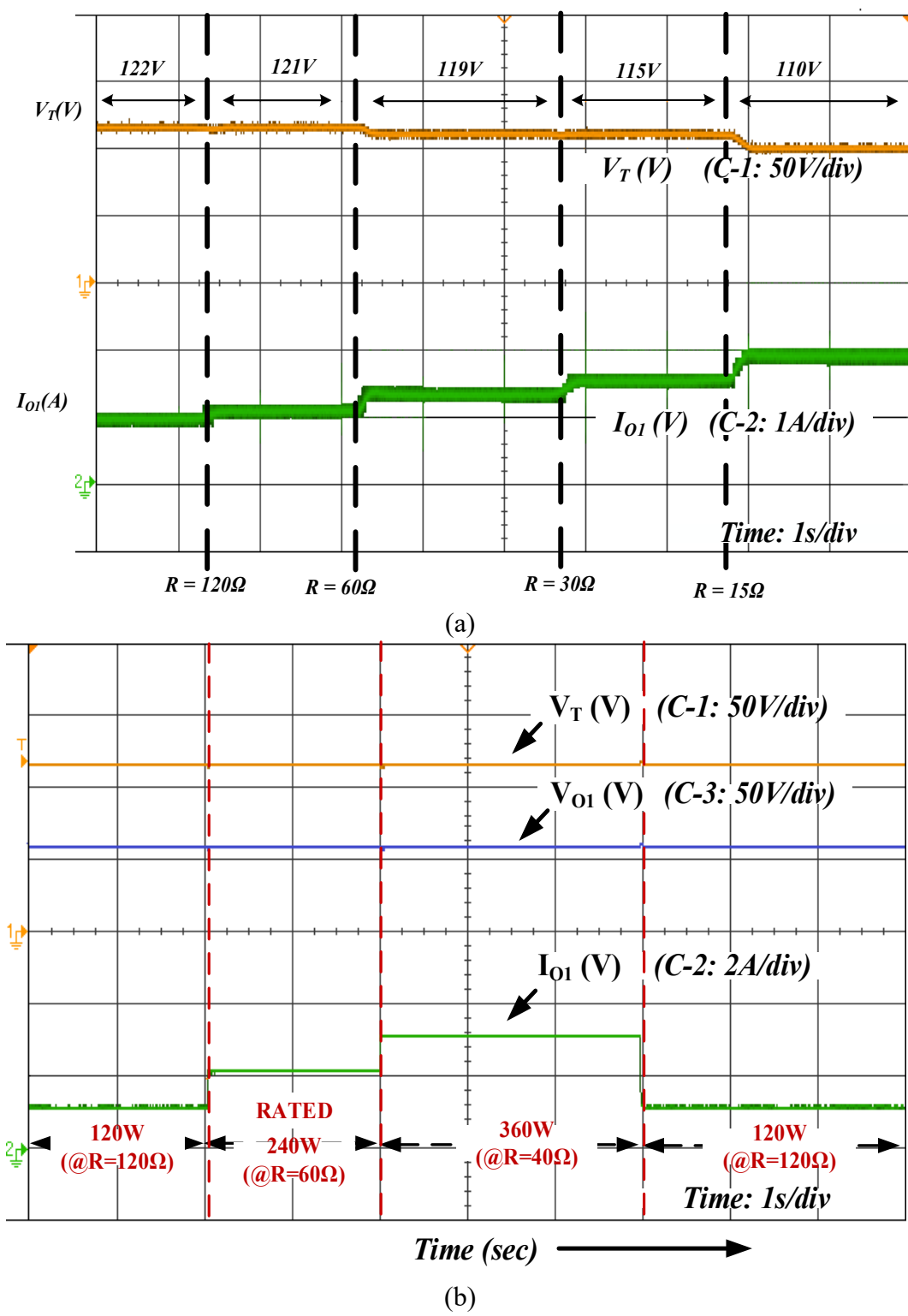


Figure 5.19. Effect of DC load variation on terminal voltage during discharging mode (a) under open loop and (b) under closed loop operation.

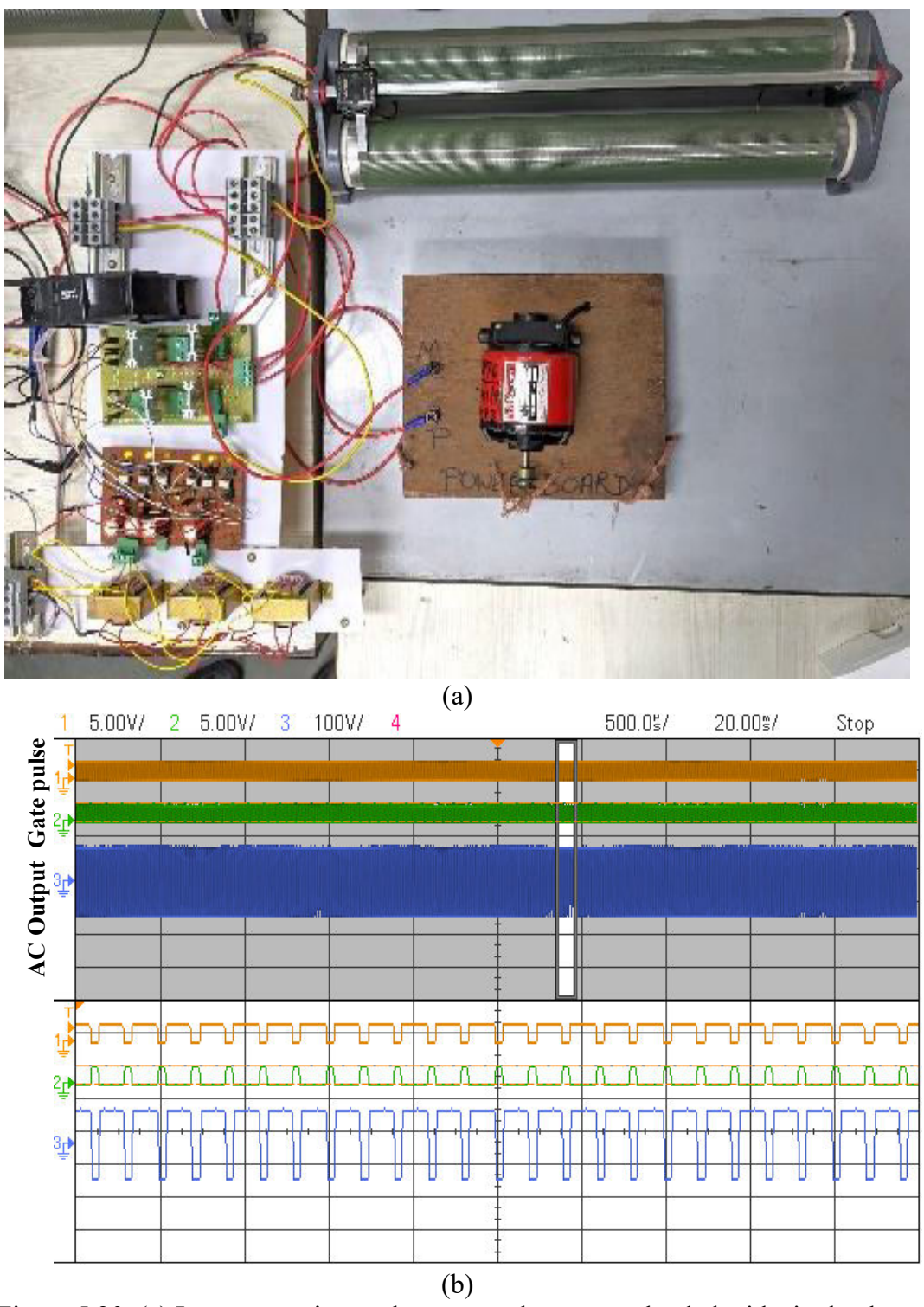


Figure 5.20. (a) Inverter section to the proposed converter loaded with single phase motor, (b) PWM inverter switching and output AC voltage waveform.

The experimental setup for the proposed MPBC is linked to both a DC load and an AC load. Figure 5.20(a) shows the section containing the inverter connected to the MPBC, which, in turn, is linked to a single-phase motor acting as a load. PWM (Pulse Width

Modulation) switching is executed to ensure a correct AC output for the load. In Fig 5.20(b), a peak-to-peak voltage of 220V is observed along with the gating pulse to the inverter. The PWM is created through the TMS320F28379D DSP controller, operating at a carrier frequency of 5kHz and a fundamental frequency of 50Hz. Experimental data is obtained for best combination of duty cycle to obtain maximum efficiency which is plotted in Fig 5.21(a). Duty cycle with  $D_1 = 60$ ,  $D_3 = 40$ ,  $D_4 = 50$ ,  $D_5 = 60$  shows maximum efficiency of 90.1% at rated condition of 240W. Fig 5.21(b) shows efficiency plot for the closed loop-controlled output of the proposed MPBC showing various loading conditions, peaking at 91.6% efficiency at 240W.

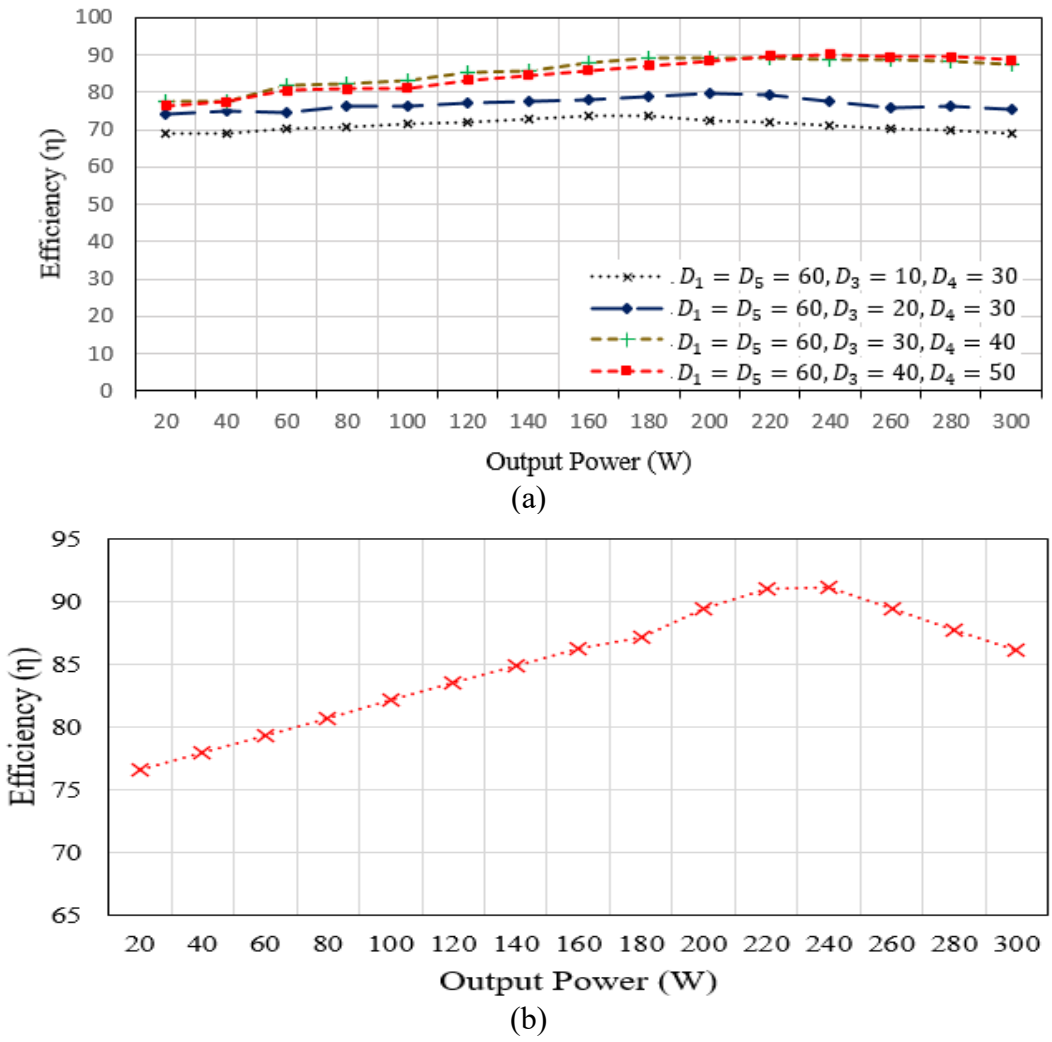


Figure 5.21. (a) Efficiency plot for different duty cycle combination of proposed MPBC at different loading conditions, and (b) efficiency plot for the controlled output of the proposed MPBC showing various loading conditions.

#### 5.7. CONCLUSIONS

This chapter presents a novel multi-input multi-output DC-DC boost converter (MPBC) with three inputs and two outputs. Evaluation and comparison against established topologies show the MPBC's efficiency, having multiple input ports, a rechargeable port for energy storage, and balanced shared output ports. The converter features a unified structure with a single inductor that integrates multiple power sources in renewable energy systems. The proposed converter is a versatile solution for hybridizing power sources, where fuel cells (FC), photovoltaic (PV), and battery are considered power sources and ESE, respectively and enables efficient energy transfer between them. It operates in two main modes: battery discharging mode, where both input sources deliver power to the output, and battery charging mode, where the input sources not only supply loads but also deliver power to the battery. The converter output offers varied DC voltage levels, execution them for connection to multilevel inverters. These different voltage levels can be employed to power AC motors through integrated inverters and provide auxiliary DC power as needed. To validate the operation of the proposed converter, experimental verification has been conducted using a low-power range prototype. Significant contributions of this chapter include thorough steady-state and small signal modeling of the MPBC, considering ESRs for stability, stress analysis (voltage and current), and performance evaluation. A fabricated 240W MPBC, coupled with improved switching strategies utilizing DSP TMS320F28379D, highlights the efficiency through comparative experimental and simulation results. The MPBC's design effectively regulates output power by efficiently distributing input power from ESE and RES, thereby reducing voltage stress on switches. The converter's capabilities were experimentally verified, and its potential applications include hybrid power systems, grid-connected PV systems, and reducing torque ripple in induction motors through multilevel inverters.

#### **CHAPTER 6**

### COMPARATIVE ANALYSIS AND SELECTION OF MULTIPORT Z-SOURCE CONVERTER TOPOLOGIES FOR RESs

#### 6.1. OVERVIEW

This chapter introduces a novel family of 128 non-isolated dual-output high-gain Z-source converters (DOHGZSC), with or without a common ground, to address the identified gaps in the existing literature.

- 1. Number of input and output ports can be arbitrarily increased without much modification to the existing HGMPC, by introducing only the respective input ports' active switch.
- 2. Independent power flow can be carried out arbitrarily from either of the output sources to the loads.
- 3. Having higher voltage gains than the counterpart non-isolated MIMOs in literature, which is an attractive feature for application in RES and distribution systems.
- 4. Inductor time multiplexing is used to achieve simultaneous power transfer from more than one output port of different voltage levels, keeping the part count fixed for any number of outputs.
- 5. A SISO controller, such as the standard double loop PI controller, is sufficient to control the output voltages despite the multiple ports of the converters.

#### 6.2. INTRODUCTION

There is a growing demand for converters with multiple ports and various voltage levels to accommodate to diverse applications in these sectors. [131]-[132]. To achieve voltage regulation and power control across different ports, multiple independent single-input single-output (SISO) converters can be utilized. However, this approach results in a high number of components, leading to increased overall cost and system volume [133]-[134]. To tackle this issue, a family of multi-input multi-output (MIMO) DC-DC converters has been introduced.

The primary advantages of such converters include the fewer conversion stages, increased system efficiency, higher power density, size, cost, and centralized power management across multiple ports compared to using multiple single-input DC-DC converters in renewable energy systems. Various multiport DC-DC converters have been developed encompassing both isolated and non-isolated topologies. Isolated topologies [135]-[138] and non-isolated topologies [139]-[142] represent two main subdivisions within these multiport converter designs. A single inductor MIMO boost converter is proposed for electric vehicle (EV) application [143]. Despite having multiple outputs with varying voltage levels, the converter's gain is low. In [144], a new multiport DC-DC converter is introduced for DC Microgrid applications. While the proposed configuration offers numerous advantages such as minimizing multiple power conversions, decreasing the number of components, and providing voltage boosting capability, it also presents drawbacks, including high switch count and controller complexity, coupled with low voltage gain.

To achieve a high voltage conversion ratio, traditional DC-DC converters operate with duty cycles below 0.1 for step-down and above 0.9 for step-up modes. However, such extreme duty cycle operation can compromise converter efficiency and transient performance [145][146]. To tackle this issue, a family of high-gain integrated multiport DC-DC converters has been introduced. High-gain multiple ports DC-DC converters (HGMPC) have gained significant attention for scenarios demanding multiple independent supply voltage levels. In a recent study, a novel collection of five nonisolated multiport DC-DC converter designs characterized by bipolar symmetric outputs with high gain. The feasibility of integrating these converters with a multilevel inverter to generate high-quality AC voltages is demonstrated [147]. A new nonisolated high step-up multiport DC-DC converter, integrated with PV modules and a Battery Storage System (BSS), is proposed for high-voltage DC bus-based hybrid renewable energy systems. It offers high voltage gain, low semiconductor stress, ZCS diodes, MPPT for PV inputs, and flexible port extension [148]. A double input high gain DC-DC boost topology with six switching states is introduced and subsequently expanded to an n-input version [149]. A high step-up DC-DC boost converter [150] with a single input and three outputs was introduced, featuring an expandable structure achieved by increasing the voltage multiplier modules, and capable of delivering high voltage gains at its output terminals without the need for higher duty cycles or the inclusion of transformers or coupled inductors in its design. A newly developed multiport DC-DC converter with high gain [151], designed to incorporate low-voltage energy storage devices into a DC microgrid, presents a three-port interface employing just a single two-winding transformer, thereby substantially simplifying control complexities. Studies [147]-[151] highlight the importance of high-gain converters in multiport configurations, emphasizing their benefits in terms of efficiency, size, cost, and control complexities.

In terms of achieving high voltage gain, impedance source or Z-source DC-DC converter shown in Fig 6.1 outperform conventional boost converters. Peng [22] first introduced the Z-source network concept, offering a solution to the issues of shootthrough and limited output voltage found in traditional voltage-source inverters, achieved by employing a configuration comprising two capacitors and two inductors interconnected in an X-shape. Numerous recent studies [153]-[157] have explored the Z-source converter and its various permutations, highlighting the advantages of this high-voltage-gain impedance source converter. An enhanced Z-source inverter, proposed in [153] and [154], mitigates capacitor voltage stress and inrush current, while a novel single-phase Z-source inverter, discussed in [155], enables shared ground between input and output. Additionally, the application of switched inductors to the Z-source network has been investigated [156]. In [157], a Z-source DC-DC converter with common ground and high voltage gain is introduced, while [158] presents a series of hybrid Z-source boost DC-DC converters tailored for PV power systems, and [159] proposes a novel structure based on ZSC DC-DC, suitable for deployment in renewable energy systems within DC or hybrid microgrids due to its high voltage gain. The proposed converter in [160], integrates a reformed Z-source converter and a switch capacitor, featuring four ports including a bidirectional port for battery charging/discharging, with innovative techniques applied to facilitate operation of the bidirectional port and accommodate the additional input source.

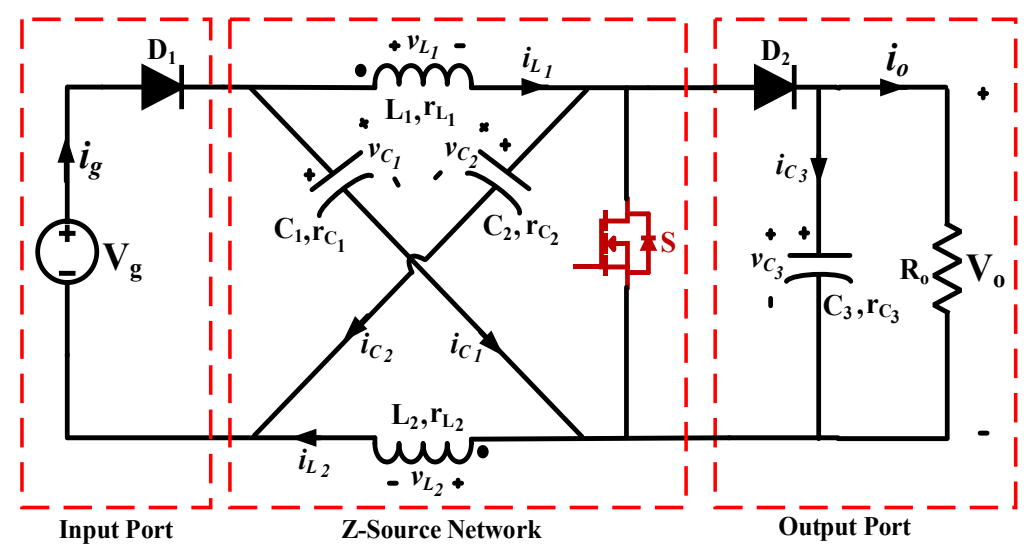


Figure 6.1. Conventional Z source DC-DC converter.

This chapter explores various research paths aimed at developing highly efficient converters capable of selecting the topology of common ground (CG) or non-common ground (NCG) dual-output high-gain Z-source converters (DOHGZSC) with enhanced operational characteristics. Additionally, there is a demand for converters capable of achieving high voltage conversion along with dual outputs (CG/NCG), which is crucial for Electric Vehicle (EV) and Isolated Microgrid (IMG) applications. Moreover, there is a need for converters configured to produce equal voltages at their outputs to facilitate their use in multilevel inverter applications.

#### 6.3. PRINCIPLE AND TOPOLOGY

Conventionally a Z-source network or impedance network is shown in Fig. 6.1, which is divided into three sections, i.e., input port (IP), Z-source network and output port (OP). It utilizes a distinctive impedance network, connecting the converter main circuit to the power source, load, or another converter, offering unique functionalities not found in traditional voltage and current source converters, which use capacitors and inductors, respectively, and employs a two-port network consisting of split-inductors ( $L_1$  and  $L_2$ ) and capacitors ( $C_1$  and  $C_2$ ) arranged in an X shape to create an impedance source (Z-source) coupling the converter to the DC source and load with a voltage gain B [153] expressed as

$$B = \frac{1}{1 - 2D} \tag{6.1}$$

where D represents the duty ratio of the converter.

Due to the converter's operation at low duty cycles and the correlation between power losses and duty cycle, its performance yields high efficiency. Additionally, the voltage stress on most of its components is minimal. As mentioned in the Introduction, in [157], a SISO Z-source converter is presented. The utilization of multi-input and multi-output configurations is crucial in various applications as it enables efficient management of load and power dynamics, necessitating the hybridization of different energy sources.

## 6.3.1. Topology Derivation of SIDO Z-source DC-DC Converters based on the Voltage-Type Ports

This chapter introduces a non-isolated multi-input multi-output DC-DC converter, with high voltage gain, as illustrated in Fig. 6.2. The converter interface n input power sources,  $V_{g1}, V_{g2}, V_{g3}, ..., V_{gn}$ , with increasing voltage levels. It comprises two inductors, two capacitors in a Z-source network, and n switches. The load resistances,  $R_1, R_2, R_3$ , and  $R_4$ , can represent different combinations of output ports, capable of providing varying or equal voltage levels suitable for EV charging connections. Table 6.1 outlines diverse dual-output impedance converter configurations, featuring both distinct and identical voltage levels, to be further examined in subsequent sections of the chapter. For ease, this chapter focuses on analyzing a family of proposed converters with a single-input and two outputs. In Fig. 6.3, taking  $V_g$  as the only source, various topologies for dual output high gain Z source NCG/CG DC-DC converter are analysed for selected module.

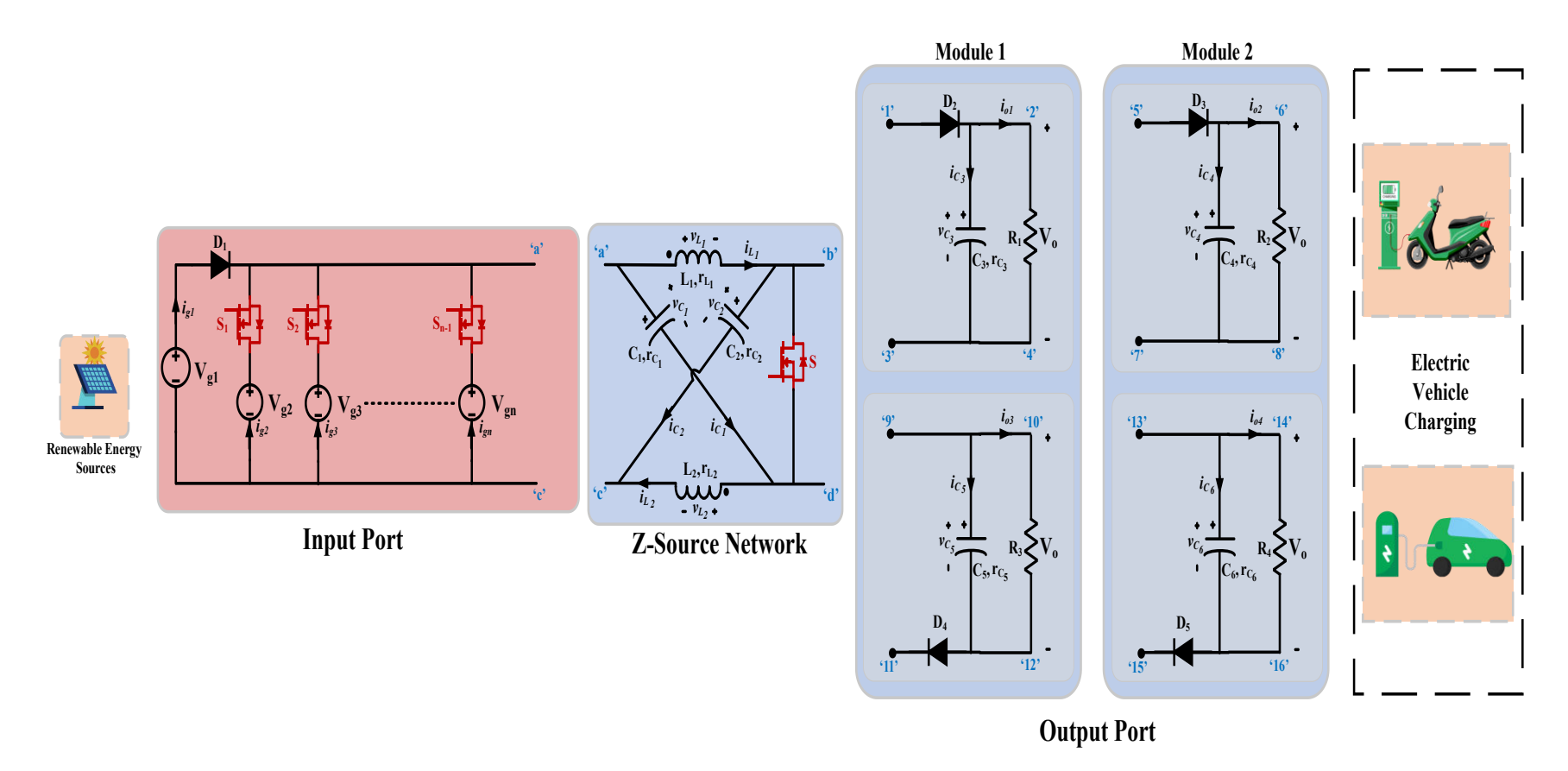


Figure 6.2. Family of non-isolated multi-input multi-output Z Source DC-DC converter.

Table 6.1. VARIOUS TOPOLOGIES FOR HIGH GAIN Z SOURCE NCG/CG DC-DC CONVERTER FOR DUAL OUTPUT CONFIGURATION AS PER FIGURE 6.2

O/P Port 1	1-b	1-a	1-b	1-a	9-b	9-а	9-b	9-а
O/P Port 2	3-d	3-d	3-c	3-c	11-d	11-d	11-c	11-c
5-2,7-4	$f_{a_{11}}$	$f_{a_{12}}$	$f_{a_{13}}$	$f_{a_{14}}$	$f_{b_{11}}$	$f_{b_{12}}$	$f_{b_{13}}$	$f_{b_{14}}$
5-b,7-4	$f_{a_{21}}$	$f_{a_{22}}$	$f_{a_{23}}$	$f_{a_{24}}$	$f_{b_{21}}$	$f_{b_{22}}$	$f_{b_{23}}$	$f_{b_{24}}$
5-a,7-4	$f_{a_{31}}$	$f_{a_{32}}$	$f_{a_{33}}$	$f_{a_{34}}$	$f_{b_{31}}$	$f_{b_{32}}$	$f_{b_{33}}$	$f_{b_{34}}$
5-2,7-c	$f_{a_{41}}$	$f_{a_{42}}$	$f_{a_{43}}$	$f_{a_{44}}$	$f_{b_{41}}$	$f_{b_{42}}$	$f_{b_{43}}$	$f_{b_{44}}$
5-b,7-c	$f_{a_{51}}$	$f_{a_{52}}$	$f_{a_{53}}$	$f_{a_{54}}$	$f_{b_{51}}$	$f_{b_{52}}$	$f_{b_{53}}$	$f_{b_{54}}$
5-a,7-c	$f_{a_{61}}$	$f_{a_{62}}$	$f_{a_{63}}$	$f_{a_{64}}$	$f_{b_{61}}$	$f_{b_{62}}$	$f_{b_{63}}$	$f_{b_{64}}$
5-b,7-2	$f_{a_{71}}$	$f_{a_{72}}$	$f_{a_{73}}$	$f_{a_{74}}$	$f_{b_{71}}$	$f_{b_{72}}$	$f_{b_{73}}$	$f_{b_{74}}$
5-a,7-2	$f_{a_{81}}$	$f_{a_{82}}$	$f_{a_{83}}$	$f_{a_{84}}$	$f_{b_{81}}$	$f_{b_{82}}$	$f_{b_{83}}$	$f_{b_{84}}$
13-2,15-4	$f_{c_{11}}$	$f_{c_{12}}$	$f_{c_{13}}$	$f_{c_{14}}$	$f_{d_{11}}$	$f_{d_{12}}$	$f_{d_{13}}$	$f_{d_{14}}$
13-b,15-4	$f_{c_{21}}$	$f_{c_{22}}$	$f_{c_{23}}$	$f_{c_{24}}$	$f_{d_{21}}$	$f_{d_{22}}$	$f_{d_{23}}$	$f_{d_{24}}$
13-a,15-4	$f_{c_{31}}$	$f_{c_{32}}$	$f_{c_{33}}$	$f_{c_{34}}$	$f_{d_{31}}$	$f_{d_{32}}$	$f_{d_{33}}$	$f_{d_{34}}$
13-2,15-c	$f_{c_{41}}$	$f_{c_{42}}$	$f_{c_{43}}$	$f_{c_{44}}$	$f_{d_{41}}$	$f_{d_{42}}$	$f_{d_{43}}$	$f_{d_{44}}$
13-b,15-c	$f_{c_{51}}$	$f_{c_{52}}$	$f_{c_{63}}$	$f_{c_{54}}$	$f_{d_{51}}$	$f_{d_{52}}$	$f_{d_{53}}$	$f_{d_{54}}$
13-а,15-с	$f_{c_{61}}$	$f_{c_{62}}$	$f_{c_{63}}$	$f_{c_{64}}$	$f_{d_{61}}$	$f_{d_{62}}$	$f_{d_{63}}$	$f_{d_{64}}$
13-b,15-2	$f_{c_{71}}$	$f_{c_{72}}$	$f_{c_{73}}$	$f_{c_{74}}$	$f_{d_{71}}$	$f_{d_{72}}$	$f_{d_{73}}$	$f_{d_{74}}$
13-a,15-2	$f_{c_{81}}$	$f_{c_{82}}$	$f_{c_{83}}$	$f_{c_{84}}$	$f_{d_{81}}$	$f_{d_{82}}$	$f_{d_{83}}$	$f_{d_{84}}$

It is seen from the above Table 6.1, 128 topologies are possible and can be studied further according to suitability of applications. In this research work  $f_{a_{ij}}$  family is studied for 24 out of 32 configurations from the highlighted section considering output ports as shown in Fig 6.3. These two ports have addition features for CG and NCG connections.

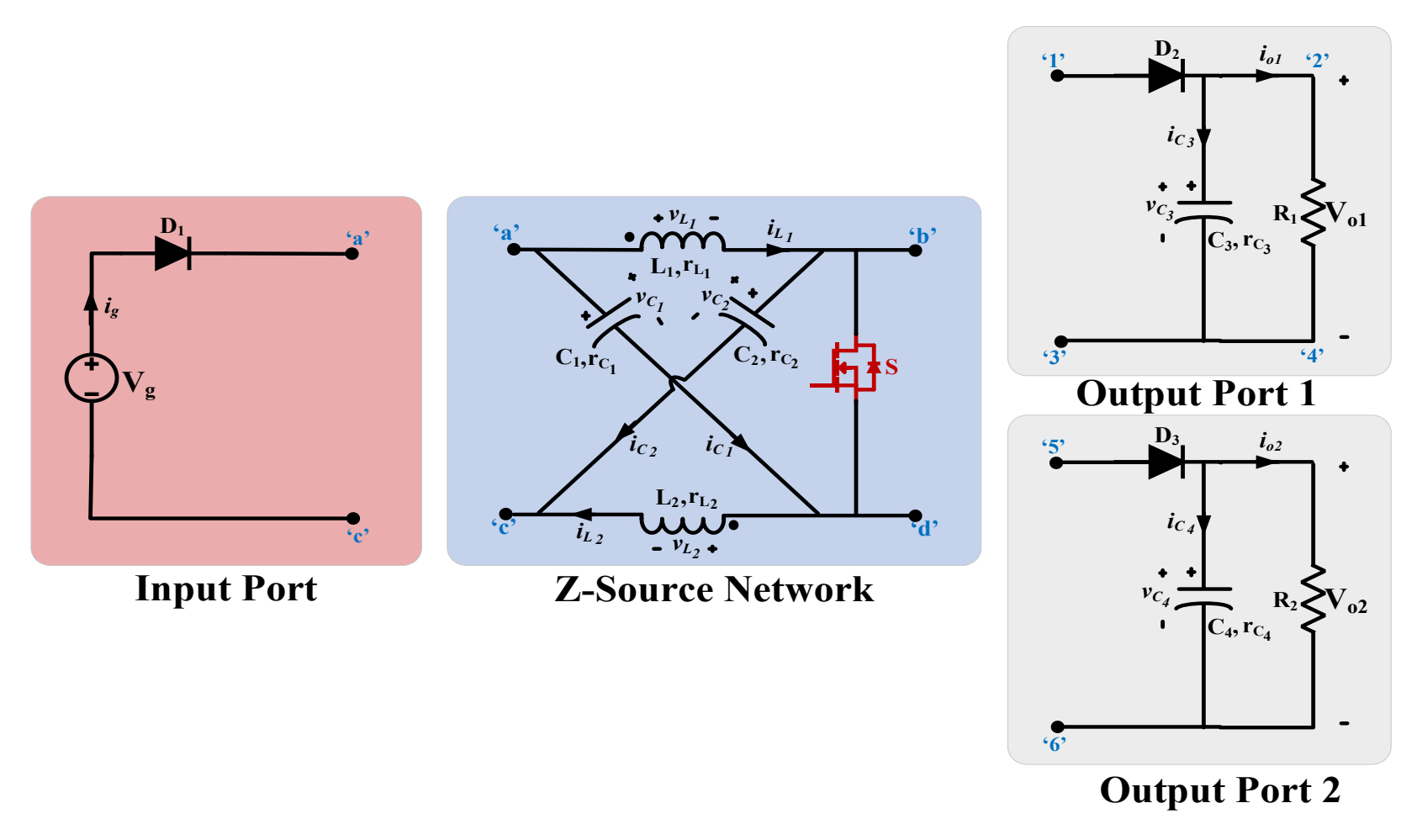


Figure 6.3. Converter configuration for single input dual output Z source DC-DC converter.

Examining Fig. 6.3, a total of 24 configurations, featuring both common ground (CG) and non-common ground (NCG), are derived and tabulated in Table 6.2 and subsequently analyzed for their performance. Among these, the most optimal configuration is selected and thoroughly evaluated.

Table 6.2. DIFFERENT CONVERTER CONFIGURATIONS FOR SINGLE INPUT DUAL OUTPUT Z-SOURCE BASED DC-DC CONVERTER

Configuration	Output Port 1	Output Port 2
1		NCG-A /5-2,6-d
2	(Family 1)	NCG-B /5-b,6-d
3	NCG-A	NCG-C /5-a,6-d
4	1-b, 3-d	CG-A/5-2,6-c
5		<b>CG-B</b> /5-b,6-c
6		CG-C /5-a,6-c
7		NCG-A /5-2,6-d
8		NCG-B /5-b,6-d
9	(Family 2) NCG-B	NCG-C /5-a,6-d
10	1-a,3-d	CG-A/5-2,6-c
11	] 1 4,5 4	<b>CG-B</b> /5-b,6-c
12		CG-C /5-a,6-c
13		NCG-A /5-2,6-d
14		NCG-B /5-b,6-d
15	(Family 3) CG-A	NCG-C /5-a,6-d
16	1-b,3-c	CG-A/5-2,6-c
17	1 0,5 0	<b>CG-B</b> /5-b,6-c
18		CG-C /5-a,6-c
19		NCG-A /5-2,6-d
20		NCG-B /5-b,6-d
21	(Family 4) CG-B 1-a,3-c	NCG-C /5-a,6-d
22		<b>CG-A</b> /5-2,6-c
23	1 4,5 0	<b>CG-B</b> /5-b,6-c
24		CG-C /5-a,6-c

Connecting output ports lead 1, 3, and 5,6 at different positions of modules 1 and 2 results in twenty-four configurations, as depicted in Table 6.2. Fig 6.4 shows the 24 different topologies of SIDO Z-source converter These configurations, with identical

design parameters as shown in Table 6.3, are evaluated for high voltage gain, output power, efficiency, low voltage stress on capacitors, diodes, and switches, and minimal input current drawn from the input source in Simulink/MATLAB. Following analysis, only one configuration is chosen.

Table 6.3. HARDWARE COMPONENT AND SIMULATION PARAMETERS OF PROPOSED SYSTEM

Simulation & Prototype Parameters	Symbols	Specification(s)
Input Voltage	$V_g$	30 <i>V</i>
Switching Frequency	$f_{sw}$	40kHz
Output Voltage	$V_{o}$	60V,60V
Inductors	$L_1$	$139.5 \mu H$
inductors	$L_2$	165μH
	$C_1$	$470\mu F\ (150V),$
Capacitors	$C_2$	$470\mu F~(150V)$
Capacitors	$C_3$	$470\mu F~(150V)$
	$C_4$	$330\mu F (150V)$
Load Desistances	$R_1$	$0-500~\Omega$
Load Resistances	$R_2$	$0-500\Omega$ ,
MOSFET	IRFP260N	200V, 50A
Diode	<b>MUR840</b>	400 V, 8 A

# 6.3.2. Topology Optimization and Performance Analysis

Various combinations/configurations are proposed as shown in Table 6.2 are simulated for performance analysis. The selection of an appropriate configuration can be based on various criteria such as high efficiency, high voltage gain, minimal input current drawn, increased power output, and other performance metrics. Table IV displays the results of open-loop simulations comparing various performance parameters of different feasible configurations of high-output voltage SIDO converters at  $R_1 = R_2 = 450\Omega$  and a duty cycle (D) of 0.2. As part of the analysis, the proposed converters are evaluated and contrasted across various potential configurations. Configurations that yield equal output voltages are specifically chosen, enabling their use in multilevel inverter applications and other suitable scenarios.

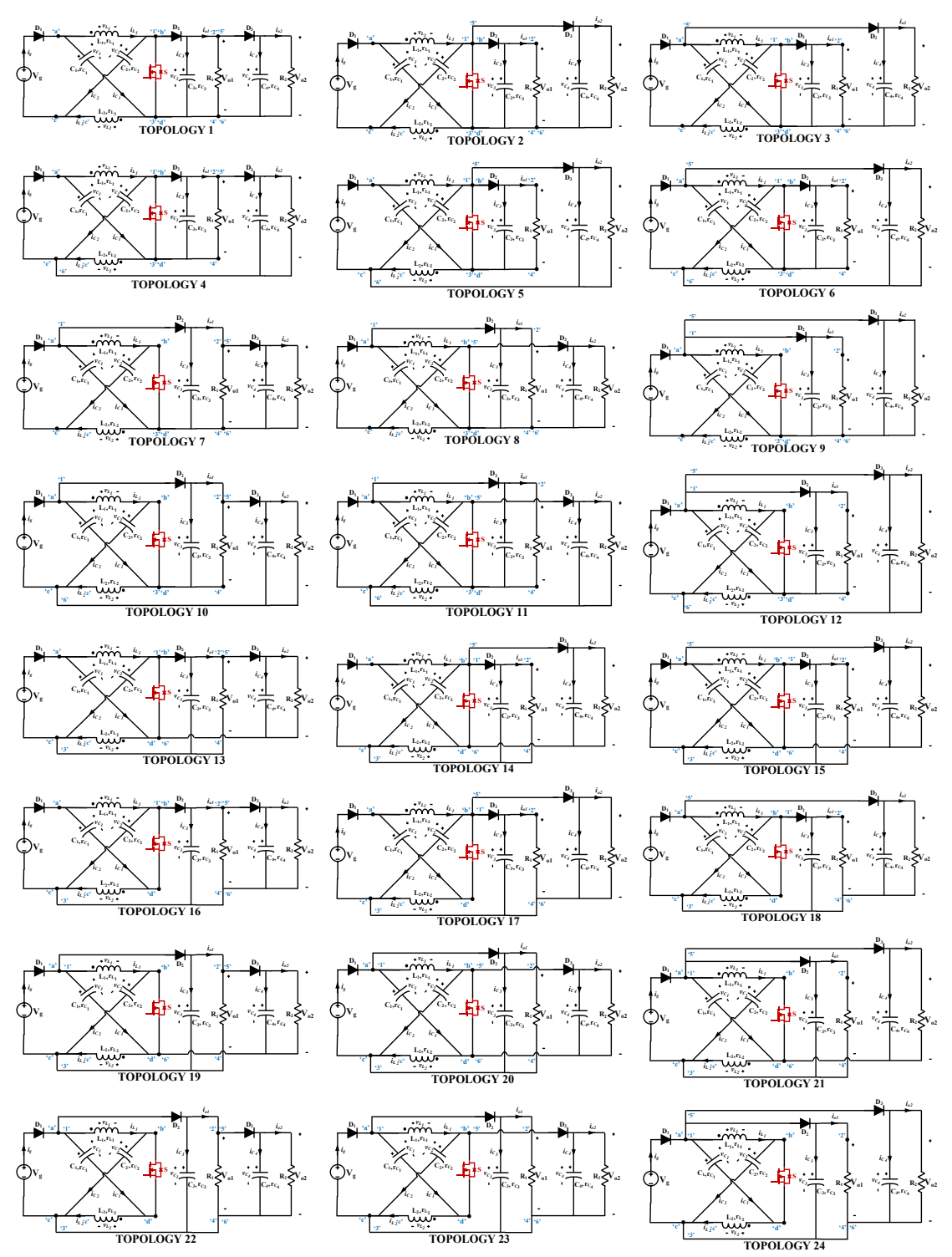


Fig. 6.4. Different converter configurations for single input dual output Z-source based dc-dc converter.

Table 6.4. COMPARISON OF VARIOUS PERFORMANCE PARAMETERS FOR DIFFERENT FEASIBLE CONFIGURATIONS OF HIGH OUTPUT VOLTAGE

SIDO CONVERTERS,  $R_1 = R_2 = 450\Omega$ , D = 0.2

Config	Output1 /	Output2 /	$I_g(A)$	$\frac{-\kappa_2 - 45}{V_{o1}(V)}$	$V_{o2}$ (V)		Efficiency
	Connections	Connections NCG-A/5-	-y ()	- 01 ( )	- 02 ( )	- 0 ( )	(%)
1		2,6-d	1.0173	79.5849	79.5847	28.2218	92.4668
2		NCG-B /5- b,6-d	1.0029	79.3646	79.3632	28.0670	93.2796
3	(Family 1) NCG-A	NCG-C /5- a,6-d	1.0954	98.2606	64.1557	30.6162	93.1648
4	1-b, 3-d	CG-A/5-2,6- c	1.1916	61.2891	106.9071	34.0382	95.2128
5		<b>CG-B</b> /5-b,6- c	1.0985	98.0290	64.0479	30.4843	92.4952
6		CG-C /5-a,6- c	1.2420	72.6931	102.6400	35.2511	94.6066
7		NCG-A /5- 2,6-d	1.4371	92.8352	92.8350	38.4637	89.2106
8		NCG-B /5- b,6-d	1.0909	63.9109	97.7612	30.3291	92.6731
9	(Family 2) NCG-B	NCG-C /5- a,6-d	1.4375	92.8737	92.8731	38.4994	89.2729
10	1-a,3-d	CG-A/5-2,6- c	1.3110	58.1839	116.3281	37.6183	95.6428
11		<b>CG-B</b> /5-b,6- c	1.4213	91.6869	91.6896	37.5431	88.0448
12		CG-C /5-a,6- c	1.31047	58.2222	116.3313	37.6293	95.7146
13		NCG-A/5- 2,6-d	1.0990	64.0810	98.1579	30.5498	92.6552
14		NCG-B /5- b,6-d	1.0736	63.8821	97.6820	30.2866	94.0264
15	(Family 3) CG-A	NCG-C /5- a,6-d	1.42138	91.6879	91.6906	37.5440	88.0457
16	1-b,3-c	CG-A/5-2,6- c	1.4371	92.8353	92.8350	38.4637	89.2100
17		<b>CG-B</b> /5-b,6- c	1.4375	92.8743	92.8738	38.4999	89.2734
18		CG-C /5-a,6- c	1.3102	58.2223	116.3114	37.6184	95.7046
19		NCG-A/5- 2,6-d	1.4068	87.6497	101.5058	40.2306	95.3232
20	(Family 4) CG-B 1-a,3-c	NCG-B /5- b,6-d	1.2401	102.5704	72.6187	35.1879	94.5786
21		NCG-C /5- a,6-d	1.3212	116.4005	58.2509	37.6697	95.0331
22		CG-A/5-2,6- c	1.4392	96.5832	96.5816	41.5544	96.2428
23		CG-B /5-b,6- c	1.3212	116.2794	58.1977	37.5931	94.8455
24		CG-C /5-a,6- c	1.4380	96.6844	96.6808	41.6403	96.5202

Table 6.4 is segmented into four sections, each containing six members, with configurations selected based on specific requirements. Among the twenty-four configurations, ten feature equal output voltages  $(V_{o1}, V_{o2})$ , namely 1, 2, 7, 9, 11, 15, 16, 17, 22, and 24. Configuration 1 and 2 exhibit equal output voltage but with lower gain and efficiency. Configuration 13 offers both positive and negative output voltages, suitable for applications requiring both types of supply. Configurations 7, 9, and 11 demonstrate high gain and efficiency but draw high input current from the supply. Conversely, configurations 22 and 24 provide high gain and efficiency while drawing minimal current. By reducing the duty cycle, configurations 7, 9, and 11 can be further explored in subsequent studies. It is observed that even under light load conditions, all configurations exhibit high efficiency, ranging from a minimum of 88.0448% for configuration 11 to a maximum of 96.5202% for configuration 24. Increasing the load and reducing the duty cycle could potentially enhance efficiency further, necessitating further investigation in subsequent studies. The performance parameters of selected configurations [1, 2, 7, 9, 11, 22, 24] of high-output voltage, high-efficiency SIDO converters are compared under varying load conditions for a duty cycle (D) of 0.2 is shown in Table 6.5.

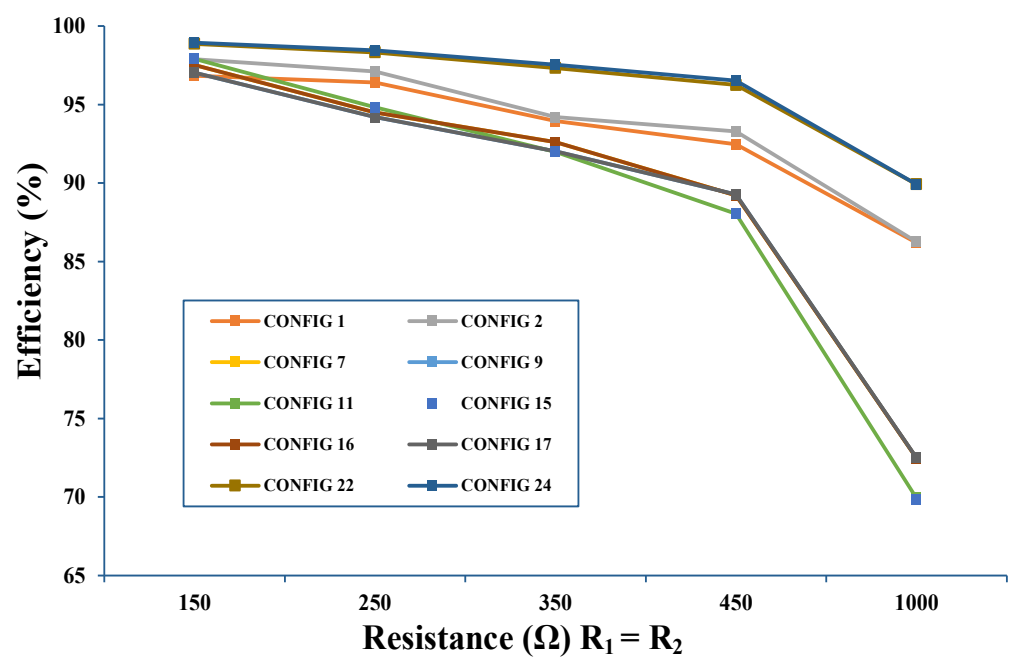


Figure 6.5. Comparison of efficiency for selected configurations [1,2,7, 9,11,22,24] of high output voltage, high efficiency SIDO converters for D=0.2 under varying load condition.

Table 6.5. COMPARISON OF VARIOUS PERFORMANCE PARAMETERS FOR SELECTED CONFIGURATIONS [1,2,7, 9,11,22,24] OF HIGH OUTPUT VOLTAGE, HIGH EFFICIENCY SIDO CONVERTERS FOR D=0.2 UNDER VARYING LOAD CONDITION.

Configuration	Output- 1/Output-2 Connections	$R(R_1=R_2)$ $(\Omega)$	$I_g(A)$	V <sub>01</sub> (V)	V <sub>02</sub> (V)	$P_o(W)$	Efficiency (%)
	(Family 1)	150	1.2060	51.0036	51.0031	35.0384	96.8427
	NCG-A /1-b,	250	1.0301	60.7880	60.7878	29.7964	96.4106
1	3-d	350	1.0147	70.5771	70.5759	28.5982	93.9407
	NCG-A /5-2,6-	450	1.0173	79.5849	79.5847	28.2218	92.4668
	d	1000	1.1131	119.7908	119.7900	28.7815	86.1860
	(Family 1)	150	1.1937	51.0180	51.0174	35.0575	97.8898
	NCG-A /1-b,	250	1.0245	60.8390	60.8379	29.8438	97.1003
2	3-d	350	1.0092	70.4805	70.4793	28.5223	94.1995
	NCG-B /5-b,6-	450	1.0029	79.3646	79.3632	28.0670	93.2796
	d	1000	1.1184	120.1231	120.1217	28.9426	86.2570
	(Family 2)	150	1.3079	53.5286	53.5286	38.2634	97.5149
	NCG-B /1-a,3-	250	1.2915	67.6408	67.6405	36.6124	94.4950
7	d	350	1.3570	81.1649	81.1649	37.6982	92.5974
	NCG-A /5-2,6-	450	1.4371	92.8352	92.8350	38.4637	89.2106
	d	1000	1.8254	138.8975	138.8971	39.6837	72.4619
	(Family 2)	150	1.3088	53.4139	53.4130	38.0997	97.0312
	NCG-B /1-a,3-	250	1.2911	67.5262	67.5255	36.4882	94.2002
9	d	350	1.3549	80.8548	80.8542	37.4076	92.0240
	NCG-C /5-a,6-	450	1.4375	92.8737	92.8731	38.4994	89.2729
	d	1000	1.8235	138.8974	138.8975	39.6952	72.4819
		150	1.2996	53.4811	53.4817	38.1701	97.8991
	(Family 2) NCG-B /1-a,3- d CG-B /5-b,6-c	250	1.2835	67.5453	67.5470	36.5104	94.8191
11		350	1.3457	80.5369	80.5391	37.1347	91.9799
		450	1.4213	91.6869	91.6896	37.5431	88.0448
		1000	1.7810	134.7868	134.7902	37.3581	69.9183
		150	1.2996	53.4811	53.4817	38.1700	97.8981
	(Family 3)	250	1.2835	67.5456	67.5473	36.5107	94.8190
15	CG-A/1-b,3-c	350	1.3457	80.5372	80.5394	37.1351	91.9798
	NCG-C /5-a,6-	450	1.4213	91.6879	91.6906	37.5440	88.0457
	d	1000	1.7799	134.6609	134.6643	37.2812	69.8182
		150	1.3079	53.5285	53.5285	38.2633	97.5139
	(Family 3) CG-A/1-b,3-c	250	1.2915	67.6407	67.6404	36.6123	94.4942
16		350	1.3570	81.1649	81.16483	37.6981	92.5967
	CG-A/5-2,6-c	450	1.4371	92.8353	92.8350	38.4637	89.2100
		1000	1.8255	138.8978	138.8974	39.6839	72.4618
		150	1.3088	53.4138	53.4130	38.0996	97.0303
	(Family 3)	250	1.2911	67.5264	67.5257	36.4884	94.2001
17	CG-A/1-b,3-c	350	1.3550	80.8552	80.8546	37.4080	92.0243
	CG-B /5-b,6-c	450	1.4375	92.8743	92.8738	38.4999	89.2734
		1000	1.8255	138.9007	138.9008	39.6970	72.4837
		150	2.9047	80.3005	80.2998	86.1546	98.8660
	(Family 4)	250	1.7867	81.0019	81.0009	52.7034	98.3248
22	CG-B /1-a,3-c	350	1.5478	88.7876	88.7864	45.1965	97.3296
	CG-A/5-2,6-c	450	1.4392	96.5832	96.5816	41.5544	96.2428
		1000	1.3555	135.1586	135.5630	36.5670	89.9167
		150	2.9024	80.3042	80.2952	86.1538	98.9434
	(Family 4)	250	1.7849	81.0131	81.0077	52.7159	98.4455
24	CG-B/1-a,3-c	350	1.5466	88.8442	88.8400	45.2528	97.5288
	CG-C /5-a,6-c	450	1.4380	96.6844	96.6808	41.6403	96.5202
		1000	1.3553	135.1409	135.1386	36.5574	89.9093

Fig. 6.5 illustrates that across all configurations, efficiency remains consistently high from no load to high load conditions based on Table 6.5. Configuration 22 and 24 exhibit the highest output voltage. Notably, at light load conditions, configurations 7, 9, 11, 15, 16, and 17 demonstrate efficiencies ranging from 69.8182% to 72.4837%, which are comparatively lower (< 15%) than other configurations. Most configurations draw nominal power from the source yet maintain high efficiency at high loading conditions, making them suitable for scenarios with limited input generation capacity. However, in configurations 22 and 24, input current is higher compared to other eligible configurations under high load, requiring control due to the fixed voltage source. Adaptation to changing loads can be achieved by either altering the configuration while keeping the duty cycle constant or adjusting the duty cycle while maintaining the configuration. This study holds significant importance as it enables the implementation of a suitable control strategy based on the loading conditions and the corresponding best possible configuration determined in advance. From Table 6.5, it is evident that among the selected configurations 1, 2, 7, 9, 11, 15, 16, 17, 22, and 24, configuration 24 achieves the maximum efficiency of 98.9434% with a voltage of 80.3042 V at  $R_1 = R_2 = 150\Omega$ , while configuration 17 attains the highest voltage of 138.9007 V with an efficiency of 72.4837% at  $R_1 = R_2 = 1000\Omega$ . However, due to the drop in efficiency during light load conditions, configurations 7, 9, 11, 15, 16, and 17 are discarded, configurations 1, 2, 22, and 24 are selected for further analysis as they exhibit high efficiency and output voltage.

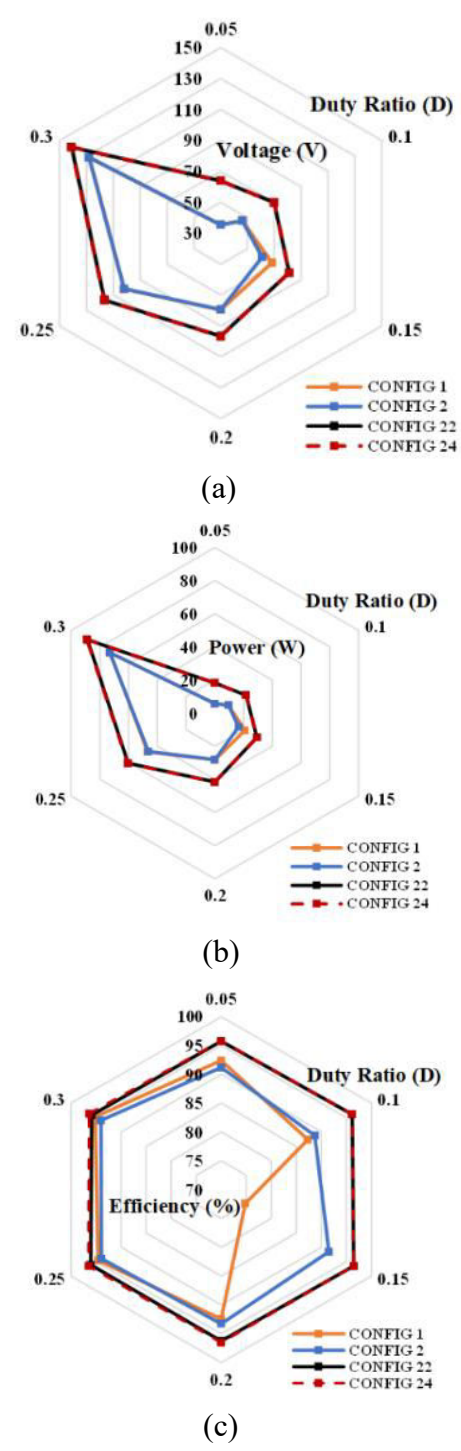


Figure 6.6. Comparison of various parameters for selected configurations [1,2,22,24] of high output voltage, high efficiency SIDO converters for  $R_1 = R_2 = 450\Omega$  under varying duty cycle condition. (a) Output voltages  $(V_{o1} = V_{o2})$ , (b) Output power  $(P_o)$ , (c) Efficiency (%).

#### 6.4. ANALYSIS OF SELECTED SIDO TOPOLOGIES

Out of the family of 24 topologies of high-gain Z-source SIDO converters, 4 configurations meeting the criterion of equal output voltage with better performance are further examined based on their loading conditions, voltages and efficiencies as discussed in earlier section.

Table 6.6. COMPARISON OF AVERAGE CURRENT AND CURRENT RIPPLES OF  $L_1$ AND  $L_2$  FOR SELECTED CONFIGURATIONS [1,2,22,24] OF Z-SOURCE SIDO CONVERTERS FOR  $R_1=R_2=450~\Omega$  UNDER VARYING DUTY CYCLE CONDITION.

Config	Output-1 / Output-2	D	(Avg)	$\Delta I_{L1}$ (A)	(A) (Avg)	$\Delta I_{L2}$ $(A)$
		0.05	-0.14	0.41	0.49	0.38
	NCG-A	0.10	-0.10	1.05	0.69	0.93
4	1-b, 3-d	0.15	0.53	1.92	0.51	1.62
1	NCG-A	0.20	1.26	3.06	0.54	2.68
	5-2,6-d	0.25	1.21	4.64	1.78	4.02
		0.30	2.53	6.70	2.22	5.68
		0.05	-0.03	0.43	0.37	0.42
	NCG-A	0.10	-0.04	1.05	0.63	0.92
2	1-b, 3-d	0.15	0.53	1.92	0.51	1.62
2	NCG-B	0.20	1.18	3.06	0.62	2.66
	5-b,6-d	0.25	1.21	4.63	1.79	4.02
		0.30	2.54	6.71	2.21	5.69
		0.05	0.30	0.49	0.30	0.35
	CG-B	0.10	0.14	0.96	0.64	0.85
22	1-a,3-c	0.15	0.59	1.71	0.57	1.45
22	CG-A	0.20	1.21	2.68	0.60	2.36
	5-2,6-c	0.25	1.16	4.06	1.70	3.54
		0.30	2.40	5.95	2.04	5.05
		0.05	0.31	0.49	0.30	0.35
	CG-B	0.10	0.06	0.96	0.72	0.86
24	1-a,3-c	0.15	0.59	1.70	0.56	1.46
44	CG-C	0.20	1.29	2.68	0.53	2.37
	5-a,6-c	0.25	1.08	4.06	1.78	3.57
		0.30	2.47	5.96	1.98	5.07

Figure 6.6 reveals that in configurations 1 and 2, efficiency initially decreases (minimum values 74.7968% and 88.7252%) and then rises with the duty cycle (maximum values 95.1968% and 94.0326%). Conversely, a reverse trend is observed in configurations 22 and 24, where efficiency first increases (maximum values 96.4919% and 96.5202%) and then decreases, with minimum values always above 95% (95.8569% and 96.3553%). Additionally, the output voltage is higher throughout the full range of duty cycle (0.05 to 0.3), ranging from 35 V to 128 V for configuration

1 and 2, and from 64 V to 142 V for configuration 22 and 24, respectively. Moreover, output power delivered is highest in configurations 22 and 24 as the duty cycle increases. Therefore, efficiency, output voltage, and output power delivered are highest in configurations 22 and 24 as the duty cycle increases.

Configuration 1 and 2 should be discarded due to the high values of inductor current and current ripples. Table 6.6 highlights a significant increase in current ripples with the duty cycle for a fixed load, indicating the necessity for control measures. Therefore, proper attention must be given to ensure optimal performance under specific operating conditions.

In Table 6.7, average values are utilized to assess the stress across capacitors  $(V_{c1}, V_{c2}, V_{c3}, and V_{c4})$  due to very low voltage ripple, while maximum negative values are employed to evaluate the stress across diodes and the active switch  $(V_{D1}, V_{D2}, V_{D3}, and V_S)$ . It is observed that the average voltage across capacitors  $C_1$  and  $C_2$  ranges from 32V to 79V for configuration 1 and 2, and 32V to 70V for configuration 22 and 24, whereas across capacitors  $C_3$  and  $C_4$ , it varies from 35V to 128V for configuration 1 and 2, and 64V to 142V for configuration 22 and 24, respectively. Consequently, capacitors  $C_1$  and  $C_2$  experience less voltage stress compared to capacitors  $C_3$  and  $C_4$  in all four configurations, aiding in the selection of suitable voltage ratings for all capacitors.

Furthermore, voltage stress on diodes  $D_1$  and  $D_2$  ranges from 34V to 126V in configuration 1 and 2, and 33V to 108V for configuration 22 and 24, while for the switch (S), it varies from 34V to 126V for configuration 1 and 2, and 33V to 109V for configuration 22 and 24, respectively. Interestingly, the voltage stress on diode  $D_3$  is zero volts for configuration 1 and 22, while it ranges from 34V to 126V for configuration 2 and 33V to 109V for configuration 24, respectively. Although approximate values are presented for description, precise values are displayed in the respective tables. Notably, configuration 22 exhibits minimum voltage stress despite the variation in duty cycle from low to high values.

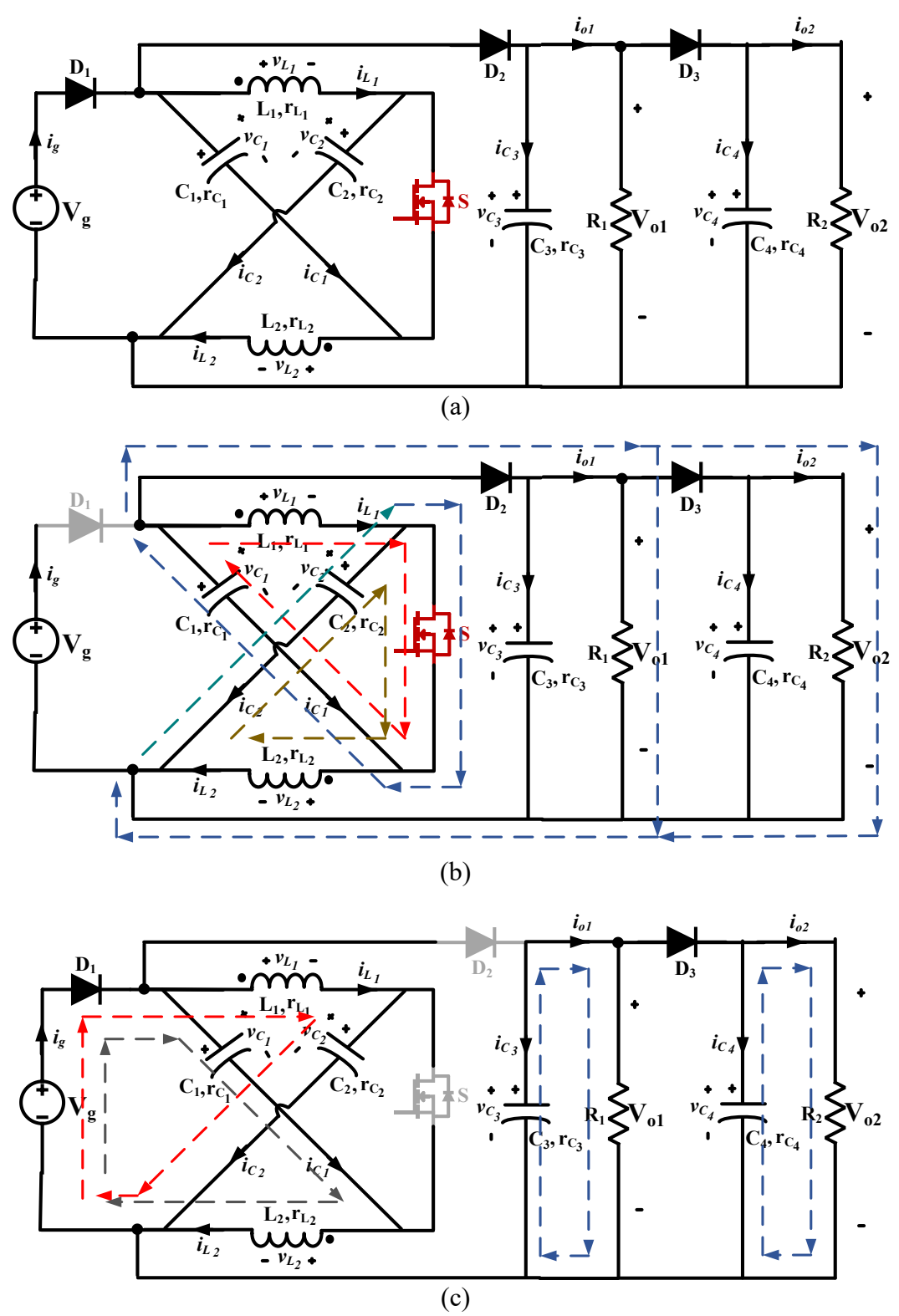
Considering the criteria of high efficiency, high output voltage, minimal voltage stress on capacitors, diodes, and the switch, as well as low inductor current and ripples, configuration 22 is ultimately selected. Furthermore, due to the lower inductor current, less energy is stored in the inductors, resulting in a smaller size, reduced weight, and cost-effectiveness of the proposed converter configuration.

Table 6.7. COMPARISON OF VOLTAGE STRESSES ON CAPACITORS, DIODES AND ACTIVE SWITCH OF Z-SOURCE SIDO CONVERTERS,  $R_1 = R_2 = 450~\Omega$  UNDER VARYING DUTY CYCLE CONDITION.

Confi		$V_{c1}$	$V_{c2}$	$V_{c3}$	$V_{c4}$	$V_{D1}$	$V_{D2}$	$V_{D3}$	$V_{S}$
g	D	(V)	(V)	(V)	(V)	(V)	(V)	(V)	(V)
	0.05	32.7382	32.7382	35.4757	35.4757	-34.1100	-34.1089	0	34.1114
	0.10	38.0607	38.0607	46.1205	46.1199	-44.5698	-44.5692	0	44.5728
1	0.15	49.0764	49.0764	68.1534	68.1528	-59.4702	-59.4751	0	59.4796
1	0.20	54.7910	54.7910	79.5849	79.5847	-78.1367	-78.1469	0	78.1511
	0.25	65.9801	65.9800	101.9708	101.9705	-100.5638	-100.5831	0	100.5827
	0.30	78.9350	78.9350	127.8972	127.8959	-126.0593	-126.0986	0	126.1037
	0.05	32.7345	32.7345	35.4678	35.4676	-34.0967	-34.1020	-34.0967	34.1034
	0.10	38.0463	38.0463	46.0922	46.0914	-44.5433	-44.5442	-44.5426	44.5479
2	0.15	45.4699	45.4699	60.9394	60.9391	-59.3303	-59.3339	-59.3316	59.3382
2	0.20	54.6805	54.6805	79.3646	79.3632	-77.8791	-77.8886	-77.8857	77.8933
	0.25	65.9705	65.9704	101.9523	101.9504	-100.5704	-100.5781	-100.5750	100.5804
	0.30	79.0846	79.0846	128.1967	128.1942	-126.2799	-126.2799	-126.3196	126.3290
	0.05	31.9772	31.9772	63.9173	63.9150	-33.0760	-33.2977	0	33.3480
	0.10	34.9072	34.9072	69.7728	69.7705	-38.8074	-38.8000	0	38.8559
22	0.15	40.5574	40.5574	81.0685	81.0665	-49.8179	-49.8135	0	49.8766
22	0.20	48.3159	48.3159	96.5832	96.5816	-53.5631	-53.5622	0	53.6341
	0.25	58.2745	58.2745	116.5027	116.5014	-84.7190	-84.7328	0	84.7927
	0.30	70.5738	70.5738	141.1122	141.1111	-108.6759	-108.6764	0	108.7903
	0.05	31.9771	31.9771	63.9172	63.9148	-33.3075	-33.2977	-33.2988	33.4532
	0.10	34.9067	34.9067	69.7720	69.7694	-38.8049	-38.7991	-38.7960	38.8541
24	0.15	40.5565	40.5565	81.06719	81.0641	-49.8171	-49.8090	-49.8090	49.8790
24	0.20	48.3661	48.3661	96.6844	96.6808	-65.1807	-65.1858	-65.1817	65.2492
	0.25	58.3894	58.3893	116.7335	116.7292	-84.9428	-84.9614	-84.9566	85.0202
	0.30	70.7765	70.7765	141.5191	141.5138	-109.0839	-109.0990	-109.0925	109.1656

#### 6.5. ANALYSIS OF TOPOLOGY 22 Z-SOURCE SIDO CONVERTER

The configuration of the proposed converter is illustrated in Fig 6.7(a). It is obvious from the diagram that the structure of the proposed converter is straightforward, comprising a Z-source network  $(L_1, L_2, C_1, and C_2)$ , a switch S, three diodes  $D_1, D_2$ , and  $D_3$ , two filter capacitors  $C_3$  and  $C_4$ , and two load resistances  $R_1$  and  $R_2$ . In comparison with the Z-source dc-dc converter represented in Fig 1, the proposed converter modifies the grounding connection and introduces additional outputs to enable Single Input Dual Output (SIDO) operation. A prominent feature of the proposed converter is the placement of the input source and load on the same side of the Z-source network, differing from traditional Z-source converters where they are



(c) Figure 6.7. Proposed Converter (a) Configuration, (b) Operating state DT, (c) Operating state (1-D)T

situated on both sides of the network (as shown in Fig 6.1). Additionally, the input voltage source and load share the same ground.

To analyse the operation of Z-source SIDO converter and to simplify the analysis, the following conditions are assumed.

- 1. All components are assumed to be ideal.
- 2. Both inductors,  $L_1$  and  $L_2$ , are not equal, and both capacitors,  $C_1$  and  $C_2$ , are assumed to be identical (C) in the Z-source network.
- 3. The currents through  $L_1$  and  $L_2$ , as well as the voltages across  $C_1$  and  $C_2$ , increase and decrease linearly over time.

Since, in the Z-source network symmetry is maintained, leading to the conclusion of the following equations:

$$\begin{cases} i_{L_1} \neq i_{L_2}, & i_{C_1} \neq i_{C_2} \\ v_{L_1} \neq v_{L_2} & v_{C_1} \neq v_{C_2} \end{cases}$$
 (6.2)

where  $i_{L_1}$ ,  $v_{L_1}$ ,  $i_{L_2}$ ,  $v_{L_2}$ ,  $i_{C_1}$ ,  $v_{C_1}$ ,  $i_{C_2}$ , and  $v_{C_2}$  are the currents and voltages of  $L_1$ ,  $L_2$ ,  $C_1$  and  $C_2$  respectively.

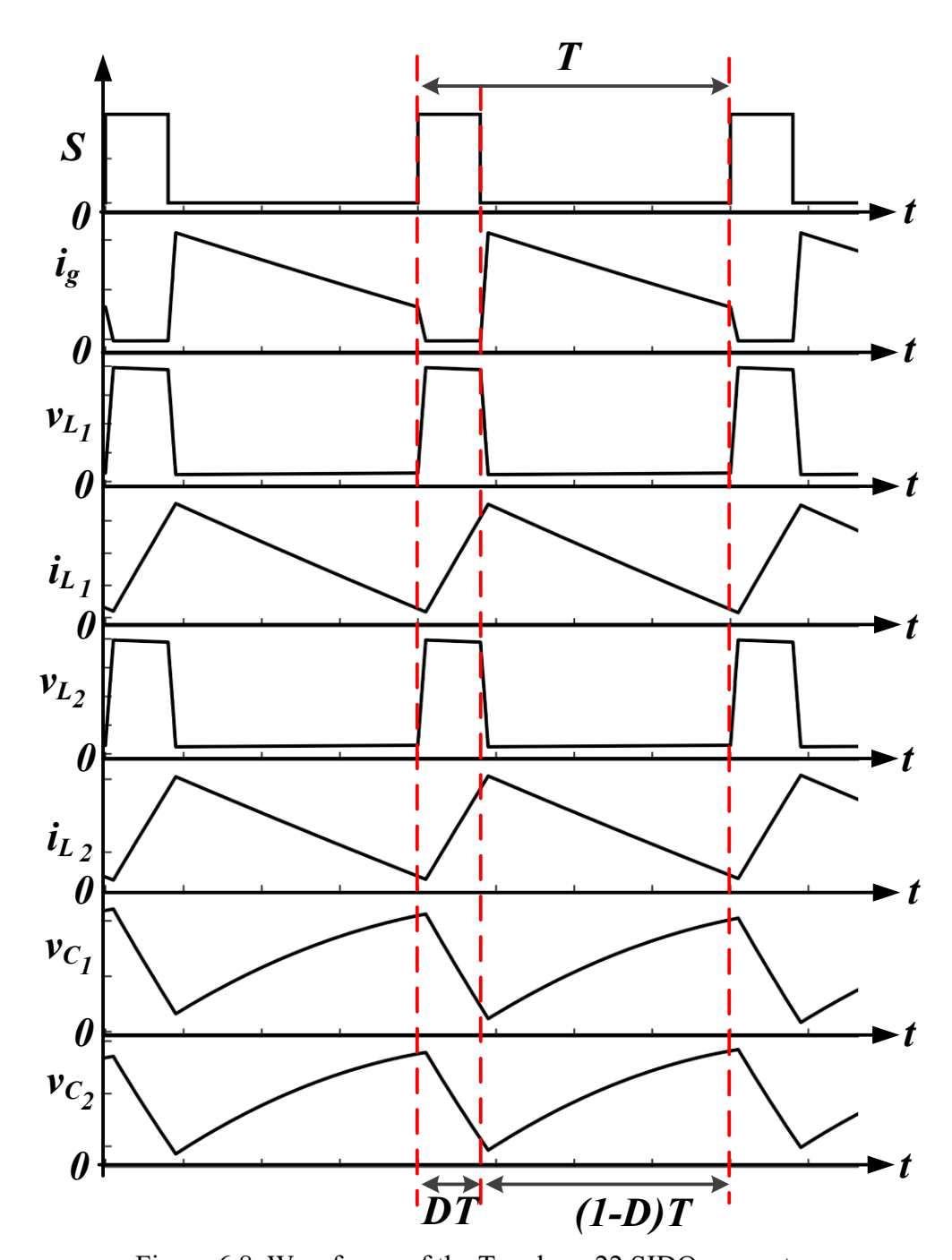


Figure 6.8. Waveforms of the Topology 22 SIDO converter.

# 6.5.1. Dynamic Operation and Analysis

The proposed converter operates in Continuous Conduction Mode (CCM) and can be described into two distinct states: Mode 1 and Mode 2. The expected waveforms of the proposed converter are depicted in Figure 6.8.

In Mode 1, demonstrated by the equivalent circuit in Fig 6.7(a), switch S and diode  $D_2$  are in the ON state, while diode  $D_1$  is OFF. Let DT represent the duration of Mode 1 within a switching cycle T, where D > 0 denotes the duty cycle of S. This state encompasses three loops:

- 1. loop 1 comprises  $L_1$ ,  $C_1$ , and S, where  $C_1$  discharges energy into  $L_1$ ;
- 2. loop 2 encompasses  $L_2$ ,  $C_2$ , and S, with  $C_2$  discharging energy into  $L_2$ ;
- 3. loop 3 involves  $C_1$ ,  $C_2$ ,  $D_2$ ,  $D_3$ ,  $C_3$ ,  $C_4$ ,  $R_1$ , and  $R_2$ . Here,  $C_1$  and  $C_2$  discharge energy into  $C_3$ ,  $C_4$ ,  $R_1$ , and  $R_2$ .

In mode 1, the following equations can be derived:

$$v_{L_1} = v_{C_1} = L_1 \left( \frac{di_{L_1}}{dt} \right) \tag{6.3}$$

$$v_{L_2} = v_{C_2} = L_2 \left( \frac{di_{L_2}}{dt} \right) \tag{6.4}$$

$$V_{o1} = V_{o2} = v_{L_1} + v_{C_1} = v_{L_2} + v_{C_2}$$
 (6.5)

$$i_{C_1} = -\left(i_{L_1} + \frac{V_{o1}}{R_1} + \frac{V_{o2}}{R_2}\right) \tag{6.6}$$

$$i_{C_2} = -\left(i_{L_2} + \frac{V_{o1}}{R_1} + \frac{V_{o2}}{R_2}\right) \tag{6.7}$$

In Mode 2, shown by the equivalent circuit in Fig 6.7(b). Mode 2 of the proposed converter is characterized by switch S and diode  $D_2$  being OFF, while diode  $D_1$  is ON. Assuming that (1 - D)T represents the duration of Mode 2 within a switching cycle T, this mode encompasses four loops:

- 1. loop 1 consists of  $L_1$ ,  $C_2$ ,  $D_1$ , and S, where input sources  $V_g$  and  $L_1$  discharge energy into  $C_2$ ;
- 2. loop 2 involves  $L_2$ ,  $C_1$ ,  $D_1$ , and S, with input sources  $V_g$  and  $L_2$  discharging energy into  $C_1$ ;
- 3. loop 3 includes  $C_3$  and  $R_1$ , where  $C_3$  releases energy to the load  $R_1$ ; 4) loop 4 comprises  $C_4$  and  $R_2$ , where  $C_4$  releases energy to the load  $R_2$ .

In mode 2, the following equations can be derived:

$$V_g = v_{L_1} + v_{C_1} = L_1 \left(\frac{di_{L_1}}{dt}\right) + v_{C_1}$$
 (6.8)

$$V_g = v_{L_1} + v_{C_1} = L_1 \left(\frac{di_{L_1}}{dt}\right) + v_{C_1}$$
(6.9)

$$i_g = i_{L_1} + i_{C_1} = i_{L_1} + C_1 \left(\frac{dv_{C_1}}{dt}\right)$$
 (6.10)

$$i_g = i_{L_2} + i_{C_2} = i_{L_2} + C_2 \left(\frac{dv_{C_2}}{dt}\right)$$
 (6.11)

$$i_{C_3} = C_3 \left(\frac{dv_{C_3}}{dt}\right) = \frac{V_{o1}}{R_1}$$
 (6.12)

$$i_{C_4} = C_4 \left(\frac{dv_{C_4}}{dt}\right) = \frac{V_{o2}}{R_2} \tag{6.13}$$

#### 6.5.2. Steady State Analysis

In steady state, the average voltage across an inductor within a switching cycle T is zero; hence, we obtain

$$\frac{1}{T} \int_0^T v_{L_1} dt = 0 (6.14)$$

By substituting equations (6.3) and (6.8) into equation (6.14), we can derive the following equation:

$$\frac{1}{T} \int_{0}^{T} v_{L_{1}} dt = \frac{1}{T} \left[ \int_{0}^{DT} v_{C_{1}} dt + \int_{DT}^{(1-D)T} (V_{g} - v_{C_{1}}) dt \right] = 0$$
 (6.15)

Since the capacitors  $C_1$  and  $C_2$  are sufficiently large, the voltage across  $C_1$  and  $C_2$  changes linearly, allowing us to obtain their average voltages.

$$V_{C_1} = \frac{1}{T} \int_0^{DT} v_{C_1} dt = \frac{1}{T} \int_{DT}^T v_{C_1} dt$$
 (6.16)

By substituting (6.16) into equation (6.15), we obtain:

$$V_{C_1}DT + (V_g - V_{C_1})(1 - DT) = 0 (6.17)$$

On simplifying,

$$V_{C_1} = \frac{1 - D}{1 - 2D} V_g \tag{6.18}$$

Substituting (6.18) into (6.5), the output voltage  $V_{o1}$  and  $V_{o2}$  is

$$V_{o1} = V_{o2} = 2V_{C_1} = \frac{2(1-D)}{1-2D}V_g$$
 (6.19)

Hence, the relationship between the voltage gain G and the duty cycle D can be expressed as:

$$G == \frac{2(1-D)}{1-2D} \tag{6.20}$$

The equation suggests that the duty cycle D ranges from 0 to 0.5. With M > 2, the voltage gain is high when the duty cycle approaches 0.5.

Assuming ideal conditions for the proposed converter and operating in Continuous Conduction Mode (CCM), we have

$$V_g I_g = V_{o1} I_{o1} + V_{o2} I_{o2} (6.21)$$

where  $I_o = I_{o1} + I_{o2}$  and  $I_g$  and  $I_o$  are the input and output average currents, respectively

Substituting (6.19) into (6.21), the average input current  $I_g$  is given by:

$$I_g = \frac{1 - D}{1 - 2D} I_o \tag{6.22}$$

The voltages and currents of components are shown in Table 6.8 and 6.9 respectively.

Table 6.8. VOLTAGE OF EACH COMPONENT IN DIFFERENT STATES

Components	Mode 1	Mode 2			
$V_{c_1} \& V_{c_2}$	$\frac{1-D}{1-2D}V_g$	$\frac{1-D}{1-2D}V_g$			
$V_{L_1} \& V_{L_2}$	$\frac{1-D}{1-2D}V_g$	$\frac{D}{1-2D}V_g$			
$V_s$	0	$\frac{1}{1-2D}V_g$			
$V_{D_1}$	$\frac{1}{1-2D}V_g$	0			
$V_{D_2}$	0	$\frac{1}{1-2D}V_g$			
Table 6.9. CURRENT OF EACH COMPONENT IN DIFFERENT STATES					

Components	Mode 1	Mode 2
$I_{c_1} \& I_{c_2}$	$\frac{3 - 7D + 4D^2}{1 - 2D}I_o$	$\frac{3D-4D^2}{1-2D}I_o$
$I_{L_1} \& I_{L_2}$	$\frac{2 - 5D + 4D^2}{1 - 2D}I_o$	$\frac{2 - 5D + 4D^2}{1 - 2D} I_o$
$I_s$	$\frac{5 - 12D + 8D^2}{1 - 2D}I_o$	0
$I_{D_1}$	0	$\frac{2(1-D)}{1-2D}I_0$
$I_{D_2}$	$I_{O}$	$\frac{1}{1-2D}I_0$

# 6.5.3. Cost Analysis of proposed SIDO converter

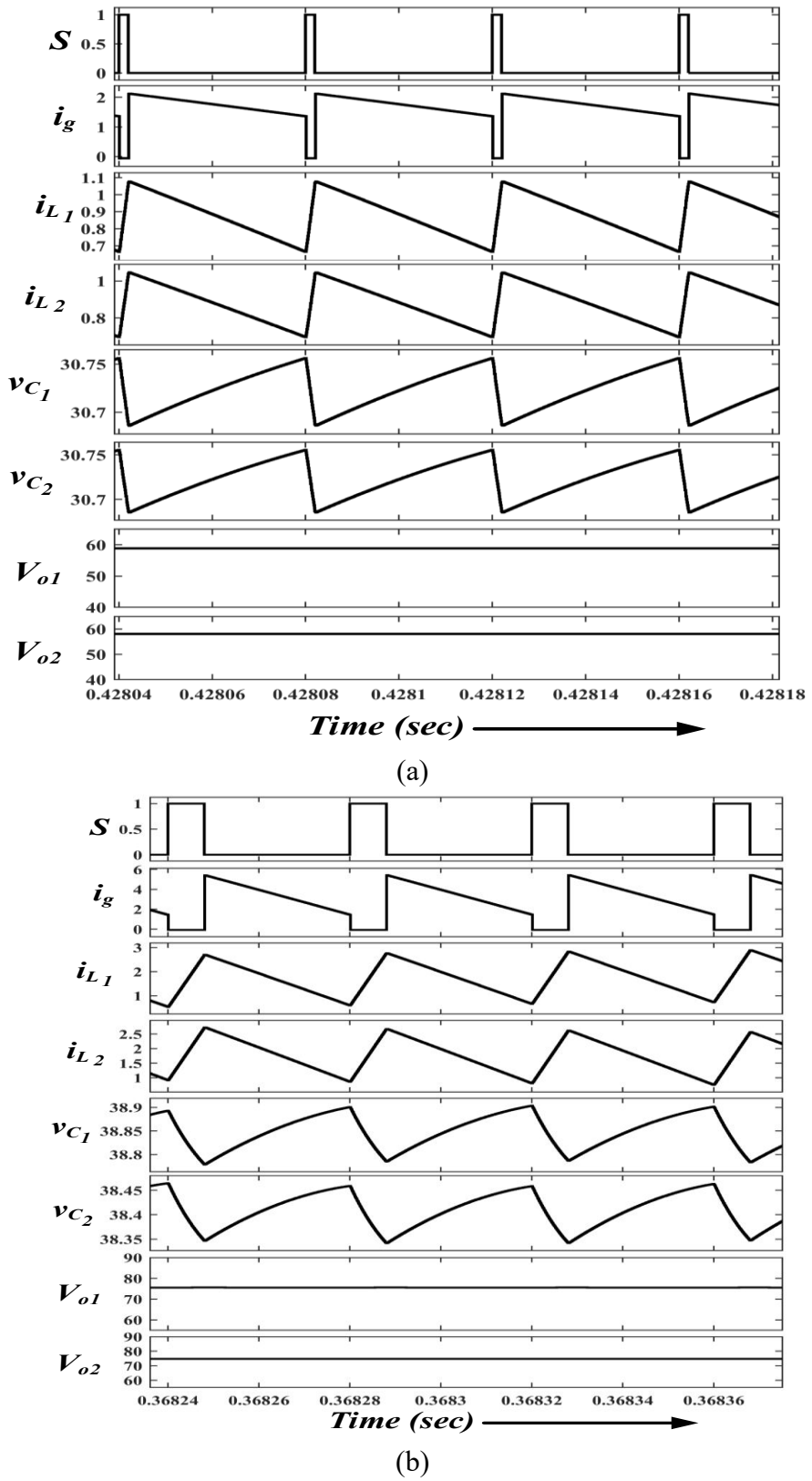
The subsequent step involves determining the cost of the proposed converter with Configuration 22. Based on Table 6.10, the total cost of the proposed converter, after subtracting the controller cost, amounts to \$21.4899. Since efficiency of proposed converter is very high (> 95%), very high voltage gain (> 4.5) ,less voltage stress and providing two equal outputs instead of one, high cost may be justified.

Components	Specs	Quantity	Unit Cost (\$)	Cost (\$)
	Core (TDK E42/21/15)	4	1.9833	7.9332
Inductor	Bobin	2	1.2093	2.4186
	Wire (SWG 15)	3 meters	0.6046	4.8978
Consciton	$470~\mu F$ , $150V$	3	1.6326	4.8978
Capacitor	$330 \ \mu F, 150V$	1	0.8586	0.8586
MOSFET	IRFP260N	1	0.4837	0.4837
Diode	MUR840	3	1.0279	3.0837
Controller	TMS320 F28379D	1	39.1099	39.1099
	60.5998			

#### 6.6. VERIFICATION AND RESULTS

The validity of the proposed converter topologies has been confirmed through numerical simulations conducted using MATLAB's Simulink. The simulation parameters can be chosen based on the specifications outlined in Table 6.3.

The simulation depicted in Fig. 6.9(a) and Fig. 6.9(b) demonstrates various waveforms: the switch S's driven voltage, the source current  $i_g$ , the inductor currents  $L_1$  and  $L_2$ , the capacitor voltages  $C_1$  and  $C_2$ , and the output voltages  $V_{o1}$  and  $V_{o2}$ . It is apparent that the converter operates in Continuous Conduction Mode (CCM) and exhibits two different states at a duty cycle of 0.5 and 0.2 with  $R_1 = R_2 = 150$  respectively. In the simulation results depicted in Figure 6.9(a), when the duty cycle is set to 0.05, the output voltages measure 59.7 V and 58.6 V, whereas the expected values are 60 V each. Similarly, with a duty cycle change to 0.2 in Fig 6.9(b), the output voltages are 76.5 V and 75.8 V, respectively, deviating slightly from the desired 80 V for each. The simulation closely aligns with the theoretical analysis, with differences primarily attributed to diode forward voltage drops.



(b) Figure 6.9. Open Loop simulation results at (a) D=0.05 and  $R_1=R_2=150\Omega$ , (b) D=0.2 and  $R_1=R_2=150\Omega$ 

A 48-W prototype of the proposed SIDO converter is fabricated to validate its operational principles, shown in Fig 6.10. The experiment employs parameters outlined in Table 6.3.

The switch S, employing IRFP260N, is driven by an isolated amplifier (TLP350), with MUR860 diodes utilized for  $D_1$ ,  $D_2$  and  $D_3$ . The switch S has an ON resistance of 40  $m\Omega$ , while the forward voltage drops of the diodes are 0.7 V. Experimental waveforms, obtained when the proposed converter is powered by a regulated DC source, are depicted in Fig 6.11-Fig 6.14. Specifically, Figures 6.11(a) to 6.11(c) shows experimental output voltage and current waveforms at duty cycles of 0.05, 0.2, and 0.3, respectively.

Fig. 6.11(a) shows the experimental waveforms of the proposed converter at a duty cycle D=0.05. The measured values of the output voltages  $V_{o1}$  and  $V_{o2}$  are 56.9V and 60V, respectively, with output currents  $I_{o1}$  and  $I_{o2}$  at  $150\Omega$  resistive load recorded as 392~mA and 415~mA, respectively, whereas the desired values are 60V for both voltages and 400~mA each for current. Fig. 11(b) displays the experimental waveforms at D=0.2, with measured values of  $V_{o1}$  and  $V_{o2}$  at 75.12~V and 78.59~V, respectively, and output currents  $I_{o1}$  and  $I_{o2}$  at  $450\Omega$  resistive load recorded as 138.26~mA and 151.83~mA, respectively, whereas the desired values are 80V for both voltages and 177.7~mA each for current. Fig. 11(c) demonstrates the experimental waveforms at D=0.3, with measured values of  $V_{o1}$  and  $V_{o2}at~97.1V$  and 99.3V, respectively, and output currents  $I_{o1}$  and  $I_{o2}$  at  $150\Omega$  resistive load recorded as 607~mA and 652~mA, respectively, whereas the desired values are 100V for both voltages and 100V for both voltages and 100V for both voltages and 100V for current.

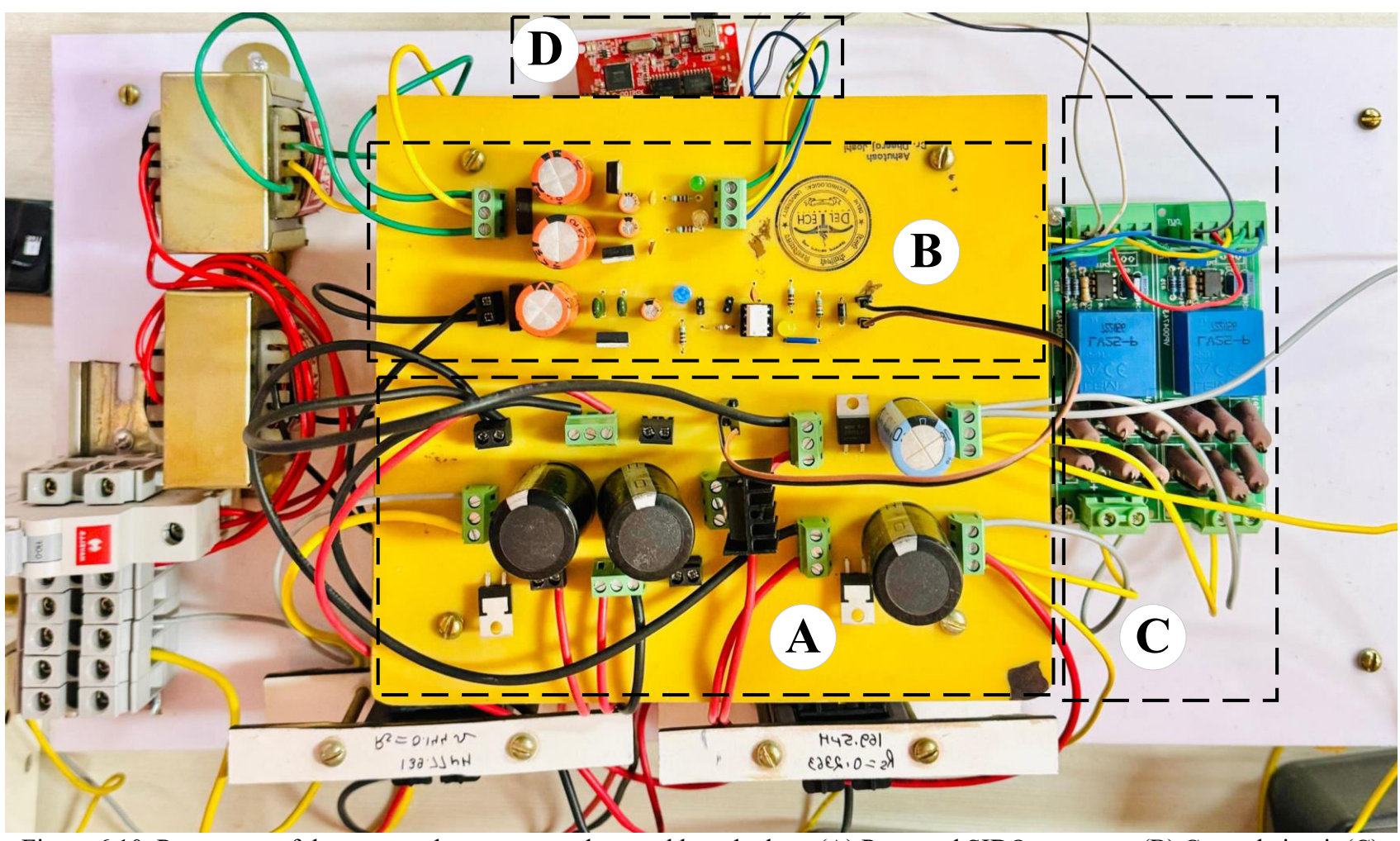


Figure 6.10. Prototypes of the proposed converter and control board where (A) Proposed SIDO converter (B) Control circuit (C) Sensor board (D) TMS320F28379D control board.

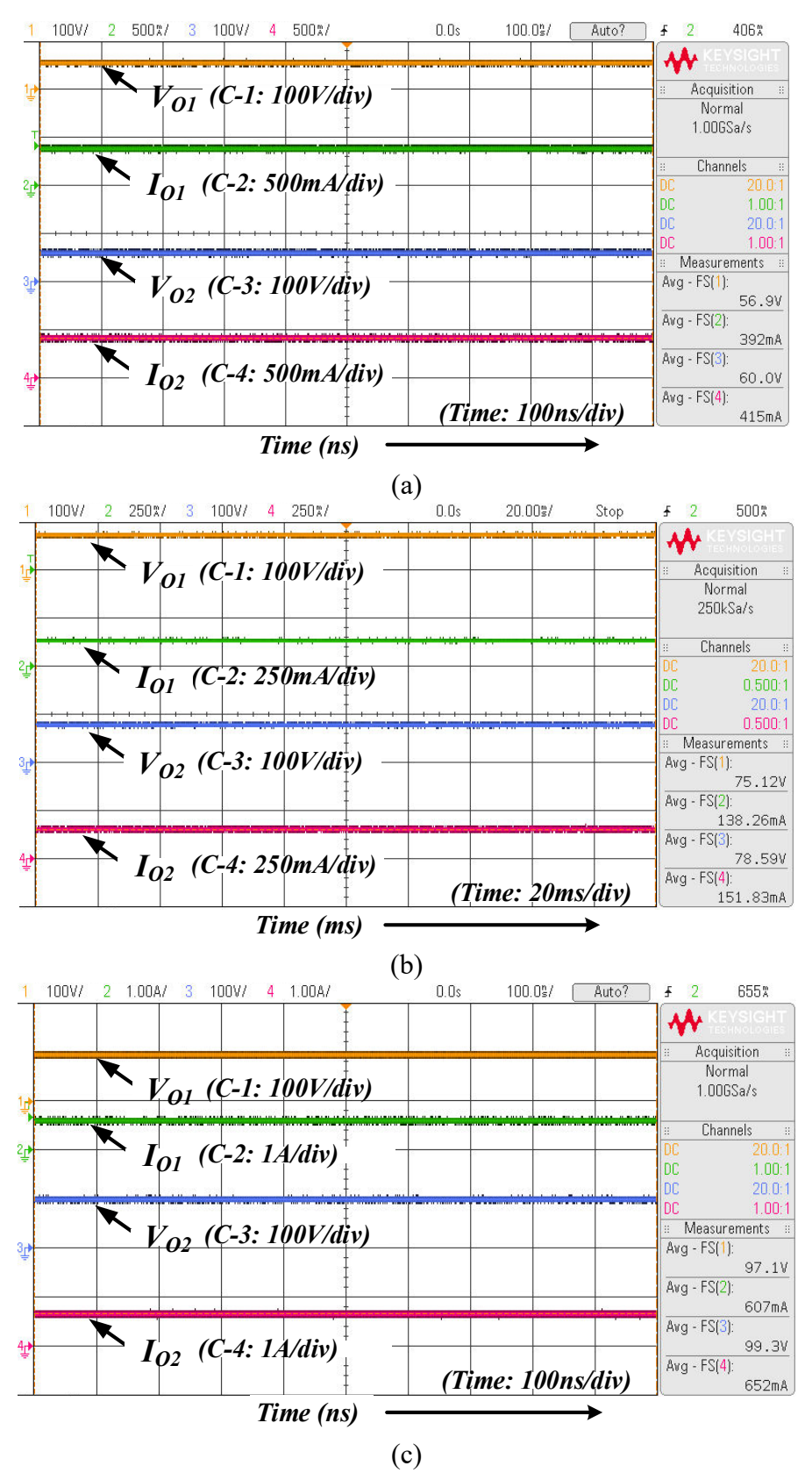


Figure 6.11. Experimental result of proposed converter at (a) D = 0.05 and  $R = 150\Omega$ , (b) D = 0.2 and  $R = 450\Omega$ , (c) D = 0.3 and  $R = 150\Omega$ .

Fig. 6.12 shows the experimental waveforms of inductor currents ( $I_{L1}$  and  $I_{L2}$ ) and capacitor voltages ( $V_{C1}$  and  $V_{C2}$ ) at two different duty cycles D = 0.05 and D = 0.2.

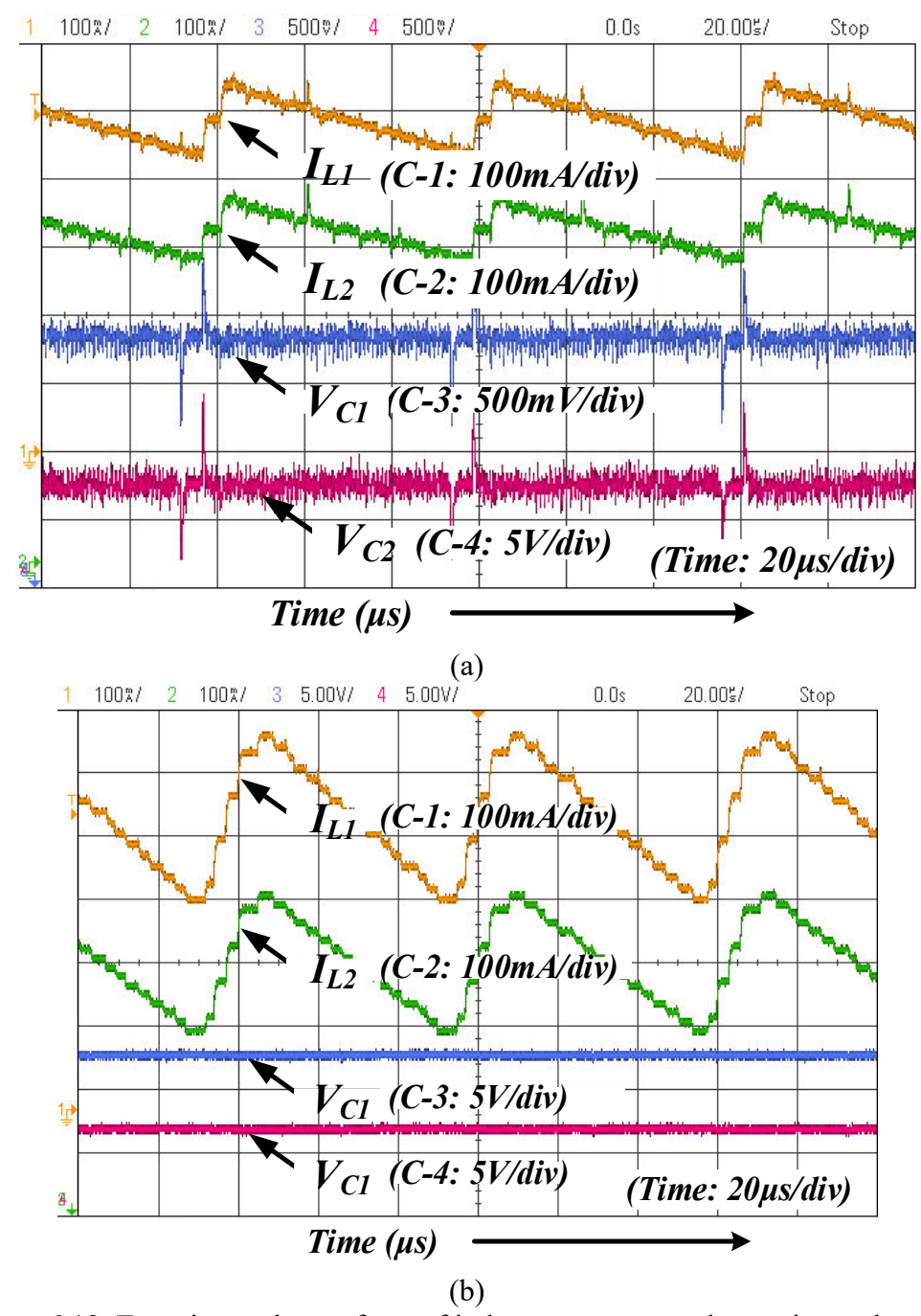


Figure 6.12. Experimental waveform of inductor currents and capacitor voltages at (a) D = 0.05, (b) D = 0.2.

The measured values as shown in Fig 6.12(a) of the average inductor currents  $I_{L_1}$  and  $I_{L_2}$  are 488.72mA and 487.99mA, respectively, with average capacitor voltages  $V_{C_1}$  and  $V_{C_2}$  recorded as 32.25 V and 32.2 V, respectively at 150 $\Omega$  resistive load and

D=0.05. The measured values of the average inductor currents  $I_{L_1}$  and  $I_{L_2}$  are 929.13 mA and 926.62 mA, respectively, with average capacitor voltages  $V_{C_1}$  and  $V_{C_2}$  recorded as 40.5 V and 40.42 V, respectively at 150 $\Omega$  resistive load and D=0.2.

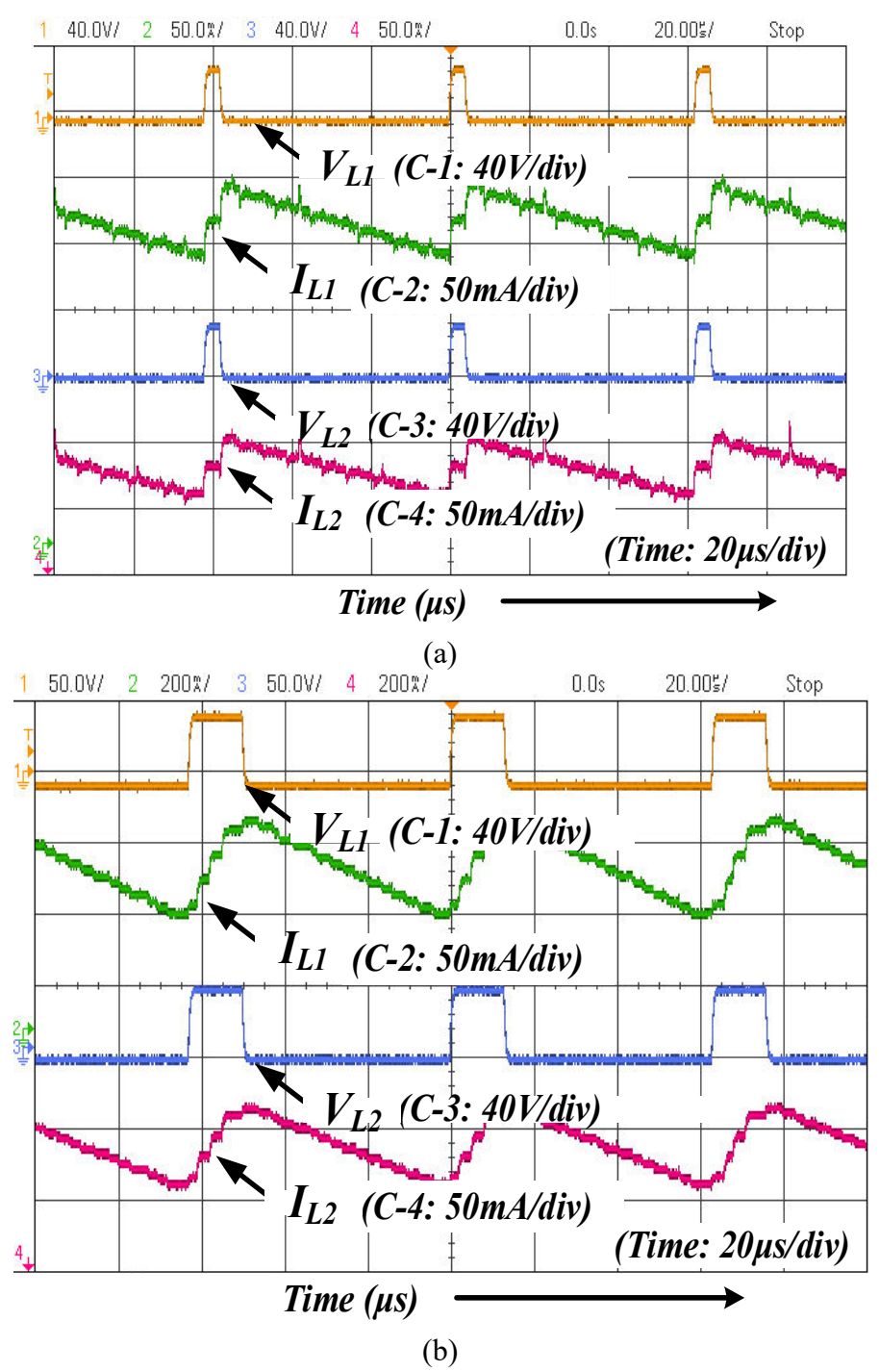


Figure 6.13. Experimental waveform of inductor voltages and currents at (a) D = 0.05, (b) D = 0.2.

Fig. 6.13 shows the experimental waveforms of inductor voltages ( $V_{L1}$  and  $V_{L2}$ ) and inductor currents ( $I_{L1}$  and  $I_{L2}$ ) at two different duty cycles D=0.05 and D=0.2. Fig 13(a) shows maximum voltage measured on inductors is 32V each at 150 $\Omega$  resistive load and D=0.05. Similarly Maximum voltage measured on inductors is 43V each at 150 $\Omega$  resistive load and D=0.2 which is shown in Fig 13(b).

Fig. 6.14 presents a comparative analysis of voltage stress on switch S and diodes  $(D_1, D_2 and D_3)$ , both through simulation and experimental waveform. A close similarity is observed between the simulation and hardware results for voltage stresses. The maximum stress observed on the switch is 36 V experimentally, while in simulation, the stress observed is 32 V for a duty cycle of 0.05, as shown in Fig. 6.14(a) and (b). Similarly, the maximum stress observed on the switch is 54 V experimentally, whereas in simulation, the stress observed is 49 V for a duty cycle of 0.2, as shown in Fig. 6.14(c) and (d).

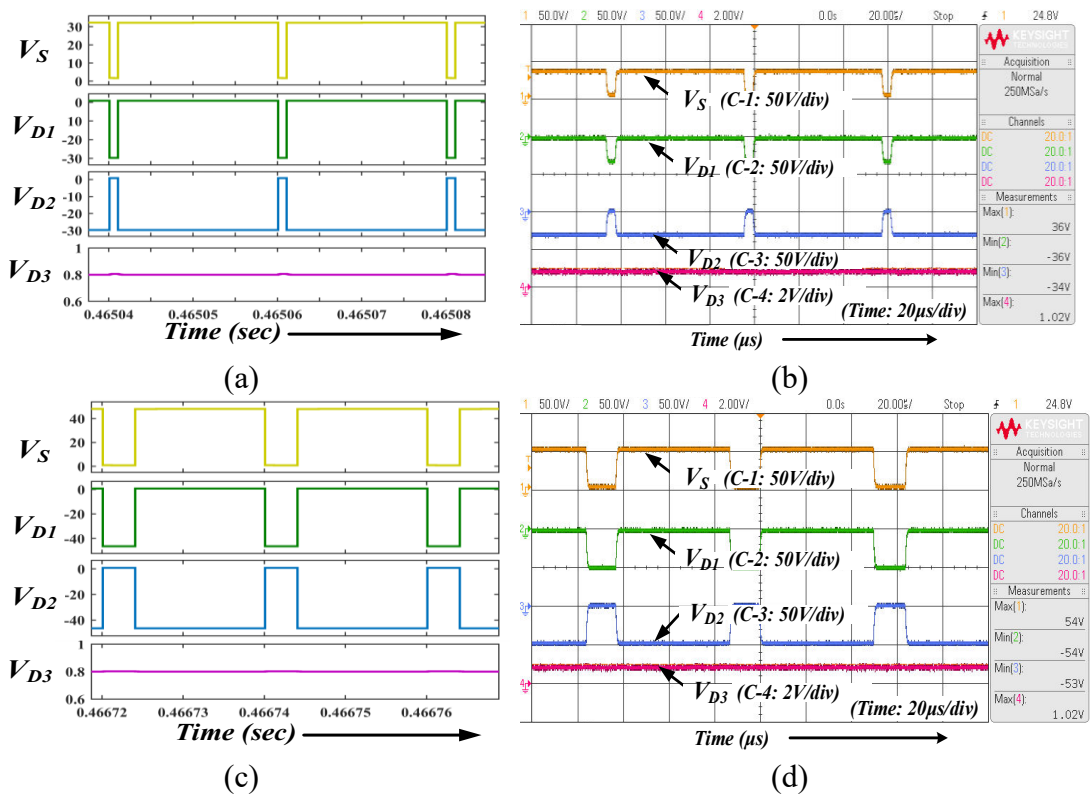


Figure 6.14. Experimental waveform of switch S and diodes  $D_1$ ,  $D_2$  and  $D_3$  voltage stress at (a) D = 0.05, (b) D = 0.2.

Fig. 6.15 presents both experimental and simulated outcomes for the proposed SIDO converter based on the Z-source. By varying the duty cycle, the impact on parameters such as input current, inductor current, capacitor voltage stress, output voltage, output power, and efficiency is examined. The close difference between experimental and simulated results validates the proposed approach, provides insights for the development of additional configurations as outlined in Table 6.1. Despite some alterations, the experimental results align closely with the simulation results, validating the features of the proposed converter and accounting for component losses. Variations between simulation and experimental data are primarily due to the forward voltage drop of diodes and the equivalent series resistance (ESR) of each device.

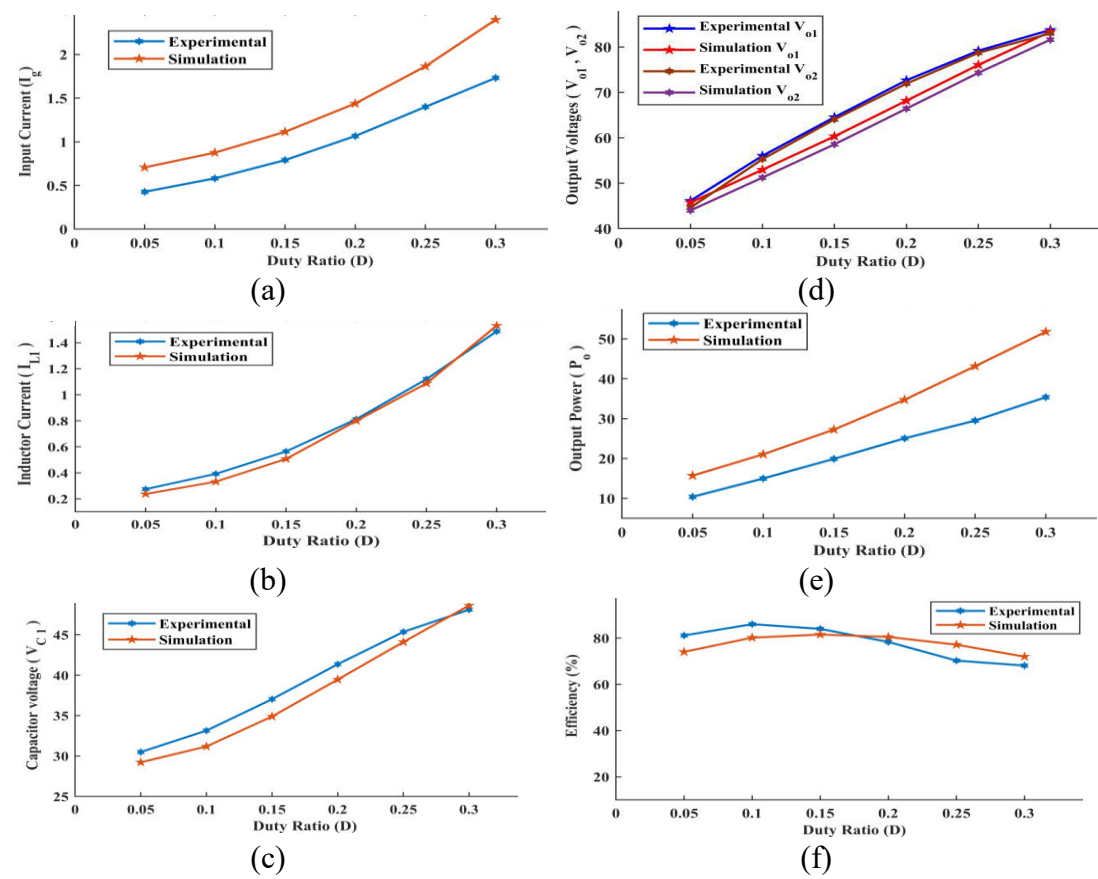


Figure 6.15. Experimental comparisons of proposed converter w.r.t. duty ratio at  $R_1 = R_2 = 450\Omega$  of (a) Input Current, (b) Inductor Current, (c) Capacitor Voltage, (d) Output Voltages, (e) Output Power, (f) Efficiency.

#### 6.7. CONCLUSION

This article researches into the topological properties and interrelationships of SIDO high-gain Z-source converter structures, focusing on three fundamental sections: input

port, Z-source network, and output port, serving as the building blocks for converter topologies. By integrating voltage or current types of source/loads to different terminals of these basic cells, various DC-DC converters can be constructed. The study introduces a converter and its methodology for selecting the topology of common ground/non-common ground Z-Source DC-DC Single Input Dual Output (SIDO), offering improved operational factors. Compared to conventional Z-source single input single output (SISO) converters, it provides high voltage gain and simultaneous CG/NCG outputs, making it advantageous for Electric Vehicle (EV) and Isolated Micro Grid applications. The proposed converters undergo analysis and comparison for various configurations, with configurations offering equal output voltages selected for potential use in multilevel inverter applications. Assessment includes maximum efficiency, voltage stress on components, inductor current, and ripples under different loads and duty cycles. With ongoing research on converter topologies, this article aims to enhance understanding of existing converter relationships and stimulate innovation in new topological developments and applications.

Overall, unlike conventional SISO converters that require cascading or duplication of stages to integrate multiple sources, the proposed multiport architecture achieves the same functionality through a single power stage with fewer switches, higher gain at lower duty, and inherently coordinated power sharing — thereby establishing a fundamentally superior alternative to traditional SISO-based designs.

#### **CHAPTER 7**

#### CONCLUSION AND FUTURE SCOPE

In this concluding chapter, the major contributions of this research project are summarized and possible future work is discussed.

#### 7.1. CONTRIBUTIONS OF THE THESIS

This work introduces theoretical concepts and presents provides a comprehensive analysis to the field of MIMO converters. Two major contributions are reported.

Firstly, two typical MIMO converters are introduced in detail, and a simple approach that can be applied in analyzing these converters is presented. The proposed two MIMO converters include a non-isolated topology and an isolated topology. Both topologies can be scaled to arbitrary numbers of inputs and outputs, and the output voltages could be regulated individually either greater than the maximum input voltage or less than the minimum. Closed-loop examples consisting of decoupler and controller are shown to provide actions for power management, voltage regulation and duty ratio adjustments. The detail models (DMs) are presented to validate the operation of the proposed MIMO converters, and the AVMs are developed and compared with the DMs. AVMs and DMs are shown to be in good agreement.

Secondly, general approaches for deriving MIMO converters are proposed. With basic building blocks, a basic structure based on DC-Link Inductor/DC-Link Capacitor DLI/DLC is proposed for the synthesis of a family of non-isolated MIMO converters. Connection rules for building blocks of PSCs and FCs are listed. Formalization of interface between multiple PSCs and FCs is realized by DLI or DLC with necessary switches. Following a uniform method, two types of DC-linked MIMO converters are obtained. In the end, a set of uniform rules for synthesizing general MIMO converters based on basic SISO converters are proposed. MIMO converters can be derived by replacing the PSC or original DC source of a conventional converter with series- or parallel connected PSCs, and the FC or original DC load with series- or parallel-connected FCs.

#### 7.2. FUTURE WORK

Realization of the proposed MIMO converters in hardware is not considered in this thesis. The theoretical derivation of the MIMO non-inverting buck—boost and flyback converters have been validated by computer simulations, but it is still worthwhile to investigate if their practical implementation would be effective for a specific application such as DC distribution system of a smart home with multiple DC sources and loads at different voltage levels.

The controllers employed with the MIMO converters proposed in Chapter 4–6 of the thesis have been demonstrated to be capable of regulating the input powers along with the output voltages. However, since the proposed methodology is based on linearization, more development and extensive analysis is required for controller tuning and optimal performance over wide range of operating conditions.

The converters presented in this thesis allows for only unidirectional power flow. However, to satisfy the application where an energy storage element is indispensable, bidirectional power flow is required. Instead of using additional converter for feeding the energy back, it would be desirable to analyze and synthesize bidirectional multiport converters.

#### REFERENCES

- [1] Central Electricity Authority, Ministry of Power, GOI, https://powermin.gov.in/en/content/power-sector-glance-all-india.
- [2] K. Hanada, Z. Litifu and K. Nagasaka, "Application of wind power generation for an agriculture region with weak wind speed," IEEE Power Engineering Society General Meeting, 2005, pp. 1262-1269, 2005, Vol. 2, doi: 10.1109/PES.2005.1489111.
- [3] V. V. Mehtre, S. G. Desai and D. S. Bankar, "Analysis of a Doubly Fed induction generator-based wind farm," 2016 IEEE Technological Innovations in ICT for Agriculture and Rural Development (TIAR), pp. 139-145, 2016, doi: 10.1109/TIAR.2016.7801228.
- [4] A. K. Mishra and B. Singh, "Solar Photovoltaic Array Dependent Dual Output Converter Based Water Pumping Using Switched Reluctance Motor Drive," in IEEE Transactions on Industry Applications, vol. 53, no. 6, pp. 5615-5623, Nov.-Dec. 2017, doi: 10.1109/TIA.2017.2732341.
- [5] N. Diaw, L. Thiaw, O. Ba, T. T. Soe, A. Swathi and G. Giridhar, "Techno-Economic Feasibility of Wind-Solar Hybrid Systems for Rural Electrification of Sioure Village in Sahel," 2019 IEEE 2nd International Conference on Renewable Energy and Power Engineering (REPE), pp. 196-201, 2019, doi: 10.1109/REPE48501.2019.9025141.
- [6] H. Wu, K. Sun, S. Ding and Y. Xing, "Topology Derivation of Nonisolated Three-Port DC–DC Converters from DIC and DOC," in IEEE Transactions on Power Electronics, vol. 28, no. 7, pp. 3297-3307, July 2013, doi: 10.1109/TPEL.2012.2221746.
- [7] J. Zeng, W. Qiao, L. Qu and Y. Jiao, "An Isolated Multiport DC–DC Converter for Simultaneous Power Management of Multiple Different Renewable Energy Sources," in IEEE Journal of Emerging and Selected Topics in Power Electronics, vol. 2, no. 1, pp. 70-78, March 2014, doi: 10.1109/JESTPE.2013.2293331.
- [8] H. Behjati and A. Davoudi, "A MIMO topology with series outputs: An interface between diversified energy sources and diode-clamped multilevel inverter," 2012 Twenty-Seventh Annual IEEE Applied Power Electronics Conference and Exposition (APEC), pp. 1-6, 2012, doi: 10.1109/APEC.2012.6165790.
- [9] B. G. Dobbs and P. L. Chapman, "A multiple-input DC-DC converter topology," in IEEE Power Electronics Letters, vol. 1, no. 1, pp. 6-9, March 2003, doi: 10.1109/LPEL.2003.813481.
- [10] A. Nami, F. Zare, A. Ghosh, and F. Blaabjerg, "Multi-output DC–DC converters based on diod-clamped converters configuration: Topology and control strategy," IET Power Electron., vol. 3, pp. 197–208, 2010.
- [11] T. Bhattacharya, V. S. Giri, K. Mathew and L. Umanand, "Multiphase Bidirectional Flyback Converter Topology for Hybrid Electric Vehicles," in IEEE Transactions on Industrial Electronics, vol. 56, no. 1, pp. 78-84, Jan. 2009, doi: 10.1109/TIE.2008.2004661.
- [12] S. M. Dehghan, M. Mohamadian, A. Yazdian and F. Ashrafzadeh, "Dual-input dual-output z-source inverter," 2009 IEEE Energy Conversion Congress and Exposition, pp. 3668-3674, 2009, doi: 10.1109/ECCE.2009.5316272.
- [13] K. Gummi and M. Ferdowsi, "Double-Input DC–DC Power Electronic Converters for Electric-Drive Vehicles—Topology Exploration and Synthesis Using a Single-Pole Triple-Throw Switch," in IEEE Transactions on Industrial Electronics, vol. 57, no. 2, pp. 617-623, Feb. 2010, doi: 10.1109/TIE.2009.2032762.
- [14] R. Ahmadi and M. Ferdowsi, "Double-Input Converters Based on H-Bridge Cells: Derivation, Small-Signal Modelling, and Power Sharing Analysis," in IEEE Transactions on Circuits and Systems I: Regular Papers, vol. 59, no. 4, pp. 875-888, April 2012, doi: 10.1109/TCSI.2011.2169910.

- [15] H. Krishnaswami and N. Mohan, "Three-Port Series-Resonant DC–DC Converter to Interface Renewable Energy Sources with Bidirectional Load and Energy Storage Ports," in IEEE Transactions on Power Electronics, vol. 24, no. 10, pp. 2289-2297, Oct. 2009, doi: 10.1109/TPEL.2009.2022756.
- [16] P. Thounthong, S. Pierfederici and B. Davat, "Analysis of Differential Flatness-Based Control for a Fuel Cell Hybrid Power Source," in IEEE Transactions on Energy Conversion, vol. 25, no. 3, pp. 909-920, Sept. 2010, doi: 10.1109/TEC.2010.2053037.
- [17] L. Wang, E. G. Collins and H. Li, "Optimal Design and Real-Time Control for Energy Management in Electric Vehicles," in IEEE Transactions on Vehicular Technology, vol. 60, no. 4, pp. 1419-1429, May 2011, doi: 10.1109/TVT.2011.2122272.
- [18] A. Payman, S. Pierfederici, F. Meibody-Tabar and B. Davat, "An Adapted Control Strategy to Minimize DC-Bus Capacitors of a Parallel Fuel Cell/Ultracapacitor Hybrid System," in IEEE Transactions on Power Electronics, vol. 26, no. 12, pp. 3843-3852, Dec. 2011, doi: 10.1109/TPEL.2009.2030683.
- [19] Bhim Singh, "Real-Time HIL Implementation of Sliding Mode Control for Standalone System Based on PV Array Without Using Dumpload" IEEE Transactions on Sustainable Energy, June 2015, volume: pp, issue: 99.
- [20] J. D. Dasika, B. Bahrani, M. Saeedifard, A. Karimi and A. Rufer, "Multivariable Control of Single-Inductor Dual-Output Buck Converters," in IEEE Transactions on Power Electronics, vol. 29, no. 4, pp. 2061-2070, April 2014, doi: 10.1109/TPEL.2013.2266616.
- [21] O. C. Onar and A. Khaligh, "A Novel Integrated Magnetic Structure Based DC/DC Converter for Hybrid Battery/Ultracapacitor Energy Storage Systems," in IEEE Transactions on Smart Grid, vol. 3, no. 1, pp. 296-307, March 2012, doi: 10.1109/TSG.2011.2150250.
- [22] Y. Liu and Y. Chen, "A Systematic Approach to Synthesizing Multi-Input DC/DC Converters," 2007 IEEE Power Electronics Specialists Conference, pp. 2626-2632, 2007, doi: 10.1109/PESC.2007.4342431.
- [23] F. Nejabatkhah, S. Danyali, S. H. Hosseini, M. Sabahi and S. M. Niapour, "Modelling and Control of a New Three-Input DC–DC Boost Converter for Hybrid PV/FC/Battery Power System," in IEEE Transactions on Power Electronics, vol. 27, no. 5, pp. 2309-2324, May 2012, doi: 10.1109/TPEL.2011.2172465.
- [24] G. A. Covic, G. L. Peters and J. T. Boys, "An improved single phase to three phase converters for low-cost AC motor drives," Proceedings of 1995 International Conference on Power Electronics and Drive Systems. PEDS 95, pp. 549-554, 1995 vol.1, doi: 10.1109/PEDS.1995.404863.
- [25] Albert Alexander S," Development of solar photovoltaic inverter with reduced harmonic distortions suitable for Indian sub-continent", Renewable and Sustainable Energy Reviews vol. 56, pp. 694–704, 2016.
- [26] I. Abdalla, J. Corda, L. Zhang," Multilevel DC-Link Inverter and Control Algorithm to Overcome the PV Partial Shading", IEEE Transactions on Power Electronics, Vol. 28, No. 1, pp. 14-18, January 2013.
- [27] Jibanesh Roy, Phanikumar Chamarthi, Vivek Agarwal," A Hybrid 9-level Inverter with Minimum Number of Switches for Single phase Grid connected Solar PV system", Proceedings of 43rd Photovoltaic Specialist Conference, pp.3252-3257, 5-10 June 2016, Portland, USA.
- [28] Asha Gaikwad, Pallavi Appaso Arbune," Study of Cascaded H-Bridge Multilevel Inverter", Proceedings of International conference on Automatic Control and Dynamic Optimization Techniques (ICACDOT), 9-10 Sept. 2016, Pune, India.

- [29] Ebrahim Babaei, Concettina Buccella, Maryam Saeedifard," Recent Advances in Multilevel Inverters and Their Applications—Part I ", IEEE transactions on industrial electronics, vol. 63, no. 11, pp. 7145-7147, November 2016.
- [30] Keliang Zhou and Danwei Wang, "Relationship between space-vector modulation and three-phase carrier-based PWM: a comprehensive analysis [three-phase inverters]," IEEE Transactions on Industrial Electronics, vol. 49, no. 1, pp. 186-196, Feb. 2002.
- [31] S. R. Bowes and Yen-Shin Lai, "The relationship between space-vector modulation and regular-sampled PWM," IEEE Transactions on Industrial Electronics, vol. 44, no. 5, pp. 670-679, Oct. 1997.
- [32] D. G. Holmes, "The general relationship between regular-sampled pulse-width-modulation and space vector modulation for hard switched converters," Conference Record of the 1992 IEEE Industry Applications Society Annual Meeting, Houston, TX, USA, vol.1, pp. 1002-1009, 1992.
- [33] R. Arulmozhiyal, K. Baskaran, N. Devarajan and J. Kanagaraj, "Space Vector Pulse Width Modulation Based Induction Motor Speed Control Using FPGA," 2009 Second International Conference on Emerging Trends in Engineering & Technology, Nagpur, pp. 742-747, 2009.
- [34] F. H. Aghdam and M. Abapour, "Reliability and Cost Analysis of Multistage Boost Converters Connected to PV Panels," in IEEE Journal of Photovoltaics, vol. 6, no. 4, pp. 981-989, July 2016, doi: 10.1109/JPHOTOV.2016.2566885.
- [35] A. Khosroshahi, M. Abapour and M. Sabahi, "Reliability Evaluation of Conventional and Interleaved DC–DC Boost Converters," in IEEE Transactions on Power Electronics, vol. 30, no. 10, pp. 5821-5828, Oct. 2015, doi: 10.1109/TPEL.2014.2380829.
- [36] M. J. Sathik, J. D. Navamani, A. Lavanya, Y. Yang, D. Almakhles and F. Blaabjerg, "Reliability Analysis of Power Components in Restructured DC/DC Converters," in IEEE Transactions on Device and Materials Reliability, vol. 21, no. 4, pp. 544-555, Dec. 2021, doi: 10.1109/TDMR.2021.3116941.
- [37] H. Tarzamni et al., "Reliability Assessment of Conventional Isolated PWM DC-DC Converters," in IEEE Access, vol. 9, pp. 46191-46200, 2021, doi: 10.1109/ACCESS.2021.3067935.
- [38] F. H. Aghdam and M. Abapour, "Reliability and Cost Analysis of Multistage Boost Converters Connected to PV Panels," in IEEE Journal of Photovoltaics, vol. 6, no. 4, pp. 981-989, July 2016, doi: 10.1109/JPHOTOV.2016.2566885.
- [39] A. Khosroshahi, M. Abapour and M. Sabahi, "Reliability Evaluation of Conventional and Interleaved DC–DC Boost Converters," in IEEE Transactions on Power Electronics, vol. 30, no. 10, pp. 5821-5828, Oct. 2015, doi: 10.1109/TPEL.2014.2380829.
- [40] F. Richardeau and T. T. L. Pham, "Reliability Calculation of Multilevel Converters: Theory and Applications," in IEEE Transactions on Industrial Electronics, vol. 60, no. 10, pp. 4225-4233, Oct. 2013, doi: 10.1109/TIE.2012.2211315.
- [41] H. Behjati and A. Davoudi, "Power budgeting between diversified energy sources and loads using a multiple-input multiple-output DC-DC converter," 49th IEEE/IAS Industrial & Commercial Power Systems Technical Conference, Stone Mountain, GA, USA, 2013, pp. 1-12, doi: 10.1109/ICPS.2013.6547333.
- [42] Y. Tong, Z. Shan, C. N.M. Ho, and J. Jatskevich, "Concept of synthesizing modular power supply for interfacing diverse energy sources and loads," in Proc. IEEE 16th Workshop Control Model. Power Electron., 2015, pp. 1–5.
- [43] B. L.-H. Nguyen, H. Cha, T. T. Nguyen, and H. G. Kim, "Family of integrated multi-input multi-output DC-DC power converters," in Proc. IEEE Int. Power Electron. Conf., 2018, pp. 3134–3139.

- [44] S. S. Amin and P. P. Mercier, "MISIMO: A multi-input single-inductor multi-output energy harvesting platform in 28-nm FDSOI for powering net-zero-energy systems," IEEE J. Solid-State Circuits, vol. 53, no. 12, pp. 3407–3419, Dec. 2018.
- [45] P. Mohseni, S. H. Hosseini, M. Sabahi, T. Jalilzadeh, and M. Maalandish, "A new high step-up multi-input multi-output DC–DC converter," IEEE Trans. Ind. Electron., vol. 66, no. 7, pp. 5197–5208, Jul. 2019.
- [46] S. Kumaravel, R. A. Narayanankutty, V. S. Rao, and A. Sankar, "Dual input—dual output DC–DC converter for solar PV/battery/ultra-capacitor powered electric vehicle application," IET Power Electron., vol. 12, no. 13, pp. 3351–3358, Nov. 2019.
- [47] W. Jiang and B. Fahimi, "Multiport power electronic interface concept, modeling, and design," IEEE Trans. Power Electron., vol. 26, no. 7, pp. 1890–1900, Jul. 2011.
- [48] D. Ma,W. Ki, C. Tsui, and P. K. T. Mok, "Single-inductor multiple-output switching converters with time-multiplexing control in discontinuous conduction mode," IEEE J. Solid-State Circuits, vol. 38, no. 1, pp. 89–100, Jan. 2003.
- [49] D. Ma, W. Ki, and C. Tsui, "A pseudo-CCM/DCM SIMO switching converter with freewheel switching," IEEE J. Solid-State Circuits, vol. 38, no. 6, pp. 1007–1014, Jun. 2003.
- [50] J. Jia and K. N. Leung, "Digital-control single-inductor triple-output DCDC converter with pre-sub-period inductor-current control," IEEE Trans. Power Electron., vol. 27, no. 4, pp. 2028–2042, Apr. 2012.
- [51] W. Ki and D.Ma, "Single-inductor multiple-output switching converters," in Proc. IEEE 32nd Annu. Power Electron. Spec. Conf., 2001, pp. 226–231.
- [52] S. Chen et al., "Embedded single-inductor bipolar-output DC–DC converter in class-D amplifier for low common noise," IEEE Trans. Power Electron., vol. 31, no. 4, pp. 3106–3117, Apr. 2016.
- [53] L. Benadero, V.Moreno-Font, R.Giral, and A. E.Aroudi, "Topologies and control of a class of single inductor multiple-output converters operating in continuous conduction mode," IET Power Electron., vol. 4, no. 8, pp. 927–935, Sep. 2011.
- [54] A. Nami, F. Zare, A. Ghosh, and F. Blaabjerg, "Multi-output DC–DC converters based on diode-clamped converters configuration: Topology and control strategy," IET Power Electron., vol. 3, no. 2, pp. 197–208, Mar. 2010.
- [55] X. Branca, B. Allard, X. Lin-Shi, and D. Chesneau, "Single-inductor bipolar-outputs converter for the supply of audio amplifiers in mobile platforms," IEEE Trans. Power Electron., vol. 28, no. 9, pp. 4248–4259, Sep. 2013.
- [56] A. A. Boora, F. Zare, and A. Ghosh, "Multi-output buck-boost converter with enhanced dynamic response to load and input voltage changes," IET Power Electron., vol. 4, no. 2, pp. 194–208, Feb. 2011.
- [57] L. Xian and Y. Wang, "Exact steady-state analysis in multiple-input converters applied with diverse time-sharing switching schemes," IET Power Electron., vol. 8, no. 5, pp. 724–734, May 2015.
- [58] J. A. A. Qahouq and Y. Jiang, "Distributed photovoltaic solar system architecture with single-power inductor single-power converter and single sensor single maximum power point tracking controller," IET Power Electron., vol. 7, no. 10, pp. 2600–2609, Oct. 2014.
- [59] A. Khaligh, J. Cao, and Y. Lee, "A multiple-input DC–DC converter topology," IEEE Trans. Power Electron., vol. 24, no. 3, pp. 862–868, Mar. 2009.
- [60] M. Jung, S. Park, J. Bang, and G. Cho, "An error-based controlled single-inductor 10-output DC–DC buck converter with high efficiency under light load using adaptive pulse modulation," IEEE J. Solid-State Circuits, vol. 50, no. 12, pp. 2825–2838, Dec. 2015.

- [61] W. Yang, H. Yang, C. Huang, K. Chen, and Y. Lin, "A High-efficiency single-inductor multiple-output buck-type LED driver with average current correction technique," IEEE Trans. Power Electron., vol. 33, no. 4, pp. 3375–3385, Apr. 2018.
- [62] Patra, A. Patra, and N. Misra, "A single-inductor multiple-output switcher with simultaneous buck, boost, and inverted outputs," IEEE Trans. Power Electron., vol. 27, no. 4, pp. 1936–1951, Apr. 2012.
- [63] H. Kim, C. S. Yoon, D. Jeong, and J. Kim, "A single-inductor, multiple channel current-balancing LED driver for display backlight applications," IEEE Trans. Ind. Appl., vol. 50, no. 6, pp. 4077–4081, Nov./Dec. 2014.
- [64] T. Gupta, A. Gupta, D. Joshi and M. A. Mallick, "Stability Analysis and Optimization of a Parasitic Buck Converter Using Leverrier's Algorithm and PI Controller," 2023 9th IEEE India International Conference on Power Electronics (IICPE), SONIPAT, India, 2023, pp. 1-6.
- [65] T. Gupta, A. Gupta and D. Joshi, "Stability Analysis and Control of Non-Ideal SEPIC Converters Using Leverrier's Algorithm and PI Controller Considering Parasitic Elements," 2023 3rd International Conference on Emerging Frontiers in Electrical and Electronic Technologies (ICEFEET), Patna, India, 2023, pp. 1-6.
- [66] P. S. Shandilya, A. Gupta and D. Joshi, "Voltage and Current Regulation in Cuk DC-DC Converters having Enhanced Closed-Loop Control using PID Controller," 2023 11th National Power Electronics Conference (NPEC), Guwahati, India, 2023, pp. 1-6.
- [67] Y.-C. Liu and Y.-M. Chen, "A systematic approach to synthesizing multi-input dc/dc converters," in Proc. IEEE PESC, 2007, pp. 2626–2632.
- [68] R. Tymerski and V. Vorperian, "Generation and classification of PWM dc-to-dc converters," IEEE Trans. Aerosp. Electron. Syst., vol. AES-24, no. 6, pp. 743–754, Nov. 1988.
- [69] D. Maksimovic and S. C'uk, "General properties and synthesis of PWM dc-to-dc converters," in Proc. IEEE PESC, 1989, vol. 2, pp. 515–525.
- [70] S. H. Choung and A. Kwasinski, "Multiple-input dc-dc converter topologies comparison," in Proc. IECON 2008, pp. 2359–2364.
- [71] W. -S. Liu, J. -F. Chen, T. -J. Liang, R. -L. Lin and C. -H. Liu, "Analysis, Design, and Control of Bidirectional Cascoded Configuration for a Fuel Cell Hybrid Power System," in IEEE Transactions on Power Electronics, vol. 25, no. 6, pp. 1565-1575, June 2010.
- [72] A. M. Imtiaz and F. H. Khan, ""Time Shared Flyback Converter" Based Regenerative Cell Balancing Technique for Series Connected Li-Ion Battery Strings," in IEEE Transactions on Power Electronics, vol. 28, no. 12, pp. 5960-5975, Dec. 2013.
- [73] M. G. Marangalu, N. V. Kurdkandi, S. H. Hosseini, H. Tarzamni, M. Dahidah and M. Sarhangzadeh, "A Modified Switched-Capacitor Based Seventeen-Level Inverter With Reduced Capacitor Charging Spike for RES Applications," in IEEE Open Journal of Power Electronics, vol. 4, pp. 579-602, 2023.
- [74] C. Pesce, R. Blasco, J. Riedemann, I. Andrade and R. Peña, "A DC-DC Converter Based On Modified Flyback Converter Topology," in IEEE Latin America Transactions, vol. 14, no. 9, pp. 3949-3956, Sept. 2016.
- [75] N. P. Papanikolaou and E. C. Tatakis, "Active voltage clamp in flyback converters operating in CCM mode under wide load variation," in IEEE Transactions on Industrial Electronics, vol. 51, no. 3, pp. 632-640, June 2004.
- [76] Marangalu, M.G., Kurdkandi, N.V., Babaei, E.: Single-source multilevel inverter based on flyback DC-DC converter. IET Power Electron. 14, 1237–1255 (2021).
- [77] J. Park, Y. -S. Roh, Y. -J. Moon and C. Yoo, "A CCM/DCM Dual-Mode Synchronous Rectification Controller for a High-Efficiency Flyback Converter," in IEEE Transactions on Power Electronics, vol. 29, no. 2, pp. 768-774, Feb. 2014.

- [78] K. Soltanzadeh, H. Khalilian, and M. Dehghani, "Analysis, design, and implementation of a zero-voltage switching two-switch CCM flyback converter," IET Circuits, Devices System, vol. 10, no. 1, pp. 20–28, Jan. 2016.
- [79] H. -J. Chiu et al., "A Single-Stage Soft-Switching Flyback Converter for Power-Factor-Correction Applications," in IEEE Transactions on Industrial Electronics, vol. 57, no. 6, pp. 2187-2190, June 2010.
- [80] Hamanah, W.M. Performance Analysis of SiC-Based DC/DC Converter for Solar Power Tower Heliostat Application. Arab J Sci Eng 48, 15207–15221 (2023).
- [81] P. Chetty, "Current injected equivalent circuit approach to modelling switching dc-dc converters," IEEE Transactions on Aerospace and Electronic Systems, vol. AES-17, no. 6, pp. 501 –505, Nov. 1981.
- [82] S. K. Pandey, S. L. Patil and S. B. Phadke, "Comment on "PWM-Based Adaptive Sliding-Mode Control for Boost DC–DC Converters" [Aug 13 3291-3294]," in IEEE Transactions on Industrial Electronics, vol. 65, no. 6, pp. 5078-5080, June 2018.
- [83] A. Gupta, K. Rana and D. Joshi, "Design and Analysis of Multioutput Flyback Converter under Continuous and Discontinuous Conduction mode using PID. Controller," 2020 First IEEE International Conference on Measurement, Instrumentation, Control and Automation (ICMICA), Kurukshetra, India, 2020, pp. 1-5.
- [84] Rajamani, M.P.E., Murugappan, M., Prakash, N.B. et al. Photovoltaic-Based Dual Output DC–DC Converter Using Gravitational Search Algorithm-Tuned PI and Sliding Mode Controllers. Arab J Sci Eng (2024).
- [85] N. Mukherjee and D. Strickland, "Control of Cascaded DC–DC Converter-Based Hybrid Battery Energy Storage Systems—Part II: Lyapunov Approach," in IEEE Transactions on Industrial Electronics, vol. 63, no. 5, pp. 3050-3059, May 2016.
- [86] A. Lekić, D. Stipanović and N. Petrović, "Controlling the Ćuk Converter Using Polytopic Lyapunov Functions," in IEEE Transactions on Circuits and Systems II: Express Briefs, vol. 65, no. 11, pp. 1678-1682, Nov. 2018.
- [87] J. M. Olm, E. Fossas, V. Repecho, A. Dòria-Cerezo and R. Grińó, "Adaptive Control-Based Voltage Regulation of a Magnetically Coupled Multiport DC-DC Converter for Electrified Vehicles Applications," 2020 IEEE International Symposium on Circuits and Systems (ISCAS), Seville, Spain, 2020, pp. 1-5.
- [88] W. Tang and P. Daoutidis, "A Bilevel Programming Approach to the Convergence Analysis of Control-Lyapunov Functions," in IEEE Transactions on Automatic Control, vol. 64, no. 10, pp. 4174-4179, Oct. 2019.
- [89] S. -M. Wi, J. S. Lee and M. Kim, "Exponentially Stable Lyapunov-Function-Based Controller for a Flyback CCM Converter," in IEEE Transactions on Industrial Electronics, vol. 65, no. 2, pp. 1213-1225, Feb. 2018.
- [90] M. G. Marangalu, N. V. Kurdkandi, K. K. Monfared, I. Talebian, Y. Neyshabouri and H. Vahedi, "A New High Step-Up SC-Based Grid-Tied Inverter With Limited Charging Spike for RES Applications," in IEEE Open Journal of Power Electronics, vol. 5, pp. 295-310, 2024.
- [91] A. Davoudi and J. Jatskevich, "Parasitics Realization in State-Space Average-Value Modeling of PWM DC–DC Converters Using an Equal Area Method," in IEEE Transactions on Circuits and Systems I: Regular Papers, vol. 54, no. 9, pp. 1960-1967, Sept. 2007.
- [92] Kumar, Vinod., Behera, Ranjan Kumar., Joshi, Dheeraj., Bansal, Ramesh. Power Electronics, Drives, and Advanced Applications. United States: CRC Press, 2020.
- [93] M. G. Marangalu, N. V. Kurdkandi, P. Alavi, S. Khadem, H. Tarzamni and A. Mehrizi-Sani, "A New Single DC Source Five-Level Boost Inverter Applicable to Grid-Tied Systems," in IEEE Access, vol. 11, pp. 24112-24127, 2023.

- [94] Battula, S, Garg, MM, Panda, AK, Senapati, L. Bidirectional quasi-Z-source DC-DC converter with Lyapunov function-based controller in stand-alone photovoltaic-connected system. Int J Circ Theor Appl. 2023; 51(5): 2327-2350.
- [95] Zhao, Q., Fang, Y., Wang, Z., Xie, Y. (2013). Small-Signal Model and Control of PV Grid-Connected Micro Inverter Based on Interleaved Parallel Flyback Converter. In: Sun, Z., Deng, Z. (eds) Proceedings of 2013 Chinese Intelligent Automation Conference. Lecture Notes in Electrical Engineering, vol 255. Springer, Berlin, Heidelberg.
- [96] N. M. Haegel and S. R. Kurtz, "Global Progress Toward Renewable Electricity: Tracking the Role of Solar," in IEEE Journal of Photovoltaics, vol. 11, no. 6, pp. 1335-1342, Nov. 2021.
- [97] Palanisamy R, Seenithangam J, Palanisamy R. A hybrid output multiport converter for standalone loads and photovoltaic array integration. Int Trans Electr Energ Syst. 2020; 30:e12410.
- [98] Tarassodi P, Adabi J, Rezanejad M. A power management strategy for a grid-connected multi-energy storage resources with a multiport converter. Int J Circ Theor Appl. 2023; 51(6): 2744-2759.
- [99] Malik MZ, Zhang S, Ali A, Farooq A. Design and implementation of a multi-port bidirectional converter for electric vehicle applications. Int J Circ Theor Appl. 2023; 51(10): 4728-4753.
- [100] H. Behjati and A. Davoudi, "Power budgeting between diversified energy sources and loads using a multiple-input multiple-output DC-DC converter," 49th IEEE/IAS Industrial & Commercial Power Systems Technical Conference, Stone Mountain, GA, USA, 2013, pp. 1-12.
- [101] A. Kwasinski, "Identification of Feasible Topologies for Multiple-Input DC–DC Converters," in IEEE Transactions on Power Electronics, vol. 24, no. 3, pp. 856-861, March 2009.
- [102] H. Matsuo, T. Shigemizu, F. Kurokawa and N. Watanabe, "Characteristics of the multiple-input DC-DC converter," Proceedings of IEEE Power Electronics Specialist Conference - PESC '93, Seattle, WA, USA, 1993, pp. 115-120.
- [103] Bizhani H, Techato K, Noroozian R, Muyeen SM, Blaabjerg F. A novel multiport converter switching scheme to integrate multiple renewable energy sources. Int J Circ Theor Appl. 2022; 50(5): 1750-1769.
- [104] Gaurav, N. Jayaram, S. Halder, K. P. Panda and S. V. K. Pulavarthi, "A Novel Design With Condensed Component of Multi-Input High Gain Non-isolated DC–DC Converter for Performance Enhancement in Carbon Neutral Energy Application," in IEEE Journal of Emerging and Selected Topics in Industrial Electronics, vol. 4, no. 1, pp. 37-49, Jan. 2023.
- [105] A. Khaligh, J. Cao and Y. -J. Lee, "A Multiple-Input DC–DC Converter Topology," in IEEE Transactions on Power Electronics, vol. 24, no. 3, pp. 862-868, March 2009.
- [106] V. A. K. Prabhala, D. Somayajula and M. Ferdowsi, "Power sharing in a double-input buck converter using dead-time control," 2009 IEEE Energy Conversion Congress and Exposition, San Jose, CA, USA, 2009, pp. 2621-2626.
- [107] Z. Li, O. Onar, A. Khaligh and E. Schaltz, "Design and Control of a Multiple Input DC/DC Converter for Battery/Ultra-capacitor Based Electric Vehicle Power System," 2009 Twenty-Fourth Annual IEEE Applied Power Electronics Conference and Exposition, Washington, DC, USA, 2009, pp. 591-596.
- [108] P. Luo, T. -J. Liang, K. -H. Chen, S. -M. Chen and J. -F. Chen, "Syntheses of Three-Port DC-DC Converters," in IEEE Transactions on Power Electronics, vol. 38, no. 12, pp. 16196-16207, Dec. 2023.

- [109] Kamaraj, V.; Chellammal, N.; Chokkalingam, B.; Munda, J.L. Minimization of Cross-Regulation in PV and Battery Connected Multi-Input Multi-Output DC to DC Converter. Energies 2020, 13, 6534.
- [110] Y. Zheng, J. Guo and K. N. Leung, "A Single-Inductor Multiple-Output Buck/Boost DC-DC Converter With Duty-Cycle and Control-Current Predictor," in IEEE Transactions on Power Electronics, vol. 35, no. 11, pp. 12022-12039, Nov. 2020.
- [111] Pathak, P.K., Yadav, A.K., Padmanaban, S., Alvi, P.A., Kamwa, I.: Fuel cell-based topologies and multi-input DC-DC power converters for hybrid electric vehicles: A comprehensive review. IET Gener. Transm. Distrib. 16, 2111–2139 (2022).
- [112] H. Wu, C. Wan, K. Sun and Y. Xing, "A High Step-Down Multiple Output Converter with Wide Input Voltage Range Based on Quasi Two-Stage Architecture and Dual-Output LLC Resonant Converter," in IEEE Transactions on Power Electronics, vol. 30, no. 4, pp. 1793-1796, April 2015.
- [113] Y. Zhang and D. Xu, "Design and Implementation of an Accurately Regulated Multiple Output ZVS DC–DC Converter," in IEEE Transactions on Power Electronics, vol. 22, no. 5, pp. 1731-1742, Sept. 2007.
- [114] X. L. Li, C. K. Tse and D. D. -C. Lu, "Single-Inductor Multi-Input Multi-Output DC-DC Converter with High Flexibility and Simple Control," 2020 IEEE International Symposium on Circuits and Systems (ISCAS), Seville, Spain, 2020, pp. 1-5.
- [115] H. Behjati and A. Davoudi, "A MIMO topology with series outputs: An interface between diversified energy sources and diode-clamped multilevel inverter," 2012 Twenty-Seventh Annual IEEE Applied Power Electronics Conference and Exposition (APEC), Orlando, FL, USA, 2012, pp. 1-6.
- [116] H. Behjati and A. Davoudi, "A Multiple-Input Multiple-Output DC–DC Converter," in IEEE Transactions on Industry Applications, vol. 49, no. 3, pp. 1464-1479, May-June 2013, doi: 10.1109/TIA.2013.2253440.
- [117] M. Salimi, F. Radmand and M. H. Firouz, "Dynamic Modeling and Closed-loop Control of Hybrid Grid-connected Renewable Energy System with Multi-input Multi-output Controller," in Journal of Modern Power Systems and Clean Energy, vol. 9, no. 1, pp. 94-103, January 2021.
- [118] Z. Saadatizadeh, P. C. Heris and H. A. Mantooth, "Modular Expandable Multiinput Multioutput (MIMO) High Step-Up Transformerless DC–DC Converter," in IEEE Access, vol. 10, pp. 53124-53142, 2022.
- [119] M. Veerachary and A. Trivedi, "Linear Matrix Inequality-Based Multivariable Controller Design for Boost Cascaded Charge-Pump-Based Double-Input DC–DC Converter," in IEEE Transactions on Industry Applications, vol. 58, no. 6, pp. 7515-7528, Nov.-Dec. 2022.
- [120] S. Rostami, V. Abbasi and M. Parastesh, "Design and Implementation of a Multiport Converter Using Z-Source Converter," in IEEE Transactions on Industrial Electronics, vol. 68, no. 10, pp. 9731-9741, Oct. 2021.
- [121] K. Filsoof and P. W. Lehn, "A Bidirectional Multiple-Input Multiple-Output Modular Multilevel DC–DC Converter and its Control Design," in IEEE Transactions on Power Electronics, vol. 31, no. 4, pp. 2767-2779, April 2016.
- [122] D. Sadeghpour and J. Bauman, "Integrated Three-Port Converter for Solar-Charged Electric Vehicle Applications," in IEEE Transactions on Industrial Electronics, vol. 71, no. 7, pp. 6907-6917, July 2024.
- [123] H. Behjati and A. Davoudi, "A Multiple-Input Multiple-Output DC–DC Converter," in IEEE Transactions on Industry Applications, vol. 49, no. 3, pp. 1464-1479, May-June 2013.

- [124] B. Wang, X. Zhang, J. Ye and H. B. Gooi, "Deadbeat Control for a Single-Inductor Multiple-Input Multiple-Output DC–DC Converter," in IEEE Transactions on Power Electronics, vol. 34, no. 2, pp. 1914-1924, Feb. 2019.
- [125] A. Nahavandi, M. T. Hagh, M. B. B. Sharifian and S. Danyali, "A non-isolated multiinput multioutput DC–DC boost converter for electric vehicle applications," in IEEE Transactions on Power Electronics, vol. 30, no. 4, pp. 1818-1835, April 2015.
- [126] Anees, M., Nasir, M., Ahmad Zaffar, N., Abbas Khan, H., Vasquez, J.C. and Guerrero, J.M. (2020), Scalable architecture of DC microgrid implemented with multi-input multioutput converter. IET Power Electronics, 13: 4480-4489.
- [127] K. Sundareswaran and V. T. Sreedevi, "Boost Converter Controller Design Using Queen-Bee-Assisted GA," in IEEE Transactions on Industrial Electronics, vol. 56, no. 3, pp. 778-783, March 2009.
- [128] K. Deb, A. Pratap, S. Agarwal and T. Meyarivan, "A fast and elitist multiobjective genetic algorithm: NSGA-II," in IEEE Transactions on Evolutionary Computation, vol. 6, no. 2, pp. 182-197, April 2002.
- [129] Kumar, Vinod., Behera, Ranjan Kumar., Joshi, Dheeraj., Bansal, Ramesh. Power Electronics, Drives, and Advanced Applications. United States: CRC Press, 2020.
- [130] M. -H. Huang and K. -H. Chen, "Single-Inductor Multi-Output (SIMO) DC-DC Converters With High Light-Load Efficiency and Minimized Cross-Regulation for Portable Devices," in IEEE Journal of Solid-State Circuits, vol. 44, no. 4, pp. 1099-1111, April 2009.
- [131] D. Tamilselvan, Sudhakar T D, Optimizing renewable energy utilization with high gain converters, Renewable and Sustainable Energy Reviews, Volume 191, 2024, 114105, ISSN 1364-0321.
- [132] Arzu Turksoy, Ahmet Teke, Alkan Alkaya, A comprehensive overview of the dc-dc converter-based battery charge balancing methods in electric vehicles, Renewable and Sustainable Energy Reviews, Volume 133, 2020, 110274, ISSN 1364-0321.
- [133] M. Rasouli, M. Mehrasa, A. Ganjavi, M. S. Sadabadi, H. Ghoreishy and A. Ale Ahmad, "Lyapunov-Based Control Strategy for a Single-Input Dual-Output Three-Level DC/DC Converter," in IEEE Transactions on Industrial Electronics, vol. 70, no. 10, pp. 10486-10495, Oct. 2023.
- [134] Abdelfatah Kolli, Arnaud Gaillard, Alexandre De Bernardinis, Olivier Bethoux, Daniel Hissel, Zoubir Khatir, A review on DC/DC converter architectures for power fuel cell applications, Energy Conversion and Management, Volume 105, 2015, Pages 716-730,ISSN 0196-8904.
- [135] B. Mangu, S. Akshatha, D. Suryanarayana, and B. G. Fernandes, "Grid connected PV-Wind-Battery-Based multi-input transformer-coupled bidirectional DC-DC converter for household applications," IEEE J. Emerg. Sel. Topics Power Electron., vol. 4, no. 3, pp. 1086–1095, Sep. 2016.
- [136] J. Deng, H. Wang, and M. Shang, "A ZVS three-port DC/DC converter for high-voltage bus-based photovoltaic systems," IEEE Trans. Power Electron., vol. 34, no. 11, pp. 10688–10699, Nov. 2019.
- [137] H. Krishnaswami and N. Mohan, "Three-port series-resonant DC–DC converter to interface renewable energy sources with bidirectional load and energy storage ports," IEEE Trans. Power Electron., vol. 24, no. 10, pp. 2289–2297, Oct. 2009.
- [138] Azuka Affam, Yonis M. Buswig, Al-Khalid Bin Hj Othman, Norhuzaimin Bin Julai, Ohirul Qays, A review of multiple input DC-DC converter topologies linked with hybrid electric vehicles and renewable energy systems, Renewable and Sustainable Energy Reviews, Volume 135, 2021, 110186, ISSN 1364-0321.

- [139] P. Prabhakaran and V. Agarwal, "Novel four-port DC–DC converter for interfacing solar PV–Fuel cell hybrid sources with low-voltage bipolar DC microgrids," IEEE J. Emerg. Sel. Topics Power Electron., vol. 8, no. 2, pp. 1330–1340, Jun. 2020.
- [140] P. Mohseni, S. H. Hosseini, M. Sabahi, T. Jalilzadeh and M. Maalandish, "A New High Step-Up Multi-Input Multi-Output DC-DC Converter," in IEEE Transactions on Industrial Electronics, vol. 66, no. 7, pp. 5197-5208, July 2019.
- [141] Gupta Ashutosh and Joshi Dheeraj, "Mathematical modeling and stress-aware stability analysis of a nonideal multiport Single Inductor DC–DC converter for renewable energy," International Journal of Circuit Theory and Applications.
- [142] M. R. Al-Soeidat, H. Aljarajreh, H. A. Khawaldeh, D. D. -C. Lu, and J. Zhu, "A reconfigurable three-port DC–DC converter for integrated PV Battery system," IEEE J. Emerg. Sel. Topics Power Electron., vol. 8, no. 4, pp. 3423–3433, Dec. 2020.
- [143] A. Nahavandi, M. T. Hagh, M. B. B. Sharifian and S. Danyali, "A nonisolated multiinput multioutput DC–DC boost converter for electric vehicle applications," in IEEE Transactions on Power Electronics, vol. 30, no. 4, pp. 1818-1835, April 2015.
- [144] A. A. Saafan, V. Khadkikar, M. S. El Moursi and H. H. Zeineldin, "A New Multiport DC-DC Converter for DC Microgrid Applications," 2021 IEEE Industry Applications Society Annual Meeting (IAS), Vancouver, BC, Canada, 2021, pp. 1-7.
- [145] A. Shahin, B. Huang, J.P. Martin, S. Pierfederici, B. Davat, New non-linear control strategy for non-isolated DC/DC converter with high voltage ratio, Energy Conversion and Management, Volume 51, Issue 1, 2010, Pages 56-63, ISSN 0196-8904.
- [146] H. Zhang, D. Dong, M. Jing, W. Liu and F. Zheng, "Topology Derivation of Multiple-Port DC–DC Converters Based on Voltage-Type Ports," in IEEE Transactions on Industrial Electronics, vol. 69, no. 5, pp. 4742-4753, May 2022.
- [147] I. Ninma Jiya, H. Van Khang, N. Kishor and R. M. Ciric, "Novel Family of High-Gain Nonisolated Multiport Converters With Bipolar Symmetric Outputs for DC Microgrids," in IEEE Transactions on Power Electronics, vol. 37, no. 10, pp. 12151-12166, Oct. 2022.
- [148] R. Liu, G. Zhou, Q. Tian and G. Xu, "Extendable Multiport High Step-Up DC–DC Converter for Photovoltaic-Battery Systems With Reduced Voltage Stress on Switches/Diodes," in IEEE Transactions on Industrial Electronics, vol. 70, no. 9, pp. 9123-9135, Sept. 2023.
- [149] H. Behjati and A. Davoudi, "Power budgeting between diversified energy sources and loads using a multiple-input multiple-output DC-DC converter," 49th IEEE/IAS Industrial & Commercial Power Systems Technical Conference, Stone Mountain, GA, USA, 2013, pp. 1-12.
- [150] Z. Saadatizadeh, P. C. Heris, E. Babaei and M. Sabahi, "A New Nonisolated Single-Input Three-Output High Voltage Gain Converter With Low Voltage Stresses on Switches and Diodes," in IEEE Transactions on Industrial Electronics, vol. 66, no. 6, pp. 4308-4318, June 2019.
- [151] A. Nahavandi, M. T. Hagh, M. B. B. Sharifian and S. Danyali, "A non-isolated multiinput multioutput DC–DC boost converter for electric vehicle applications," in IEEE Transactions on Power Electronics, vol. 30, no. 4, pp. 1818-1835, April 2015.
- [152] Fang Zheng Peng, "Z-source inverter," in IEEE Transactions on Industry Applications, vol. 39, no. 2, pp. 504-510, March-April 2003.
- [153] Y. Tang, S. Xie and C. Zhang, "An Improved Z -Source Inverter," in IEEE Transactions on Power Electronics, vol. 26, no. 12, pp. 3865-3868, Dec. 2011.
- [154] , An overview for the Z-Source Converter in motor drive applications, Renewable and Sustainable Energy Reviews, Volume 61, 2016, Pages 537-555, ISSN 1364-0321.
- [155] Y. Tang, S. Xie and C. Zhang, "Single-Phase Z-Source Inverter," in IEEE Transactions on Power Electronics, vol. 26, no. 12, pp. 3869-3873, Dec. 2011.

- [156] M. Zhu, K. Yu and F. L. Luo, "Switched Inductor Z-Source Inverter," in IEEE Transactions on Power Electronics, vol. 25, no. 8, pp. 2150-2158, Aug. 2010.
- [157] H. Shen, B. Zhang, D. Qiu and L. Zhou, "A Common Grounded Z-Source DC–DC Converter With High Voltage Gain," in IEEE Transactions on Industrial Electronics, vol. 63, no. 5, pp. 2925-2935, May 2016.
- [158] H. Shen, B. Zhang and D. Qiu, "Hybrid Z-Source Boost DC–DC Converters," in IEEE Transactions on Industrial Electronics, vol. 64, no. 1, pp. 310-319, Jan. 2017.
- [159] M. Abbasi Shahabi, M. Mardaneh, A. Rajaei, A. Nabinezhad, E. Jamshidpour and P. Poure, "Symmetric Wide-Input-Voltage Range Boost Z-Source DC–DC Converter With Reduced Current of Source and Active Components," in IEEE Transactions on Power Electronics, vol. 38, no. 8, pp. 9961-9971, Aug. 2023.
- [160] S. Rostami, V. Abbasi and M. Parastesh, "Design and Implementation of a Multiport Converter Using Z-Source Converter," in IEEE Transactions on Industrial Electronics, vol. 68, no. 10, pp. 9731-9741, Oct. 2021.
- [161] X. L. Li, C. K. Tse and D. D. -C. Lu, "Single-Inductor Multi-Input Multi-Output DC-DC Converter with High Flexibility and Simple Control," 2020 IEEE International Symposium on Circuits and Systems (ISCAS), Seville, Spain, 2020, pp. 1-5.
- [162] H. Behjati and A. Davoudi, "A Multiple-Input Multiple-Output DC–DC Converter," in IEEE Transactions on Industry Applications, vol. 49, no. 3, pp. 1464-1479, May-June 2013.
- [163] M. Salimi, F. Radmand and M. H. Firouz, "Dynamic Modeling and Closed-loop Control of Hybrid Grid-connected Renewable Energy System with Multi-input Multi-output Controller," in Journal of Modern Power Systems and Clean Energy, vol. 9, no. 1, pp. 94-103, January 2021.

## LIST OF PUBLICATIONS

#### Journals

- D. Joshi and A. Gupta, "Controller Design and Modeling of a Single-Switch Fifth-Order High-Voltage-Gain Converter with Parasitics for Electric Vehicle Charging," in IEEE Transactions on Transportation Electrification, vol. 11, no. 4, pp. 10647-10659, Aug. 2025, doi: 10.1109/TTE.2025.3553705.
- Gupta A, Joshi D. "Mathematical Modeling and Stress-aware Stability Analysis of a Nonideal Multiport Single Inductor DC–DC converter for Renewable Energy". International Journal of Circuit Theory and Applications. 2025; 53(5): 2602-2633. doi:10.1002/cta.4234
- A. Gupta and D. Joshi, "Mathematical Analysis and Topology Derivation for a Family of Novel Dual Output High-Voltage Gain Z-Source Converter for Renewable Energy Application," International Journal of Circuit Theory and Applications 53, no. 8 (2025): 4735–4753, doi: 10.1002/cta.4369.
- Urooj, S., Joshi, D., Gupta, A. et al. Derivation Analysis and Control of Multiport Flyback Converter with Lyapunov Function-Based Controller in Renewable Energy Systems Considering Circuit Parasitics. Arab J Sci Eng 50, 5711–5725 (2025). doi: 10.1007/s13369-024-09493-6
- Shandilya, Praanshu Srijan and Gupta, Ashutosh and Joshi, Dheeraj, "Proportional Integral Derivative-Based Closed-Loop Voltage Mode Control for Addressing Non-Idealities in Ćuk Converters for Renewable Energy Application", Johnson Matthey Technology Review, 2025, (69)-4, 602-612. doi: 10.1595/205651325X17335005701531

## Conferences

- A. Gupta and D. Joshi, "Design and Analysis of Novel Tristate Quasi-Z-Source Converter with Improved Dynamic Performance," 2025 IEEE North-East India International Energy Conversion Conference and Exhibition (NE-IECCE), Silchar, India, 2025, pp. 1-6, doi: 10.1109/NE-IECCE64154.2025.11183030.
- A. Gupta and D. Joshi, "Analysis and Modeling of Induction Motor with Advanced Capacitor Braking Using Adaptive Neural Network," 2023 9th IEEE India International Conference on Power Electronics (IICPE), SONIPAT, India, 2023, pp. 1-6, doi: 10.1109/IICPE60303.2023.10474911.
- A. Gupta and D. Joshi, "Electric Vehicle Battery Charging Utilizing High Gain Luo Converter with Power Factor Correction," 2023 3rd International Conference on Emerging Frontiers in Electrical and Electronic Technologies (ICEFEET), Patna, India, 2023, pp. 1-6, doi: 10.1109/ICEFEET59656.2023.10452201.
- T. Gupta, A. Gupta and D. Joshi, "Stability Analysis and Control of Non-Ideal SEPIC Converters Using Leverrier's Algorithm and PI Controller Considering Parasitic Elements," 2023 3rd International Conference on Emerging Frontiers in Electrical and Electronic Technologies (ICEFEET), Patna, India, 2023, pp. 1-6, doi: 10.1109/ICEFEET59656.2023.10452208.
- T. Gupta, A. Gupta, D. Joshi and M. A. Mallick, "Stability Analysis and Optimization of a Parasitic Buck Converter Using Leverrier's Algorithm and PI Controller," 2023 9th IEEE India International Conference on Power Electronics (IICPE), SONIPAT, India, 2023, pp. 1-6, doi: 10.1109/IICPE60303.2023.10474949.
- P. S. Shandilya, A. Gupta and D. Joshi, "Voltage and Current Regulation in Cuk DC-DC Converters having Enhanced Closed-Loop Control using PID Controller," 2023 11th National Power Electronics Conference (NPEC), Guwahati, India, 2023, pp. 1-6, doi: 10.1109/NPEC57805.2023.10385025.
- P. S. Shandilya, Ashutosh, D. Joshi and N. Kumar, "Modelling of PID-based Closed-Loop Voltage Mode Control for Cuk Converter with Circuit Parasitics," 2024 IEEE 4th International Conference on Sustainable Energy and Future Electric

Transportation (SEFET), Hyderabad, India, 2024, pp. 1-5, doi: 10.1109/SEFET61574.2024.10718041.